Yang, Xiaobo (2002) *Numerical study of film cooling in hypersonic flows.* PhD thesis.

Numerical Study of Film Cooling in Hypersonic Flows

Xiaobo Yang, B.Eng.

Thesis submitted to the Department of Aerospace Engineering,
Faculty of Engineering, University of Glasgow
for the degree of Doctor of Philosophy

November 2002

Declaration

I hereby declare that this dissertation is a record of work carried out in the Department of Aerospace Engineering at the University of Glasgow during the period from October 1999 to October 2002. The dissertation is original in content except where otherwise indicated.

November 2002

[redacted]

(Xiaobo Yang)

Abstract

In this thesis, a numerical study of film cooling in hypersonic laminar and turbulent flows has been performed using an in-house Navier-Stokes solver. The aim of this computational work is to investigate the mechanism and effectiveness of film cooling in hypersonic laminar and turbulent flows.

Hypersonic flow over a flat plate without film cooling was first studied to provide a reference datum to check the effectiveness of film cooling. For laminar film cooling ($M_\infty = 9.9$), three different primary flow conditions were first used for validation. The inclusion of the development of the flow in the plenum chamber upstream of the slot was found to provide better heat prediction than a uniform boundary condition at the slot exit. Detailed information of the flow field including velocity profile, Mach contour, temperature contour and heat transfer rate was presented. The mechanism of film cooling has been revealed according to the plots of calculated velocity profiles, Mach contours and temperature contours downstream of the slot. The coolant fluid was found to affect the primary boundary layer in two ways: 1) initially a separate layer established by the coolant fluid itself in the near slot area, 2) later a mixing layer between the primary and coolant flow streams. Then five coolant injection rates between 2.95×10^{-4} and $7.33 \times 10^{-4}\, kg/s$ and three slot heights, 0.8382, 1.2192, 1.6002 mm, were examined in hypersonic laminar film cooling.

For turbulent film cooling ($M_\infty = 8.2$), for the geometry used in the experiment, the injection at an angle of 20° was found to be appropriate. Different turbulence models including Wilcox's $k - \omega$ model, Menter's baseline and SST model have been tested. It is concluded that the Wilcox's $k - \omega$ turbulence model with dilatation-dissipation correction provides the best heat prediction. Again, five coolant injection rates varied from 5.07×10^{-4} to $30.69 \times 10^{-4}\, kg/s$ and three slot heights (the same as studied in the laminar film cooling) were studied to check the influence on film cooling effectiveness.

Both the coolant and the primary flow were air. Film cooling was found to be an effective way to protect wall surfaces that are exposed under a high heat transfer environment especially in hypersonic laminar flow. Increasing the coolant injection rate can obviously increase the film cooling effectiveness. Again, this works better in laminar flow than in turbulent flow. The coolant injection rate in turbulent flow should be considered to be high enough to give good heat protection. Slot height in both laminar and turbulent flows under the flow conditions in this study was found to be less important, which means other factors can be considered in priority when constructing film cooling systems.

With the application of curve fitting, the cooling length was described using power laws according to curve fitting results. A two-equation film cooling model has been presented to illustrate the relation between the film cooling effectiveness and the parameter $x/(h\,\dot{m})$. For film cooling effectiveness in log-log coordinates, a second-order polynomial curve can be used to fit the laminar flows, whilst a straight line is suitable for the turbulent flows.

Acknowledgement

I would like to express my heartfelt appreciation to Dr. Ken J. Badcock and Prof. Bryan E. Richards for the provision of the research student position in the Department of Aerospace Engineering and their excellent supervision during my study at the University of Glasgow.

I would also like to thank Dr. George N. Barakos and other members in the CFD group and the Department for their very useful help of my study.

This work was supported by the University of Glasgow Postgraduate Scholarship and the Committee of Vice-Chancellors and Principals (CVCP) of the Universities of the United Kingdom through the Overseas Research Students (ORS) Awards Scheme.

Finally, I would like to express my special thanks to my wife, Hongmei, my son, Hao and my parents.

Contents

List of Tables

List of Figures

Nomenclature

c	speed of sound
c_p	specific heat (constant pressure), $c_p = 1004.5\, J/(kg\, K)$ for air at $300\, K$
C_p	pressure coefficient, $C_p = (p - p_\infty)/(\frac{1}{2}\rho_\infty U_\infty^2)$
C_f	skin friction, $C_f = \tau_w/(\frac{1}{2}\rho_\infty U_\infty^2)$
E	total energy per unit mass
F, G, H	functions/fluxes
$\mathbf{F}, \mathbf{G},$	convective fluxes
h	step height (slot height plus lip height)/enthalpy, $h = c_p T$
$H(x)$	Heaviside step function
$\mathbf{I}$	identity matrix
$\mathbf{J}$	Jacobian matrix
k	kinetic energy of turbulent fluctuations, $k = \frac{1}{2}\overline{u_i^{'} u_i^{'}} = \frac{1}{2}\left(\overline{u_i^{'2}} + \overline{u_i^{'2}} + \overline{w^{'2}}\right)$
	/thermal conductivity
l	lip height
L	length of flat plate/length of flat plate downstream of the slot exit
$\dot{m}$	the ratio of coolant mass flux per unit area to primary stream mass
	flux per unit area, $\dot{m} = \rho_c u_c/\rho_\infty u_\infty$
M	Mach number
p	pressure
P	production term
Pr	Prandtl number, $Pr = \mu c_p/k = 0.72$
Pr_t	turbulent Prandtl number, $Pr_t = \mu_t c_p/k = 0.90$

$\dot{q}$	heat transfer rate
$\mathbf{Q}$	vector of conservative variables
q_x, q_y	heat flux vector components
R	perfect gas constant
$\mathbf{R}$	residual vector
Re	Reynolds number
s	slot height
S	source term
S_{ij}	mean strain rate tensor, $S_{ij} = \frac{1}{2}\left(\frac{\partial u_i}{\partial x_j} + \frac{\partial u_j}{\partial x_i}\right)$
t	time
T	temperature
u, v	velocity components
u_τ	friction velocity, $u_\tau = \sqrt{\tau_w/\rho_w}$
$u_i^{'}, u_j^{'}$	temporal average of fluctuating velocities
V	control volume
$\dot{w}$	injection rate
x, y	cartesian coordinates
y^+	dimensionless wall distance, $y^+ = u_\tau y/\nu$
y_1^+	y^+ at next point away from the wall

Greek Symbols

α	injection angle/closure coefficient
β, β^*	closure coefficients
β_0^*	closure coefficient of turbulence model
β_1, β_2	closure coefficients of turbulence model
γ	specific heat ratio/closure coefficient
γ_1, γ_2	closure coefficients of turbulence model

δ	thickness of the mixing layer
Δy_1	distance to the point next to the wall
ϵ	turbulent dissipation rate, $\epsilon = \nu \overline{\frac{\partial u_i'}{\partial x_k}\frac{\partial u_i'}{\partial x_k}}$
η	film cooling effectiveness, $\eta = 1 - \dot{q}_c/\dot{q}_0$
κ	von Karman constant, $\kappa = 0.41$
Λ	closure coefficient of turbulence model
μ	laminar molecular viscosity
μ_t	turbulent eddy viscosity
ν	kinematic molecular viscosity, $\nu = \mu/\rho$
ν_t	kinematic eddy viscosity, $\nu_t = \mu_t/\rho$
$\widetilde{\nu}$	undamped eddy viscosity in the S-A turbulence model
ξ, η, ζ	curvilinear coordinates
ξ^*	closure coefficient of turbulence model
ρ	density
σ, σ^*	closure coefficients of turbulence model
σ_k, σ_ω	closure coefficients of turbulence model
$\sigma_{k1}, \sigma_{\omega 1}$	closure coefficients of turbulence model
$\sigma_{k2}, \sigma_{\omega 2}$	closure coefficients of turbulence model
τ	stress
ω	specific turbulent dissipation rate, $\omega = \epsilon/k$
Ω	absolute value of vorticity

Superscripts

i	inviscid
v	viscous
$*$	non-dimensionalised value

Subscripts

0	stagnation/reference values
ad	adiabatic values
c	coolant flow values
i, j, k	location of control volume
p	primary flow values
t	turbulent values
w	wall values
x, y	components in x, y directions
∞	freestream values

Acronyms

CFD	computational fluid dynamics
CFL	Courant-Freidrick-Levy
LFC	laminar film cooling
LFP	laminar flow over a flat plate
MUSCL	Monotone Upstream-Centred Schemes for Conservation Laws
PFC	primary flow conditions
PMB	Parallel Multi-Block
TFC	turbulent film cooling
TFP	turbulent flow over a flat plate

Chapter 1

Introduction

1.1 Film cooling models

1.1.1 Definition of film cooling

In 1966, Goldstein *et al.* [1] defined film cooling as

"The employment of a secondary fluid injected through discrete slots to insulate thermally a solid surface from a gas stream flowing over it is called film cooling."

From this definition, it is clear that film cooling introduces a secondary fluid into the primary flow stream in order to decrease the heat transfer rate from the primary flow stream to the solid wall or the wall temperature. With the wall surface temperature at a lower level, less expensive materials can be used in structural fabrication. Film cooling might be used on blades of gas turbines, scramjet intake surfaces and combustor walls of high-speed vehicles, rocket nozzles and the extension surfaces of rockets all of which usually work under high heating loads.

Fig. 1.1 gives two examples of the application of film cooling. In Fig. 1.1(a), film cooling is applied in a scramjet engine combustor wall with some hydrogen fuel injected parallel to the wall through small supersonic slots to provide a lower energy buffer layer between the engine core flow and the structure (Olsen *et al.* [2]). In Fig. 1.1(b), an

ACE turbine geometry and cooling arrangement are shown schematically (Garg [3]). Modern gas turbine engines are designed to operate at inlet temperatures of 1800-2000 K, which are far beyond allowable metal temperature. The turbine blades need to be cooled under these conditions in order to increase their lifetime. So an efficient cooling system is required. Discrete jet film cooling is applied in this turbine blade with 93 holes on each blade.

Although film cooling is a technique to give heat protection for wall surfaces, it was first studied by Wieghardt as a method for de-icing airplane wings in 1940s. Here it could be described more aptly as "film heating". Subsequently, film cooling was considered as a technique which could be used to protect solid surfaces encountering a high heat transfer or high temperature environment. In [4], Kanda *et al.* suggested using a combination of film cooling and regenerative cooling to achieve thermal protection while minimising fuel flow requirements in a scramjet engine combustor.

Fig. 1.2 given by Kanda *et al.* [4] shows three cooling systems: a) film cooling only, b) regenerative cooling only and c) a combination of film and regenerative cooling. Usually hydrogen is used as the propellant and it is also used as the coolant in all the three types of scramjet engines. In the engine with only film cooling, it is cooled with the cold hydrogen injection while in the engine with only regenerative cooling, it is cooled by heating the fuel - hydrogen. The engine using a combination of the two cooling methods together was found to provide best cooling efficiency.

Besides providing heat protection for the wall surfaces, film cooling can also be used to control flow separation. When the coolant fluid is injected downstream through a rearward facing tangential slot, the skin friction generally increases or decreases according to whether the specific momentum of the coolant flow is greater than or less than that of the primary flow stream. With the coolant flow stream momentum greater than the primary flow stream momentum, the flow configuration is often referred to as a wall jet, which will increase the skin friction and may be used to delay separation.

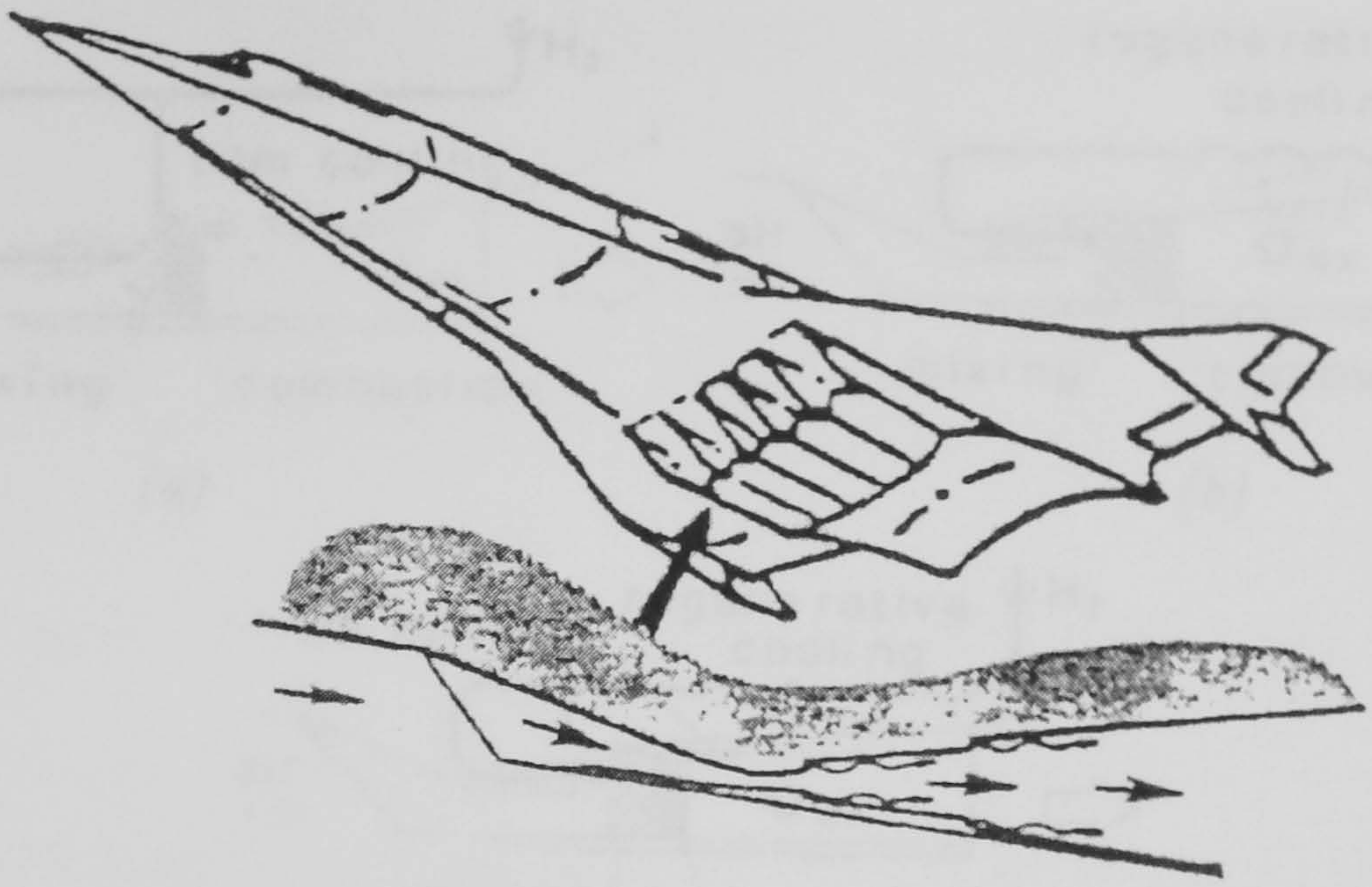

(a) Scramjet engine

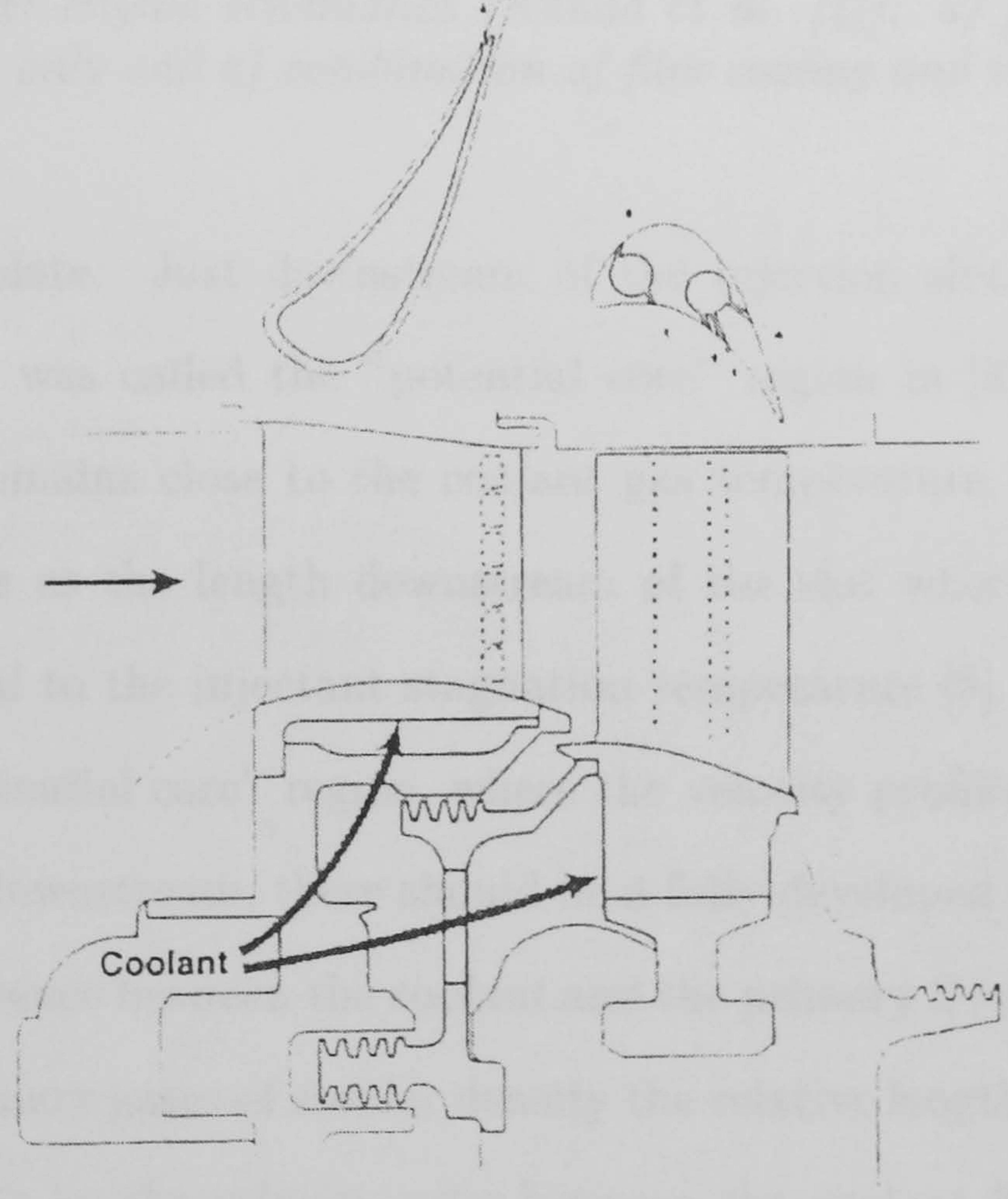

(b) ACE turbine blade

Figure 1.1: *Film cooling applications: a) scramjet engine (Olsen et al. [2]), b) ACE turbine blade (Garg [3])*

1.1.2 Stollery and El-Ehwany's film cooling model

A film cooling model was first described by Stollery and El-Ehwany [8]. In Fig. 1.3, three separate regions were recognised in film cooling using coolant injection through

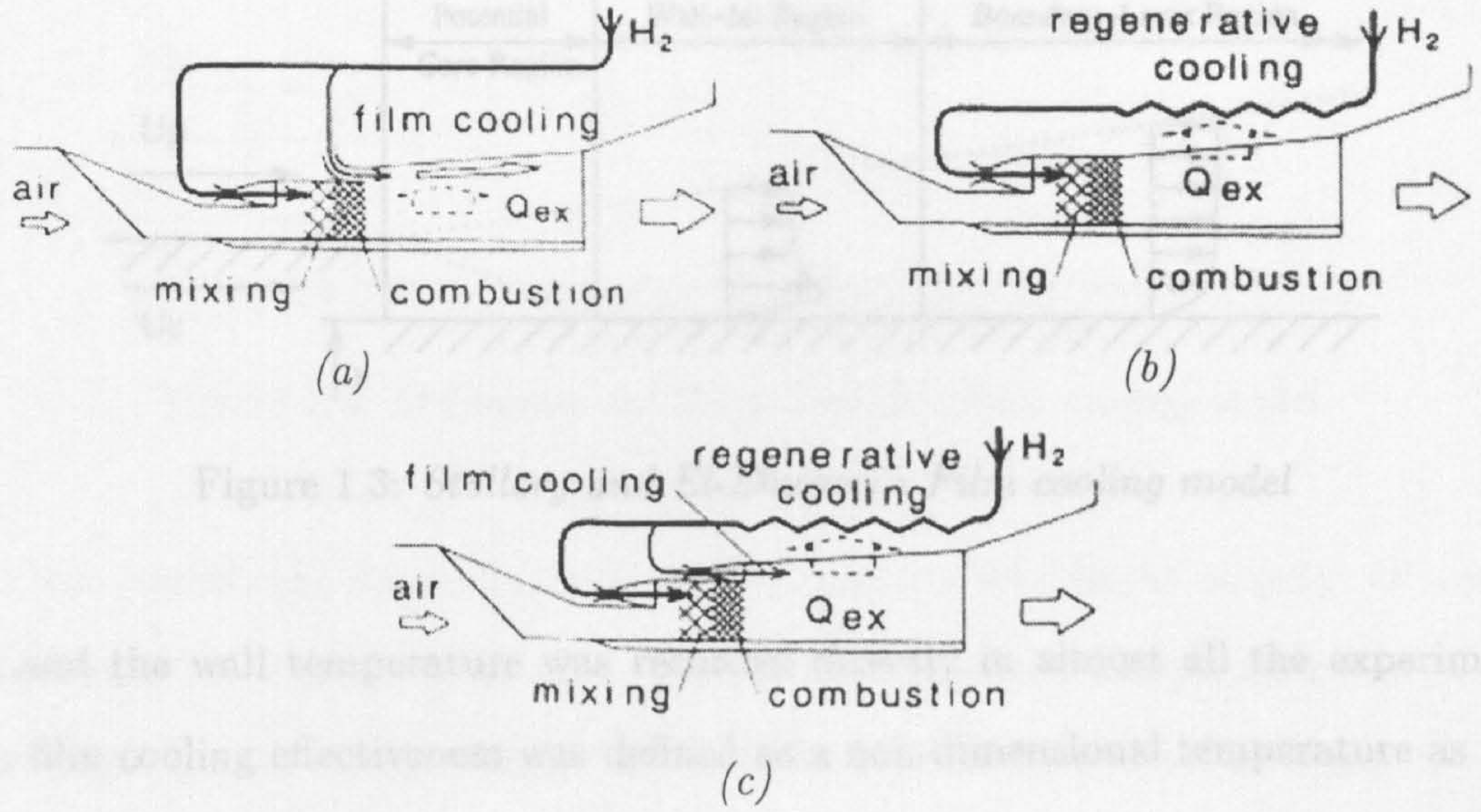

Figure 1.2: *Scramjet engine schematics (Kanda et al. [4]): a) film cooling only, b) regenerative cooling only and c) combination of film cooling and regenerative cooling*

a slot over a flat plate. Just downstream of the injection slot, there is a mixing-layer region, which was called the "potential core" region in [8]. In this zone, the wall temperature remains close to the coolant gas temperature. The cooling length can be defined here as the length downstream of the slot where the adiabatic wall temperature is equal to the injectant stagnation temperature [9]. A "wall-jet" region exists after the "potential core" region, where the velocity profile is similar to that of a wall jet. Farther downstream, there should be a fully developed turbulent boundary-layer when the difference between the coolant and the primary flow streams disappears. For coolant and primary gases of similar density the relative length of the three regions is determined mainly by the velocity ratio between the coolant flow and the primary flow, u_c/u_p. When $u_c \gg u_p$, a simple jet model suggested by Spalding [10] for the second zone may be appropriate. When $u_c < u_p$, the second region is non-existent. Although some experiments have been done to investigate the former condition, the latter one is more commonly used in both experiment and practice.

This film cooling model was published in 1965. At that time, experiments were mainly focused on subsonic film cooling. An adiabatic wall boundary condition was

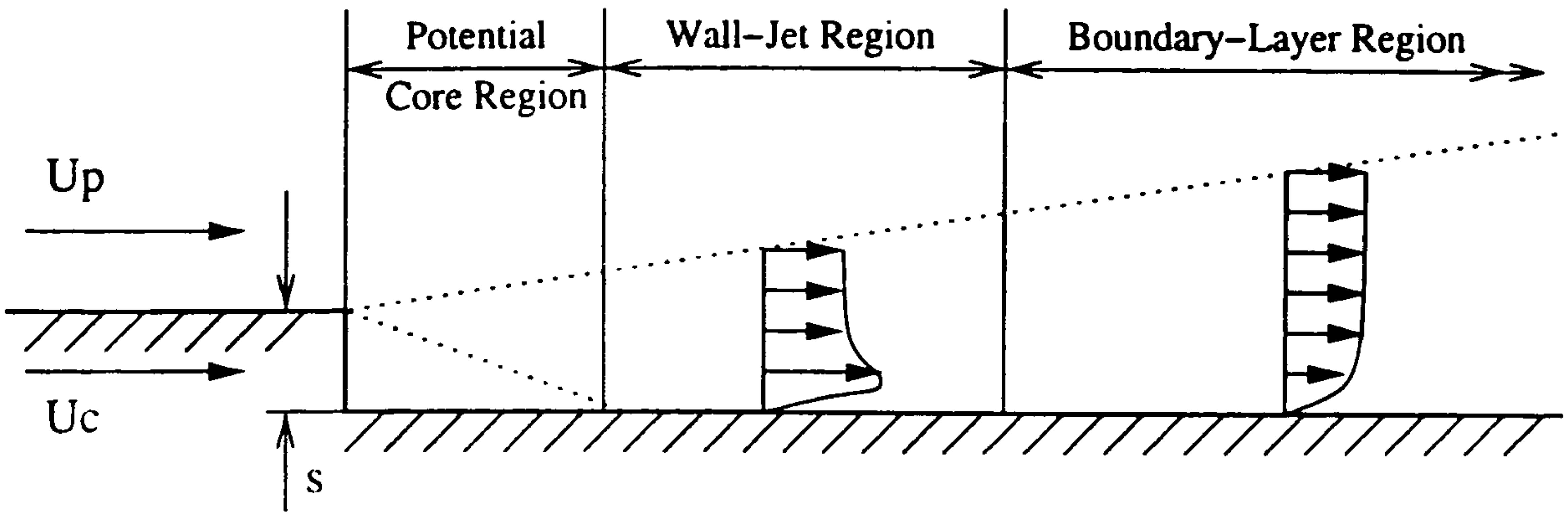

Figure 1.3: *Stollery and El-Ehwany's Film cooling model*

used and the wall temperature was recorded directly in almost all the experiments. Then film cooling effectiveness was defined as a non-dimensional temperature as

$$\eta = \frac{T_{ad,w} - T_\infty}{T_c - T_\infty}. \tag{1.1}$$

Here $T_{ad,w}$, T_c and T_∞ in Eqn. (1.1) represent the adiabatic wall, coolant and freestream flow temperatures, respectively. This definition is applicable when adiabatic conditions are observed in the experiment.

As mentioned above, this film cooling model was originally introduced for subsonic film cooling. It is the most popular model and called the turbulent boundary-layer model by Kanda *et al.* [4]. It was also indicated in [4] that this model eventually adopts the growth rate of the turbulent boundary layer. It can predict the decay tendency of film cooling efficiency far downstream from the injection slot. The model has been applied to predict the flow condition near the slot with several combinations of gas properties as parameters, e.g., density, heat capacity, etc. But these combinations do not seem to be so well-grounded physically. Moreover, it does not seem reasonable to apply this model in the near slot region since the boundary layer of the primary flow stream and the coolant are separated near the injection slot.

1.1.3 O'Connor and Haji-Sheikh's film cooling model

O'Connor and Haji-Sheikh [11] gave a slightly different film cooling model as shown in Fig. 1.4.

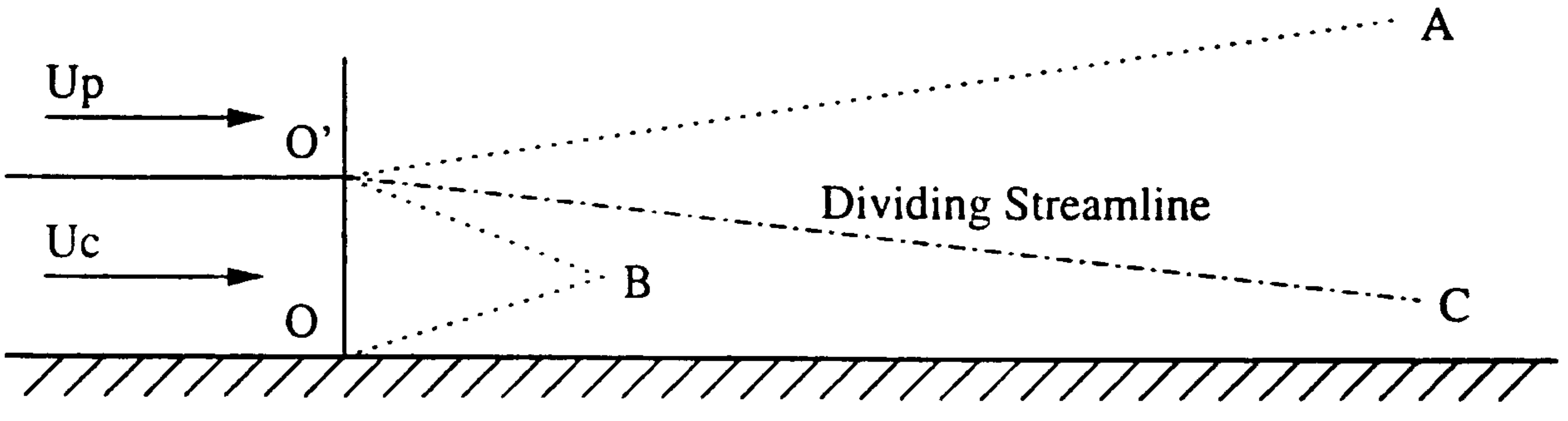

Figure 1.4: *O'Connor and Haji-Sheikh's Film cooling model*

In this model, the boundary layer for the primary flow starts at point O' and for the coolant flow at point O. A mixing shear layer between the primary and coolant flow streams occurs in the region A-O'-B. Only coolant flow exists in region O'-B-O, and no mixing occurs between the two streams. This will reduce the convective heat transfer from the primary flow to the wall. Line O'-C is a streamline that theoretically divides the primary stream from the coolant stream. In the actual flow, turbulent mixing between the primary and the coolant flow streams causes fluid particles to travel across this streamline.

In both models, there is a mixing region just downstream of the slot. The difference lies in O'Connor and Haji-Sheikh's model, where a separate region O'-B-O is indicated to give more details within the "Potential core" region.

1.1.4 Kanda *et al.*'s film cooling model

Another film cooling model was constructed by Kanda *et al.* [4]. It was based on experimental results on the compressible mixing layer and on an analysis using a turbulent boundary layer. According to experimental results, the film cooling efficiency η was found to have a relation with the distance from the exit of a coolant injection slot $x/(h \cdot \dot{m})$. This relation is plotted with logarithm scales in Fig. 1.5.

The model is illustrated in Fig. 1.6. The flow region of film cooling is divided into two parts: 1) a mixing-layer region near the injection slot and 2) a turbulent boundary-layer region far from the slot. At position A, the mixing layer is assumed to reach the wall, and the concept of the mixing layer was applied from the injection slot exit to A.

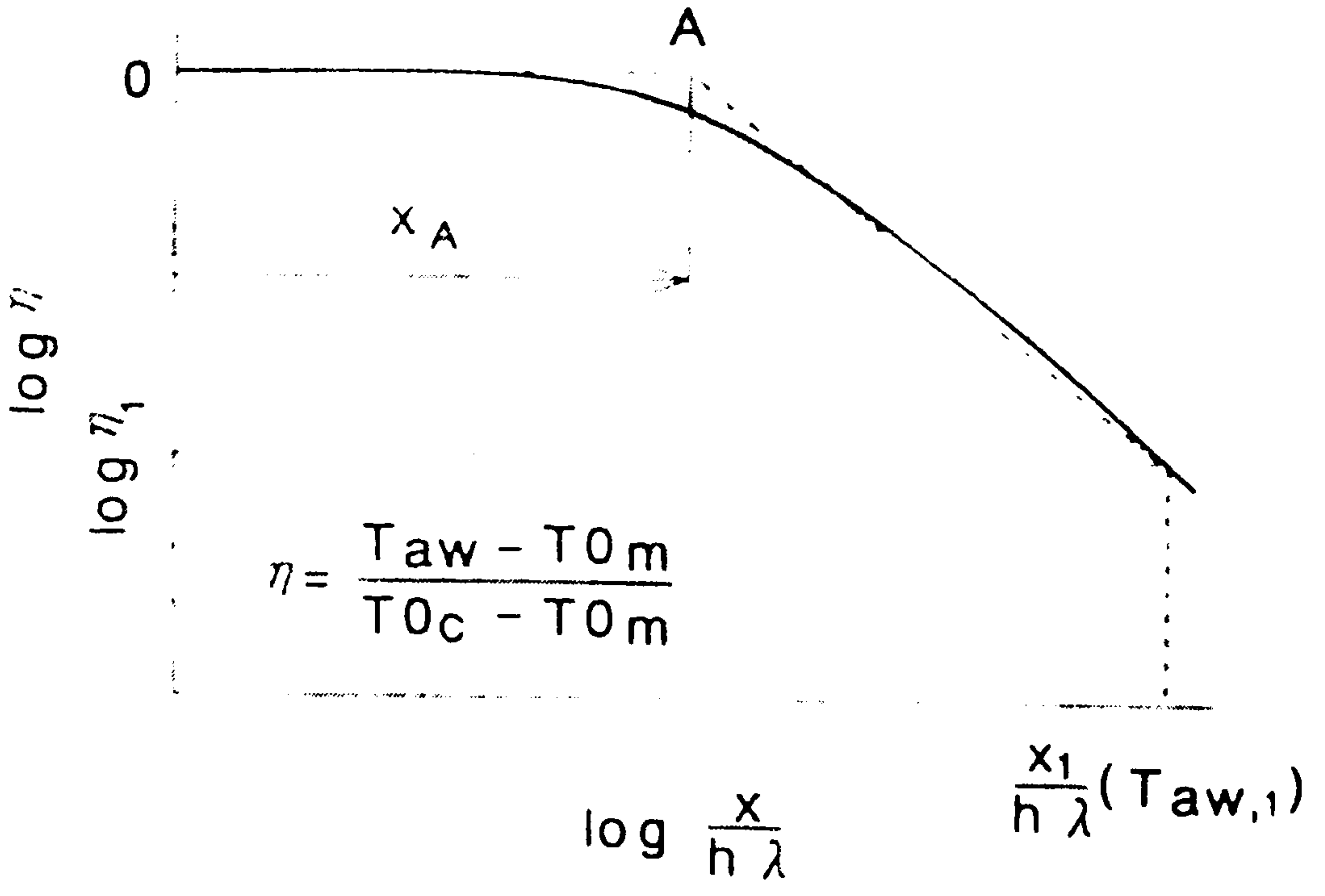

Figure 1.5: *Film cooling efficiency (Kanda et al. [4])*

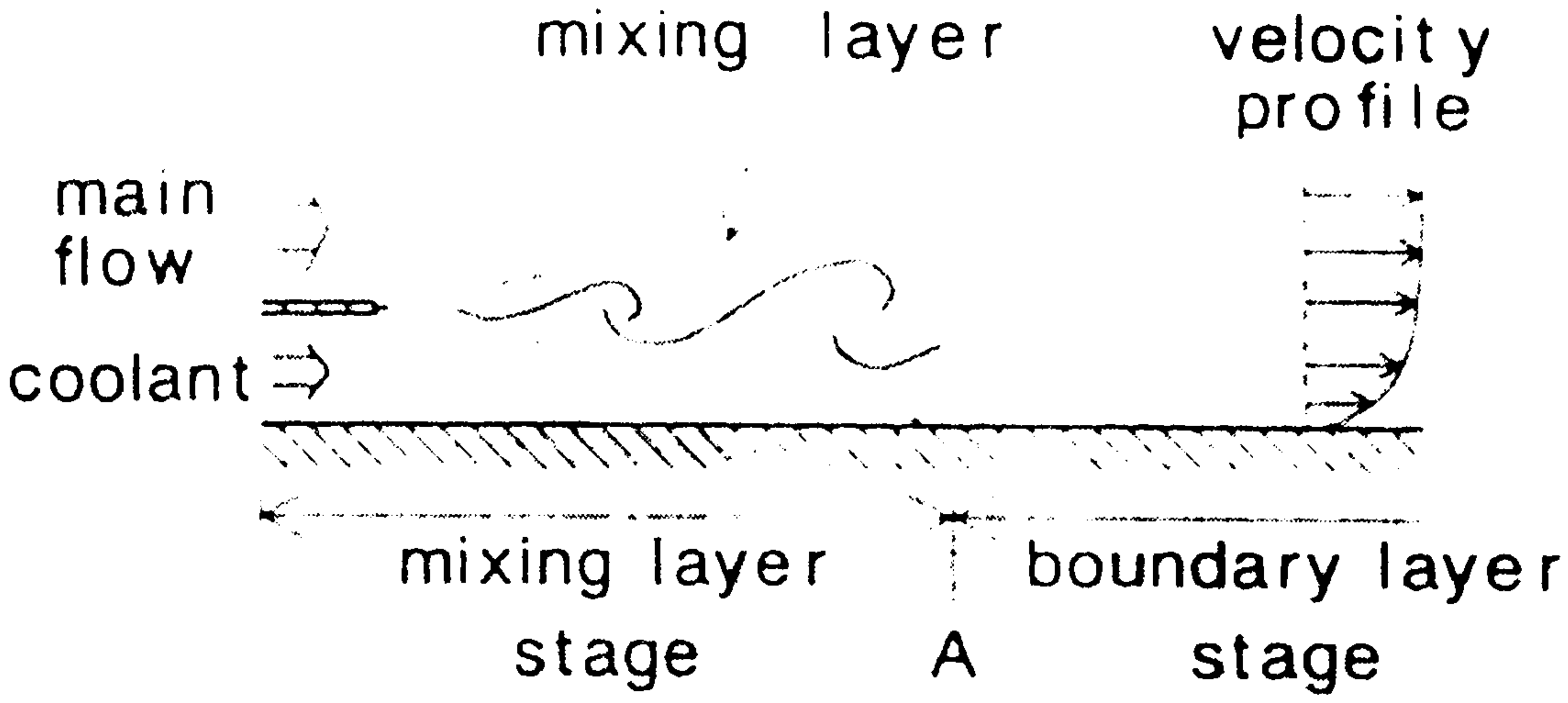

Figure 1.6: *Kanda et al.'s film cooling model (Kanda et al. [4])*

The thickness of the boundary layer on the wall under the coolant was much thinner than both the slot height and the thickness of the mixing layer, so the effect of the coolant side boundary layer was neglected. The feature of turbulent boundary layer was then applied to the area downstream of position A.

No attempt was made to model the flow between the slot exit and position A in previous models, for example, Stollery and El-Ehwany's turbulent boundary-layer model [8]. Rather, prediction of x_A was attempted by extension of the turbulent boundary-layer model. The film cooling model constructed by Kanda *et al.* has the ability to predict the distance of the mixing layer region indicated by x_A in Fig. 1.5 with the assumption that the mixing layer grows symmetrically both in the main flow and in the coolant. In this model, static pressure of the coolant was assumed to be the same as that of the mainstream at the slot exit. The length of the mixing layer region x_A can be estimated using Eqn. (1.2) in which δ is the mixing layer thickness

$$x_A = h/\left(\frac{1}{2}\frac{d\delta}{dx}\right). \tag{1.2}$$

In Chapters 4 and 5 numerical results obtained in this study will be analysed to clearly reveal the mechanism of film cooling in hypersonic flows.

1.2 Experimental studies of film cooling

Many experimental results have been published for subsonic, supersonic and hypersonic film cooling. Although primary and coolant flow stream velocities are often quite different, the flow is distinguished by the primary flow stream velocity. Film cooling effectiveness was found to be influenced by many parameters. Researchers offered different empirical equations to predict the effectiveness of film cooling. But usually such equations are only valid in a narrow scope related to similar conditions used in the experiment. Different parameters were studied such as slot height, lip thickness, flow density and velocity ratios between the primary and the coolant flow and a coolant gas different from the primary one. This section offers a review of the experimental work done on film cooling in the past forty years.

1.2.1 Subsonic film cooling experimental study

In the late fifties and early sixties, subsonic film cooling in both the mainstream and the coolant flow stream was studied experimentally. Seban and Back [12, 13] presented some experimental results on subsonic film cooling with coolant fluid injected tangentially through a single slot near the leading edge of a flat plate. Air was used both for the film and for the free stream fluids. In this study, injection velocities covered a range from much less to much greater than the free stream velocity. For mass-velocity ratios less than unity, particularly for ratios less than 0.9, a power-law region was found for the effectiveness. Also Seban and Back found that immediately downstream of the slot, there exists a flow region which is at first similar to that of the free jet boundary, but which was later altered by the presence of the wall.

Chin *et al.* [14] reported some experimental results for film cooling of an adiabatic plate, downstream of one to ten slots and two to twenty rows of discrete punched louvres in a subsonic turbulent flow under zero pressure gradient. The film cooling effectiveness for louvres was found to decay at a short distance from the last louvre row and at a faster rate than for the continuous slots. Then farther downstream the louvres were found to be as effective as the slots.

Hartnett *et al.* [15] gave a detailed study of the boundary-layer velocity and temperature profiles at a number of positions downstream of the slot. The experiments included both adiabatic and constant heat input-wall boundary conditions. Hartnett *et al.* compared their results with previous measurements and found it possible to make reasonable estimates of the heat-transfer performance with film cooling in a zero-pressure gradient flow.

Burns and Stollery [16] performed some experiments on low-speed film cooling using mixtures of Freon-12 with air, and helium with air. With pure Freon-12 as coolant, it was found that an increase in velocity ratios between the coolant and primary flow would produce higher effectiveness values while the improvements in effectiveness were small when the velocity ratios were greater than unity. But for pure helium injection the effectiveness was improved with very large velocity ratios. The consequence of thickening the slot lip was a decrease in effectiveness. The influence of mainstream boundary layer thickness on film effectiveness was found to be small. For a given mass flow of injectant issuing from a thin lipped slot the highest temperature effectiveness values were achieved using the lightest gas (pure helium).

The effectiveness of film cooling based on adiabatic wall temperature, η in Eqn. (1.1), was used in the above results. It was considered to be a function of at least the non-dimensional distance downstream of the slot and $\dot{m}$ $(= \rho_c u_c / \rho_\infty u_\infty)$, the ratio of coolant mass flux per unit area to primary stream mass flux per unit area, i.e. $\eta = f(x/s, \dot{m})$.

Some experiments were performed more recently on the subsonic film cooling problem with more parameters considered. Lebedev *et al.* [17] studied the effects of turbulence on film cooling efficiency and found that an increasing turbulence decreases film cooling effectiveness. It was found that at small injection rates ($\dot{m} < 1$) a high turbulence intensity results in a significant decrease of the film cooling effectiveness compared to low-turbulence flow. The effect of turbulence decreases at large injection parameters ($\dot{m} > 1$) due to the fact that the energy of the primary flow is a lot less than the average kinetic energy of the injected wall jet. Thus the wall boundary layer is quite stable to external disturbances.

Lee *et al.* [18] investigated the effects of bulk flow pulsation on film cooling with compound angled holes. A row of five film cooling holes was considered with orientation angles of 0°, 30°, 60° and 90° at a fixed inclination angle of 35°. Static pressure pulsations were produced with the pulsation frequency fixed at 36 Hz. It was observed that as the orientation angle increases, the injectant concentration spreads further into the spanwise direction because of pulsations than for the steady case. With pulsations the adiabatic film cooling effectiveness value decreases regardless of the orientation angle. According to the boundary layer temperature, pulsations induced large disruptions to the boundary layer temperature distribution and the film coverage.

Lee *et al.* [19] carried out experiments to study film cooling effectiveness around shaped holes with compound angle orientations. The shaped holes with compound angle injection were found to provide improved film cooling effectiveness up to 55% in comparison with round hole data at high blowing ratios.

1.2.2 Supersonic film cooling experimental study

Goldstein *et al.* [1] were the first to report an experimental investigation of film cooling in a supersonic free stream flowing along a flat plate. The main flow consisted of air at a Mach number of 3.01. Both air and helium were injected sonically through a tangential rearward-facing slot. Three different slot heights of 1.6256, 3.1242, and 4.6228 *mm.* with a constant lip thickness 1.4478 *mm.* were used for air. A slot height of 1.6002 *mm* was used for helium. The total temperature of the main flow stream was close to the room temperature while the temperature of the wall at the point of injection varied between 418° and 655° R for air and from 562.8° to 663.7° R for helium. In the experiments, both the primary flow boundary layer and the coolant flow boundary layer were found to be laminar. For the air injection, two empirical equations of film cooling effectiveness were obtained for different cases of the ratio of coolant to mainstream mass flux per unit area being less or greater than 0.12. From the limited data of injection with helium, it was found that its larger specific heat compared to air causes a higher film cooling effectiveness. Also it was noted that the supersonic film cooling effectiveness was much greater than that for subsonic film cooling. But the film cooling effectiveness decreased more rapidly when the primary stream is supersonic.

Clark *et al.* [20], Hyde *et al.* [21], and Kwok *et al.* [22], all from the Virginia Polytechnic Institute and State University, reported their experimental results for supersonic tangential slot injection into supersonic flow. Existence of organised structures were found in both the helium-injected and air-injected shear layers.

Bass *et al.* [23] examined two coolant gases, hydrogen and nitrogen, two nozzle shapes, two coolant Mach numbers, three slot heights, three lip thicknesses, two levels of mainstream total temperature, two levels of flowpath divergence, and a wide range of the ratio of coolant mass flux per unit area to mainstream mass flux per unit area in supersonic film cooling. A correlation parameter was found to give reasonable results for film cooling effectiveness. The cleaner flow field Prandtl-Meyer designed nozzles had slightly better effectiveness than the two-dimensional design with its accompanying wakes. Axial pressure gradient was found to have a significant effect on effectiveness.

Stafford and Hartfield [24] investigated sonic tangential slot injection into supersonic flow with an adverse pressure gradient. In the experiment, a shock train was established within a diverging Mach 2 test-section to create the pressure gradient. It was found that the shear layer moved toward the primary flow and became less coherent as the shock train advanced upstream. The movement of the shock train upstream also caused the shock structures to be less defined due to the increasing tunnel pressure. Enhanced mixing was observed which may lessen the cooling effectiveness of tangential slot injection with an adverse pressure gradient. The result is important since in a supersonic combustion ramjet, the pressure rise associated with combustion can generate an adverse pressure gradient in the combustor due to the combustor geometry.

Hansmann *et al.* [25] studied the influences of density and velocity ratios between the primary and secondary flow on the film cooling process. Stationary air flows with static temperatures between $2000K$ and $3000K$ and the Mach number varying between 0.5 and 1.0 were used in the experiments. The air and helium cooling gases were injected through a slot, inclined at 45° to the primary flow stream direction. The range of blowing rates was between 0.4 and 2.6. It was observed that the velocity and density gradients between cooling and primary flows had a considerable influence on the cooling effectiveness. Comparison of different cooling gases showed that the injection of helium led to significantly higher cooling efficiency than the injection of air, at constant mass flux densities. It should be noted that in the experiment, the wall was treated as isothermal due to the high hot gas temperatures. The film cooling effectiveness was defined in [25] as the ratio between the heat transfer coefficients with and without film cooling in accordance with the following equation:

$$\eta = 1 - \frac{\dot{q}_c}{\dot{q}_0} \tag{1.3}$$

where $\dot{q}_c$ and $\dot{q}_0$ are the heat transfer rate coefficients with and without film cooling.

Juhany, Hunt, and Sivo [26] examined the dependence of film cooling effectiveness on the injection Mach number, velocity, and mass flux. The freestream Mach number was 2.4, and the injection Mach numbers ranged from 1.2 to 2.2 for both air and helium injection. It was found that for a heated injection with velocity ratio greater than 1, the wall temperature increased downstream with the slot, resulting in an effectiveness greater than one. Also the comparison between helium and air experiments indicated that the effectiveness increased with the heat capacity of the gas, which was observed earlier by Goldstein *et al.* [1] and Hansmann *et al.* [25].

Juhany and Hunt [27] also investigated the flowfield of supersonic slot injection and its interaction with a two-dimensional shock wave. Similar parameters were selected as in [26]. The total pressure profiles perpendicular to the wall were measured at different axial locations, the farthest being at 90 slot heights. With heated gas injection, experiments were conducted to determine the adiabatic wall temperatures and the wall static pressures. The same measurements were then repeated including the impingement of two-dimensional shock waves at 60 slot heights downstream of the slot. The shock strengths were selected to illustrate the differences on the flow caused by separated and attached flows. With the oblique shock impingement, the temperature measurements of the flow indicated that the slot injection was beneficial for maintaining the surface at a desired temperature. However, the effectiveness of the film coolant decreased.

Kanda *et al.* [28, 29] also studied supersonic film cooling with shock wave interaction. It was found that the decrease of the film cooling effectiveness in the region of the shock wave/film cooling interaction may not have been caused by mixing of the coolant with the primary gas, but rather by the decrease of the Mach number of the coolant. In the vicinity of the wall surface, mixing between the coolant and the primary fluid was unimportant, and the coolant layer produced effective film cooling in the region of shock wave/film cooling interaction. Also a flow structure model was constructed to simulate the pressure distribution.

As described by Goldstein *et al.* [1], the following equation can be used to estimate air film cooling effectiveness downstream of the cooling length. Different researchers obtained different coefficients of A, b and c or similar equations.

$$\eta = A \cdot (x/h)^b \cdot \dot{m}^c \tag{1.4}$$

It should be noted that in different equations given by different researchers, h may be the slot height or the step height which equals the slot height plus the lip thickness. The coefficients given by Goldstein *et al.* [1] are listed in Table 1.1. Here h is the step height.

Coolant gas	M_c	M_∞	$\dot{m}$	A	b	c
Air	1.0	3.0	$\dot{m} \leq 0.12$	550.0	-2.0	0.8
Air	1.0	3.0	$\dot{m} > 0.12$	162.0	-1.2	1.2
Helium	1.0	3.0	$0.01 \leq \dot{m} \leq 0.02$	10,000.0	-2.0	0.8

Table 1.1: Coefficients given by Goldstein *et al.* [1]

1.2.3 Hypersonic film cooling experimental study

Parthasarathy and Zakkay [9] executed hypersonic film cooling with the main stream at Mach number 6.0 and the coolant stream at sonic velocity. Four different gases, air, helium, hydrogen and argon, were selected as coolants in the experiments. Three distinct regions were found downstream of the coolant injection. Close to the slot there was a region where the adiabatic wall temperature was equal to the coolant stagnation temperature. The second region existed downstream of the first region, where the mixing exhibited a nonsimilar nature. It was called the transition region in [9]. Farther downstream from the slot, that is, in the third region, the effectiveness decayed to a power-law form. For different coolant gas, the power-law was found to be different due to the different heat capacity. A comparison between the film cooling effectiveness with supersonic and subsonic primary flow was performed. Significantly higher cooling performance was achieved in hypersonic flow.

Richards and Stollery [30, 31, 32] investigated both turbulent ($M = 7.5$, 8.2) and laminar ($M = 10.0$) hypersonic film cooling at isothermal wall conditions with effectiveness as defined in Eqn. (1.3). In the turbulent case, two equations were obtained to estimate the effectiveness of film cooling in regions close to and far away from the slot. Also experiments were carried out in which air was injected into a laminar boundary layer at Mach number 7.5, when transition to turbulent flow occurred after injection. It was observed that just downstream of the transition point heat transfer rates occurred which were higher than the case without injection. In the laminar case, the effect of slot height, flow conditions, and differing coolant gases were examined. A simple discrete layer theory was found to give fair agreement with the experimental results close to the slot.

Cary and Hefner [7] performed experiments to investigate the effects of slot height, coolant mass-flow rate, injection gas temperature, and heat conduction from the mainstream through the slot lip for a Mach 6 mainstream with sonic tangential slot injection. The efficiency was found to be significantly improved compared with cases at lower Mach numbers, as described in [9]. Skin friction downstream of the slot was found to be reduced with the greatest reductions occurring near the slot. Heat conduction from the mainstream through the slot lip was observed to significantly alter the slot temperature profile and thus modify the downstream effectiveness of the slot when the temperature of the injected gas was sufficiently different from that of the freestream flow.

Zakkay *et al.* [33] investigated tangential slot injection with a streamwise adverse pressure gradient in a Mach 6 axisymmetric wind tunnel. The results indicated that the better film cooling effectiveness could be obtained when an adverse pressure gradient was present.

Majeski and Weatherford [34] found that film cooling was an effective means of reducing heat transfer to a sensor window at Mach number 8. An empirical correlation model was also developed to be used to extrapolate to flight conditions.

Olsen *et al.* [2] performed experiments to study coolant delivery pressure, slot height and lip thickness, and incident shock effects in two-dimensional hypersonic film cooling. Some design guidelines were published as follows. Coolant pressure matched to the local boundary layer edge pressure was found to be most effective. Larger slot heights are more effective than smaller slot heights. And, lip thickness, in [2], has no net effect on film cooling and can therefore be set by other design considerations. Incident shocks degrade film cooling effectiveness.

Equations similar to Eqn. (1.4) were also used in [9, 31, 7, 33] to give an estimation of film cooling effectiveness. Zakkay *et al.* [33] also considered the Reynolds number as a factor which also changes film cooling effectiveness.

1.3 Numerical studies of film cooling

With the development of computational techniques and the computer itself, CFD becomes an increasingly important tool to simulate complex flow. It is very difficult to obtain practically the hypersonic flow conditions at reasonable power levels, thus experiments in hypersonic film cooling are usually done in short duration facilities. Techniques have been developed however to achieve reasonably accurate measurements. However, the merit of the computational study of film cooling is obvious especially in hypersonic flows.

An early numerical study of film cooling was performed by Beckwith and Bushnell [35] in 1971. An implicit finite-difference method was utilised to solve the boundary-layer equations for the conservation of mass, momentum, and total enthalpy for the mean flow. A method based on eddy-diffusivity and mixing-length concepts was developed in order to calculate the rapidly changing profiles of velocity, temperature, and concentration of multi-species gases just downstream of the slot and in the subsequent relaxation region (where the profiles relax to those for an undisturbed boundary layer far downstream of the slot). Comparisons of predicted velocity profiles, boundary-layer thickness, heat transfer, skin friction, and recovery temperatures had been made with experimental data from early investigations at freestream Mach numbers of 3 and 6.

In general, good results were obtained especially in the area just downstream of the slot.

Cary and Hefner [7] compared their experimental effectiveness and skin-friction data with the predictions obtained from the above code. Good agreement was observed. The following assumptions were made in the code: 1) air-to-air injection, 2) constant pressure field across the boundary layer ($dp/dy = 0$ everywhere, no shocks), and 3) a thin slot lip (causing no flow separation or recirculation). Skin friction was also investigated in this study and was observed to decrease downstream of the slot, with the greatest reductions occurring near the slot.

Wang [36] developed a boundary layer code which was used to predict the film cooling effectiveness for the optical window on a hypersonic vehicle. An inviscid-viscous coupling approach was used together with the $k - \epsilon$ [37] turbulence model. This approach assumed that viscous effects were limited to the mixing-layer region and in the immediate vicinity of the wall. Outside the mixing-layer, the flow was treated as inviscid and the flow phenomena were modelled by the Euler equations. An implicit finite difference technique was used to solve the governing equations. A series of parameters, such as coolant slot height, coolant exit conditions, tunnel or flight conditions were studied using the code. The predicted surface pressures and heat transfer rates were shown to agree well with the experimental data.

O'Connor and Haji-Sheikh [11] numerically simulated the experimental work done by Goldstein *et al.* [38]. Three different slot heights, 1.62, 3.12, and 4.62 mm were used. Six coolant airflow values were selected for each slot height, resulting in secondary-to-primary airflow ratios ($\dot{m} = \rho_c u_c / \rho_p u_p$) between 0.5 and 8%. The coolant air stream was injected parallel to a flat plate in a Mach 3.0 divergent nozzle. In this numerical study, the two-dimensional Navier-Stokes equations were solved using the HAWK2D code with a two-equation $k - kl$ turbulence model [39]. This turbulence model was derived from a Reynolds stress closure model and modified for compressible flow. The Beam and Warming approximation factorisation algorithm was applied in HAWK2D to solve the equations produced by central differencing of the N-S equations on a regular grid. This algorithm employed the alternating direction implicit (ADI) style formulation to reduce computational time. The local Reynolds number of the primary flow at the splitter plate based on local conditions and primary flow passage height was 4.4×10^5, indicating a laminar boundary layer. It was found that film cooling through a rearward-facing slot into a supersonic flow stream can be effective. The cooling effectiveness dropped due to mixing between the primary and secondary streams at some downstream location. Also the rate at which the effectiveness decreased was greater than for subsonic primary flow conditions. The step or slot height was found to be neglected under a given coolant injection rate. All these conclusions agree well with the experimental results. An adiabatic wall boundary condition was used so that only the wall temperature was considered which is unusual in hypersonic and some supersonic experimental film cooling studies. Moreover, only laminar flow was considered in this study.

Takita [5] tackled the supersonic film cooling problem on a cylinder body, rather than on a flat plate (Fig. 1.7). The cylinder with one slot was placed behind a detached shock wave in a supersonic airflow. A coolant gas issued uniformly from a slot located over 5 degrees from the centerline of the cylindrical body. Both reactive gas (hydrogen) and inert gases (nitrogen and helium) were simulated as the coolant.

The two-dimensional multispecies Navier-Stokes equations including full chemistry were solved using a finite difference method. It was found that if the effect of the reaction was omitted, hydrogen had the greatest efficiency of all the gases because it had the highest heat capacity and lowest molecular weight. When combustion occurred, the cooling efficiency would decrease. The cooling effectiveness was found to dramatically decrease when the injection angle was changed from 0 to 90 degrees. Although the authors were quite confident that the results obtained by CFD were of sufficient quality, this is difficult to judge because of the lack of experimental data. Again, an adiabatic wall was assumed in the study.

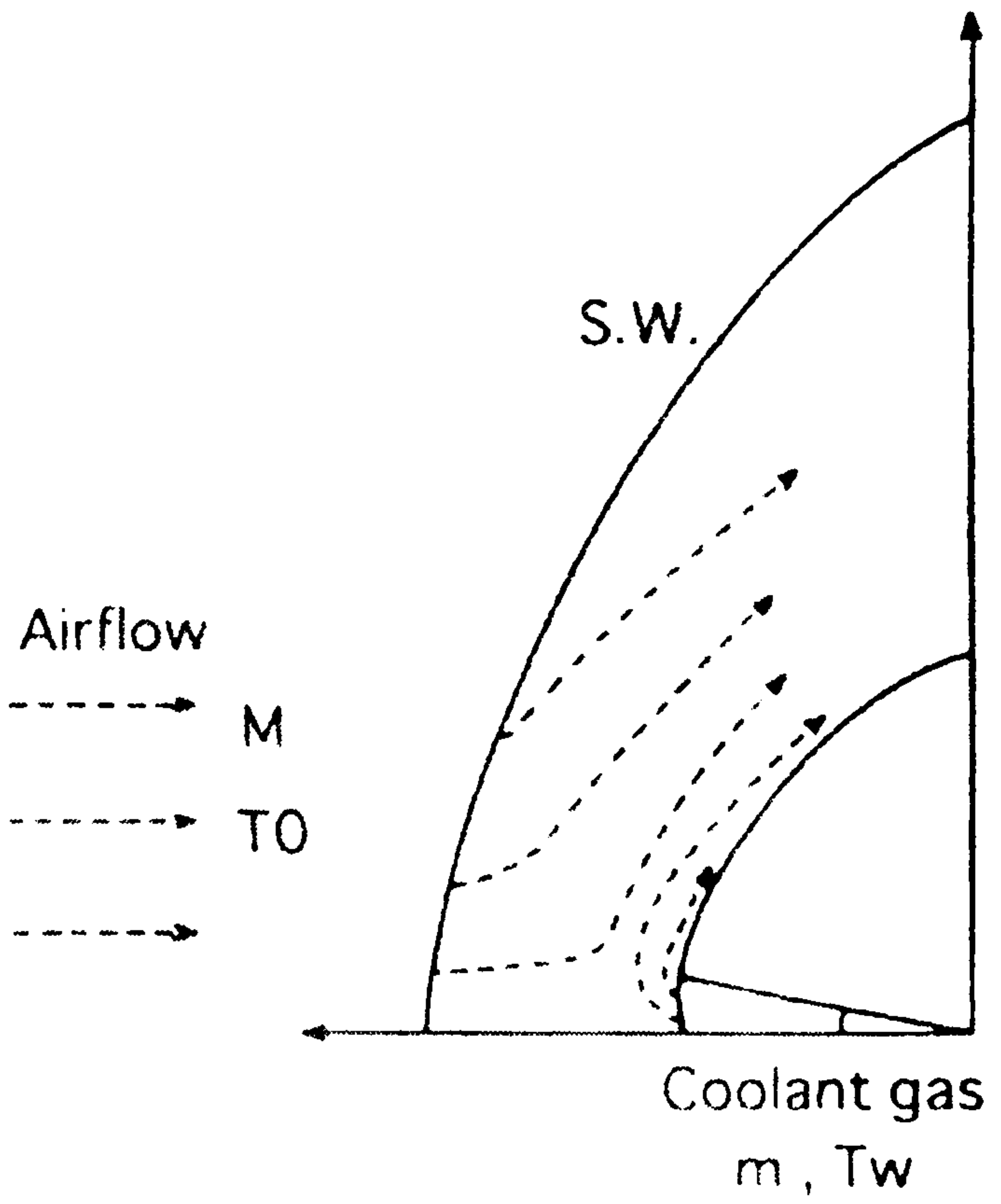

Figure 1.7: *Film cooling on a cylinder body (Takita [5])*

Aupoix *et al.* [40] performed both an experimental and a numerical study at ONERA to simulate supersonic film cooling in a rocket engine. Two injector heights and cold and ambient temperature films, as well as matched and under- and over-expanded films have been studied. A mixture of air and vaporised liquid nitrogen was used as the coolant to be injected into the main air flow. In the numerical study, compressible boundary-layer equations were solved using a finite volume technique. From the experimental wall temperature profiles, it was found that some heat transfer occurred. Since it was not high, all calculations were executed using adiabatic wall conditions. In this numerical study, many turbulence models were tested. First, the Cebeci and Smith [41] and the Baldwin and Lomax [42] algebraic models were tested because of their simplicity and cheapness. Then five $k-\epsilon$ models (Jones and Launder [37], Launder and Sharma [43], Chien [44], Nagano and Tagawa [45], and So *et al.* [46]) and the Wilcox $k-\omega$ [47] two-equation model were studied. Finally, a four-equation model due to Sommer *et al.* [48] was tested. The goal was to get rid of the assumption of a constant turbulent Prandtl number to compute the turbulent heat fluxes as experiments tend to show that the turbulent Prandtl number is roughly constant in boundary layers and in mixing layers but with different levels. The Sarkar's dilatation dissipation correction [49] was also implemented in Chien's $k - \epsilon$ model. Algebraic turbulence models were not found to be well suited to predict film cooling flows, whereas two-equation models correctly reproduce the key features of the flow. The So *et al.* model [46] was found to provide the best prediction of the flow field among all the models tested, even though the deviation of the adiabatic wall temperature was very large. The authors attributed this to the turbulence model and the boundary-layer approach, which however was not representative near the injector lip where a small downwash of the mixing layer was predicted. However, the boundary-layer approach is an efficient and inexpensive way to investigate film cooling.

Garg [3] investigated heat transfer on a film-cooled transonic rotating turbine blade using three different turbulence models. A three-dimensional Navier-Stokes code was used with the Baldwin-Lomax model [42], the Wilcox $k - \omega$ [50] and the Coakley $q - \omega$ [51] models. All models were observed to provide a reasonably good prediction of the heat transfer on the suction surface of the film-cooled rotor blade when compared to the experimental data. The B-L model was found to give a better prediction than the two-equation models at the leading edge. On the pressure surface, the $k - \omega$ turbulence model was found to provide the best heat transfer prediction in general. Both the B-L and $q - \omega$ models under-predicted the surface heat transfer considerably. In this numerical study, uniform distribution of the coolant velocity (relative to the blade), temperature, turbulence intensity and length scale at the hole exit was specified.

Kassimatis *et al.* [52] developed a pressure-type boundary condition, based on uniform total pressure, for the film cooling problem to yield more accurate results than the widely used uniform velocity assumption for blowing ratios greater than 0.5 ($u_c/u_p > 0.5$). At high blowing ratios, the viscous effects are small and hence the total pressure can be treated as constant and provide a better boundary condition. But during each iteration, the uniform total pressure needs to be adjusted so that the mass flow through the slot equals the required value.

Takita and Masuya [53] solved the two-dimensional multispecies compressible Navier-Stokes equations with the $k-\epsilon$ low-Reynolds-number turbulence model [54]. Sarkar's correction [49] for the compressibility effect was also applied to the source term in the equation for k. A H_2/O_2 combustion model was included with 9 species and 37 elementary reactions. N_2 was assumed to be an inert gas, so that its reactions were omitted. The 3rd-order MUSCL TVD scheme was used for the discretisation of convective terms. Effects of combustion and shock impingement on supersonic film cooling by hydrogen were investigated. No large difference due to the effect of the shock impingement on the film cooling between H_2 and the nonreactive coolant appeared.

Gartshore *et al.* [6] executed both an experimental and a computational study to investigate the effect of hole shape. Two sets of compound-oriented holes, one square and the other round with the same cross-sectional area, as sketched in Fig. 1.8, were tested under the same three blowing ratios, 0.5, 1.0 and 1.5. The square holes were found to be slightly superior only very close to the injection point and only at low jet-to-crossflow velocity ratio. For all higher blowing ratios and at large downstream distances, the round holes were better due to the lower integrated momentum flux away from the wall plane at the hole exit. The standard $k-\epsilon$ turbulence model was used. The numerical results were too high for both geometries. The authors suggested the use of more complicated turbulence models and wall function representations to improve the comparison.

Lin *et al.* [55] performed a blind-test (in which experimental data were not released until the CFD simulations were completed and submitted) to investigate the three-dimensional flow and heat transfer about a semi-cylindrical leading edge with a flat afterbody that was cooled by film-cooling jets, injected from a plenum through three staggered rows of compound-angle holes with one row along the stagnation line and two rows along ± 25°. Comparison with experimentally measured temperature distributions and adiabatic effectivenesses indicated the computational result to be reasonable and

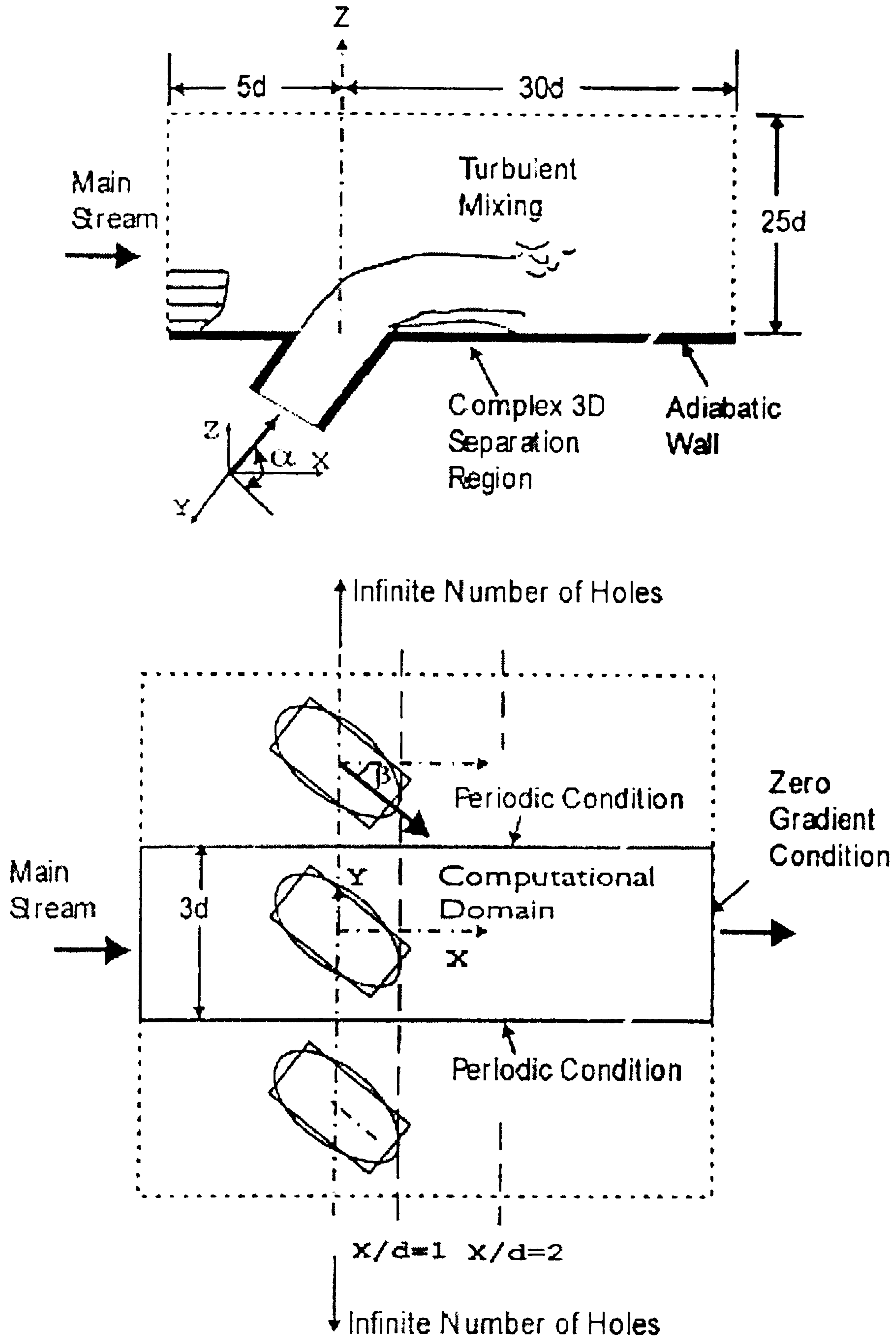

Figure 1.8: *Film cooling injection hole geometry (Gartshore et al. [6])*

physically meaningful. But discrepancies were obvious in coolant jet spreading rate and the amount of hot gas entrainment. The computations were observed to under predict normal spreading, over predict lateral spreading above the surface, and under predict lateral spreading on the surface. Lin *et al.* attributed these errors to the isotropic turbulence model used, which could not account for the Reynolds stress redistribution as eddies flatten as they approach the wall. All the computations were performed by using the CFL3D code with the Menter SST turbulence model [56].

1.4 Objectives

There has been a continous interest in mixing problems in hypersonic flow over the past forty years during the development of supersonic scramjet engines. Mixing is involved with both the injection of the fuel into the combustion chamber and the cooling of heated surfaces in the high speed flow. It is more appropriate to tackle the latter problem before the former one. From the review presented above, it is clear that a lot of experimental work has been done during the past forty years. But since the film cooling problem is very complex, it is found that it is difficult to achieve a universal equation to predict the film cooling effectiveness from the experimental results. Thus there is a need to perform a numerical study of film cooling to enable satisfactory prediction. Usually the slot height is very small (a few millimetres), therefore, it is difficult to obtain detailed information by experiment on the flow in the near slot area. CFD provides the possibility of investigating the full flow field including the near slot region in detail.

Although some numerical studies have been performed to investigate the film cooling problem, they are mainly focused on subsonic and supersonic flows. Nowadays, there is a resurgence of interest in hypersonic flight and rockets, so it is important to execute a numerical study of film cooling in hypersonic flows. The literature search identified the data of Richards and Stollery [30, 31, 32] as being suitable to validate the numerical methods. The method of measuring heat transfer rate has not changed significantly until today. The approach used in this study is to simulate film cooling in both hypersonic laminar and turbulent flows based on the experimental work done by Richards [30]. The experiments in hypersonic flow were carried out at sufficiently high freestream densities that the flow can be considered as continuous, and that the Navier-Stokes equations are the appropriate ones to solve.

The objectives of this numerical simulation are: 1) to validate the Navier-Stokes solver, PMB2D, in hypersonic flows, 2) to use the PMB2D code instead of boundary layer solvers used by previous researchers to investigate the mechanism of film cooling in both hypersonic laminar and turbulent flows, and 3) to study the effects of different parameters including the coolant injection rate and the slot height in the film cooling process.

In the following Chapter the governing equations and numerical methods are briefly described. Chapter 3 gives a numerical study on both hypersonic laminar and turbulent flows over a flat plate. The flat plate flow can be treated as a particular case of the simple film cooling problem by setting the slot height and the coolant injection rate to zero. It can also provide a reference datum to check the effectiveness of film cooling. Different turbulence models are considered for calculations in the turbulent flow regime. Chapters 4 and 5 contain detailed numerical studies of hypersonic laminar and turbulent film cooling respectively. In laminar flow, a uniform boundary condition at the slot exit has been found to be inadequate for predicting the heat transfer, whilst an extended coolant inlet gives improvement. In turbulent flow, a dilatation-dissipation correction to the $k-\omega$ turbulence model has been introduced which gives improved prediction of the experimental data. The coolant fluid was observed to affect the primary boundary layer in two ways: 1) a separate layer set up by the coolant fluid itself, 2) a mixing layer between the primary and coolant flow streams. Curve fitting of the cooling length and the film cooling effectiveness has been applied to study the relationship between the film cooling effectiveness and a grouping of variables, $x/(h\dot{m})$. A two-equation model has been presented to illustrate the relationship for not only the laminar but also the turbulent flows. For film cooling effectiveness in log-log coordinates, a second-order polynomial curve can be used to fit the laminar flows, whilst a straight line is suitable for the turbulent flows. Conclusions and suggestions for future work are presented in Chapter 6. Finally, implementation and validation of the Spalart-Allmaras one-equation turbulence model which the author had contributed to the PMB code development is included in Appendix A for completeness.

Chapter 2

Model Equations and Numerical Methods

2.1 PMB2D code

The PMB2D code developed at the University of Glasgow is used in this study to examine film cooling in hypersonic flow. This code is a generic CFD code which has been used to successfully model steady and unsteady flows including aerofoils, wings, jets and cavities in subsonic and transonic flows. The PMB2D code was used by Feszty [57] to investigate hypersonic flows over bodies of revolution. With Harten's entropy fix, both inviscid and laminar cases were calculated successfully. A brief introduction of the PMB2D code is given in this chapter.

2.1.1 Governing equations

The Navier-Stokes equations are the model equations of motion for a continuous viscous fluid. The two-dimensional Navier-Stokes equations can be written in non-dimensional conservative form in Cartesian coordinates as

$$\frac{\partial \mathbf{Q}}{\partial t} + \frac{\partial \left(\mathbf{F}^{i} - \mathbf{F}^{v}\right)}{\partial x} + \frac{\partial \left(\mathbf{G}^{i} - \mathbf{G}^{v}\right)}{\partial y} = 0, \tag{2.1}$$

where $\mathbf{Q} = (\rho,\ \rho u,\ \rho v,\ \rho E)^T$ denotes the vector of conservative variables, ρ is the density of the fluid and u and v are the two Cartesian components of the velocity. The specific total energy is defined as

$$\rho E = \frac{p}{\gamma - 1} + \frac{1}{2}\rho\left(u^2 + v^2\right). \tag{2.2}$$

The inviscid flux vectors $\mathbf{F}^{\mathrm{i}}$ and $\mathbf{G}^{\mathrm{i}}$ are,

$$\mathbf{F}^i = \begin{pmatrix} \rho u \\ \rho u^2 + p \\ \rho uv \\ u(\rho E + p) \end{pmatrix}, \quad \mathbf{G}^i = \begin{pmatrix} \rho v \\ \rho uv \\ \rho v^2 + p \\ v(\rho E + p) \end{pmatrix}.$$

The viscous flux vectors $\mathbf{F}^{\mathrm{v}}$ and $\mathbf{G}^{\mathrm{v}}$ are given by

$$\mathbf{F}^v = \frac{1}{Re}\left(0, \tau_{xx}, \tau_{xy}, u\tau_{xx} + v\tau_{xy} + q_x\right)^T,$$
$$\mathbf{G}^v = \frac{1}{Re}\left(0, \tau_{xy}, \tau_{yy}, u\tau_{xy} + v\tau_{yy} + q_y\right)^T,$$

where the components of the stress tensor and of the heat flux vector are modelled in the following way

$$\tau_{xx} = -\left(\mu + \mu_t\right)\left(2\frac{\partial u}{\partial x} - \frac{2}{3}\left(\frac{\partial u}{\partial x} + \frac{\partial v}{\partial y}\right)\right)$$
$$\tau_{yy} = -\left(\mu + \mu_t\right)\left(2\frac{\partial v}{\partial y} - \frac{2}{3}\left(\frac{\partial u}{\partial x} + \frac{\partial v}{\partial y}\right)\right)$$
$$\tau_{xy} = -\left(\mu + \mu_t\right)\left(\frac{\partial u}{\partial x} + \frac{\partial v}{\partial y}\right)$$
$$q_x = -\frac{1}{(\gamma - 1)M_\infty^2}\left(\frac{\mu}{P_r} + \frac{\mu_t}{P_{rt}}\right)\frac{\partial T}{\partial x}$$
$$q_y = -\frac{1}{(\gamma - 1)M_\infty^2}\left(\frac{\mu}{P_r} + \frac{\mu_t}{P_{rt}}\right)\frac{\partial T}{\partial y}.$$

The turbulent eddy viscosity μ_t is set to zero in a laminar calculation and evaluated by another model (Section 2.2.1) in turbulent flows. The laminar viscosity μ is evaluated using Sutherland's law

$$\frac{\mu}{\mu_0} = \left(\frac{T}{T_0}\right)^{1.5} \frac{T_0 + 110}{T + 110},$$

where μ_0 is the reference viscosity at a reference temperature T_0, taken as $\mu_0 = 1.7894 \times 10^{-5}\, kg/(m \cdot s)$ with $T_0 = 288.16\, K$.

Finally, the closure of the N-S equations requires the perfect gas equation:

$$p = \rho RT. \tag{2.3}$$

2.1.2 Numerical procedures

The equations are transformed from the physical domain (x, y, t) to the computational domain (ξ, η, τ) with the grid spacing in the computational space being uniform and of unit length. This produces a Cartesian computational domain which is a cuboid and has a regular uniform mesh.

The N-S equations are discretised in space using a cell-centred finite volume approach. The convective terms are discretised using either the Osher or Roe [58] scheme. All calculations in this study were obtained using the Roe scheme since it has been proven to be better suited for hypersonic flows [59]. The Harten entropy fix [60] was introduced in the Roe scheme in order to avoid the occurrence of non-physical expansion shocks. MUSCL variable interpolation is employed to achieve 2nd order spatial accuracy. The diffusive terms are discretised by central differencing. A time-marching scheme is performed to get a steady solution. Further details of the numerical method used in PMB2D can be found in [61, 62, 63].

2.2 Turbulence models

2.2.1 The Wilcox $k-\omega$ turbulence model

The $k-\omega$ turbulence model [64] is the original model implemented in the PMB2D code to calculate the eddy viscosity μ_t. This model can be written in non-dimensional form as

$$\begin{cases} \dfrac{\partial(\rho k)}{\partial t} + \dfrac{\partial(\rho u_j k)}{\partial x_j} - \dfrac{\partial}{\partial x_j}\left(\dfrac{\mu + \sigma^* \mu_t}{Re}\dfrac{\partial k}{\partial x_j}\right) = P_k - \beta^* \rho \omega k \\ \dfrac{\partial(\rho \omega)}{\partial t} + \dfrac{\partial(\rho u_j \omega)}{\partial x_j} - \dfrac{\partial}{\partial x_j}\left(\dfrac{\mu + \sigma \mu_t}{Re}\dfrac{\partial \omega}{\partial x_j}\right) = \alpha\dfrac{\omega}{k}P_k - \beta \rho \omega^2. \end{cases} \tag{2.4}$$

The turbulent eddy viscosity is defined by

$$\mu_t = Re\, \rho\, \frac{k}{\omega}. \tag{2.5}$$

The production term P_k and closure coefficients are given as

$$P_k = \frac{\mu_t}{Re}\left[\frac{1}{2}\left(\frac{\partial u_i}{\partial x_j} + \frac{\partial u_j}{\partial x_i}\right)^2 - \frac{2}{3}\left(\frac{\partial u_k}{\partial x_k}\right)^2\right],$$

$$\alpha = 5/9, \quad \beta = 0.075, \quad \beta^* = 0.09, \quad \sigma = 0.5, \quad \sigma^* = 0.5.$$

It is suggested that the smooth wall boundary condition is applied within the range $0 < y^+ < 2.5$. The exact solution of the transport equation for ω as $y \to 0$ is adopted, i.e., $\omega = 6\mu_w/(\beta \rho y^2)$. Wilcox originally suggested that this condition should be applied to several cells within the viscous sub-layer. However, the Menter interpretation of this boundary condition [56] is widely adopted, by applying a single value at the wall of

$$k_w = 0, \qquad \omega_w = 10\frac{6\mu_w}{Re\beta\rho(\Delta y_1)^2}, \tag{2.6}$$

where Δy_1 is the distance to the next point away from the wall. The above equation simulates the smooth wall boundary condition as long as $\Delta y_1^+ < 3$.

The convective terms of Eqn. (2.4) are discretised by the Engquist-Osher method, considering the k and ω equations as decoupled scalar equations with a prescribed velocity field. The spatial discretisation is either first or third order accurate using MUSCL interpolation with the Anderson or Van Albada limiter. The viscous diffusion terms are discretised using the central difference method. The source terms are also evaluated at the cell centre. So similar numerical methods to the mean flow solver are used to solve the $k-\omega$ transport equations.

2.2.2 The Menter baseline turbulence model

Menter proposed two turbulence models in 1994 [56]. The first model, which is called the baseline (BSL) model, retains the formulation of the Wilcox $k-\omega$ model in the near wall region, and takes advantage of the freestream independence of the $k-\epsilon$ model in the outer part of the boundary layer. The original Wilcox $k-\omega$ model is used in the sub- and log-layer and is gradually switched to the standard $k-\omega$ model in the wake region of the boundary layer by introducing a blending function F_1. The $k-\epsilon$ model is also used in free shear layers. This BSL model is found to be very similar to the original $k-\omega$ model for boundary layer flows, but it avoids the strong sensitivity to the freestream flow conditions of that model. The following nondimensional equations describe the BSL model:

$$\left\{\begin{aligned} &\frac{\partial(\rho k)}{\partial t}+\frac{\partial(\rho u_j k)}{\partial x_j}-\frac{\partial}{\partial x_j}\left(\frac{\mu+\sigma_k\mu_t}{Re}\frac{\partial k}{\partial x_j}\right)=S_k \\ &\frac{\partial(\rho\omega)}{\partial t}+\frac{\partial(\rho u_j \omega)}{\partial x_j}-\frac{\partial}{\partial x_j}\left(\frac{\mu+\sigma_\omega\mu_t}{Re}\frac{\partial \omega}{\partial x_j}\right)=S_\omega. \end{aligned}\right. \tag{2.7}$$

S_k and S_ω in the above equations are the source terms which can be written as

$$\left\{\begin{aligned} &S_k=P_k-\beta^*\rho\omega k \\ &S_\omega=\gamma\frac{\rho}{\mu_t}P_k-\beta\rho\omega^2+2(1-F_1)\frac{\rho\sigma_{\omega 2}}{\omega Re}\frac{\partial k}{\partial x_j}\frac{\partial \omega}{\partial x_j}. \end{aligned}\right. \tag{2.8}$$

The constants ϕ of the BSL model can be calculated from the constants, ϕ_1, ϕ_2, as follows:

$$\phi = F_1\phi_1 + (1 - F_1)\phi_2. \tag{2.9}$$

The constants of set 1 (ϕ_1) are (Wilcox):

$$\begin{aligned} \sigma_{k1} = 0.5, \quad \sigma_{\omega 1} = 0.5, \quad \beta_1 = 0.075 \\ \beta^* = 0.09, \quad \kappa = 0.41, \quad \gamma_1 = \beta_1/\beta^* - \sigma_{\omega 1}\kappa^2/\sqrt{\beta^*}. \end{aligned} \tag{2.10}$$

The constants of set 2 (ϕ_2) are (standard $k - \epsilon$):

$$\begin{aligned} \sigma_{k2} = 1.0, \quad \sigma_{\omega 2} = 0.856, \quad \beta_2 = 0.0828 \\ \beta^* = 0.09, \quad \kappa = 0.41, \quad \gamma_2 = \beta_2/\beta^* - \sigma_{\omega 2}\kappa^2/\sqrt{\beta^*}. \end{aligned} \tag{2.11}$$

The function F_1 is designed to blend the model coefficients of the Wilcox $k - \omega$ model in boundary layer zones with the transformed $k - \epsilon$ model in free-shear layer and freestream zones. This function takes the value of one on no-slip surfaces and near to one over a large portion of the boundary layer, and goes to zero at the boundary layer edge. The auxiliary blending function is defined as

$$\begin{aligned} F_1 &= tanh(arg_1^4) \\ arg_1 &= min\left[max\left(\frac{\sqrt{k}}{0.09\omega y}; \frac{500\mu}{Re\rho y^2\omega}\right); \frac{4\rho\sigma_{\omega 2}k}{CD_{k\omega}y^2}\right], \end{aligned} \tag{2.12}$$

where y is the distance to the next surface and $CD_{k\omega}$ is the positive portion of the cross-diffusion term of the ω-transport equation

$$CD_{k\omega} = max\left(2\rho\sigma_{\omega 2}\frac{1}{\omega}\frac{\partial k}{\partial x_j}\frac{\partial \omega}{\partial x_j}, 10^{-20}\right). \tag{2.13}$$

The turbulent eddy viscosity is defined the same as the $k - \omega$ model in Eqn. (2.5). The following choice of freestream values was recommended by Menter

$$k_\infty = \mu_{t\infty}\frac{\omega_\infty}{\rho_\infty}, \quad \omega_\infty = (1 \to 10)\frac{u_\infty}{L}, \quad \mu_{t\infty} = 10^{-(2\to 5)}\mu_\infty, \tag{2.14}$$

where L is the approximation length of the computational domain. The boundary condition for ω at the wall surface is the same as mentioned before, Eqn. (2.6).

2.2.3 The Menter *SST* turbulence model

The other model proposed by Menter, the *SST* (shear-stress transport) model [56], combines several desirable elements of the $k-\epsilon$ and $k-\omega$ turbulence models. The above BSL model gives good results for mild adverse pressure gradient flows, but fails to accurately predict flows with strong pressure gradients and separation [56] like previous two-equation models. This is a serious deficiency leading to an underestimation of the effects of viscous-inviscid interaction which generally results in too optimistic performance estimates for aerodynamic bodies. The reason for this deficiency is that these models do not account for the important effects of transport of the turbulence stresses. From the J-K model [65], significant improvements can be obtained with the half-equation model by modelling the transport of the shear stress as being proportional to that of the turbulent kinetic energy. With the same transport governing equations used, the second model proposed by Menter results from a modification to the definition of the eddy viscosity in the BSL model, which accounts for the effect of the transport of the principal turbulent shear stress.

$$\mu_t = \frac{Re\rho k/\omega}{max\left[1; \Omega F_2/(a_1\omega)\right]}, \tag{2.15}$$

where $a_1 = 0.31$ and Ω is the absolute value of the vorticity. F_2 is given by

$$\begin{gathered} F_2 = tanh(arg_2^2) \\ arg_2 = max\left(2\frac{\sqrt{k}}{0.09\omega y}; \frac{500\mu}{Re\rho y^2\omega}\right). \end{gathered} \tag{2.16}$$

The constants of set 2 in the *SST* model are the same as the BSL model. But the constants of set 1 are changed to:

$$\begin{gathered} \sigma_{k1} = 0.85, \quad \sigma_{\omega 1} = 0.5, \quad \beta_1 = 0.075 \\ \beta^* = 0.09, \quad \kappa = 0.41, \quad \gamma_1 = \beta_1/\beta^* - \sigma_{\omega 1}\kappa^2/\sqrt{\beta^*}. \end{gathered} \tag{2.17}$$

Because the SST model includes the effect of the transport of the principal turbulent shear stress, major improvements in the prediction of adverse pressure gradient flows have been observed by many researchers [66, 67]. Both the Menter's BSL and SST models have been implemented into the PMB2D code in order to study the effect of turbulence models in hypersonic turbulent film cooling.

2.2.4 The Spalart-Allmaras turbulence model

Another model tried in this computational study is the Spalart-Allmaras turbulence model. This turbulence model is a one-equation model developed by Spalart and Allmaras [68, 69]. It was inspired from an earlier model developed by Baldwin and Barth [70]. The transport equation and coefficients of the S-A model were defined using dimensional analysis, Galilean invariance, and selected empirical results. In Eqn. (2.18), the transport equation of the S-A model in fully turbulent flow is non-dimensionalised using the freestream flow variables. In the original S-A model, transition was also considered, but is ignored here. The transport equation is then given by

$$\frac{\partial \widetilde{\nu}}{\partial t} + \frac{\partial \left(u_j \widetilde{\nu}\right)}{\partial x_j} - \frac{\partial}{\partial x_j}\left(\frac{\nu + \widetilde{\nu}}{\sigma Re}\frac{\partial \widetilde{\nu}}{\partial x_j}\right) = S, \tag{2.18}$$

where the source term is divided into the following four parts $S = S_1 + S_2 + S_3 + S_4$ where

$$\left\{ \begin{array}{l} S_1 = c_{b1}\widetilde{\Omega}\widetilde{\nu} \\ S_2 = \frac{c_{b2}}{\sigma Re}\left[\left(\frac{\partial \widetilde{\nu}}{\partial x}\right)^2 + \left(\frac{\partial \widetilde{\nu}}{\partial y}\right)^2 + \left(\frac{\partial \widetilde{\nu}}{\partial z}\right)^2\right] \\ S_3 = -\frac{c_{w1} f_w}{Re}\left[\frac{\widetilde{\nu}}{d}\right]^2 \\ S_4 = \widetilde{\nu}\left(\frac{\partial u}{\partial x} + \frac{\partial v}{\partial y} + \frac{\partial w}{\partial z}\right). \end{array} \right. \tag{2.19}$$

All the auxiliary functions are redefined in non-dimensional form as

$$\chi \equiv \frac{\widetilde{\nu}}{\nu}, \quad f_{v1} = \frac{\chi^3}{\chi^3 + c_{v1}^3}, \quad f_{v2} = 1 - \frac{\chi}{1 + \chi f_{v1}}$$

$$f_w = g\left[\frac{1 + c_{w3}^6}{g^6 + c_{w3}^6}\right]^{1/6}, \quad g = r + c_{w2}\left(r^6 - r\right), \quad r \equiv \frac{\widetilde{\nu}}{\widetilde{S}\kappa^2 d^2} \cdot \frac{1}{Re}$$

$$\widetilde{\Omega} = \Omega + \frac{\widetilde{\nu}}{\kappa^2 d^2} f_{v2} \cdot \frac{1}{Re}, \quad \Omega \equiv \sqrt{2\Omega_{ij}\Omega_{ij}} \tag{2.20}$$

$$\sigma = 2/3, \quad c_{b1} = 0.1355, \quad c_{b2} = 0.622, \quad \kappa = 0.41$$

$$c_{v1} = 7.1, \quad c_{w1} = c_{b1}/\kappa^2 + (1 + c_{b2})/\sigma, \quad c_{w2} = 0.3, \quad c_{w3} = 2.$$

The S-A model has been implemented and validated by many researchers in the past ten years [66, 67, 71, 72, 73, 74, 75, 76]. The S-A turbulence model was highly recommended [66, 67] for attached flows. It can give results that are often similar to the two-equation models, particularly to the Menter's *SST* model. However it performs less well in separated flows.

This model was implemented by the author in the PMB3D code, which is a 3-D version of the PMB code. The implementation and validation can be found in Appendix A.

Chapter 3

Hypersonic Flat Plate Study

3.1 The gun tunnel

All experiments done by Richards [30] were performed using the Imperial College gun tunnel. In brief, it is a blowdown tunnel with a shock compression heater. The shock is generated by compressed air driving a free light piston down a 6.096 m long barrel filled with the test gas. Unit Reynolds number, u_∞/ν_∞, can be varied for constant total temperature, T_0, by varying the driving pressure, p_d, and the barrel pressure, p_b, keeping p_d/p_b constant. The total temperature can be varied for constant total pressure by keeping p_d constant and varying p_b. A 10° half angle conical nozzle with interchangeable throat inserts provides nominal test section Mach numbers of 7.5 and 10.0, whilst a contoured nozzle provides a uniform flow at Mach number of 8.2. The nozzles have 0.2032 m and 0.1905 m exit-plane diameters respectively giving a useful core of about 0.1524 m. An open jet test section was used, and the useful running time was approximately 40 milliseconds.

Two film cooling models were used in the experiments. Model B, which was used for the test matrix used in this thesis, is shown in Fig. 3.1. Fig. 3.2 shows the cross section of the film cooling model through the plenum chamber. The plenum chamber was fed from two pipes from the rear, which led to a rearward facing slot through a 180° bend. This was used to enable the coolant to be injected tangentially along the model away from the leading edge.

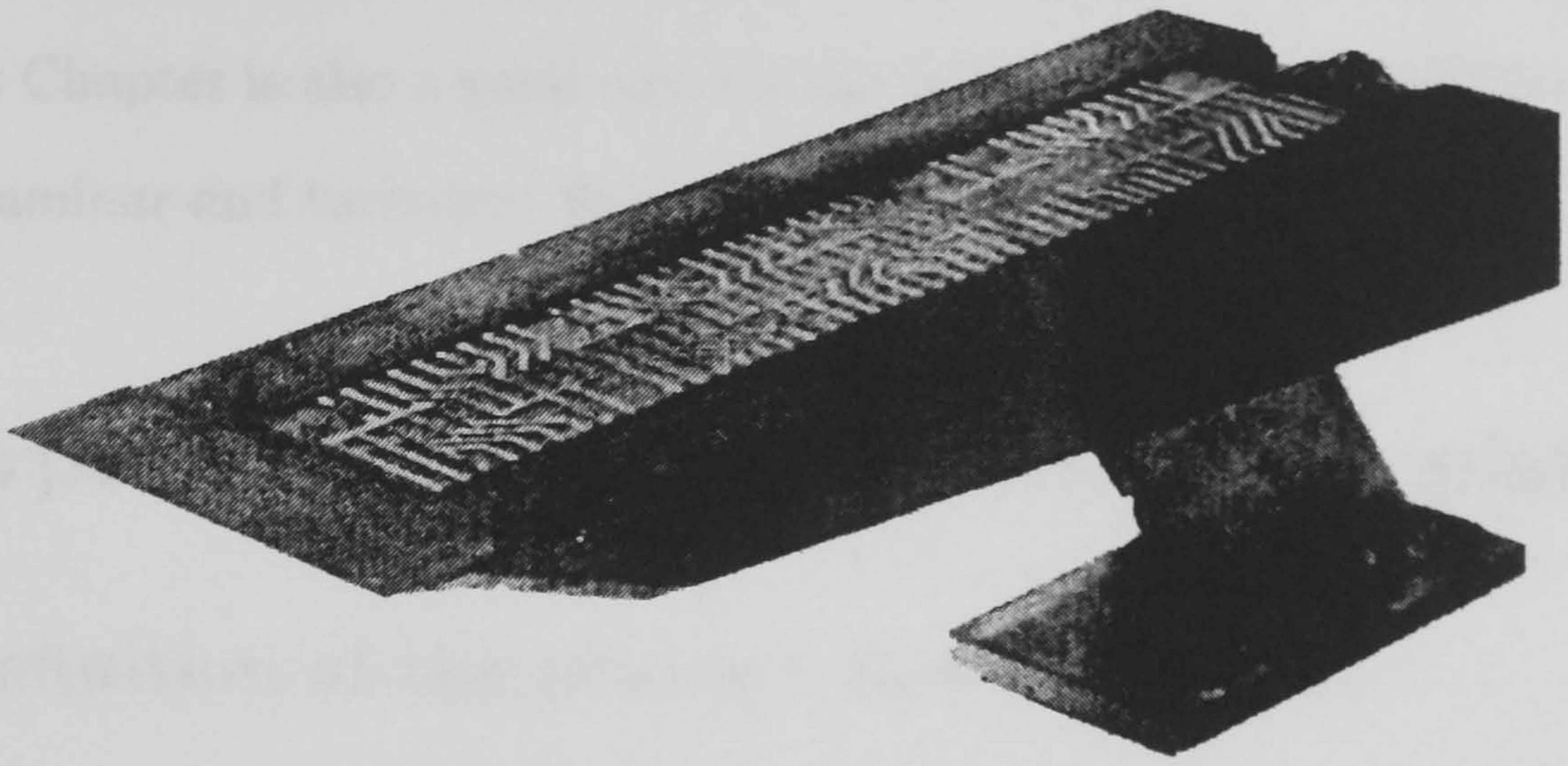

Figure 3.1: *Experimental film cooling model*

This film cooling model was instrumented with thin film platinum resistance gauges in order to measure the heat transfer rate. The instrumented section in Fig. 3.2 could be raised or lowered so that different slot heights could be obtained. All experiments in hypersonic laminar flow were executed using the $M = 10.0$ conical nozzle, while for experiments in turbulent flow the $M = 8.2$ contoured nozzle was used. In all experiments, isothermal wall conditions were applied. Although different coolant gases including air, freon, helium and argon were used in the experimental study, only air is considered for both the primary and the coolant flow in this CFD study.

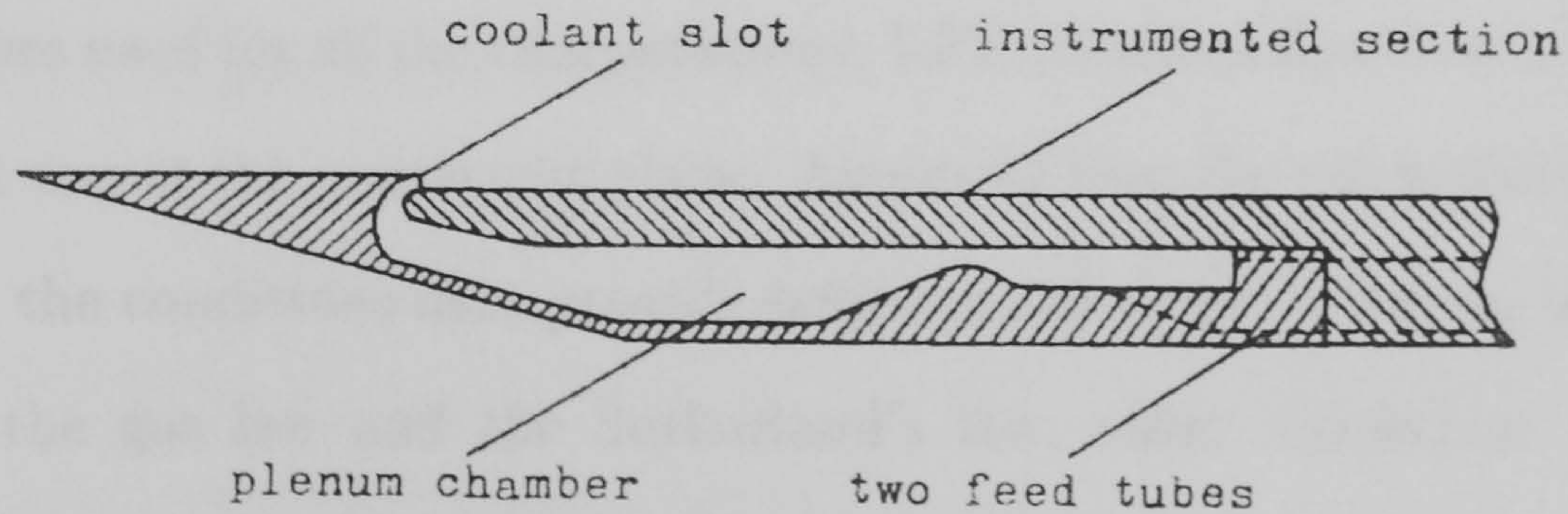

Figure 3.2: *Cross section of the film cooling model through the plenum chamber*

For the flat plate study described in this Chapter, the slot height is set to zero. The flat plate flow can be treated as a particular case of the simple film cooling problem by setting the slot height and the coolant injection rate to zero. It can also provide a reference datum to check the effectiveness of film cooling. The flat plate flow investigated in this Chapter is also a good case for the validation of the PMB2D code in both hypersonic laminar and turbulent flows.

3.2 Hypersonic laminar flow over a flat plate

3.2.1 Definition of the primary flow conditions

In Table 3.1, three primary flow conditions (PFC) in the experiments at the nozzle exit are selected at the same nominal Mach number of 10.0. The flow conditions in this table and subsequent ones are given to 2 places of decimal. This was done so, not to reflect the accuracy of the experiment, but to provide consistency in the numerical calculations.

LFP Case	M_∞	Re/m	$T_0\,(K)$
1	10.0	6.30×10^6	1290.00
2	10.0	5.31×10^6	1170.00
3	10.0	4.13×10^6	1030.00

Table 3.1: Three different primary flow conditions at the nozzle exit for the laminar experiments

Despite the experiments being performed in a conical nozzle, constant freestream conditions were used for all the computations. LFP (laminar flow over a flat plate) Case 1 in Table 3.1 was at the nozzle exit plane. Assuming that the gas is thermodynamically perfect, then the conditions here provide sufficient information for the definition of the flow. From the gas law and the Sutherland's law, other conditions of the primary flow stream can be calculated giving the freestream static pressure $281.0\,N/m^2$ and freestream static temperature $61.43\,K$.

The position of the slot is important in the simulation of film cooling (to be discussed in Chapter 4) and this was not specified in [30], although it was expected to be close to the nozzle exit. The experimental pressure distribution on the zero slot model used to provide the zero film cooling pressure and heat transfer measurements was available and this was influenced by the viscous interaction. It had an experimental value of 475.7 N/m^2 at the slot position. Predictions of this interaction were calculated numerically and compared with the experiments. It was found from comparison of the experimental and calculated pressure variation, which naturally included the viscous interaction, that the Mach number at the position of the slot within the conical nozzle was 9.9, i.e., slightly upstream of the nozzle exit (where the Mach number was 10.0). It was thought the best choice of condition to specify the slot position was by equating these pressure values. The new freestream conditions were then taken as $M_\infty = 9.9$, $T_0 = 1290.0\,K$ and Re/m of 6.46×10^6, $p_\infty = 476.00\,N/m^2$, $T_\infty = 62.62\,K$ etc. The other conditions of the experiment are calculated accordingly. In Table 3.2, three PFCs are achieved from Table 3.1 using the above method. It is stated here that all the PFCs mentioned in the following discussions in Chapters 3 and 4 will be those in Table 3.2, unless specified otherwise.

LFP Case	M_∞	Re/m	$p_\infty\,(Pa)$	$T_0\,(K)$	$T_\infty\,(K)$	$T_w\,(K)$
1	9.90	6.46×10^6	476.00	1290.00	62.62	290.00
2	9.90	5.45×10^6	341.00	1170.00	56.79	290.00
3	9.90	4.24×10^6	214.00	1030.00	50.00	290.00

Table 3.2: Calculated three different primary flow conditions for laminar flows

3.2.2 Grid dependence test

The computational domain of the flat plate is illustrated in Fig. 3.3. Two blocks are included in the topology. In the laminar film cooling study, the first block was defined by the distance from the sharp leading edge to the slot of 33.02 mm, corresponding to the experimental configuration. The second block was defined by the distance 254.00 mm downstream of the slot. In the normal direction, the computational domains were chosen to be 76.20 mm, which is sufficiently far from the plate such that the oblique shock wave passed out of the flowfield at the downstream boundary. The grid for the flat plate calculation is extracted from the film cooling grid. A fine grid and a coarse grid were tested. For the fine grid, there are 95 x 133 and 301 x 133 grid points in the two blocks in Fig. 3.3. The coarse grid was generated by extracting one grid point from every two grid points in the fine grid. So for the coarse grid, there are 48 x 67 and 151 x 67 grid points in these two blocks. Freestream conditions were set at the leading edge and top of the computational domain. A simple first-order extrapolation from the interior was applied at the outlet. Similar boundary conditions were applied in all film cooling calculations.

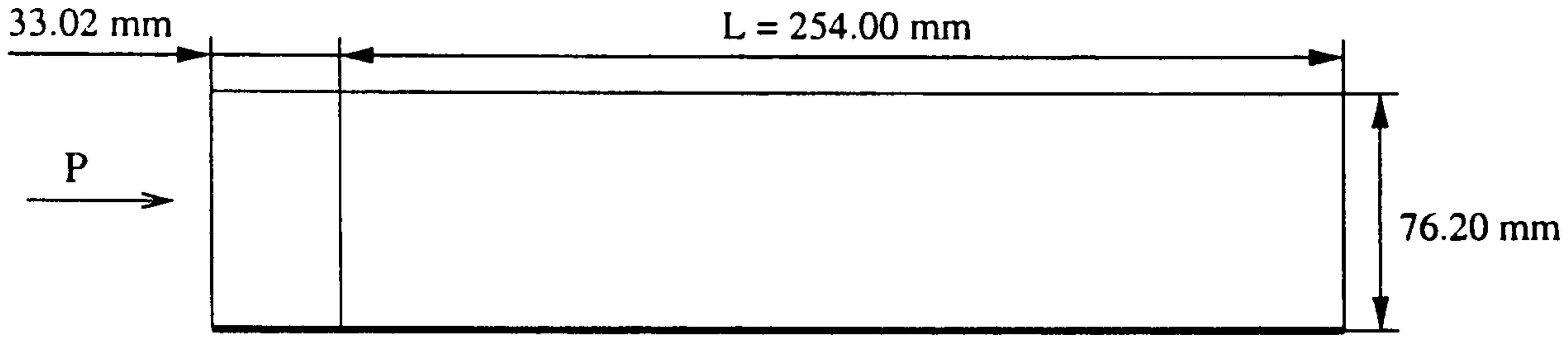

Figure 3.3: *Flat plate geometry description of laminar case*

It is found that the farfield freestream temperature T_∞ is very low compared with the wall temperature T_w, the temperature gradient is thus high in the area very close to the wall surface. So an iteration procedure using incremental values of T_∞ is found to be needed to approach the required value T_w/T_∞ (about 5.0). A typical temperature iteration in LFP Case 1 is $T_w/T_\infty = 1.5, 2.5, 4.0, 4.63$. In each iteration, the flow field of the last step was used as the initial flow field for the following case.

According to the isothermal wall condition applied in the experiment, all physical surfaces are modelled as no-slip (viscous flow) isothermal wall surfaces. Zero pressure gradient is used on these wall surfaces.

Both the coarse and fine grids were tested with all the three flow conditions listed in Table 3.2 for validation of the PMB2D code. Static pressure and heat transfer distributions are compared with experimental data in Fig. 3.4 and 3.5, respectively.

In these two figures, symbols indicate the experimental data while lines indicate computational data. In the experiments, heat transfer rate and static pressure were measured from the position of the slot ($x/L = 0$), only values from this point are

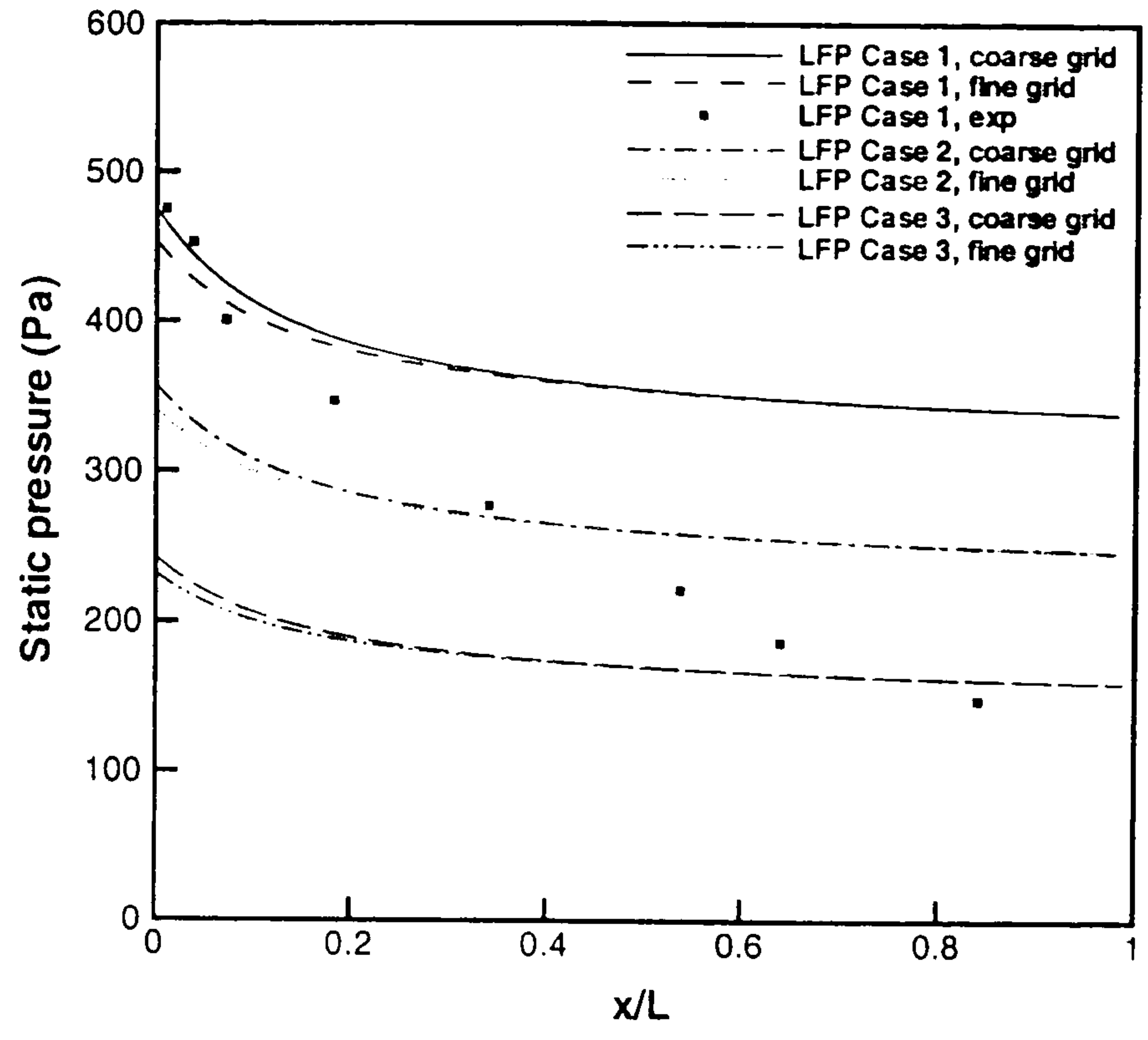

Figure 3.4: *Static pressure distributions over a flat plate, laminar flow*

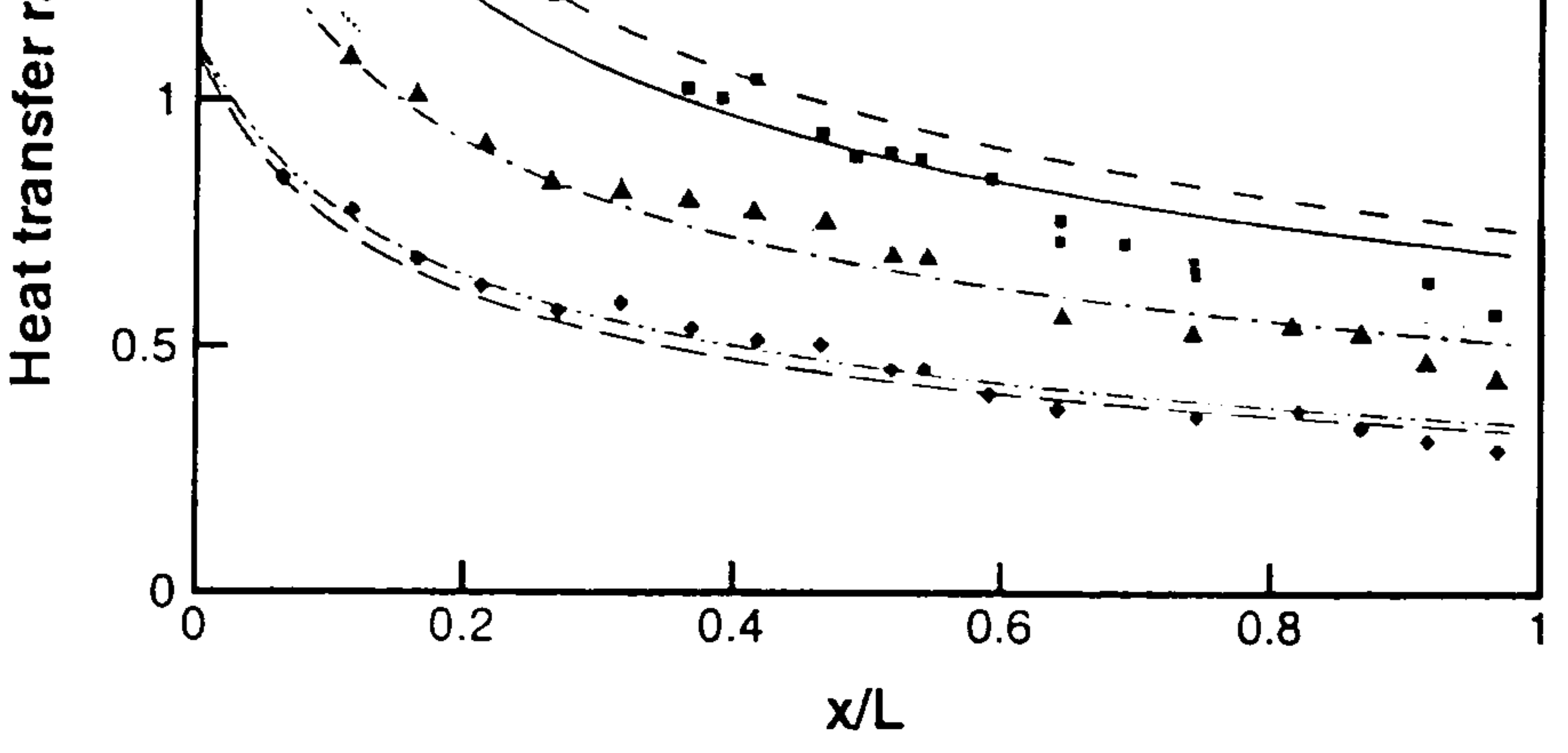

Figure 3.5: *Heat transfer rate distributions over a flat plate, laminar flow*

compared here. As we can see in Fig. 3.4, due to the conical nozzle used in the experiment, the static pressure decreased rapidly along the flat plate as the Mach number increased. As mentioned before, our interest is to match the static pressure value at the beginning of the slot. It is clear that both the coarse and fine grids give similar static pressure distribution. Heat transfer rate distributions in Fig. 3.5 agree very well with the experimental data.

The relationship between enthalpy and velocity is given by the equation for conservation of energy.

$$\begin{aligned} &h + \tfrac{1}{2}v^2 = h_0 = Constant, \text{ or} \\ &c_pT + \tfrac{1}{2}v^2 = c_pT_0 = Constant \text{ for a perfect gas.} \end{aligned} \tag{3.1}$$

At high Mach numbers the total enthalpy is nearly all converted into kinetic energy, and the remaining enthalpy changes little with Mach number in the conical nozzle. Furthermore the heat transfer rate is proportional to the difference between the recovery temperature and the wall temperature, and the recovery temperature has a fixed relation with total temperature through $T_r = Pr^{2/3}T_0$, thus also the heat transfer rate is insensitive to the Mach number in the conical nozzle.

Although the heat transfer rate is not as sensitive as the static pressure, obvious discrepancies can be observed near the trailing edge of the flat plate especially under high Reynolds number (LFP Case 1). Again, the difference between the coarse and fine grids is small in all cases.

From this grid dependence study, it was concluded that a grid density of 199×67 is sufficient and that an increased grid density did not significantly alter the results. All the calculations above converged well. Calculation details of LFP Case 1 are shown in Table 3.3.

3.2.3 Temperature profiles

Static and total temperature profiles of LFP Case 1 normal to the wall at $x/L = 0.2$, 0.5 and 0.8 are depicted in Fig. 3.6. The thickness of the thermal boundary layer is clearly growing. At $x/L = 0.5$, the temperature boundary layer is about $5\,mm$, that is, in such a thin layer, large temperature gradient exists at the wall leading to strong

Grid size	T_w/T_∞	Explicit steps /CFL number	Implicit steps /CFL number	log residual
199 × 67	1.5	4000/0.1	517/5	-4
	2.5	20/0.3	322/20	-4
	4.0	20/0.3	135/50	-4
	4.63	20/0.3	287/100	-8
396 × 133	1.5	4000/0.1	1142/5	-4
	2.5	20/0.3	797/20	-4
	4.0	20/0.3	314/50	-4
	4.63	20/0.3	941/100	-8

Table 3.3: Calculation details of LFP Case 1

heat transfer from the fluid to the wall. The static temperature contours illustrated in Fig. 3.7 again clearly shows the development of the temperature profile through the boundary layer including a high temperature layer in the vicinity of the wall. In Fig. 3.7, the leading edge of the flat plate is located at the start point with $x/L = -0.13$.

3.3 Hypersonic turbulent flow over a flat plate

In this section, the PMB2D code was tested for its ability to simulate hypersonic turbulent flow. As mentioned before, this code has been used to successfully model steady and unsteady flows including aerofoils, wings, jets and cavities in subsonic and transonic flows. It has also been successfully used to study the high-speed unsteady spiked body laminar flows. The hypersonic turbulent flat plate flow is a good test case to validate the PMB2D code in hypersonic turbulent flow. Besides the Wilcox $k - \omega$ turbulence model, the Menter's baseline and SST model have also been implemented into the code.

The only working condition in the turbulent experiments tested was: $M_\infty = 8.2$, $Re/m = 2.21 \times 10^7$, $p_\infty = 957.0\,Pa$, $T_0 = 775.0\,K$, $T_\infty = 53.64\,K$.

In the experimental configuration, the flat plate was extended 152.40 mm upstream of the slot in order to enable a turbulent boundary layer to be developed before coolant injection. The length of the flat plate downstream of the slot was again 254.00 mm.

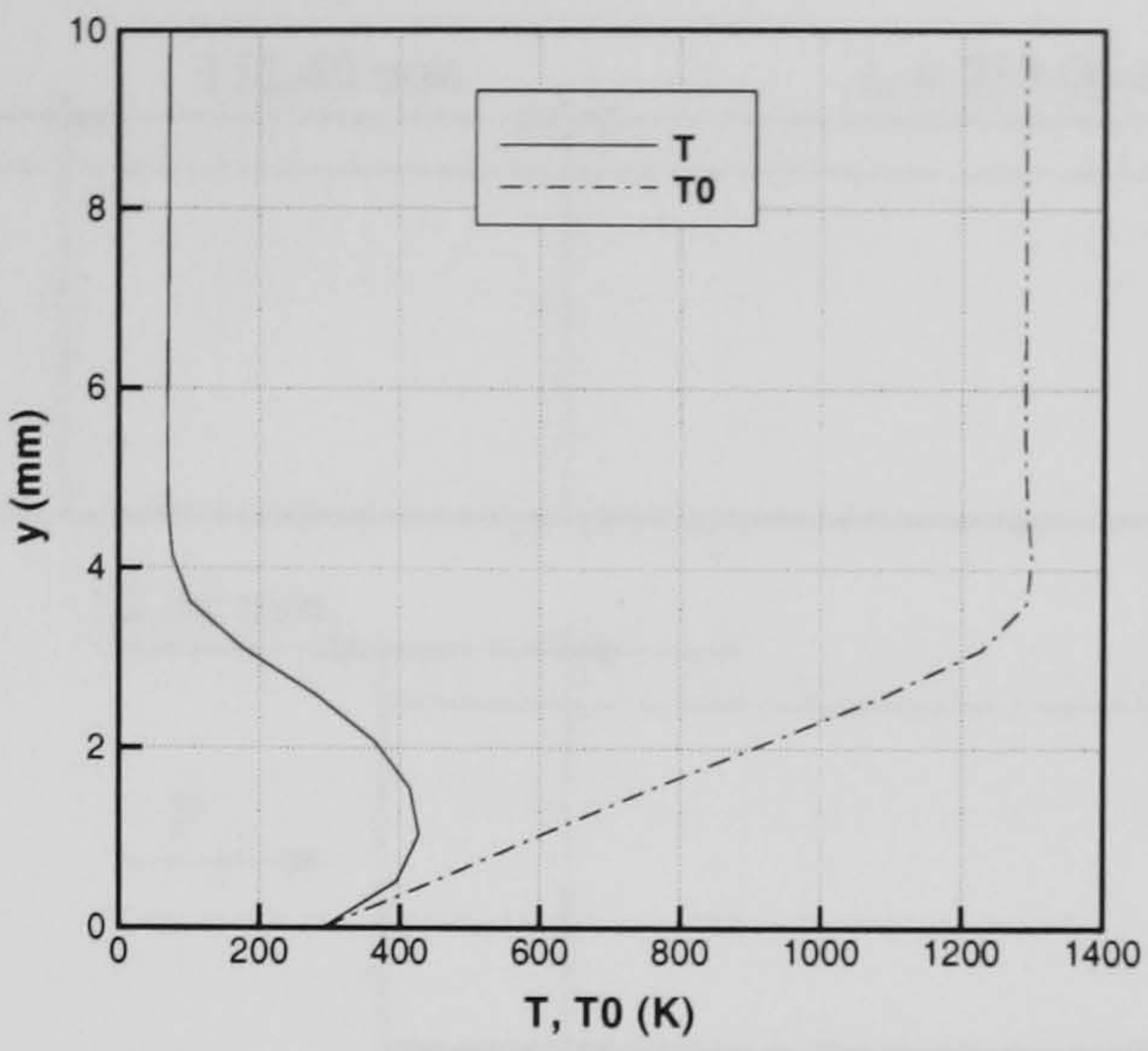

(a) *x/L = 0.2*

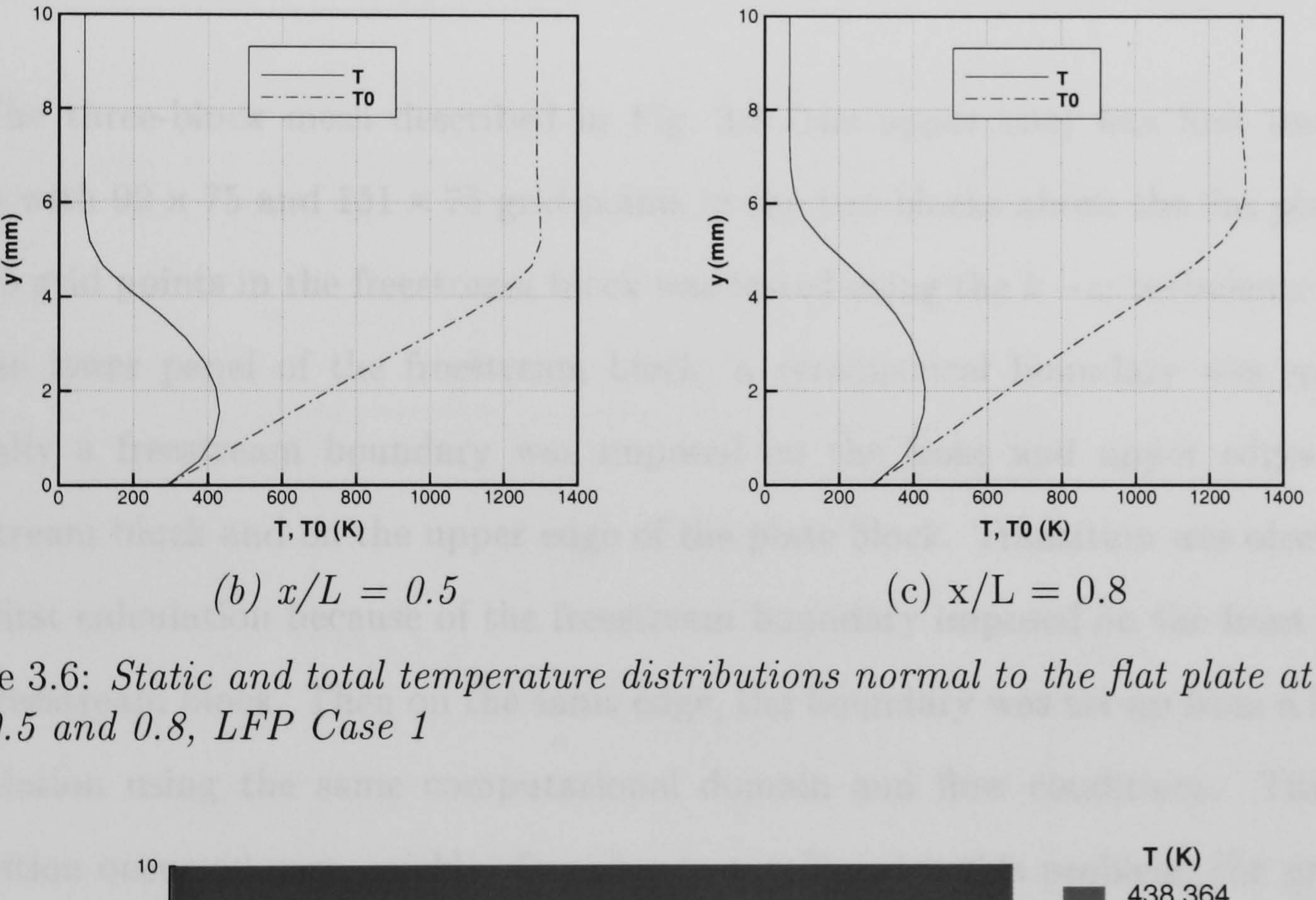

(b) *x/L = 0.5* (c) x/L = 0.8

Figure 3.6: *Static and total temperature distributions normal to the flat plate at $x/L =$ 0.2, 0.5 and 0.8, LFP Case 1*

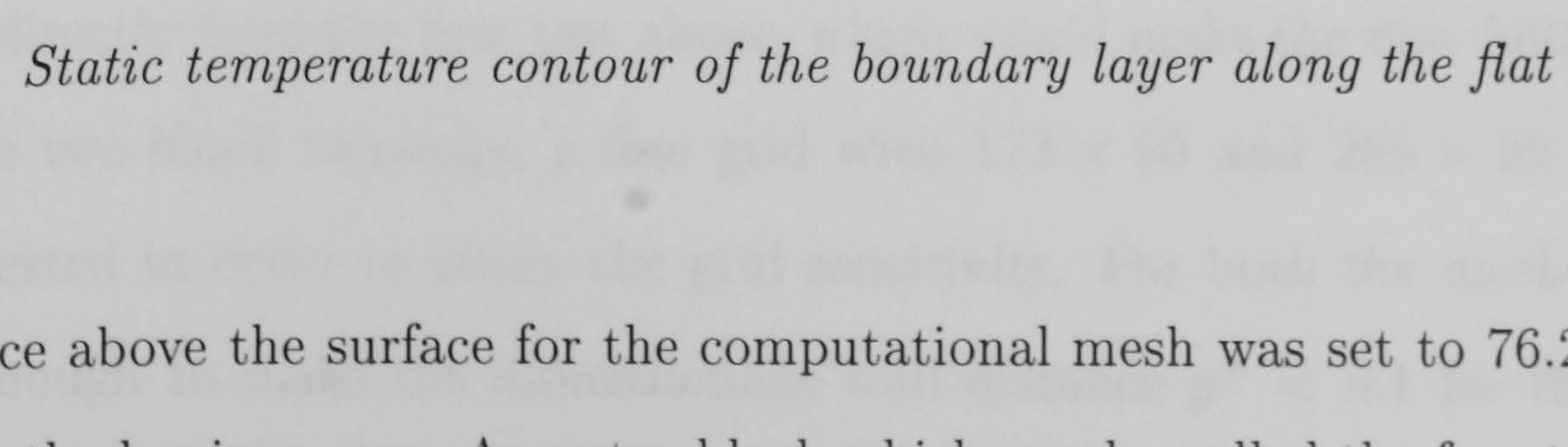

Figure 3.7: *Static temperature contour of the boundary layer along the flat plate, LFP Case 1*

The distance above the surface for the computational mesh was set to 76.20 *mm*, the same as for the laminar case. An extra block which can be called the freestream block was added upstream of the leading edge of the flat plate in this calculation. The computational geometry is sketched in Fig. 3.8.

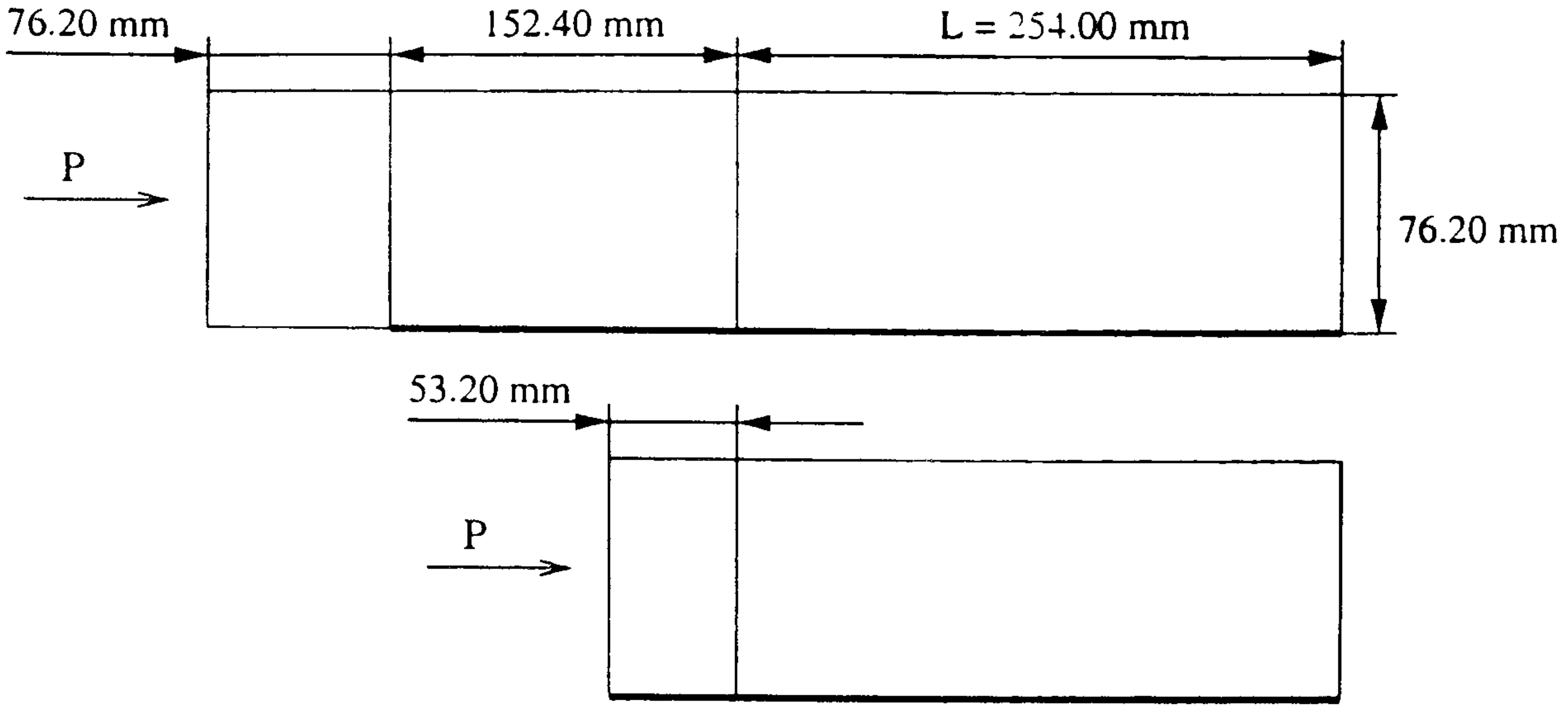

Figure 3.8: *Flat plate geometry description of turbulent case*

The three-block mesh described in Fig. 3.8 (the upper one) was first tested. A mesh with 92 × 75 and 151 × 75 grid points in the two blocks above the flat plate plus 7 × 75 grid points in the freestream block was tested using the $k-\omega$ turbulence model. In the lower panel of the freestream block, a symmetrical boundary was specified. Initially a freestream boundary was imposed on the front and upper edges of the freestream block and on the upper edge of the plate block. Transition was observed in this first calculation because of the freestream boundary imposed on the front edge of the freestream block. Then on the same edge, the boundary was set up from a laminar calculation using the same computational domain and flow conditions. This time, transition occurred very quickly. In order to totally solve this problem, the geometry was split into two blocks (the lower one in Fig. 3.8). The length of the modified block is 53.20 mm with 81 × 75 grid points in it. At station, P, a given profile boundary was prescribed based on previous calculations. Density, velocity, pressure, k and ω were all extracted directly from the first test above, which would make the flow fully turbulent.

For the two-block topology, a fine grid with 173 × 99 and 289 × 99 grid points was also tested in order to study the grid sensitivity. For both the meshes, the grid was fine enough to make the dimensionless wall distance $y^+ < 0.1$ for the first grid point above the wall. Again as in the laminar calculations it was needed to set up an iteration of T_w/T_∞ to converge the solutions. All calculations then converged well.

The convergence history of the fine grid tested is given in Table 3.4.

T_w/T_∞	Explicit steps /CFL number	Implicit steps /CFL number	log residual mean/turbulent solver
1.5	4000/0.05	2000/5	-3.84/-1.62
2.0	20/0.2	2000/10	-4.60/-2.43
3.5	20/0.4	1695/20	-4.53/-4.00
5.41	20/0.4	3995/50	-8.86/-8.00

Table 3.4: Calculation details of turbulent flat plate flow

The heat transfer rate comparison is depicted in Fig. 3.9. The experimental heat transfer rates were only available downstream of the slot position of the film cooling model, so only this region was used for comparison with the CFD results. The agreement between the computational and the experimental result is very good for both meshes.

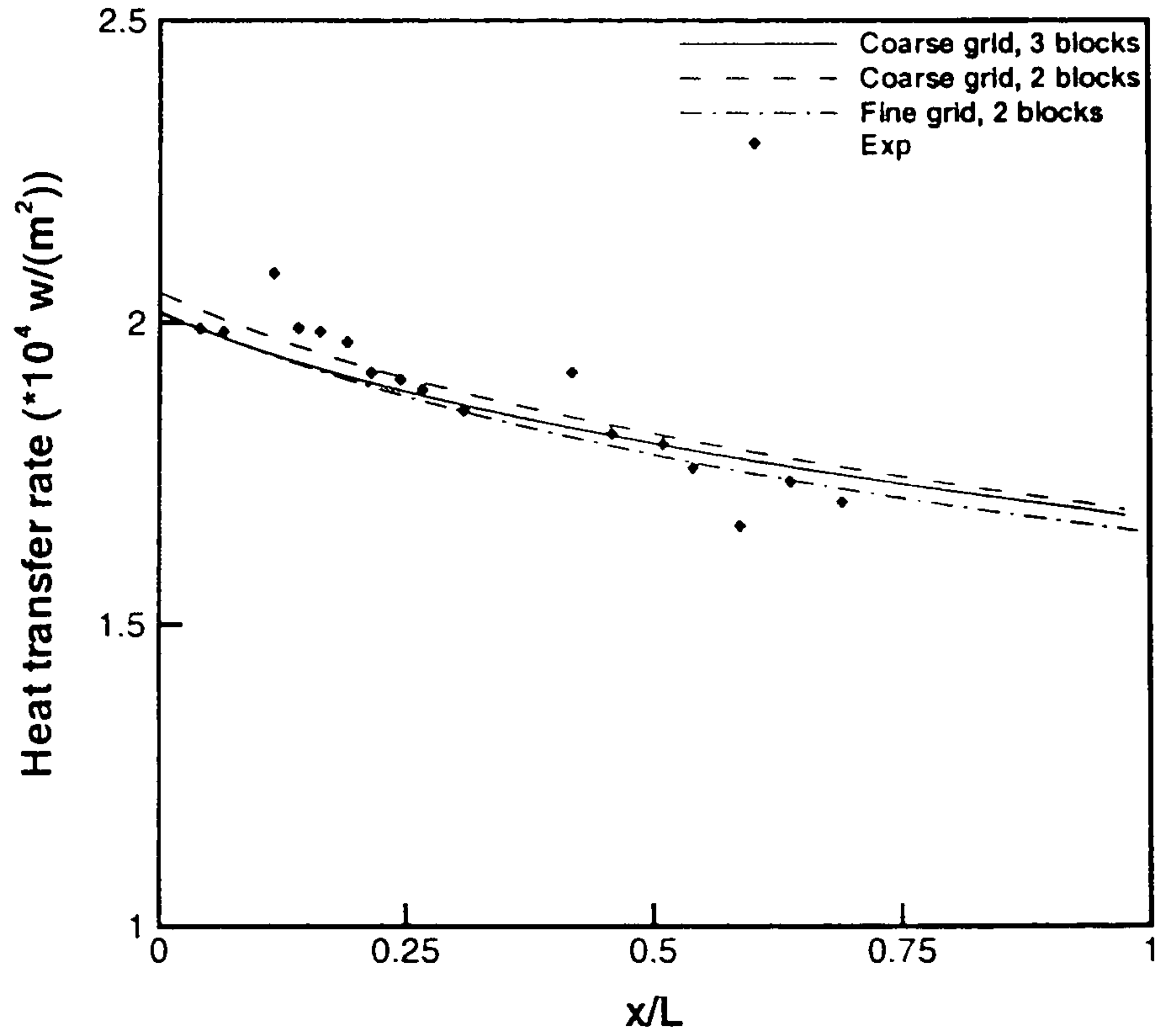

Figure 3.9: *Heat transfer rate distributions over a flat plate, turbulent flow*

In Fig. 3.10, static and total temperature distributions normal to the wall at $x/L = 0.5$ are shown. Comparing with the laminar case in Fig. 3.6, the temperature boundary layer of the turbulent flow is much thicker than the one of the laminar flow. And the temperature in the near wall region changes very rapidly in turbulent flow.

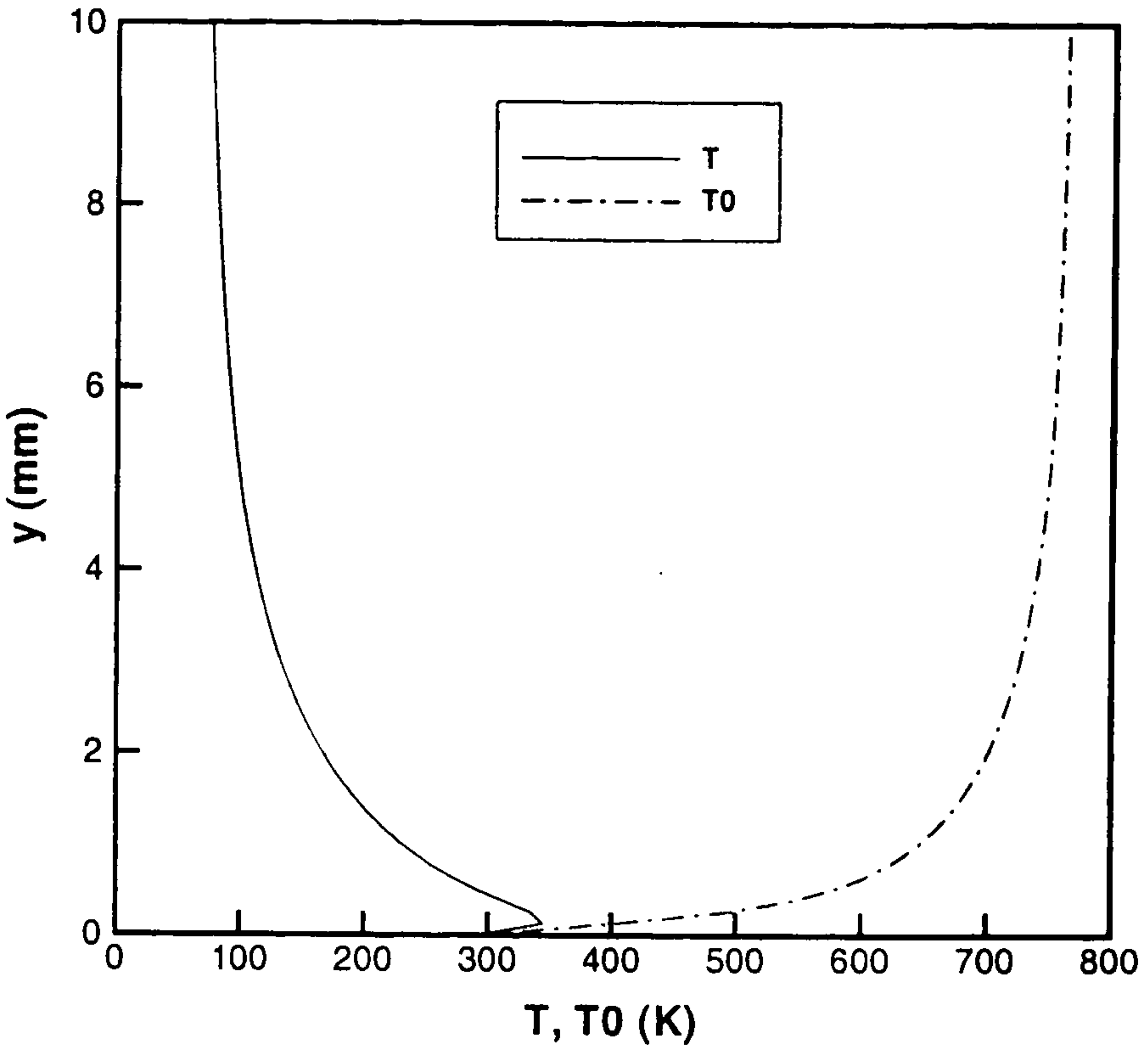

Figure 3.10: *Static and total temperature distributions normal to the flat plate at x/L = 0.5, turbulent flow*

The Menter's baseline and *SST* turbulence models were tested and found to give similar results to the $k-\omega$ model for this hypersonic turbulent flat plate flow. But the Spalart-Allmaras was found disappointingly to be not suitable for this hypersonic flow since it converged very slowly when compared with the two-equation turbulence model in this study. The low convergence of the S-A model was also observed by Hellsten [77] and Goldberg [78].

A heat transfer rate comparison is shown in Fig. 3.11. The solid line indicates the 2-D result using the PMB2D with the $k - \omega$ turbulence model. The dash-dot line indicates the 3-D result using the PMB3D with the S-A turbulence model. The coarse 3-block grid was used for the 2-D calculation. For 3-D calculation this grid was extended in the z-direction. Since freestream inlet boundary was used, transition from laminar flow to turbulent flow was observed in both cases. From the result of the S-A model in Fig. 3.11, turbulence of the flow over a flat plate develops very slowly so the flow stays laminar. Then after transition, heat tranfer rate is over-predicted by this model, which was observed by Goldberg [78] for hypersonic flow over a compression ramp.

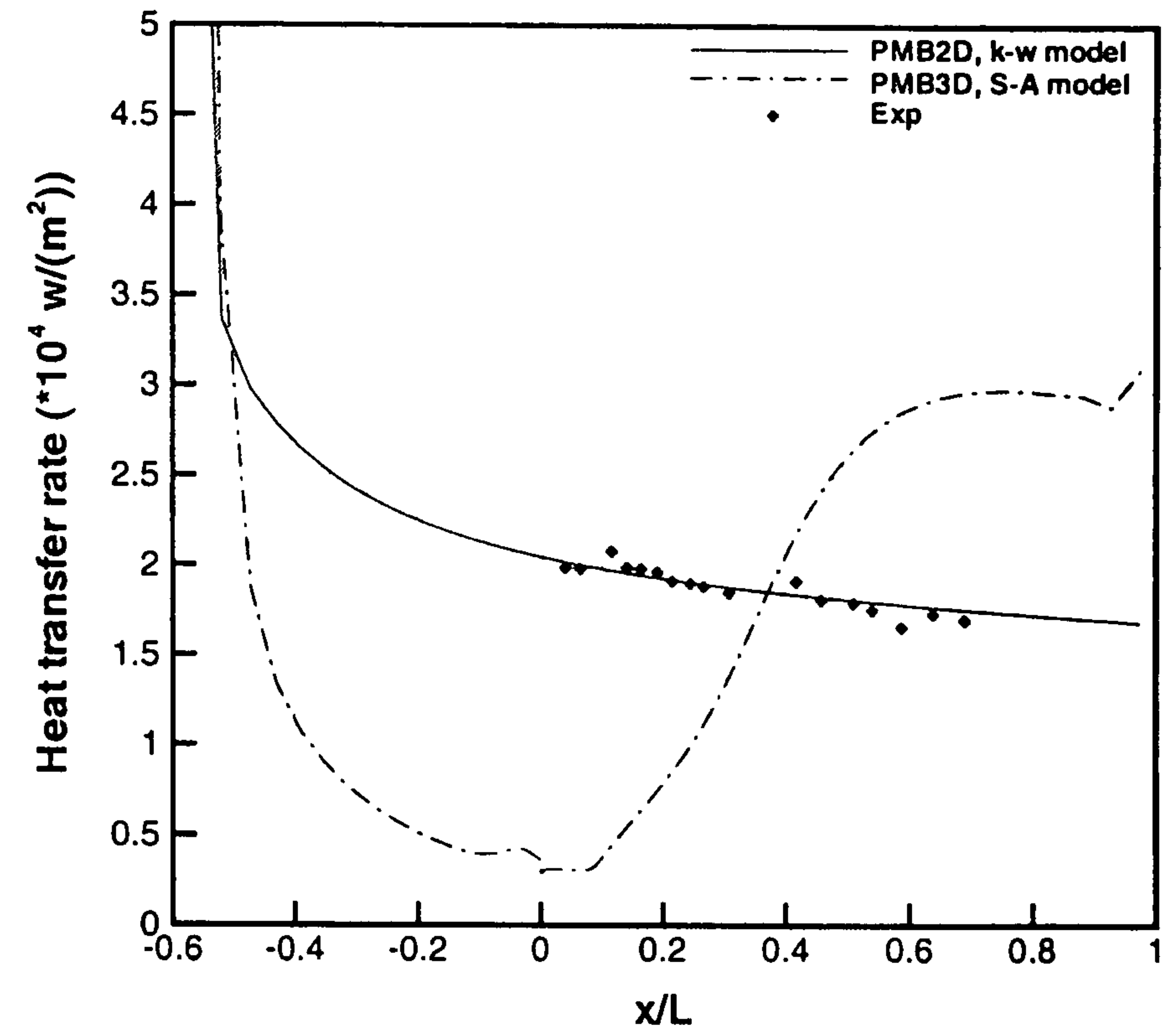

Figure 3.11: *Heat transfer rate comparison of different turbulence models*

According to results from Paciorri *et al.* [76] and Goldberg [78], the Spalart-Allmaras could be applied in heat prediction of hypersonic attached flow. But in this study, this model did not work very well (mainly because of its very slow convergence) thus it was not used in the film cooling study. For subsonic and supersonic flat plate flows, this model had been tested and found to work well. Further validation of the mean flow solver for hypersonic flows is needed which may help to make the S-A model work.

3.4 Summary

Hypersonic flow over a flat plate is a very basic but important case for the validation of a CFD code in the application of simulating hypersonic flow. Both laminar and turbulent flows were studied here. The main interest concerns prediction of the heat transfer rate from the fluid to the wall surface. Good agreement was achieved when compared with the experimental data which also gave confidence in the integrity of the experimental measurements for the film cooling study. In Fig. 3.5 and 3.9, the calculated heat transfer rate is commonly in agreement of the experimental data within ±8%. The grid dependence study has shown that the computational results obtained are grid independent. These flat plate results would provide the basic information for the calculations of film cooling effectiveness in the following chapters.

Chapter 4

Hypersonic Laminar Film Cooling

4.1 Analysis of the experimental flow conditions

Although most studies of film cooling have been executed on turbulent flow, laminar flow is a common case for vehicle surfaces operating at high Mach numbers and at low wall temperature conditions. The effect of slot height, streamwise slot position, primary flow conditions and different coolant gases were examined by Richards [30] on a flat plate in a gun tunnel under isothermal wall conditions. The wall and coolant temperature were at the laboratory level of $290.0\,K$.

Three groups of experiments in hypersonic laminar film cooling were executed. The first group (LFC Cases 1 and 2 with 5) involved different primary flow conditions with the same slot height ($s = 1.2192\,mm$) and coolant mass flow rate ($\dot{w}_c = 5.07 \times 10^{-4}\,kg/s$). The second group (LFC Cases 3-7) involved the same primary flow conditions ($Re/m = 6.46 \times 10^6$, $T_0 = 1290.0\,K$) and slot height ($s = 1.2192\,mm$) with changing coolant mass flow rate. The third group (LFC Cases 8 and 9 with 5) involved constant primary flow conditions ($Re/m = 6.46 \times 10^6$, $T_0 = 1290.0\,K$) and coolant mass flow rate ($\dot{w}_c = 5.07 \times 10^{-4}\,kg/s$) with changing slot height.

Please note that all the flow conditions listed in Table 4.1 have been re-calculated due to the conical nozzle used in the experiments as described in Section 3.2.1. For the specification of the film cooling initial conditions at the slot exit, the mid coolant

LFC Case	Group	M_∞	Re/m	$T_0\,(K)$	$s\,(mm)$	$\dot{w}_c\,(kg/s)$
1	1	9.9	5.45×10^6	1170.0	1.2192	5.07×10^{-4}
2		9.9	4.24×10^6	1030.0	1.2192	5.07×10^{-4}
3	2	9.9	6.46×10^6	1290.0	1.2192	2.95×10^{-4}
4		9.9	6.46×10^6	1290.0	1.2192	4.08×10^{-4}
5		9.9	6.46×10^6	1290.0	1.2192	5.07×10^{-4}
6		9.9	6.46×10^6	1290.0	1.2192	6.12×10^{-4}
7		9.9	6.46×10^6	1290.0	1.2192	7.33×10^{-4}
8	3	9.9	6.46×10^6	1290.0	0.8382	5.07×10^{-4}
9		9.9	6.46×10^6	1290.0	1.6002	5.07×10^{-4}

Table 4.1: Experimental cases selected for numerical study (laminar flow)

mass flow case ($5.07\times10^{-4}\,kg/s$) for a slot height $1.2192\,mm$ is taken as an illustration. The slot width is $0.1143\,m$ giving a slot area of $1.39\times10^{-4}\,m^2$. With the film reservoir temperature of room temperature, $290.0\,K$, and the conditions of the film at the slot exit, which is assumed to be a nozzle throat, and the coolant flow sonic, then the pressure in the reservoir to give this mass flow rate is $1532.0\,Pa$ and the flow conditions at the throat are: $\rho_c = 0.01167\,kg/m^3$, $p_c = 809.34\,Pa$, $T_c = 241.67\,K$. Coolant flow conditions at the slot exit for all cases are listed in Table 4.2.

LFC Case	Group	M_c	$\rho_c\,(kg/m^3)$	$p_c\,(Pa)$	$T_c\,(K)$
1	1	1.0	1.17×10^{-2}	809.34	241.67
2		1.0	1.17×10^{-2}	809.34	241.67
3	2	1.0	6.79×10^{-3}	471.11	241.67
4		1.0	9.40×10^{-3}	652.30	241.67
5		1.0	1.17×10^{-2}	809.34	241.67
6		1.0	1.41×10^{-2}	978.46	241.67
7		1.0	1.69×10^{-2}	1171.73	241.67
8	3	1.0	1.17×10^{-2}	809.34	241.67
9		1.0	1.17×10^{-2}	809.34	241.67

Table 4.2: Coolant flow conditions (laminar flow)

4.2 Preliminary study

4.2.1 Grid sensitivity study

In this preliminary study, LFC Case 5 was selected for the grid dependence study. The computational domain is shown in Fig. 4.1.

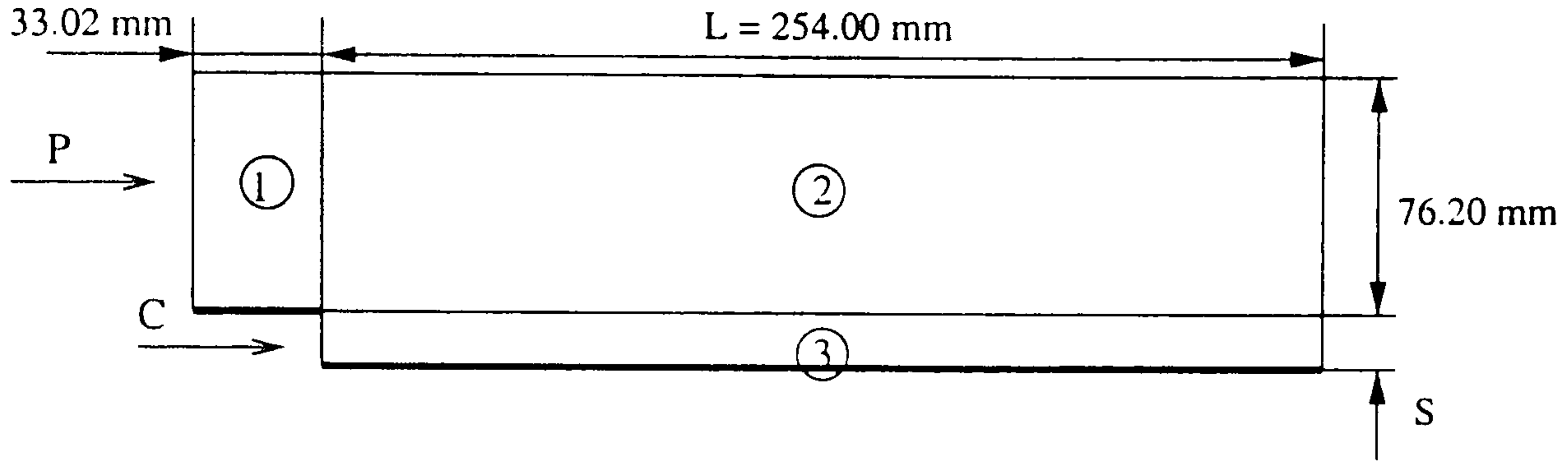

Figure 4.1: *Hypersonic laminar film cooling, description of the geometry*

Because of the simple geometry, only three blocks were necessary. Two sets of two-dimensional structured multiblock grids were generated using ICEMCFD Hexa^{TM} [79]. Denser grid distributions were set up in the near wall and the near slot area. The grid in the near slot region is shown in Fig. 4.2. The reference length L is the length of the flat plate downstream of the slot.

A fine grid and a coarse grid were created. For the fine grid, there are 67×99, 251×99 and 251×51 grid points in blocks 1, 2 and 3 in Fig. 4.1. For the coarse grid, 51×67, 151×67 and 151×43 grid points are included in these blocks. At the slot exit, uniform boundary conditions were set up with values of all the conservative variables, e.g., ρ_c, u_c, v_c, and p_c as defined in Table 4.2. On the wall surface, the velocity was set to zero. The coolant fluid was assumed to be parallel to the primary flow stream, thus v_c was set to zero.

The calculated static pressure and heat transfer distributions for these two grids in Fig. 4.3 and 4.4 show that the calculations are grid independent. The static pressure distribution is compared with the computational flat plate result under the same primary flow conditions in Fig. 4.3. Just downstream of the slot, a pressure peak occurs due to the interaction of the coolant flow with the primary flow stream. After

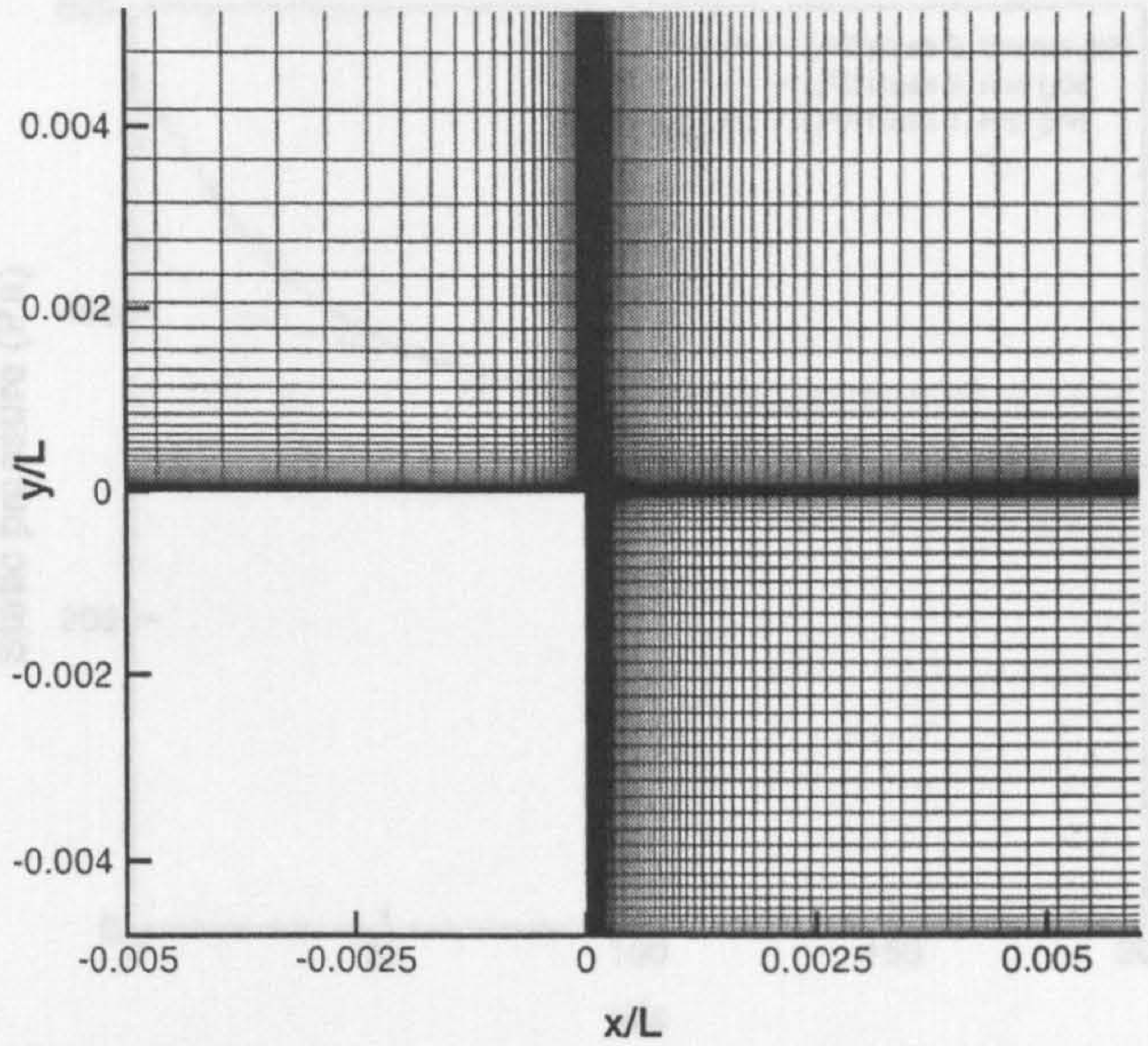

Figure 4.2: *Grid topology in the near slot region*

about 50 s downstream of the slot, the disturbance to the static pressure disappears. In Fig. 4.4 the heat transfer rate is compared not only with the experimental data, but also with the flat plate results. It is obvious that film cooling for this laminar flow case is very effective. Here the length from the slot to the point where heat transfer rate becomes greater than zero is defined as the "cooling length". Under the flow conditions in LFC Case 5, the cooling length is about 20 s. The wall surface is thus fully protected from heating from the primary flow within the cooling length.

4.2.2 Changing primary flow conditions

LFC Cases 1 and 2 were also calculated using the same coarse grid. Again, static pressure distributions are compared in Fig. 4.5 with the flat plate results. In Fig. 4.6 heat transfer rate distributions are compared with the experimental data. With total temperature and static pressure decreasing, heat transfer rate will obviously decrease. Although heat transfer rate is under-predicted in all three cases, the tendency is clearly predicted.

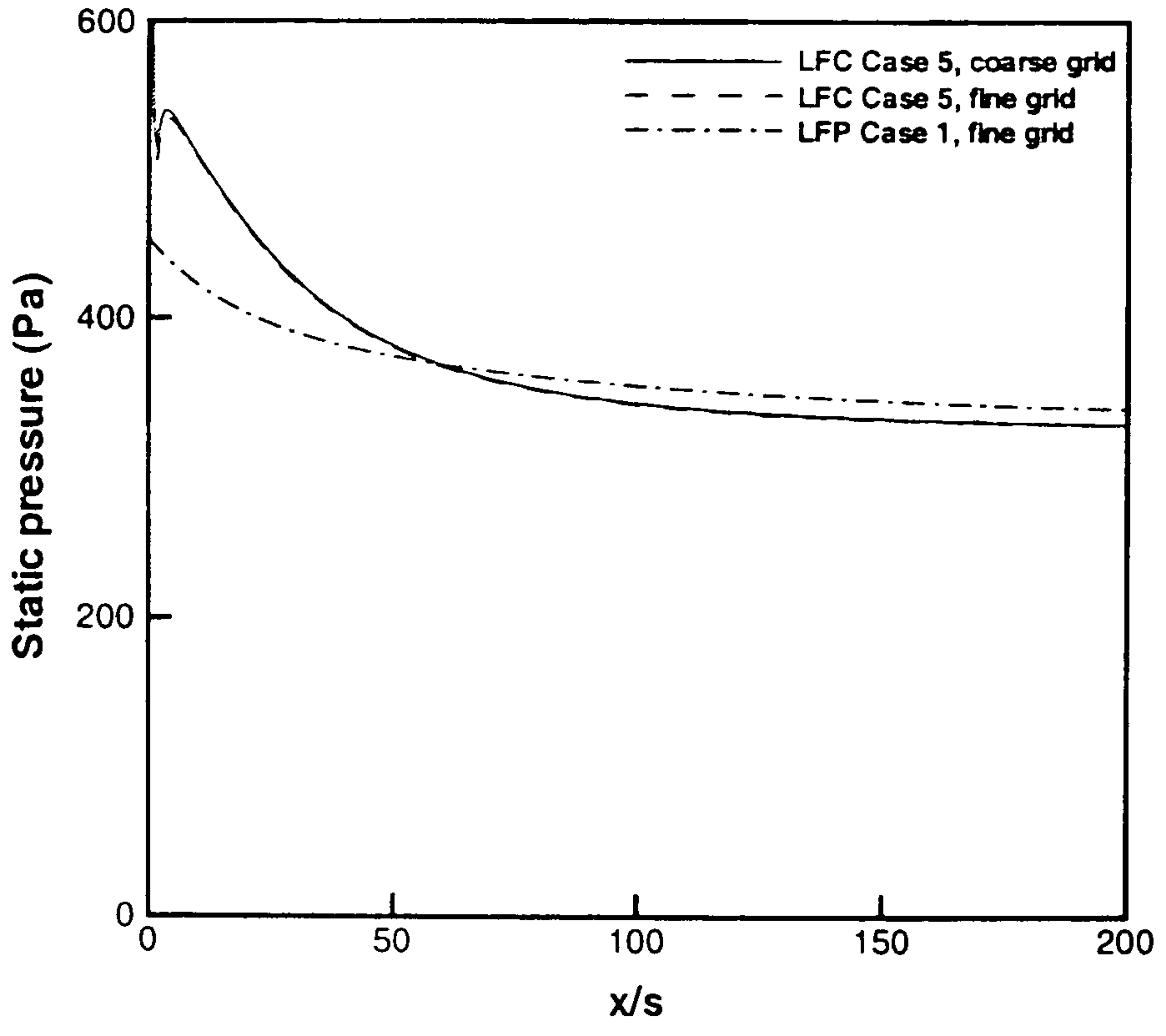

Figure 4.3: *Grid sensitivity study: static pressure distribution*

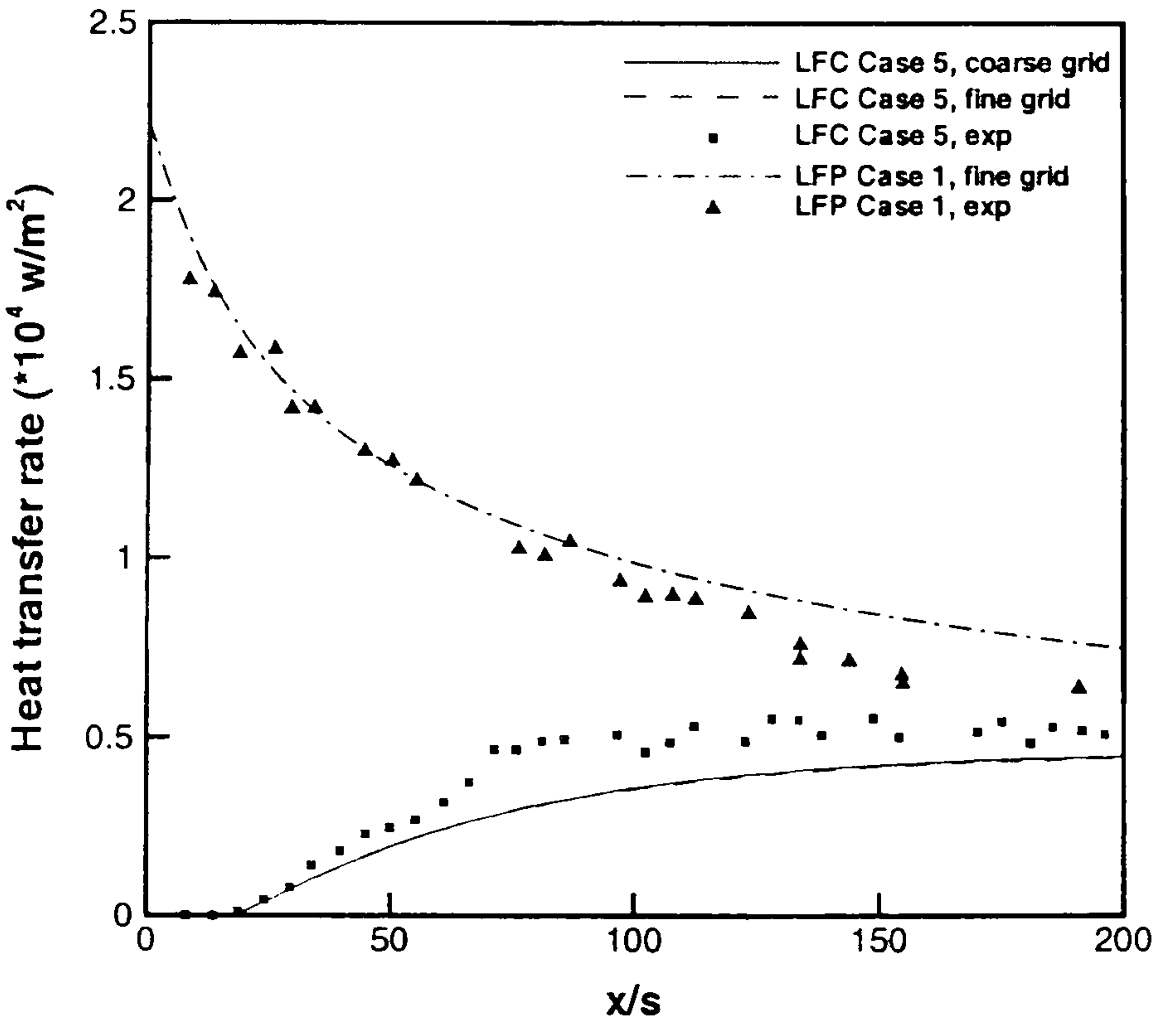

Figure 4.4: *Grid sensitivity study: heat transfer rate distribution*

4.2.3 Coolant inlet extension

Since the heat transfer rate was not predicted well, it is necessary to investigate why this happened. A possible cause is the uniform boundary condition used in this preliminary

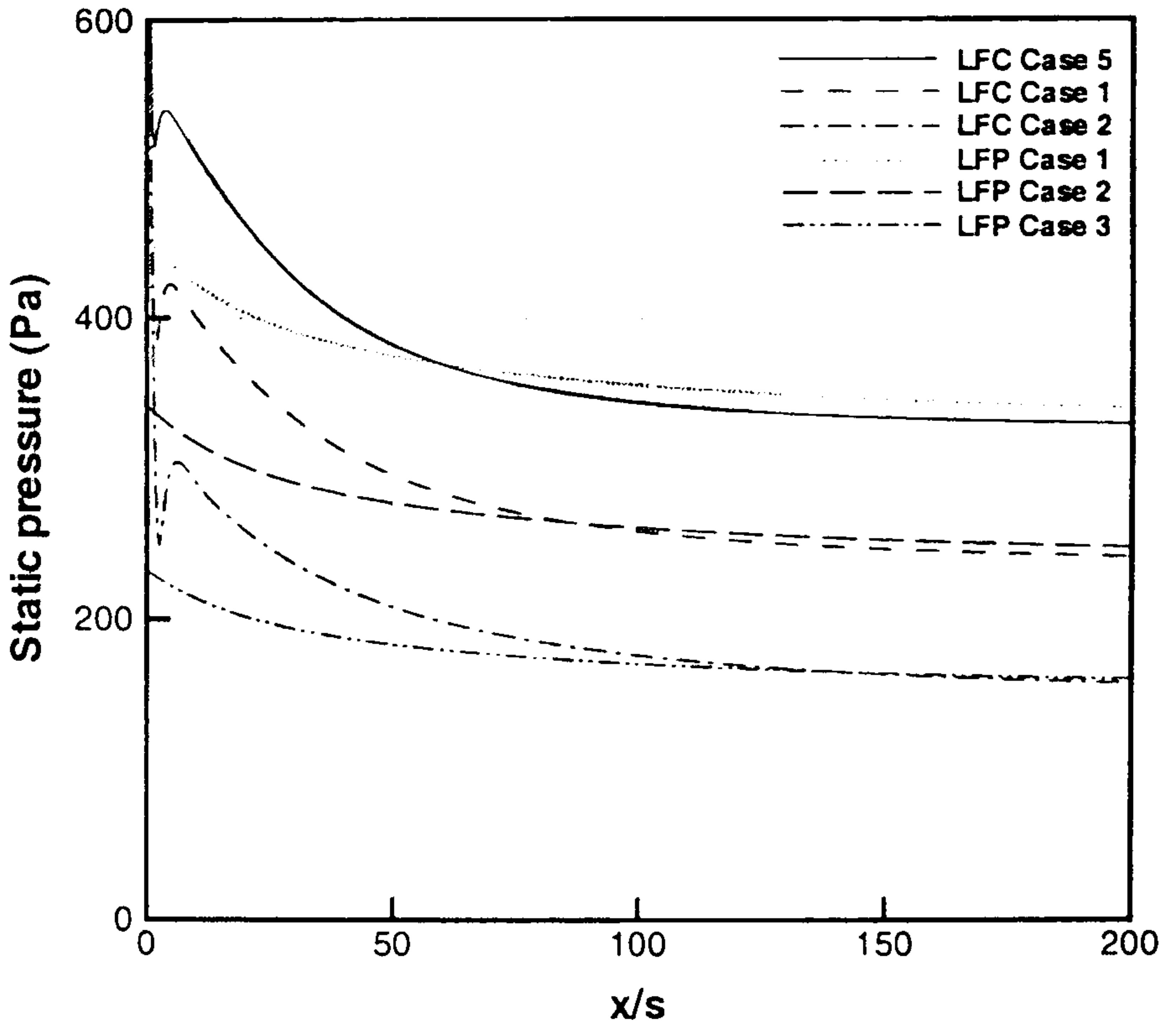

Figure 4.5: *Changing primary flow conditions: static pressure distribtuion*

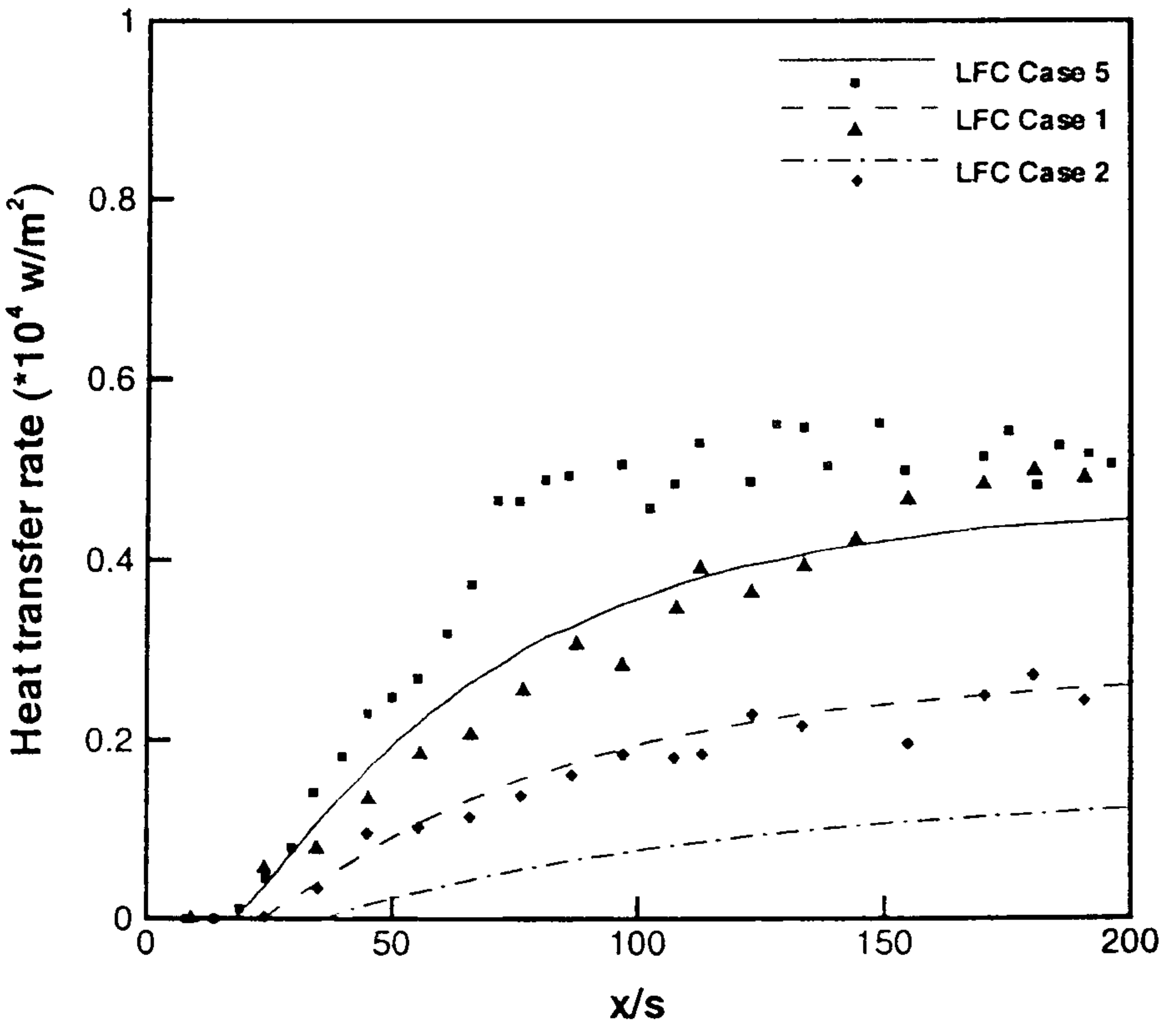

Figure 4.6: *Changing primary flow conditions: heat transfer rate distribtuion*

study and the coolant flow leaving parallel to the primary flow at the slot, which may not accurately describe the flow. Cary and Hefner [7] measured the velocity and total temperature profiles at the slot exit and found different types of profiles generated according to the mass flow rate (Fig. 4.7). Thus it is quite important to set up correct profiles of flow parameters if the slot exit boundary is used in the numerical study.

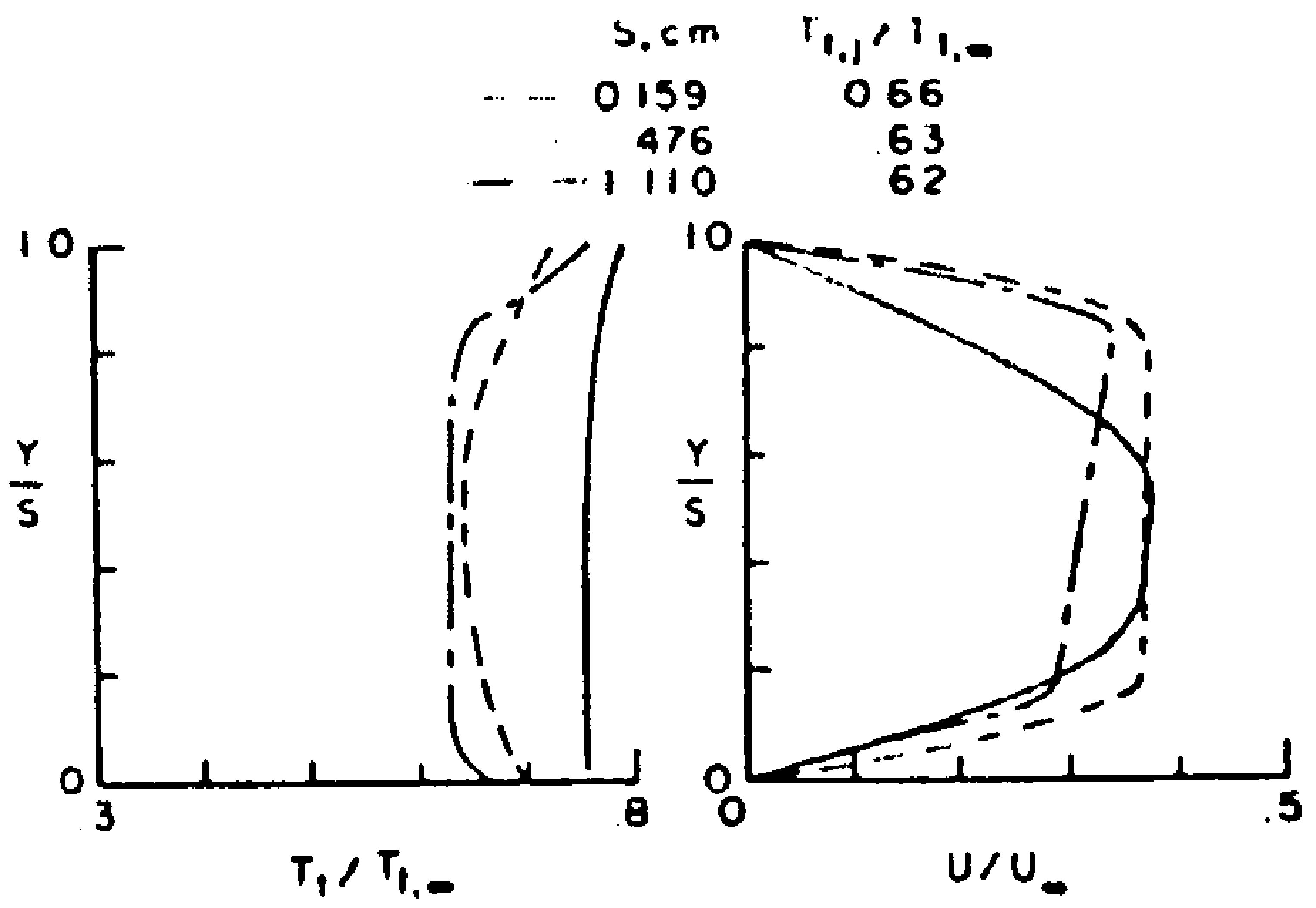

(a) "HOT" FLOW

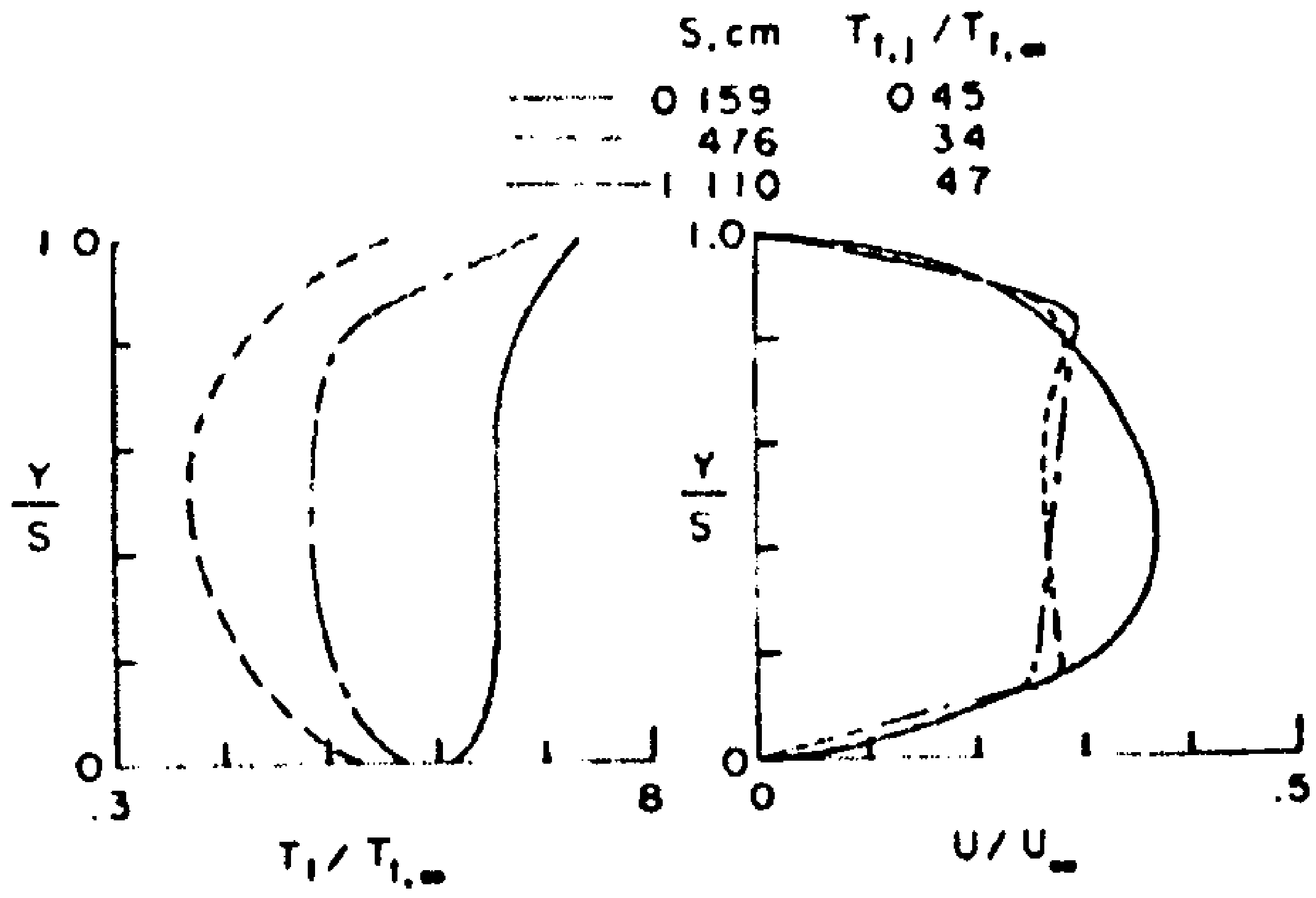

(b) "COLD" FLOW

Figure 4.7: *Temperature and velocity rofiles measured at the slot exit by Cary and Hefner [7]*

Kassimatis *et al.* [52] analysed this uniform boundary condition, which was called uniform velocity boundary in [52], as well as a boundary condition based on a uniform total pressure boundary. It was found that the former one is an inappropriate boundary condition. Although the latter boundary condition was found to give improved result at high mass flow rate ($u_c/u_p > 0.5$), a better approach was thought to be to include the development of the flow in the coolant inlet. Therefore, an upstream extension to the coolant inlet was considered.

Since detailed information on the original geometry was not available, a coolant inlet of approximate dimensions was set up from the sketch drawn by Richards [30]

(Fig. 3.2 in Chapter 3). Fig. 4.8 gives detailed information about the inlet duct. OB1 is the lip with the nominal and small thickness of 0.0508 mm. B1A1 is the slot. The radius of arc A1A2A3 is equal to the slot height, s, and the radius of arc B1B2B3 is 2.5 s. The length of A4B4 is 5.8218 times the slot height. A3A4 and B3B4 are both tangential to the relevant arc. The coolant injection rate used to calculate new boundary conditions for the calculations was that measured in the experiment.

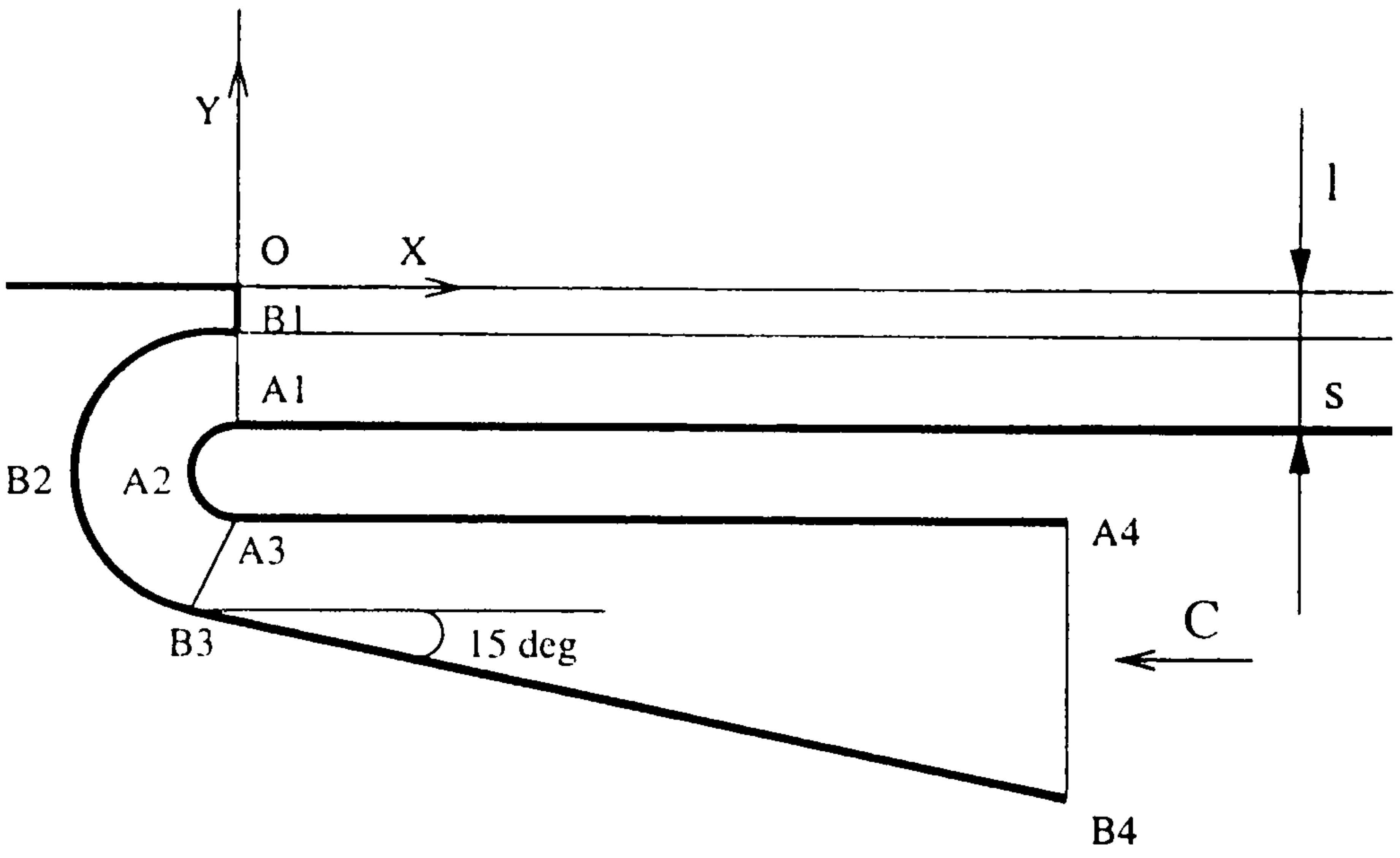

Figure 4.8: *Laminar film cooling geometry description with coolant inlet extension and lip*

For the coolant inlet extension, the coolant flow conditions at the slot exit listed in Table 4.2 were recalculated to apply to A4B4 in Fig. 4.8 and listed in Table 4.3.

LFC Case	Group	M_c	$\rho_c\,(kg/m^3)$	$p_c\,(Pa)$	$T_c\,(K)$
1	1	0.10	1.83×10^{-2}	1521.25	289.42
2		0.10	1.83×10^{-2}	1521.25	289.42
3	2	0.10	1.07×10^{-2}	885.50	289.42
4		0.10	1.47×10^{-2}	1226.08	289.42
5		0.10	1.83×10^{-2}	1521.25	289.42
6		0.10	2.21×10^{-2}	1839.12	289.42
7		0.10	2.65×10^{-2}	2202.40	289.42
8	3	0.10	1.83×10^{-2}	1521.25	289.42
9		0.10	1.83×10^{-2}	1521.25	289.42

Table 4.3: Laminar coolant flow conditions with coolant inlet extension and lip

The prediction of the heat transfer rate using these new boundary conditions given in Fig. 4.9 is seen to be improved when compared with the uniform slot exit boundary calculation in Fig. 4.6. In general, the agreement is fairly good for all three cases. For LFC Case 1, deficiencies in the experiment such as the conicity of the freestream flow and the deterioration of the 2-dimensionality of the flow noted in the experiment far downstream in [30] may explain the differences far from the slot exit. Discrepancy in the near slot area is noticeable in LFC Cases 1 and 5. The velocity profile at the slot exit for LFC Case 5 is shown in Fig. 4.10. The coolant flow is shown not to be parallel to the primary flow as was assumed in the previous Section. The Mach number at the slot exit was found to be sonic in these calculations, which indicated that the coolant flow choked at this position as expected since this was at the minimum duct area. Since the curved inlet extension was only roughly simulated, the flow parameters at the slot exit may still not be adequately represented, which may signal why some lack of agreement can still be observed in the near slot region.

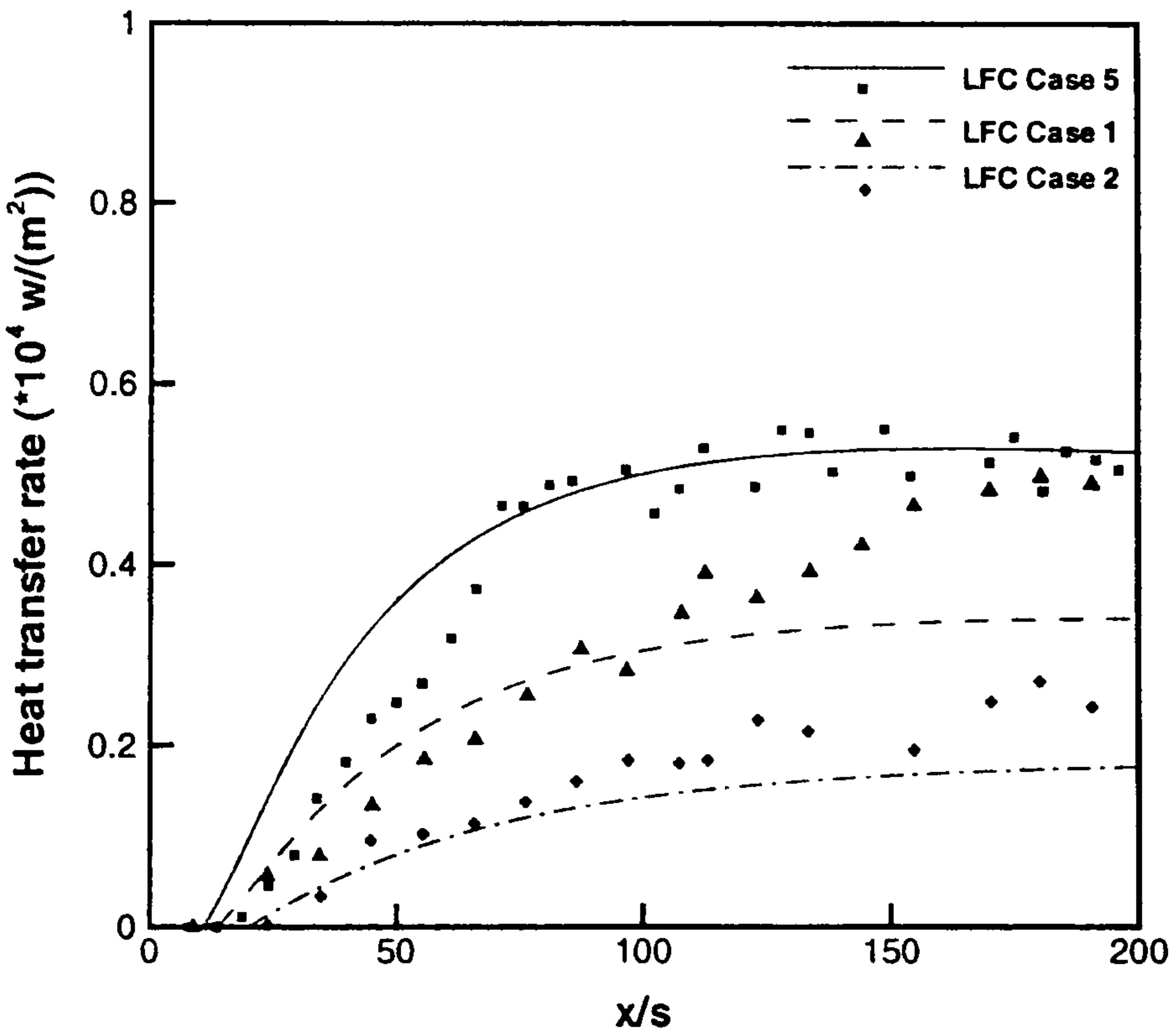

Figure 4.9: *Heat transfer rate comparison under different primary flow conditions with coolant inlet extension and lip*

For LFC Case 5, velocity profiles at eight different positions downstream of the slot are shown in Fig. 4.11. The discrete flow features of the coolant and primary flow is strongly evident. The development of the mixing layer can be clearly observed

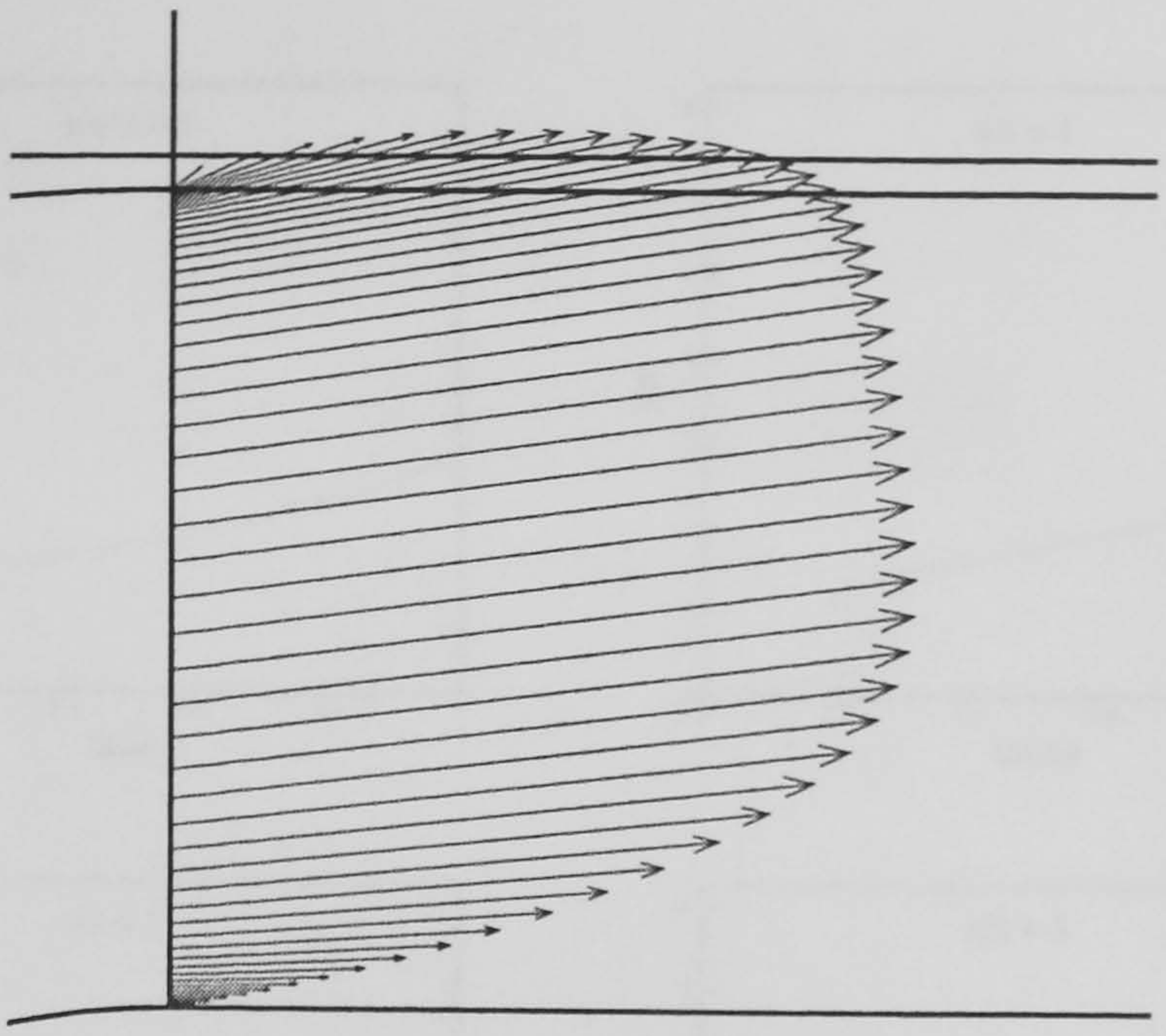

Figure 4.10: *Velocity profile at the slot exit with coolant inlet extension and lip for LFC Case 5*

from 0.5 s to about 20 s downstream of the slot. After that, the separate identity of the coolant and the primary flow stream disappears. The two flows finally evolve to a single boundary layer, which signals the full merging of the coolant and the main flow. It is seen in Fig. 4.9, that only after about 10 s (the cooling length in this case) downstream of the slot, does the heat transfer exceed zero and then start increasing.

Fig. 4.12 graphically illustrates the effect of kinetic heating to a film cooled isothermal surface in hypersonic flow. Upstream of the slot it is seen that there is a band of high temperature air which provides the positive temperature gradient, hence heating at the wall. The effect of the coolant is to initially remove this temperature gradient. However further downstream there is a mixing of the flows when the initial profile is re-established although more diffused resulting in an increasing heat transfer rate. An amplified static temerature contour in the near slot area is shown in Fig. 4.13 which clearly shows heat protection of the wall surface in the near slot area.

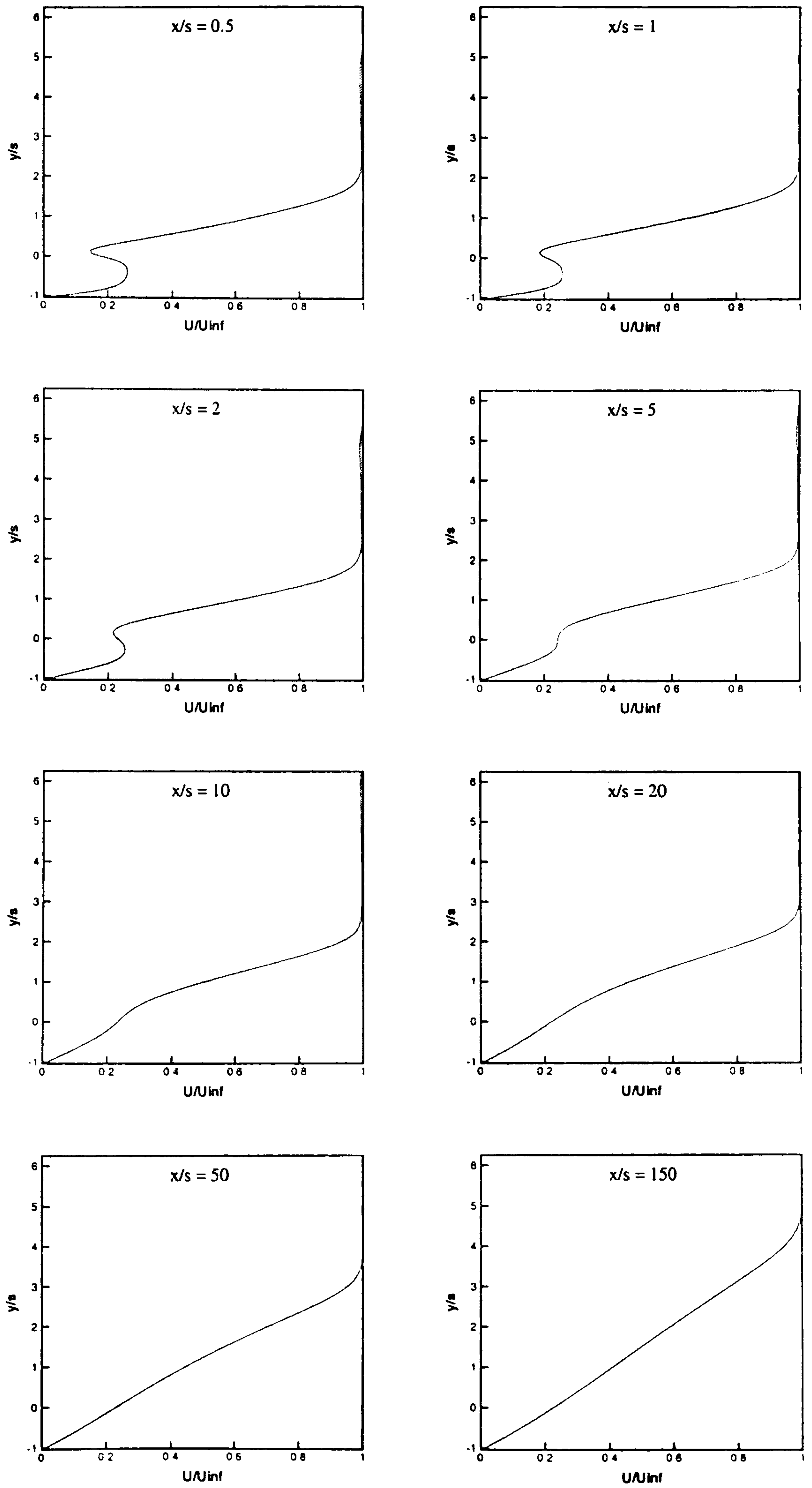

Figure 4.11: *Velocity profiles of laminar film cooling problem for LFC Case 5*

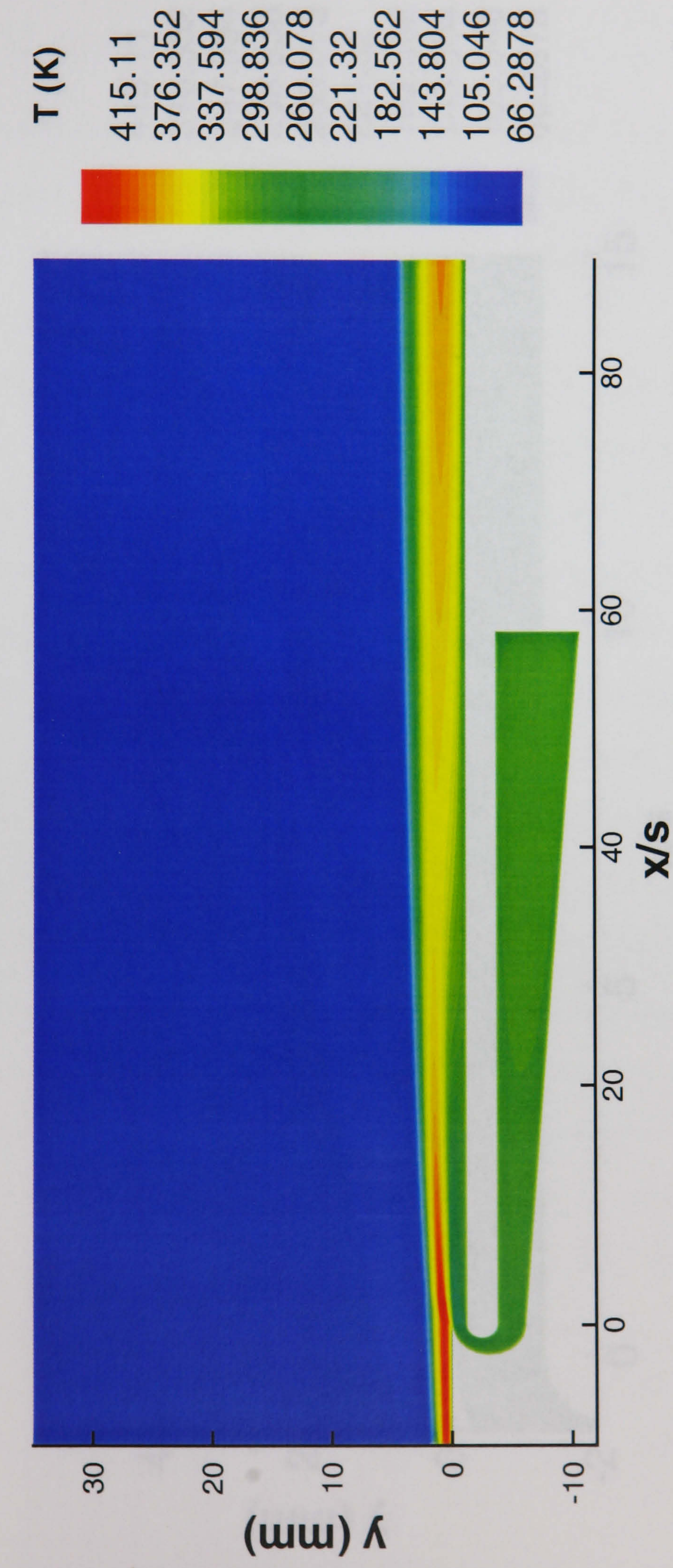

Figure 4.12: *Static temperature contour of LFC Case 5*

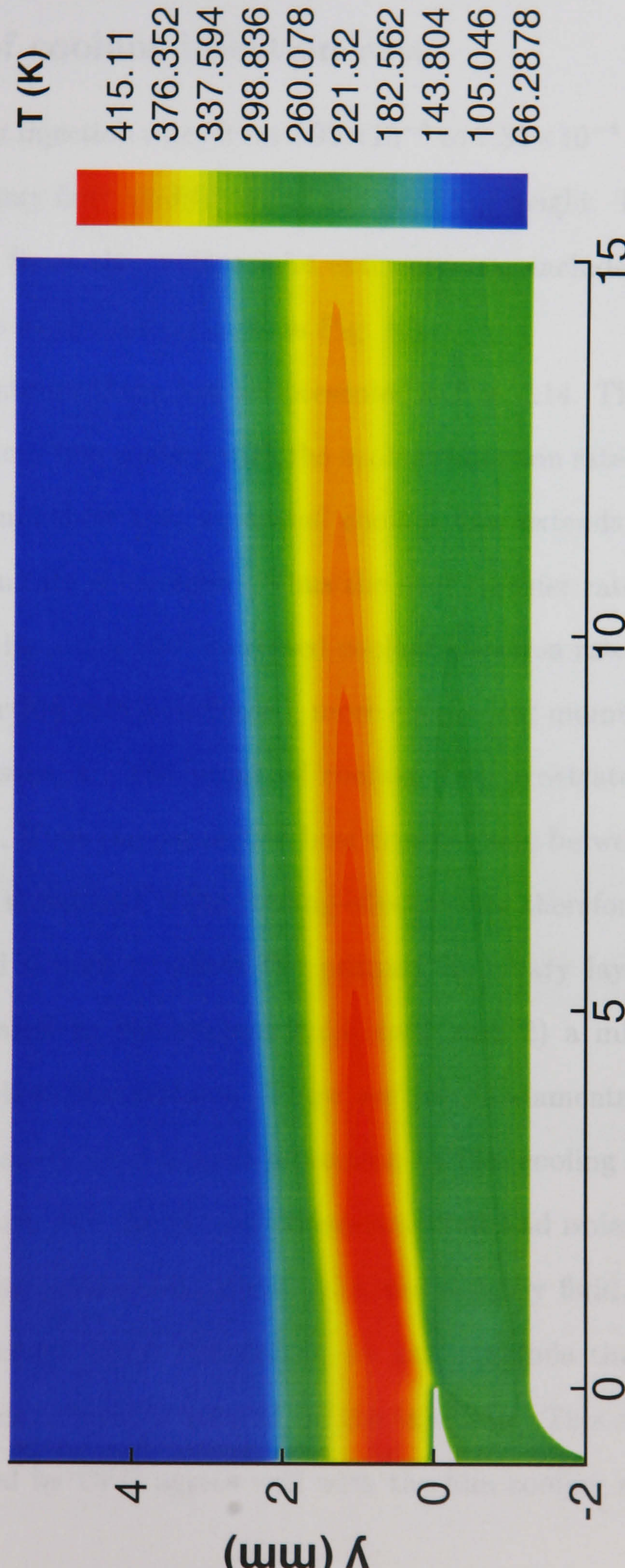

Figure 4.13: *Amplified static temperature contour in the near slot area of LFC Case 5*

4.3 Laminar film cooling study

4.3.1 Effect of coolant injection rate

Five different coolant injection rates from 2.95×10^{-4} to 7.33×10^{-4} kg/s were computed under the same primary flow conditions and the same slot height. These are LFC Cases 3 to 7 in Table 4.1. Since the coolant inlet extension was included, a simple uniform boundary was set up at the inlet, i.e., C in Fig. 4.8.

Mach number contours of the flow are presented in Fig. 4.14. The five Mach number contours are for laminar film cooling with the coolant injection rate increased. Here the Mach number contours show that separated coolant flow extends downstream as the coolant flow injection rate is increased. Thus the heat transfer rate decreases and film cooling effectiveness increases with increased coolant injection rate. This is because as the coolant flow injection rate is increased, more energy and momentum are contained in the coolant flow stream. The unmixed coolant flow penetrates the primary flow further from the slot. Thus the convective heat transfer rate between the primary flow and the wall surface is reduced. Film cooling effectiveness therefore increases.

The coolant fluid is seen to affect the primary boundary layer in two ways: 1) a separate layer created by the coolant fluid itself, and 2) a mixing layer between the primary and coolant flow streams. These are two fundamental characters of film cooling. The main contribution to heat protection by film cooling is that the separate coolant layer penetrates into the primary boundary layer and isolates it from the wall. At the same time, the coolant fluid mixes with the primary fluid, from which finally develops a new boundary layer. Therefore, we can conclude that the development of the primary boundary layer is delayed by the injection. This detailed view of the flow processes enabled by CFD agrees well with the film cooling models presented in Chapter 1.

Under all five coolant flow injection rates, the coolant flow is found to be choked at the slot. The coolant flow will accelerate as it expands from the slot and become

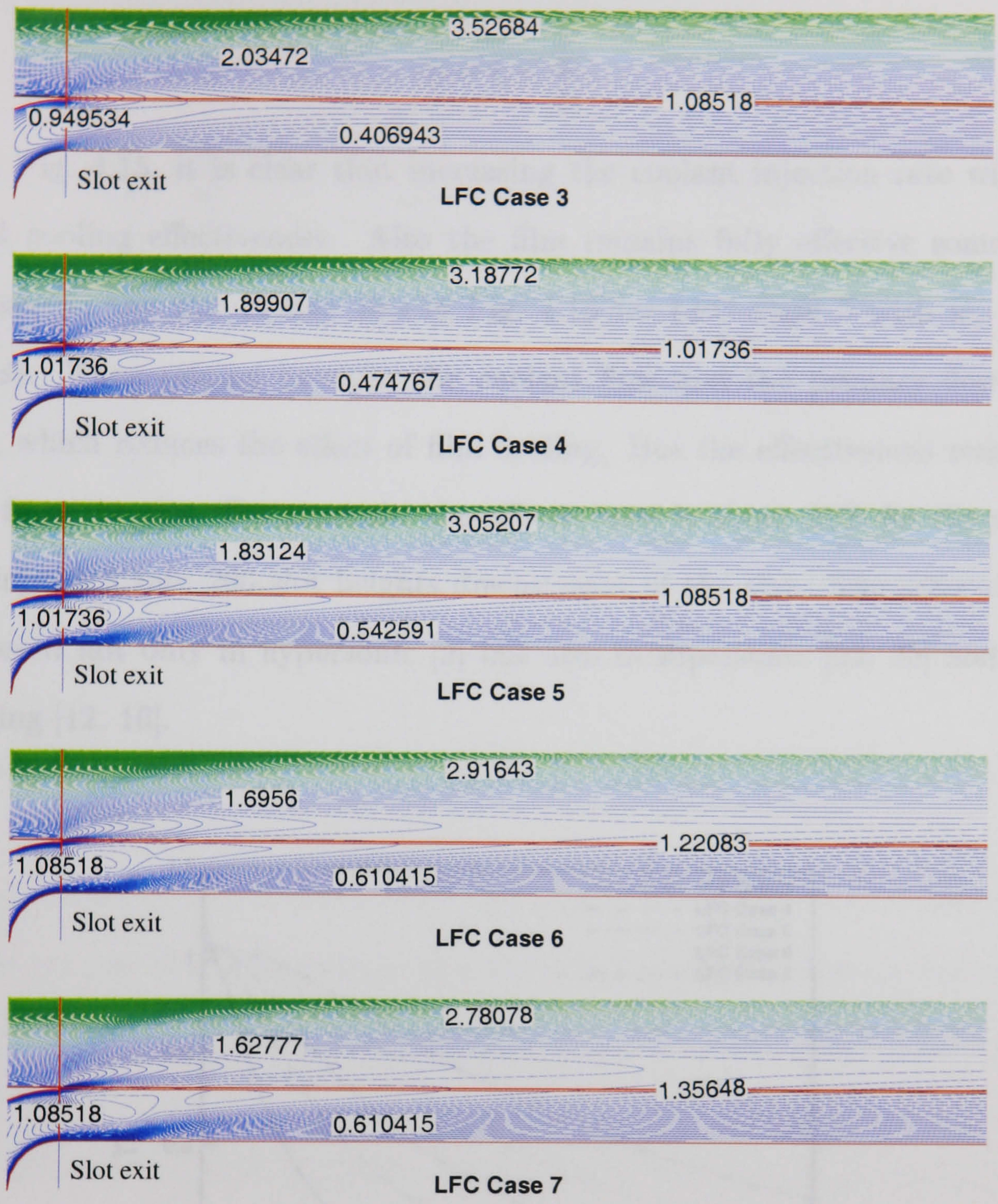

Figure 4.14: *Mach contours of different coolant injection rates*

supersonic downstream of the slot. An effective slot height s' was used by Richards [30] as the coolant layer height in application of the discrete layer theory. It was calculated assuming there was no mixing of the layers. Fig. 4.11 and Fig. 4.14 demonstrate that this phenomenon is logical. Just after the slot, there is no upper wall surface so that the expansion can occur. It is not however easy to calculate an accurate effective slot height from the computational results.

Film cooling effectiveness is defined directly in these calculations by the heat transfer rate, as in the experiments, using

$$\eta = 1 - \frac{\dot{q}_c}{\dot{q}_0}. \tag{4.1}$$

From Fig. 4.15, it is clear that increasing the coolant injection rate will provide improved cooling effectiveness. Also the film remains fully effective some distance downstream of the slot (about $10\,s$ in Fig. 4.15 for LFC Case 5 with $\dot{w}_c = 5.07 \times 10^{-4}\,kg/s$). Then mixing between the coolant flow and the primary flow becomes stronger, which reduces the effect of film cooling. But the effectiveness remains high even far from the slot. For example, the effectiveness is about 30% for the mid range coolant injection rate 200 slot heights downstream of the slot. The same conclusion was achieved not only in hypersonic [9] but also in supersonic [23, 25] and subsonic film cooling [12, 16].

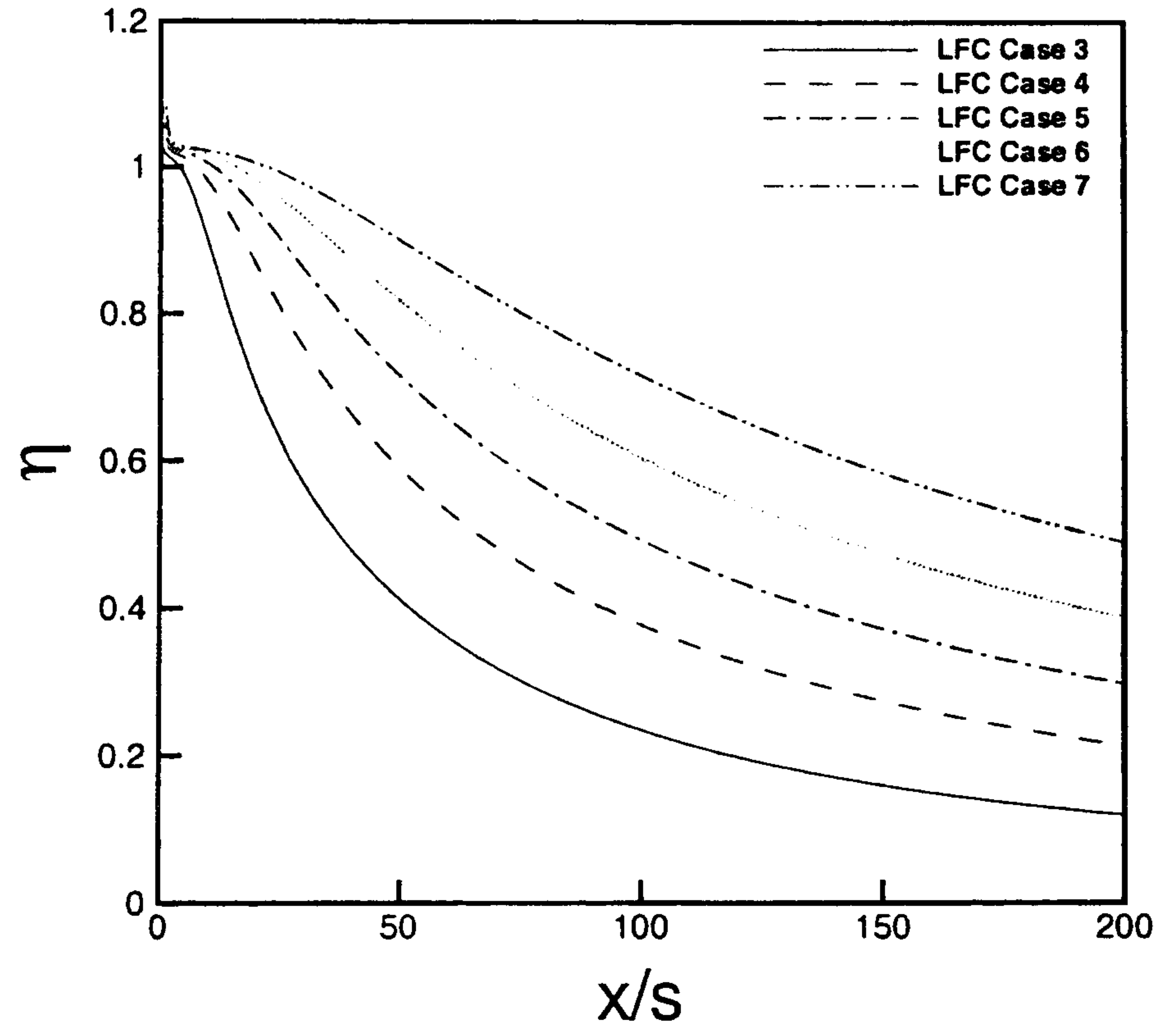

Figure 4.15: *Laminar film cooling effectiveness of different coolant injection rates*

Heat transfer rates are compared with the experimental data in Fig. 4.16. After 100 slot heights, the agreement is quite good while in the near slot area the computational results are higher than the experimental results. As mentioned above, inaccurate inlet geometry could play an important role here. Also in the experiments, it was found

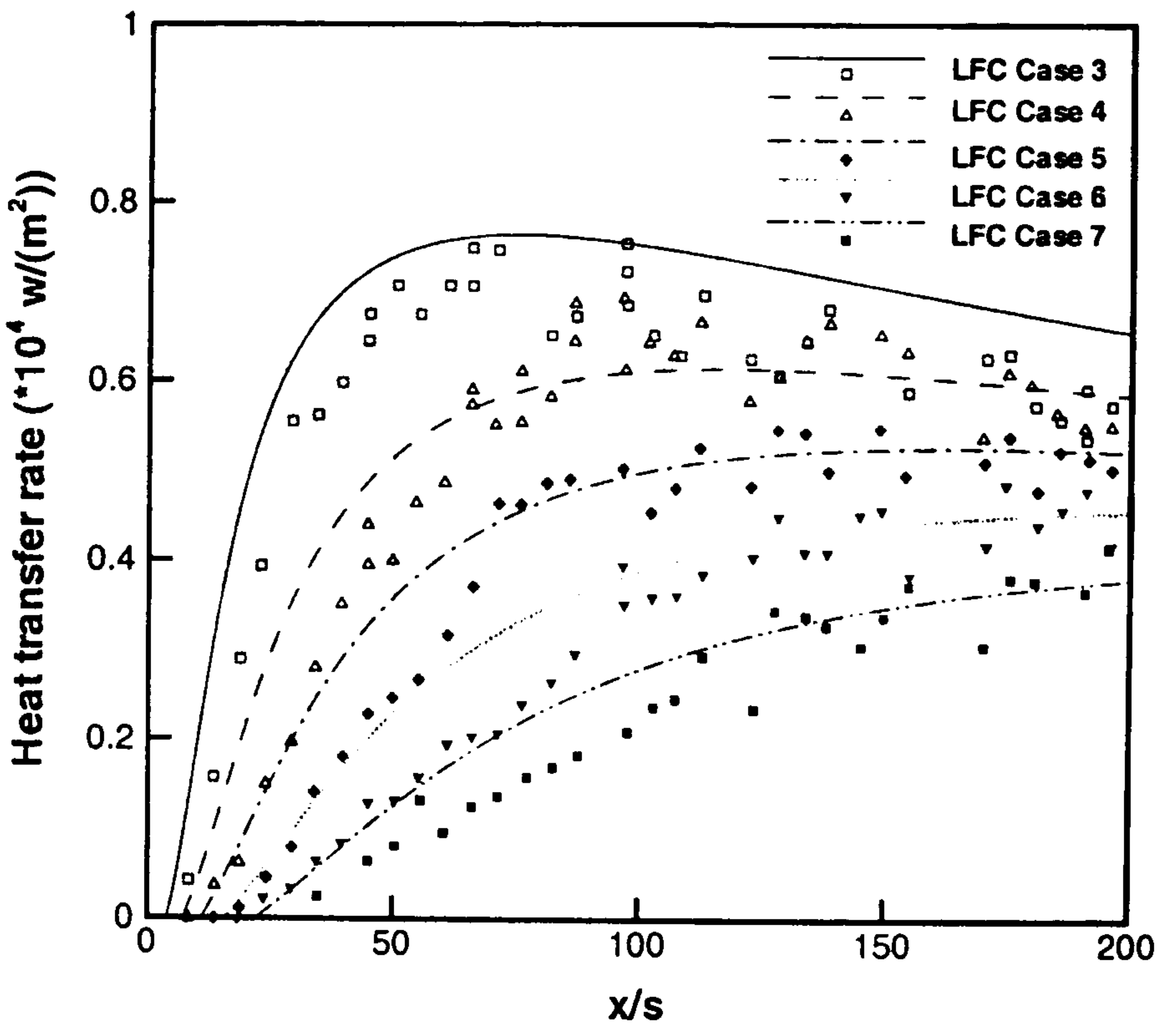

Figure 4.16: *Heat transfer rate comparison of different coolant injection rates*

difficult to obtain fully two dimensional injection of the coolant. Furthermore the flow conditions used in the computation were extracted from the experimental data since they were not directly measured which may cause some minor uncertainties.

4.3.2 Effect of slot height

The second factor investigated is the slot height. Three different slot heights, $s = 0.8382, 1.2192, 1.6002\,mm$, representing LFC Cases 8, 5 and 9 (from Table 4.1) respectively were examined under the same coolant and freestream flow condition as LFC Case 5 in Table 4.1 with constant coolant injection rate ($\dot{w}_c = 5.07 \times 10^{-4}\,kg/s$).

The computational results in Fig. 4.17 show that the effectiveness of film cooling is only slightly increased with an increase of the slot height. Increasing the slot height increases the thickness of the unmixed coolant flow at injection and evidently to increased film cooling effectiveness. But as mentioned before, coolant flow chokes at the slot position so the coolant speed at the exit stays constant. The slightly improved effectiveness appears to be achieved by introducing the coolant into the flow with less perturbation to it.

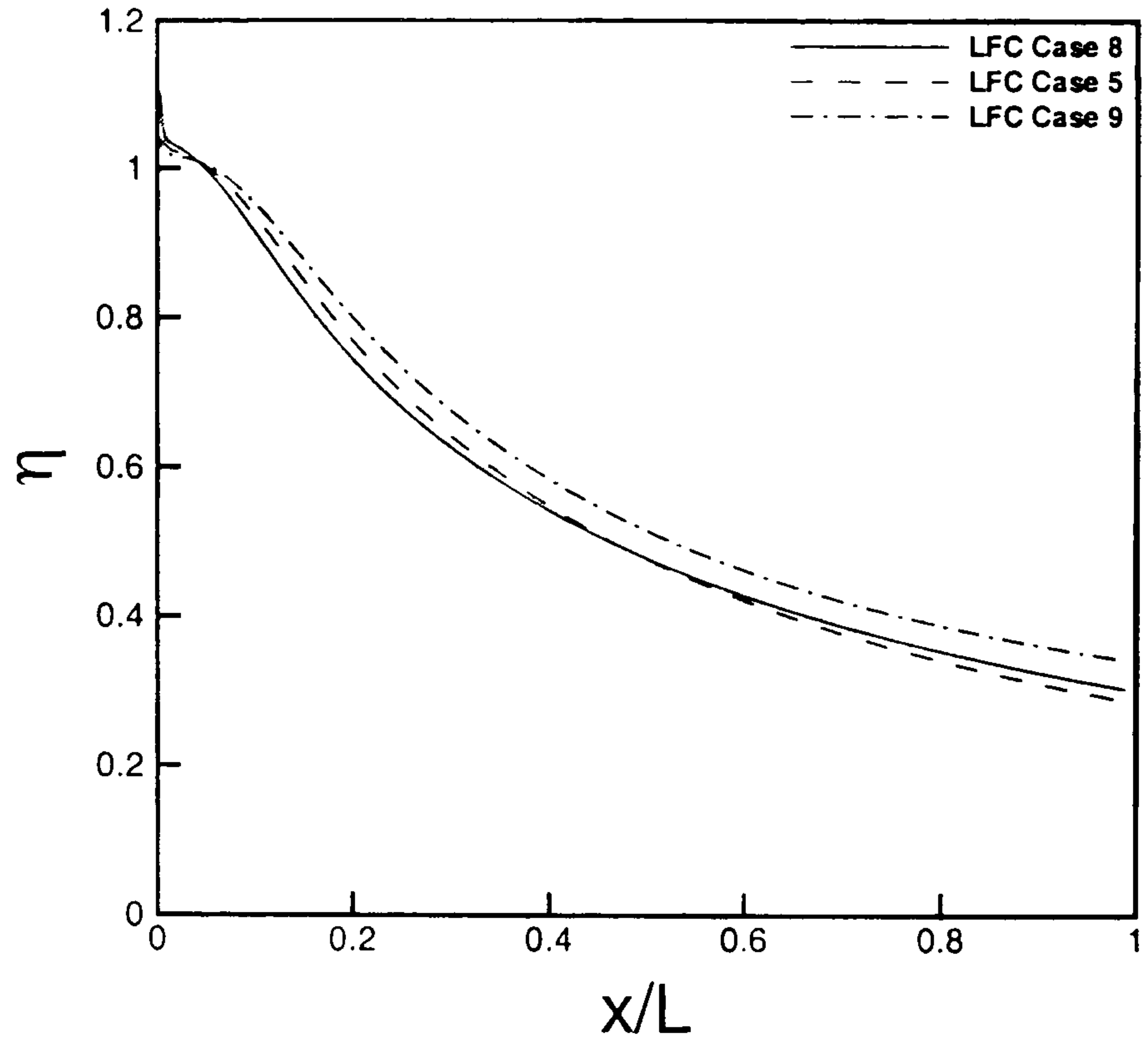

Figure 4.17: *Laminar film cooling effectiveness of different slot heights*

4.4 Curve fitting – laminar film cooling

Curve fitting is commonly used to analyse the results of nearly all previous experimental and numerical film cooling studies [1, 7, 9, 11, 12, 14, 16, 17, 25, 26, 33, 34]. Fig. 1.5 in Chapter 1 is re-drawn here (Fig. 4.18) in order to illustrate the relationship between a grouping of variables and the film cooling effectiveness.

According to experimental data, the film cooling efficiency η downstream of the cooling length away from the slot is usually described in these works as a function of the nondimensional distance from the slot exit x/h (h may be the slot height s or the step height $s+l$, l is the lip height) combined with the ratio of coolant mass flux per unit area to primary stream mass flux per unit area $\dot{m}$ ($\dot{m} = \rho_c u_c / \rho_\infty u_\infty$), i.e., $\eta = f\left(\frac{x}{h\dot{m}}\right)$. Based on previous experimental results, this function was usually plotted in log-log coordinates, $log_{10}\eta = f\left(log_{10}\frac{x}{h\dot{m}}\right)$. Suppose that $y = log_{10}\frac{x}{h\dot{m}}$, the function described in Fig. 4.18 can be divided into three segments: 1) $y \leq y_A$, from the slot exit to the end

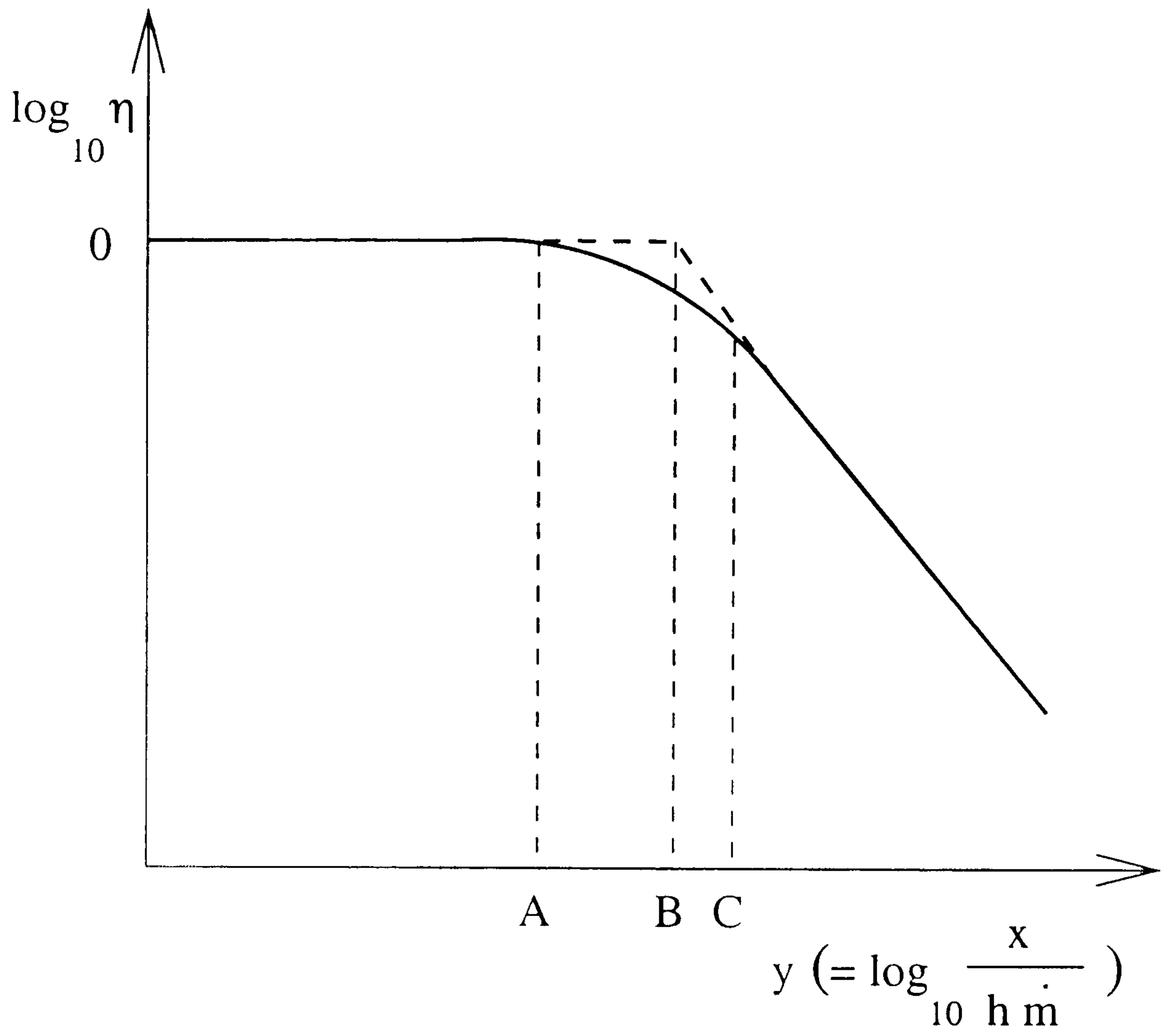

Figure 4.18: *Film cooling efficiency*

of the cooling length when the wall surface is fully cooled, i.e., $\eta \geq 1$, 2) $y_A < y < y_C$, when mixing between the primary and the cooling flow streams occurs in this region, 3) $y \geq y_C$, when the coolant and primary flow streams tend to be fully merged. In the latter region, a power law was found suitable to describe the relationship. In Fig. 4.18, the X and Y axes are both logarithmic, so that the effectiveness makes a straight line.

It is very difficult to predict position A and C in the actual film cooling flow field. Thus to simplify this behaviour only two regions had been recognised in previous research, $y \leq y_B$ and $y > y_B$, where y_B is obtained from the extrapolation of the two straight lines in the log-log coordinates. Although it is clear to use y here, usually x is used directly for the prediction of film cooling length since the effect of the cooling injection rate $\dot{m}$ is normally very small in the log-log representation. For example, as introduced in Section 1.1.4 Kanda *et al.* [4] gave an estimation of the distance of the mixing layer region indicated by x_B in Fig. 4.18 with the assumption that the mixing layer grows symmetrically both in the main and coolant flows.

$$x_B = h / \left(\frac{1}{2} \frac{d\delta}{dx} \right). \tag{4.2}$$

Cary and Hefner [7] gave an equation to predict the cooling length directly for the $M_\infty = 6$, $Re/m = 2.4 \times 10^7$, $T_0 = 478\,K$, $T_c/T_0 = 0.63$ case, i.e.,

$$x_A/s = 89\,\dot{m}^{0.8}. \tag{4.3}$$

Based on the previous discussion it is appropriate to write the above equation as $x_A/(s\,\dot{m}) = 89\,\dot{m}^{-0.2}$, but normally Eqn. (4.3) is used for clarity.

In this study, a similar power law was selected to predict the cooling length for LFC Cases 3 to 9 (in Table 4.1) which covered one flow condition ($M_\infty = 9.9$, $Re = 6.46 \times 10^6$, $T_0 = 1290.0\,K$). The step height h was used instead of the slot height s in Eqn. (4.3). Using the least-square-method, the following equation was found to give the best estimate of film cooling length under the same primary flow conditions.

$$x_A/h = 411.72\,\dot{m}^{1.86} \tag{4.4}$$

A comparison of the cooling length is listed in Table 4.4 with both computational results ($x_A/h\,(a)$) and results obtained using Eqn. (4.4) ($x_A/h\,(b)$). In Table 4.4, it is clearly seen that the estimated cooling length agrees well with the computational results for LFC Cases 3 to 7 (five coolant injection rates). Results of LFC Case 8 and 9 show the limitation of Eqn. (4.4) because of its simple treatment of the step height.

The film cooling effectiveness of LFC Cases 3 to 7 are depicted in log-log coordinates in Fig. 4.19. According to this figure, only two separate regions were recognised: 1) $y \leq y_A$, inside the cooling length, 2) $y > y_A$, outside of the cooling length. A second power curve (bold line) was inserted to describe the effectiveness of the second region in Fig. 4.20. y_A here can be defined as an average value of $log_{10} x_A/(h\,\dot{m})$ for all the cases considered in Table 4.4, i.e.,

LFC Case	$\dot m$	$x_A/h\,(a)$	$x_A/h\,(b)$
3	0.08	3.85	3.75
4	0.11	6.94	6.79
5	0.14	10.42	10.63
6	0.17	14.76	15.25
7	0.20	20.81	20.63
8	0.14	13.70	10.63
9	0.14	8.55	10.63

(a) estimated from the numerical result
(b) from Eqn. (4.4)

Table 4.4: Cooling length estimation (laminar flow)

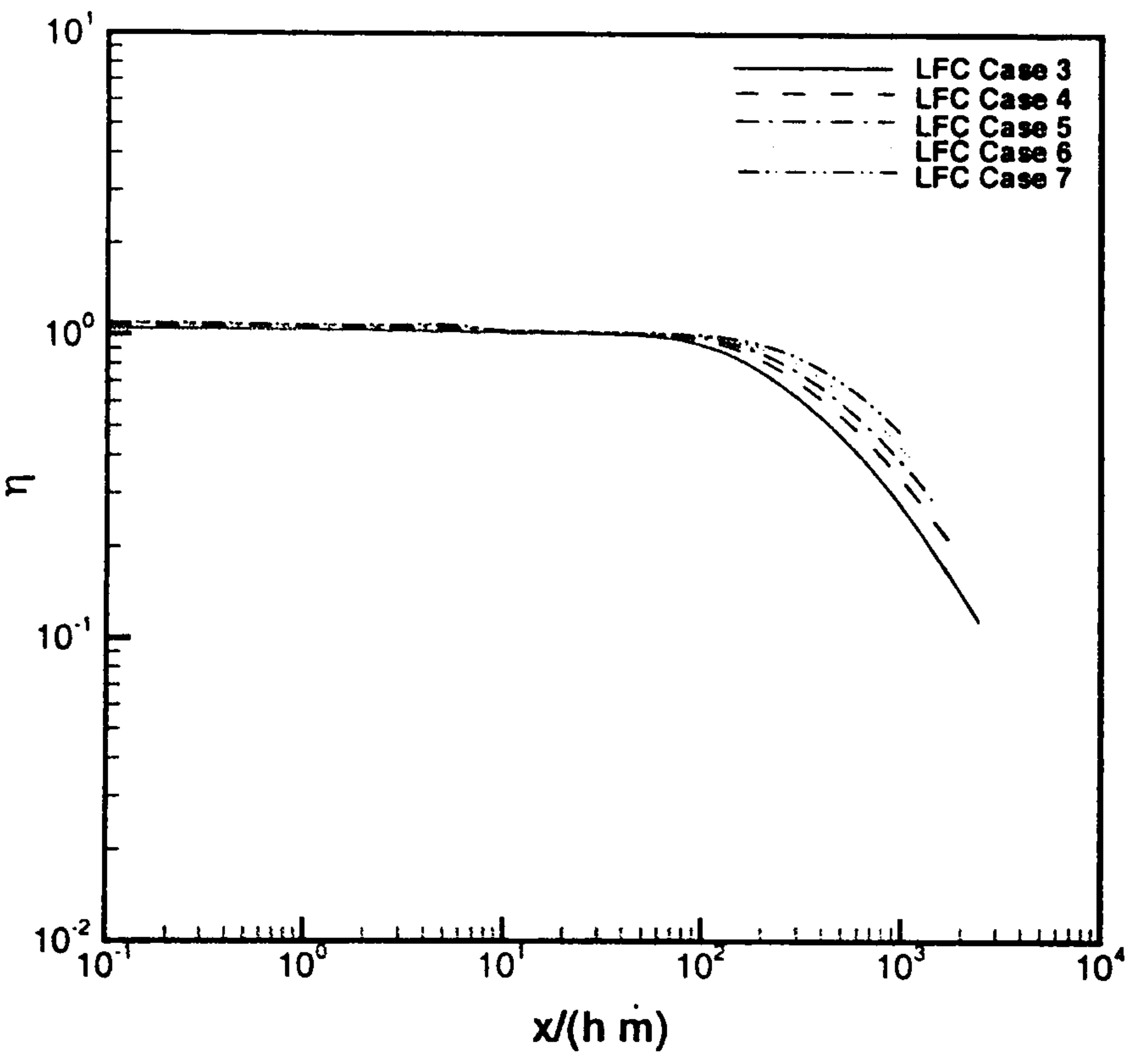

Figure 4.19: *Film cooling effectivenesses of LFC Cases 3 to 7*

$$y_A = \frac{1}{n}\sum_{i=1}^{n}\left(log_{10}\frac{x_A}{h\,\dot m}\right). \tag{4.5}$$

Film cooling effectiveness is described by Eqn. (4.6) with $y = log_{10}\frac{x}{h\dot m}$. Different from the previous study in laminar flows [1], a second power curve was directly set up to describe the film cooling effectiveness after the cooling length. This provides a more accurate estimation of the effectiveness of film cooling just downstream of the cooling

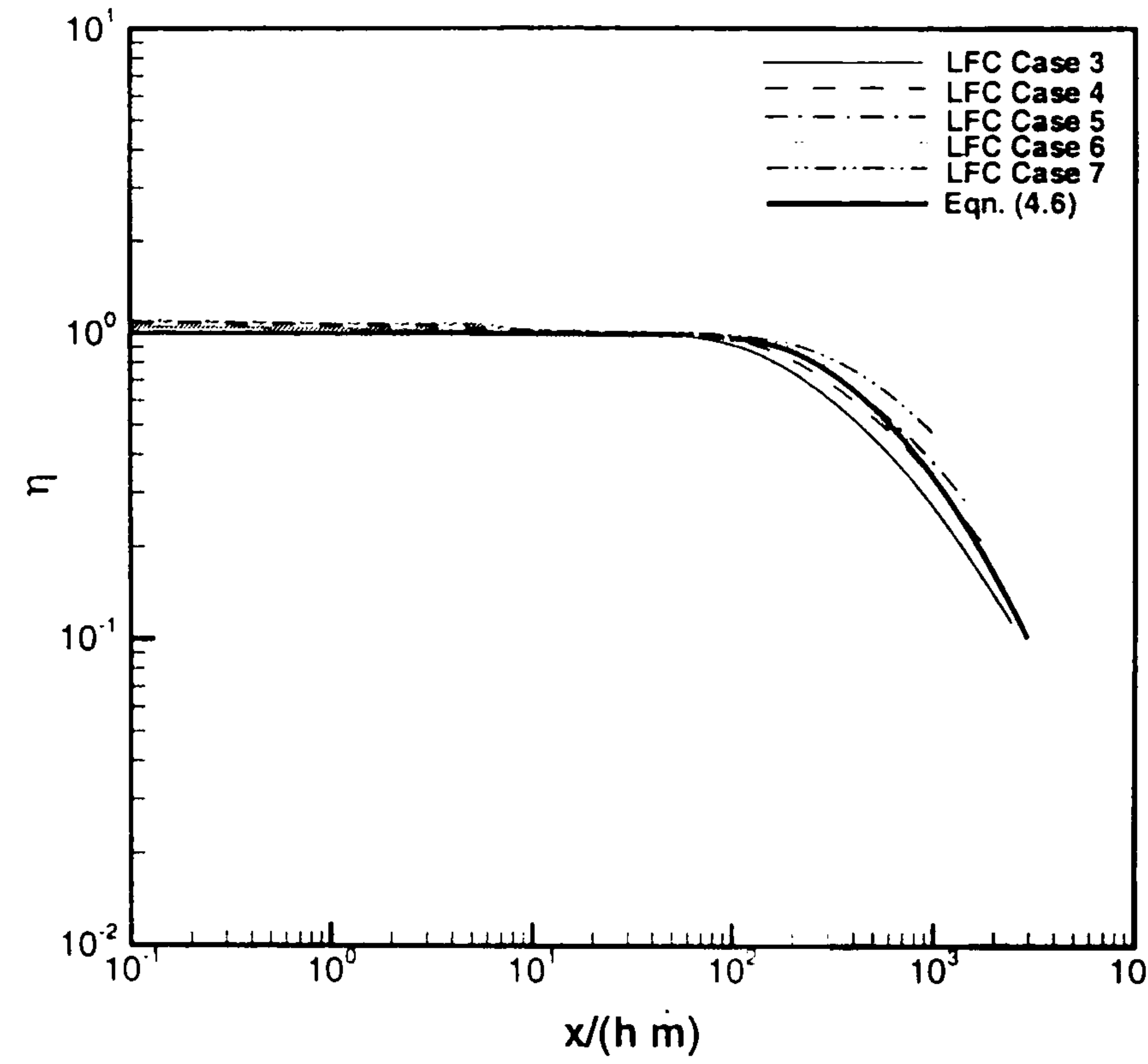

Figure 4.20: *Film cooling effectivenesses of LFC Cases 3 to 7 comparing with curve fitting result*

length.

$$log_{10}\eta = \begin{cases} 0 & y \leq y_A \\ -0.45y^2 + 1.79y - 1.80 & y > y_A \end{cases} \tag{4.6}$$

4.5 Adiabatic wall calculations

The adiabatic wall effectiveness was also investigated in this numerical study of hypersonic laminar film cooling using otherwise the same flow and coolant conditions. The film cooling effectiveness for an adiabatic wall can be defined as

$$\eta = \frac{T_{ad,w} - T_0}{T_c - T_0}. \tag{4.7}$$

This definition has been more widely used in the literature, mainly because continuous/long duration wind tunnels have been used to generate data, when adiabatic conditions have been achieved. Also designers tend to use information about effectiveness in this form. This exercise is thus useful to determine how similar results can be achieved from these two definitions. Also the benefit of using the adiabatic wall instead of the isothermal wall is to reduce the computational cost because there exists no large temperature gradient between the fluid and the wall surface.

The film cooling effectiveness is compared in Fig. 4.21. The agreement between these two different wall boundary conditions is reasonably good in the near slot region. In this region, the isothermal wall gives slightly higher film cooling effectiveness. While in the area far from the slot, the adiabatic wall gives a much higher effectiveness. In this computational study, the conical nozzle was not simulated. Although the heat transfer rate was found not to be sensitive to the geometry configuration, discrepancy in the region far from the slot position should be larger than the area near the slot. Thus film cooling effectiveness calculated by the heat transfer rate is more meaningful in the near slot area. Therefore, accepting small errors the adiabatic wall could be used instead of the isothermal wall with the benefit of reduction of the computational cost.

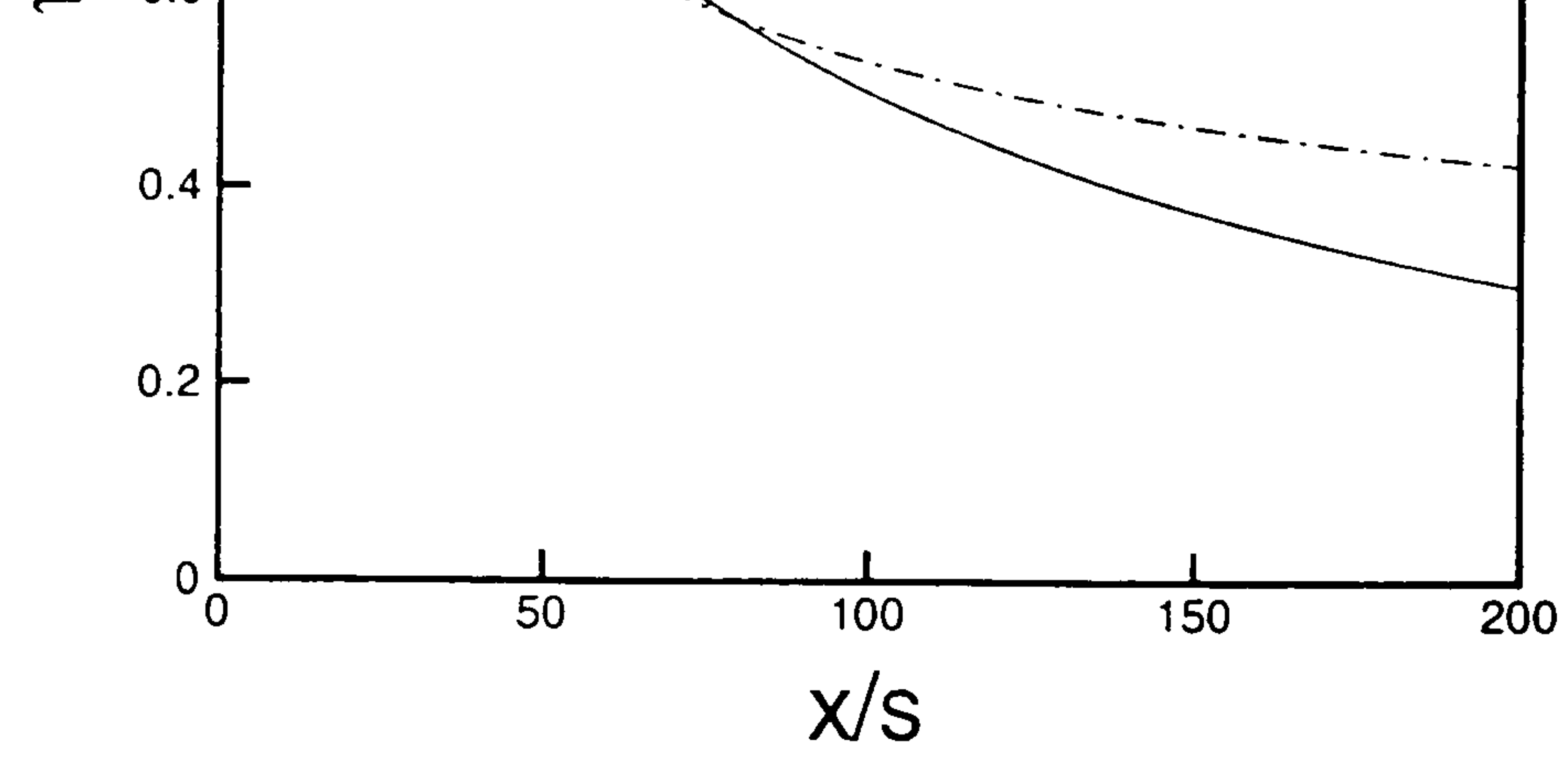

Figure 4.21: *Laminar film cooling effectiveness of LFC Case 5 using different wall conditions*

This result may also reveal that the wall temperature in the experiments does change slightly even though duration of each experiment was very short (about $40\,ms$). It is also noted that in practice that during a flight of a hypersonic vehicle the wall conditions are likely to be somewhere in between an isothermal and an adiabatic wall case.

4.6 Comments on the comparisons with experimental measurements

Only the coolant inlet extension has been considered to explain discrepancies between the experiment and the calculation, but there are more uncertainties in this study. The following will be helpful to understand minor discrepancies between the computational and experimental results.

(1) The numerical calculation does not take the conical freestream flow conditions into account.

(2) Flat plate pressure measurement is very difficult because of the small values in the experiments. For the comparison of the numerical prediction, it is expected that the viscous interaction is well predicted for a laminar flow case.

(3) The heat transfer measurement technique used in the experiments, i.e. thin film thermometry method, is reliable, nevertheless it is difficult to calibrate the technique accurately.

(4) The coolant gas flow rate was measured by a floating ball flowmeter. The accuracy is given in terms of a percentage of maximum mass flow through the flowmeter, so the lower mass flow rate measurements are likely to be less accurate than the high ones.

(5) There are likely to be errors in the measurement and uniformity of the slot height which could affect the ejected flow conditions although the conditions are based on the mass flow rate which is reasonably accurate and also the errors are likely to be consistent.

(6) The conditions of the film are calculated based on inviscid flow equations, although errors from this source are likely to be small.

(7) The flow out of the slot may not be fully uniform across the width of the slot. However this was checked out in the experiment by the use of a small pitot probe positioned at the half height position in the slot exit plane and scanned across the width of the slot. This was done without the external flow but with the external pressure kept at the measured static pressure at the slot position. These pitot measurements indicated that reasonably constant flow conditions were achieved across the slot. Furthermore these pitot pressure measurements were used to calculate the coolant flow rate assuming that the measurement was taken at the choked exit of the slot and using the geometric conditions. The flow rates calculated agreed reasonably well with those read from the flowmeter.

(8) In the experiment, it was generally difficult to create 2-D flow. Apart from the free stream source flow then there were likely to be some end effects happening due to the limited model width, and this becomes more important at larger distances from the leading edge. There is likely to be some splaying of the film sideways as it emerges from the slot which means the film thickness is thinner than that calculated resulting in lower effectiveness.

4.7 Summary

Film cooling in hypersonic laminar flow has been numerically investigated for three primary flow conditions, five coolant injection rates and three slot heights. By modelling the flow in the coolant inlet, heat transfer rate is better predicted compared with using a uniform boundary at the slot exit. The following conclusions are drawn:

(1) Film cooling in hypersonic flow can be very effective in laminar flow. At some distance downstream of the slot the effectiveness is fully effective. The effectiveness drops further downstream due to mixing between the coolant and the primary flow streams. In laminar flow, the effectiveness was found to be still quite high even far

downstream of the slot.

(2) Increasing the coolant injection rate can obviously increase the film cooling effectiveness for laminar cases. Another cooling method such as regenerative cooling is suggested to be used in combination with film cooling to further enforce the cooling of surfaces in hypersonic flow.

(3) Primary flow conditions are important as expected. Under the same slot height and the same coolant injection rate, lower heat transfer rate can be obtained when total temperature and static pressure of the primary flow decrease.

(4) Slot height does not play an important role under the flow conditions here although a larger slot for the same coolant mass flow rate causes less disturbance to the flow resulting in slightly improved effectiveness. This factor is thus not important when designing the structure of the film cooling system.

(5) Coolant flow expansion was observed just downstream of the slot position. The simulation of the plenum before the inlet is found to be necessary to improve the CFD results.

(6) A simple two-equation model, Eqn. (4.6) can be used to describe the relationship between the film cooling effectiveness and a grouping of parameters, $x/(h\,\dot{m})$. Different from previous study in hypersonic laminar flow [1], a relationship has been established in the log-log coordinates directly after the cooling length which provides a better prediction of the region just after the cooling length.

(7) Using adiabatic wall conditions as an assumption in the calculation instead of isothermal wall conditions is shown to be helpful to reduce the computational cost of determining approximation film cooling effectiveness.

Chapter 5

Hypersonic Turbulent Film Cooling

5.1 Introduction

With hypersonic laminar film cooling successfully simulated in the previous Chapter, a numerical study of turbulent film cooling in hypersonic flow is now considered. In Chapter 4, film cooling in hypersonic laminar flow was proven to be able to provide efficient heat protection for wall surface downstream of the slot exit. Many real flows are however turbulent, e.g., flow in combustors of rockets and flow around turbine blades. In such an environment, heat transfer between the flow stream and the wall surface is much stronger than in laminar flow. Although special materials could be used to alleviate the effect of heat, it is economic to employ film cooling in order to extend the life of such components. Some experiments [2, 7, 9, 31, 33, 34] have been performed to study the hypersonic film cooling problem in turbulent flow, but only a few numerical studies [35, 36] have been carried out. Most of the CFD studies in film cooling were concentrating on subsonic and supersonic problems [3, 5, 6, 11, 40, 52, 53, 55]. Therefore, there is a need to explore the application of CFD in hypersonic film cooling.

In this Chapter, the 2-D Reynolds-averaged N-S equations are solved with the $k-\omega$ two-equation turbulence model using PMB2D. Coolant inlet geometry, coolant flow turbulence level and coolant injection angle were studied in order to investigate their effects on film cooling. Dilatation-dissipation corrections of the $k-\omega$ turbulence model have been tested and found to be very important in predicting the heat transfer rate. Coolant injection rate and slot height are the two parameters which were studied. Menter's baseline and *SST* turbulence models have also been implemented into the PMB2D code in order to study the effect of turbulence model in predicting the heat transfer rate of the film cooling problem.

5.2 Description of the experiment

Experiments were carried out by Richards [30] on a flat plate in a gun tunnel under isothermal wall conditions. A contoured nozzle was used instead of the conical nozzle as in the laminar film cooling study, enabling a uniform field in the test section in the turbulent case. The wall and coolant temperatures were at the laboratory level of $290.0\,K$. The coolant flow rate was varied from 5.07×10^{-4} to $30.69 \times 10^{-4}\,kg/s$ for air. The primary flow conditions were kept the same in all the turbulent experiments with $M_\infty = 8.2$, $Re/m = 2.21 \times 10^7$, $p_\infty = 957.0\,Pa$, $T_0 = 775.0\,K$, $T_\infty = 53.64\,K$. Both the primary and coolant flow were air.

Two groups of experiments were performed, 1) five different coolant injection rates under the same slot height ($1.2192\,mm$), and 2) three slot heights under the same coolant injection rate ($14.21 \times 10^{-4}\,kg/s$). All these cases are listed in Table 5.1.

TFC Case	Group	M_∞	Re/m	$T_0\,(K)$	$s\,(mm)$	$\dot{w}_c\,(kg/s)$
1	1	8.2	2.21×10^7	775.0	1.2192	5.07×10^{-4}
2		8.2	2.21×10^7	775.0	1.2192	8.47×10^{-4}
3		8.2	2.21×10^7	775.0	1.2192	14.21×10^{-4}
4		8.2	2.21×10^7	775.0	1.2192	21.02×10^{-4}
5		8.2	2.21×10^7	775.0	1.2192	30.69×10^{-4}
6	2	8.2	2.21×10^7	775.0	0.8382	14.21×10^{-4}
7		8.2	2.21×10^7	775.0	1.6002	14.21×10^{-4}

Table 5.1: Experimental cases selected for numerical study (turbulent flow)

The coolant flow was considered to be choked at the slot exit in the experiments. All coolant flow conditions at the slot exit were calculated in a similar way to that used in the laminar problem. These are listed in Table 5.2.

TFC Case	Group	M_c	$\rho_c\,(kg/m^3)$	$p_c\,(Pa)$	$T_c\,(K)$
1	1	1.0	1.17×10^{-2}	809.34	241.67
2		1.0	1.95×10^{-2}	1352.93	241.67
3		1.0	3.27×10^{-2}	2270.98	241.67
4		1.0	4.84×10^{-2}	3358.16	241.67
5		1.0	7.07×10^{-2}	4904.36	241.67
6	2	1.0	4.76×10^{-2}	3303.25	241.67
7		1.0	2.49×10^{-2}	1730.27	241.67

Table 5.2: Coolant flow conditions (turbulent flow)

5.3 Parametric study

5.3.1 Effect of the coolant inlet geometry

TFC Case 3 in Table 5.1 was selected as the validation case because it is representative of the experiments in terms of both varying slot height and coolant injection rate studies. Based on the experience of laminar film cooling, the coolant inlet geometry was expected to play an important role, so this effect was considered first. In Table 5.3, Cases 1 and 2 are with and without the coolant inlet extension respectively. For both cases a lip thickness of 0.0508 mm is considered.

Case	M_c	$\rho_c\,(kg/m^3)$	$p_c\,(Pa)$	T_c	k	ω
1	1.0	3.27×10^{-2}	2270.98	241.67	0.001	1.0
2	0.1	5.13×10^{-2}	4268.57	289.42	0.001	1.0

Table 5.3: Coolant flow conditions with and without coolant inlet, TFC Case 3

The computational domain is shown in Fig. 5.1, in which blocks 1, 2 and 3 were used in the turbulent flat plate calculation. The geometry of the lip and the curved inlet duct is the same as used in the laminar calculation. A coarse grid was used first with 7 × 75, 92 × 75, 151 × 75, 151 × 9, 65 × 53, 31 × 53 and 151 × 53 grid points in blocks 1 to 7. The primary flow stream inlet boundary was again set up from a laminar calculation using the same computational domain. Then a turbulent boundary profile could be set up at the dash line position to reduce computational cost.

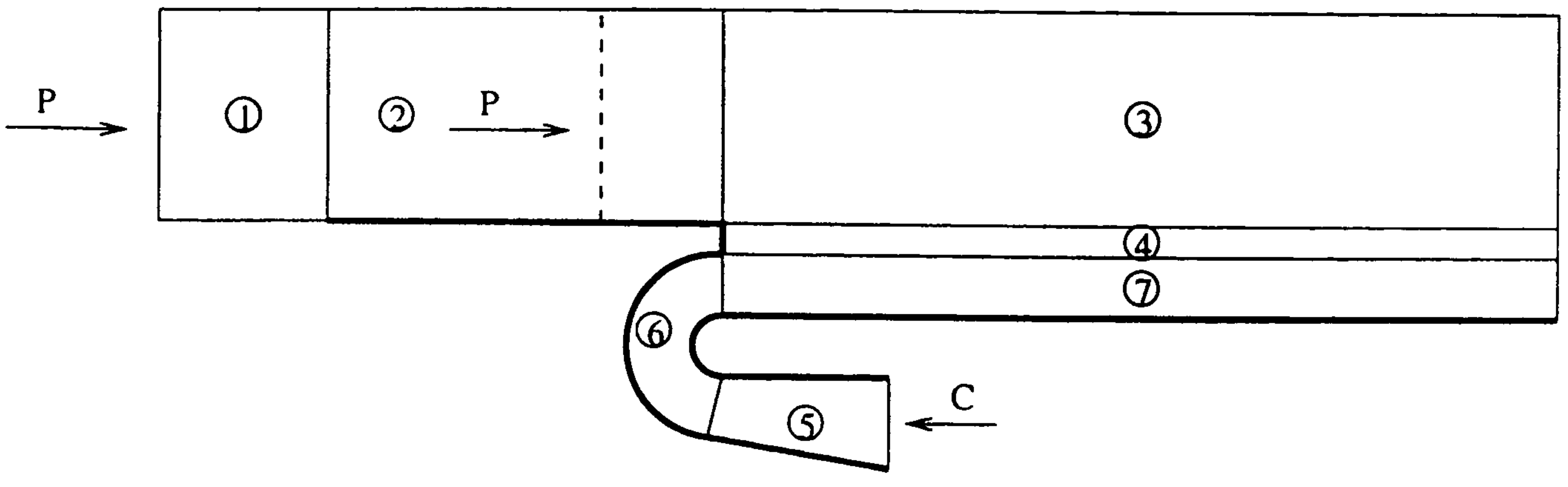

Figure 5.1: *Geometry description with lip and coolant inlet duct*

A problem encountered is that due to the lack of experimental data, the coolant flow turbulence at the slot exit is difficult to determine. The turbulent eddy viscosity μ_t for both cases at the coolant inlet boundaries was first taken to be $0.001\,\mu_\infty$. The effect of varying the turbulence level of the coolant flow will be discussed later.

Heat transfer rates for Cases 1 and 2 are compared with experimental data in Fig. 5.2. For both cases, the general trend of the heat transfer rate agrees well with the experimental data. The cooling length is almost the same in Cases 1 and 2 and is over-predicted compared with experimental measurements. For Case 2, the heat transfer rate increases slightly more rapidly than Case 1 in the near slot area. As described in the laminar film cooling study, the coolant flow at the slot exit is not parallel to the primary flow stream but exits at an angle. This should lead to a higher heat transfer rate than Case 1. The effect seems to be small so that the coolant flow stays laminar even with the coolant inlet extension. This means the assumption of the low turbulence level of the coolant flow is not correct. In the area far from the slot both cases over-predict the heat transfer rate.

A fine mesh without coolant curve inlet (blocks 1, 2, 3, 4 and 7 in Fig. 5.1) was then used for a grid resolution study. In each block, there are 13 × 149, 183 × 149, 301 × 149, 301 × 17 and 301 × 105 grid points, respectively. Heat transfer rate between these two meshes is compared in Fig. 5.3. The difference between these meshes shows that the

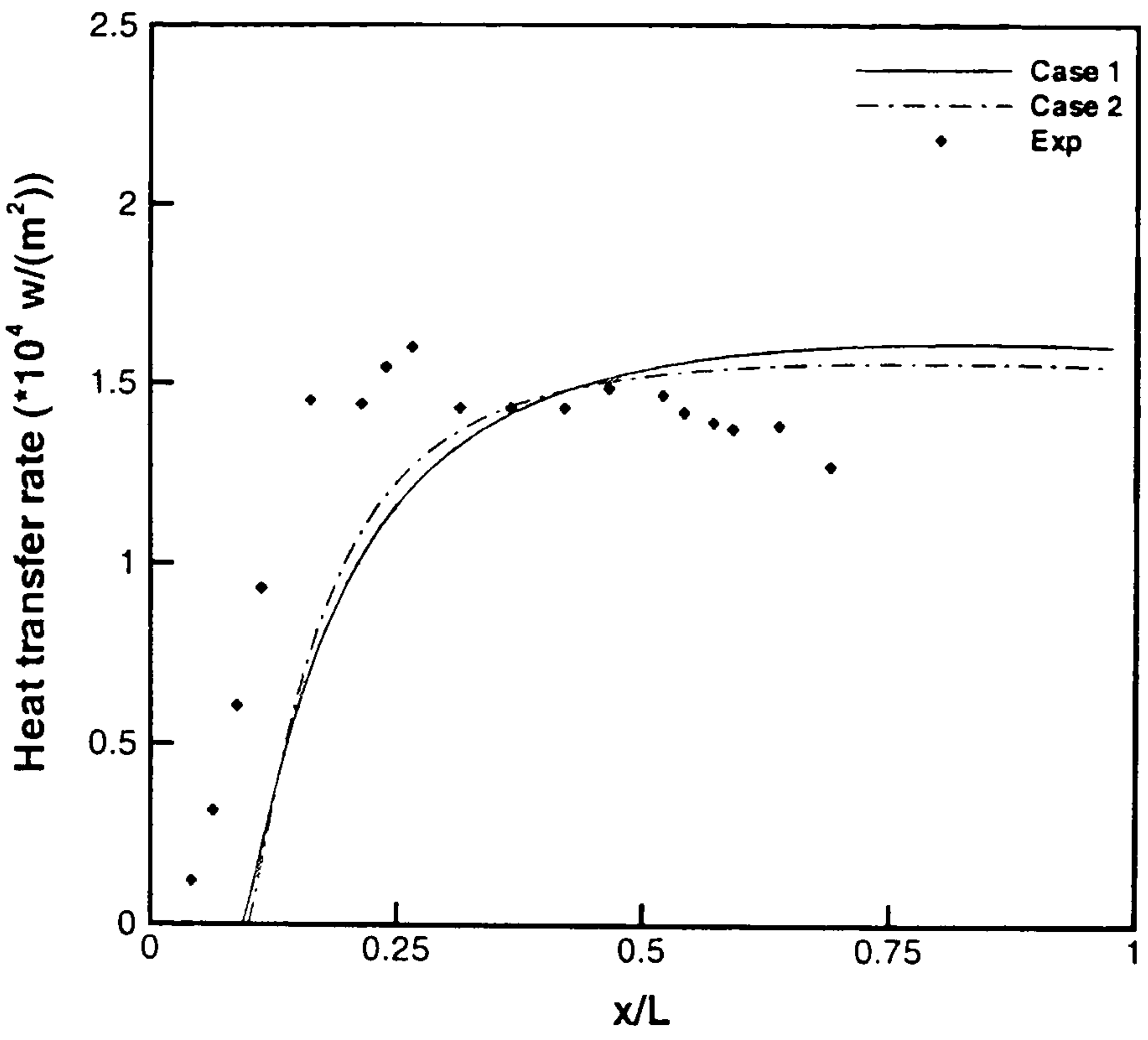

Figure 5.2: *Heat transfer rate comparison with and without coolant inlet extension*

coarse grid used above provides sufficient accuracy in this computational study.

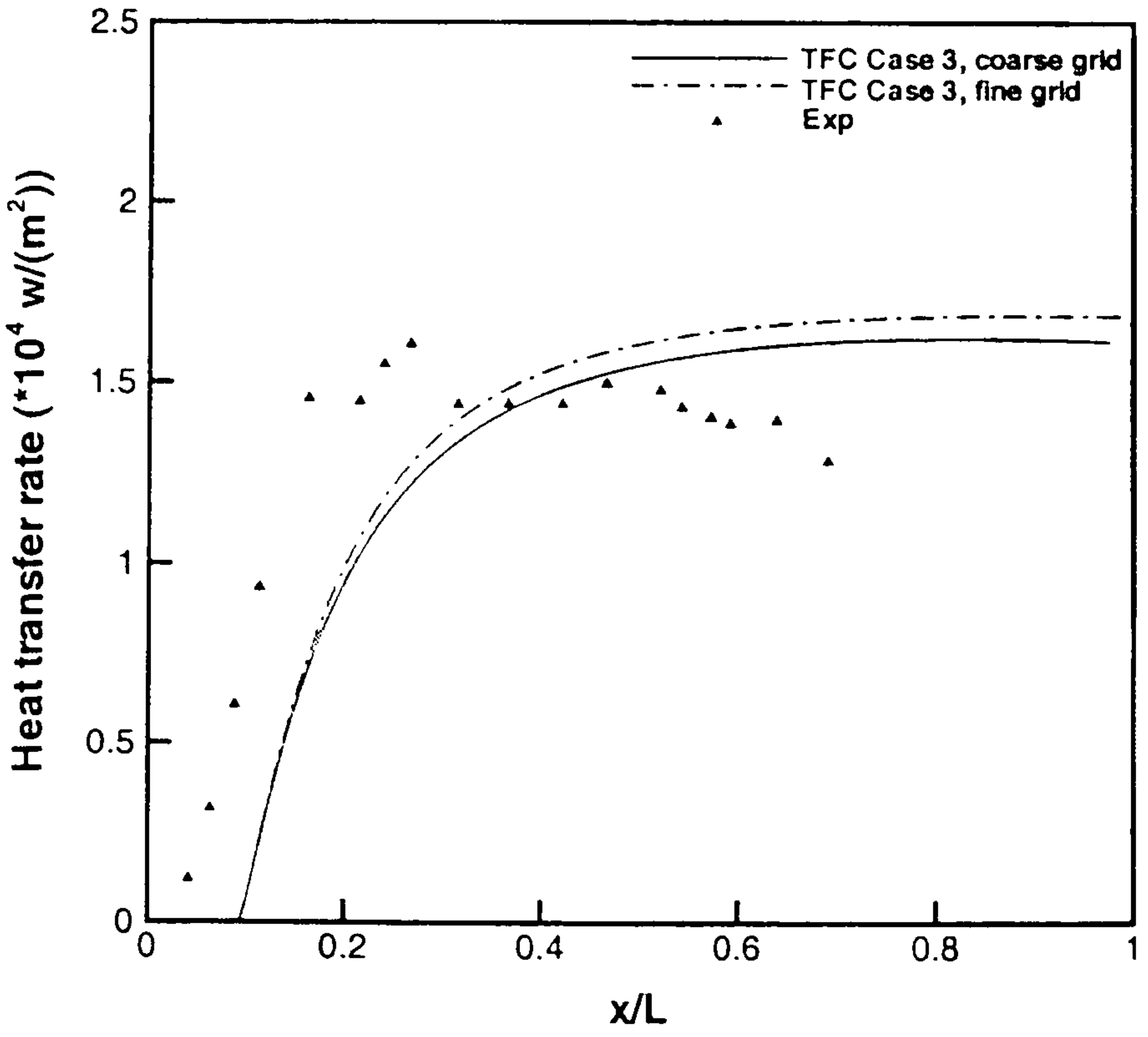

Figure 5.3: *Grid resolution study: heat transfer rate comparison between coarse and fine meshes of TFC Case 3*

5.3.2 Effect of the turbulence level of the coolant flow

The over-predicted cooling length in Fig. 5.2 indicates that the coolant flow is remaining laminar in the calculation before the heat transfer rate increases from zero. It is apparent in the experiment that transition happens rapidly following which the flow becomes fully turbulent. This discrepancy illustrates the importance of getting the turbulence level of the coolant flow right. The assumption that the turbulent eddy viscosity μ_t is equal to $0.001\,\mu_\infty$ used in previous calculations could be incorrect and so different turbulence levels were tested.

In Fig. 5.4, Cases 1 and 2 use essentially the same conditions as in last section. Cases 3 and 4 are the same as Case 2 except that the turbulence level at the inlet coolant flow boundary was set to $4,000\,\mu_\infty$ and $20,000\,\mu_\infty$, respectively. A value of $\mu_t = 4,000\,\mu_\infty$ is typical within the log-law layer where the eddy viscosity dominates the molecular viscosity. Case 4 is in fact a numerical experiment using μ_t set to $20,000\,\mu_\infty$.

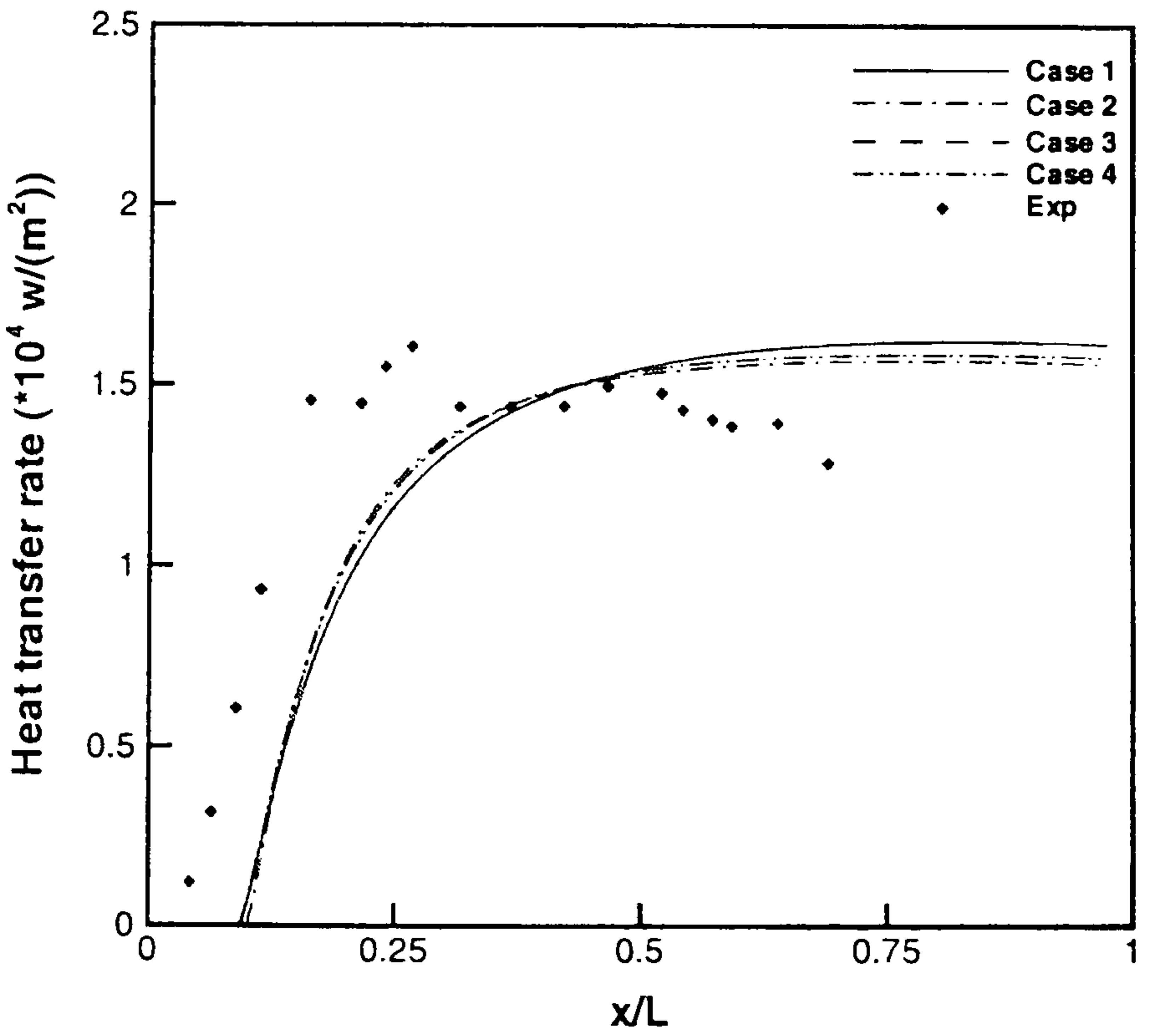

Figure 5.4: *Heat transfer rate comparison of different coolant turbulence levels*

For the three different cases (Cases 2, 3 and 4), the turbulent eddy viscosity was varied from $0.001\,\mu_\infty$ to $4,000\,\mu_\infty$ and $20,000\,\mu_\infty$, however only minor differences were observed in the heat prediction, with the cooling length almost constant. Therefore in the calculation the coolant flow was suspected to be laminar in the coolant inlet and some distance downstream of the slot. Both turbulent eddy viscosity contours and turbulent kinetic energy contours of Cases 2, 3 and 4 are compared in Fig. 5.5 and Fig. 5.6 to check the development of the coolant flow.

Fig. 5.5 shows that the turbulent eddy viscosity in the coolant inlet is very low. In Case 4, when μ_t was set to $20,000\,\mu_\infty$ at the coolant inlet boundary, it is observed that as the coolant flows downstream, the turbulent eddy viscosity decreases and finally the coolant flow becomes laminar. The length of the inlet duct here is about $71.12\,mm$ and the height of the inlet is only about $7.10\,mm$. The slot height is $1.22\,mm$. In fact, the thickness of the turbulent boundary layer of the above flat plate flow is only about $7\,mm$. So it is difficult to achieve turbulent flow in the inlet duct in the calculation. It is pointed out that the slot height was small as a result of requiring the coolant flow to be choked in the experiment in order to obtain a uniform distribution of the flow across the slot.

The turbulent kinetic energy contours in Fig. 5.6 also illustrate that the turbulent kinetic energy is diminishing along the inlet duct. It can also be clearly seen that turbulent kinetic energy remains quite low after about $0.1\,L$ in the boundary separating the coolant flow downstream of the slot. Obviously transition happens in all three cases. This agrees well with the heat prediction in Fig. 5.4. So the problem here is how to find the correct flow parameters for the coolant flow especially k and ω. The coolant inlet extension in this study was found to make no effect, so it was decided not to consider this in the following studies.

Without the coolant inlet extension, μ_t was again set to $4,000\,\mu_\infty$ (Case 5) and $20,000\,\mu_\infty$ (Case 6) by setting suitable k value at the slot exit. In Fig. 5.7, it is seen that the turbulence level of the coolant flow does affect the cooling length. As the turbulence level is increased, the cooling length decreases although the effect is small. In the area far from the slot, heat transfer rate becomes lower than Cases 1 and 2.

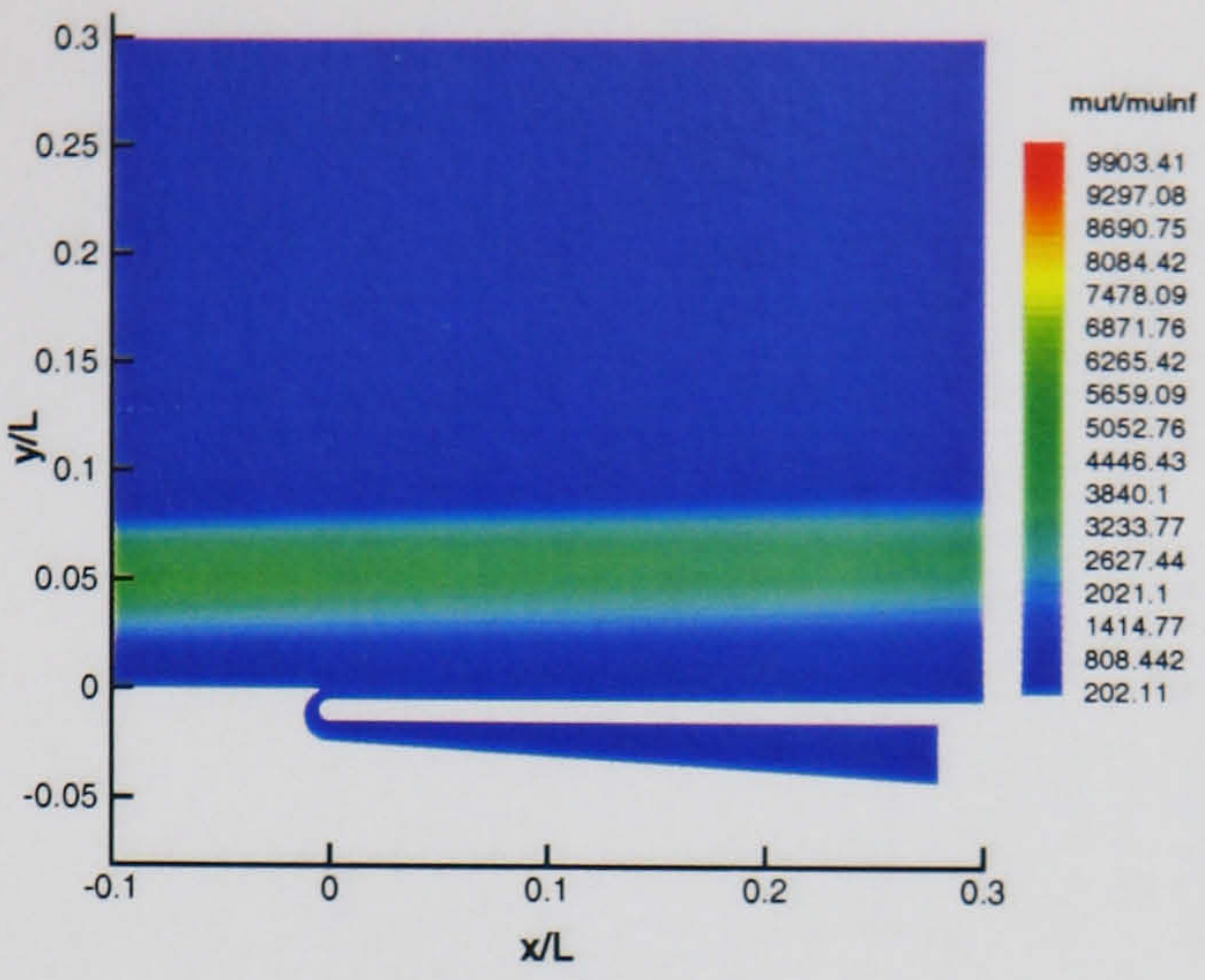

(a) $\mu_t = 0.001\,\mu_\infty$

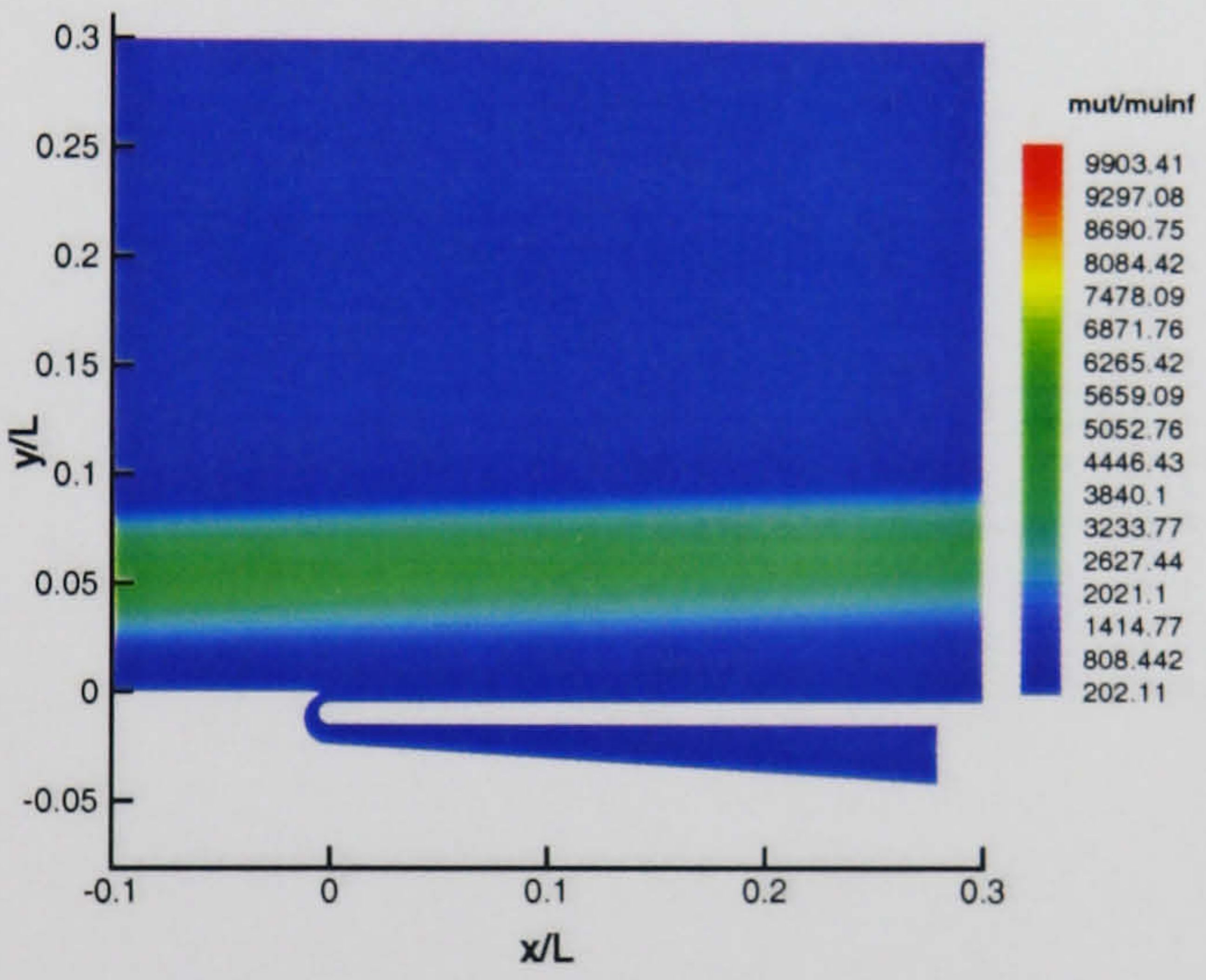

(b) $\mu_t = 4,000\,\mu_\infty$

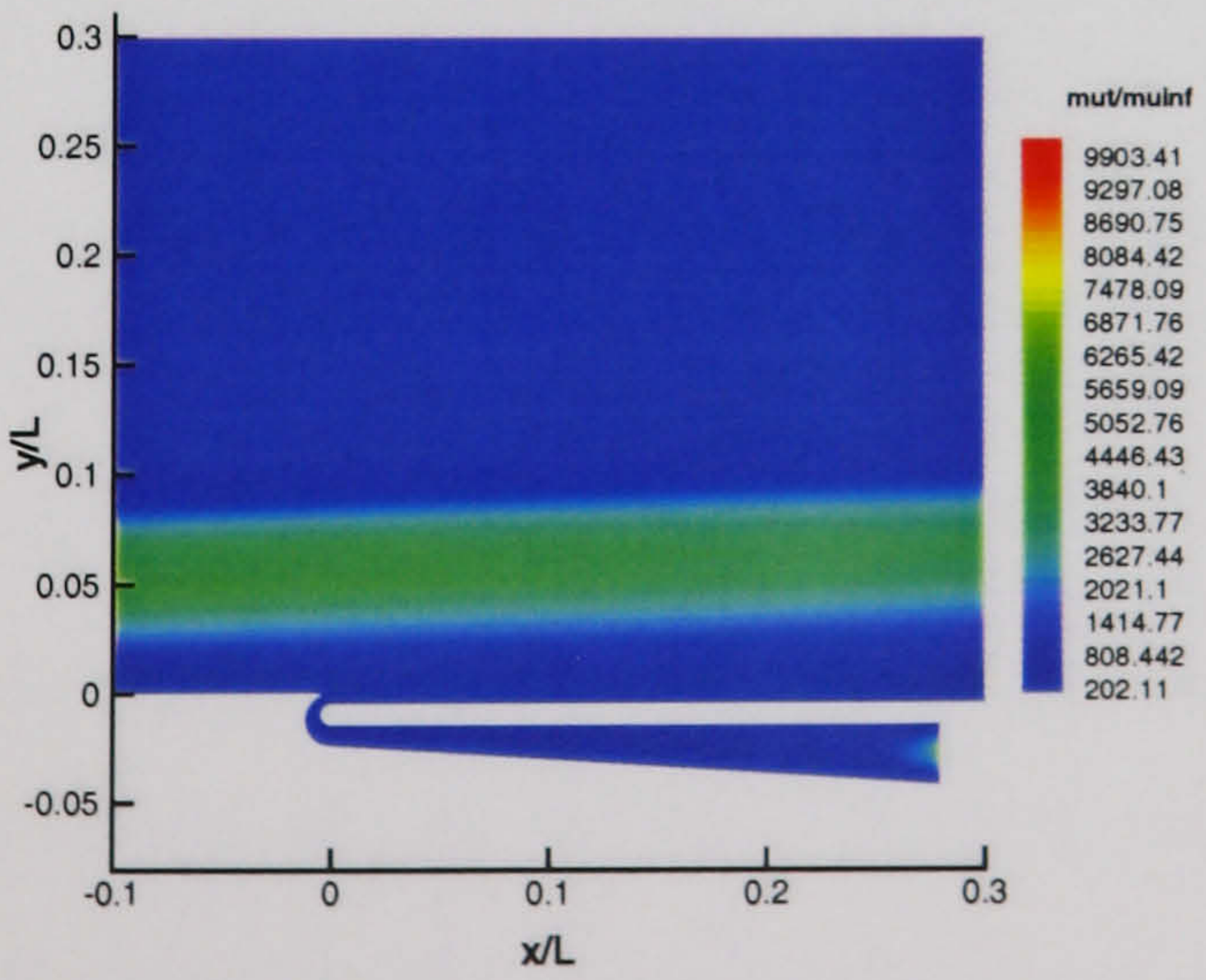

(c) $\mu_t = 20,000\,\mu_\infty$

Figure 5.5: *Turbulent eddy viscosity comparison of different coolant turbulence levels*

Fig. 5.8 shows the propagation of the turbulent eddy viscosity downstream of the slot. In a very short distance, turbulence disappears. This agrees well with boundary

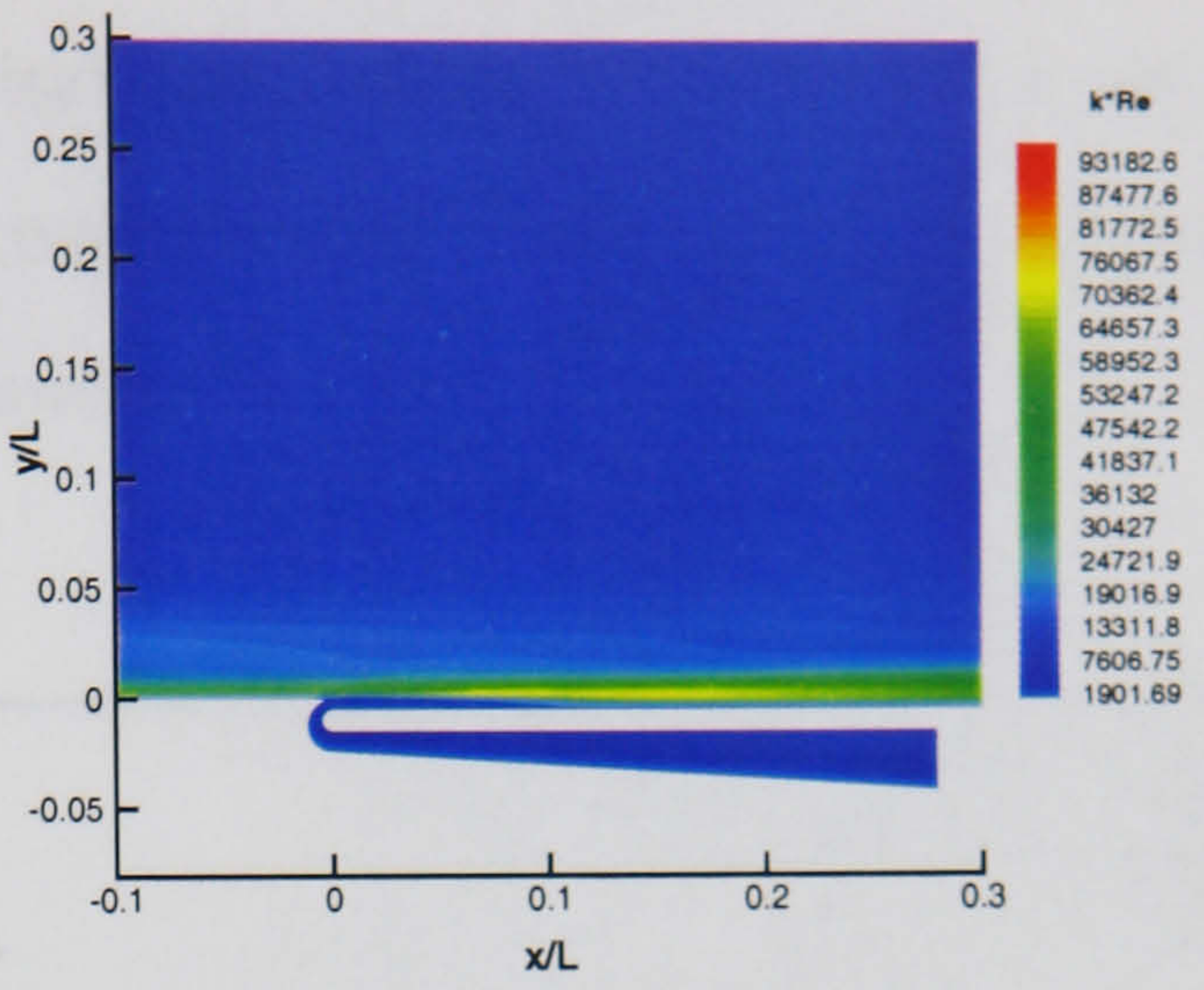

(a) $\mu_t = 0.001\,\mu_\infty$

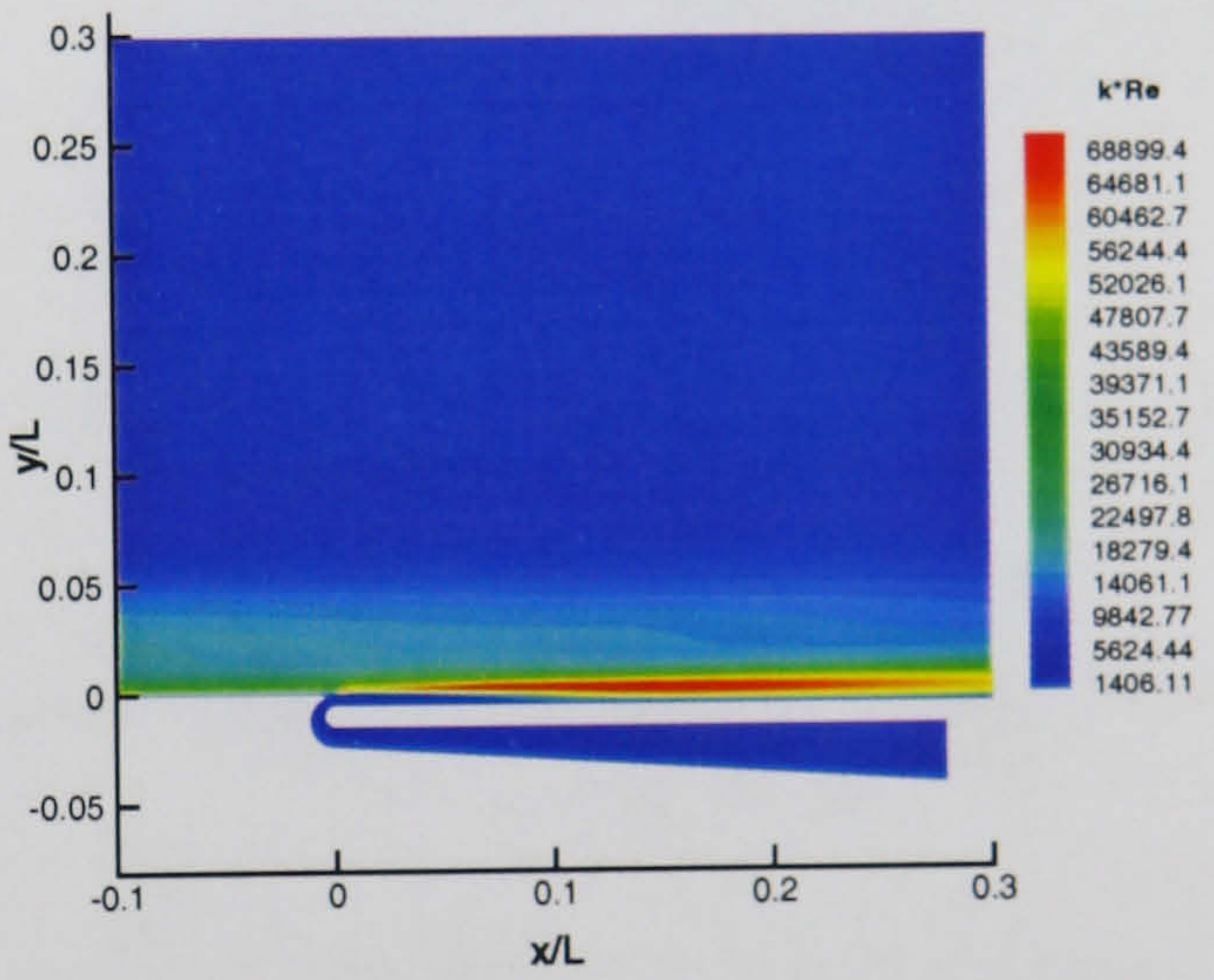

(b) $\mu_t = 4{,}000\,\mu_\infty$

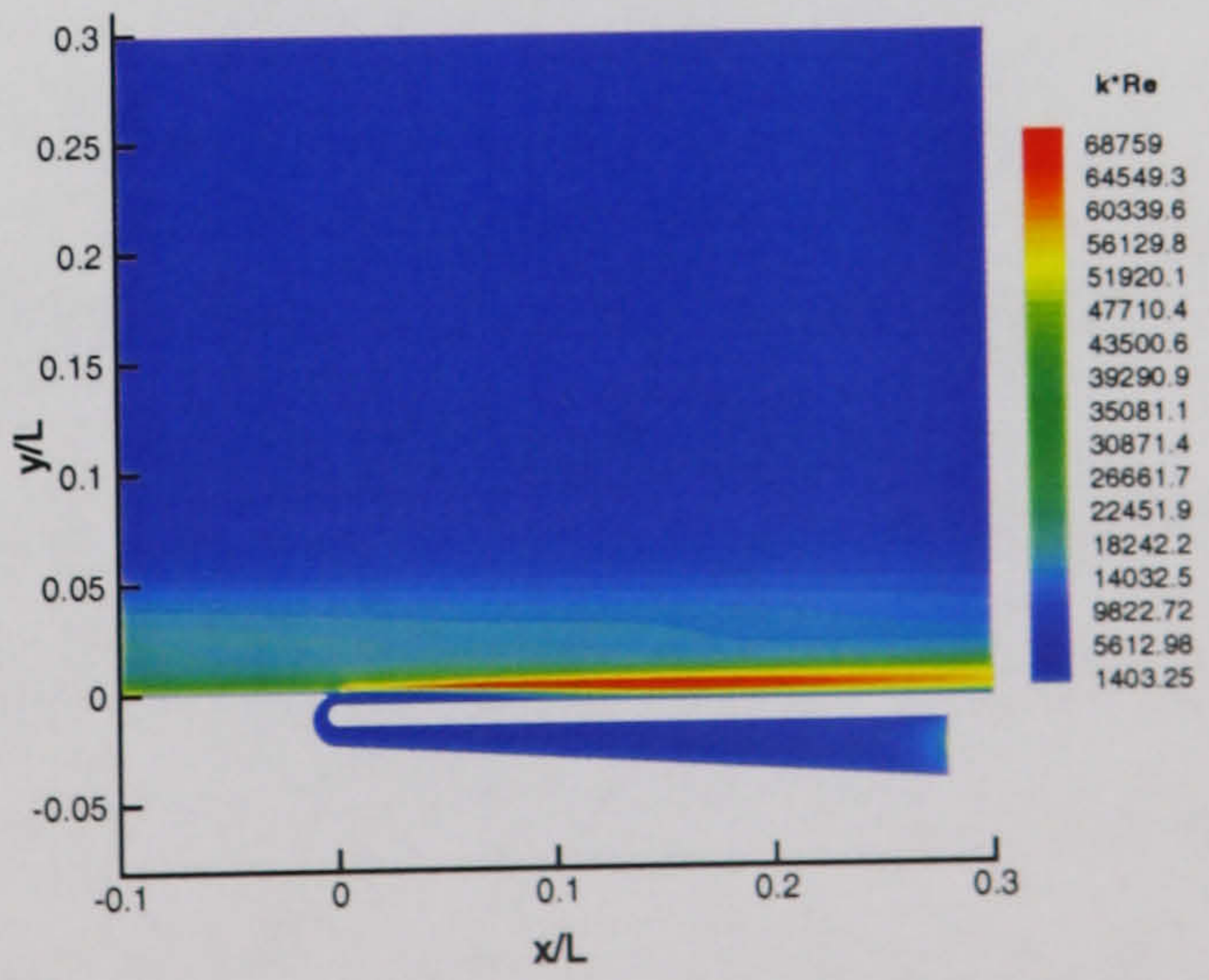

(c) $\mu_t = 20{,}000\,\mu_\infty$

Figure 5.6: *Turbulent kinetic energy comparison of different coolant turbulence levels*

layer theory. In the near wall region, or laminar sub-layer, there is no turbulence, hence the diffusion is dominated only by the molecular viscosity rather than the turbulent eddy viscosity. Any turbulence will peter out in this region. This can explain what happened in the numerical experiments. So it could be concluded here that it is not possible to predict the cooling length by increasing the turbulence level of the coolant flow because of the geometric limitation.

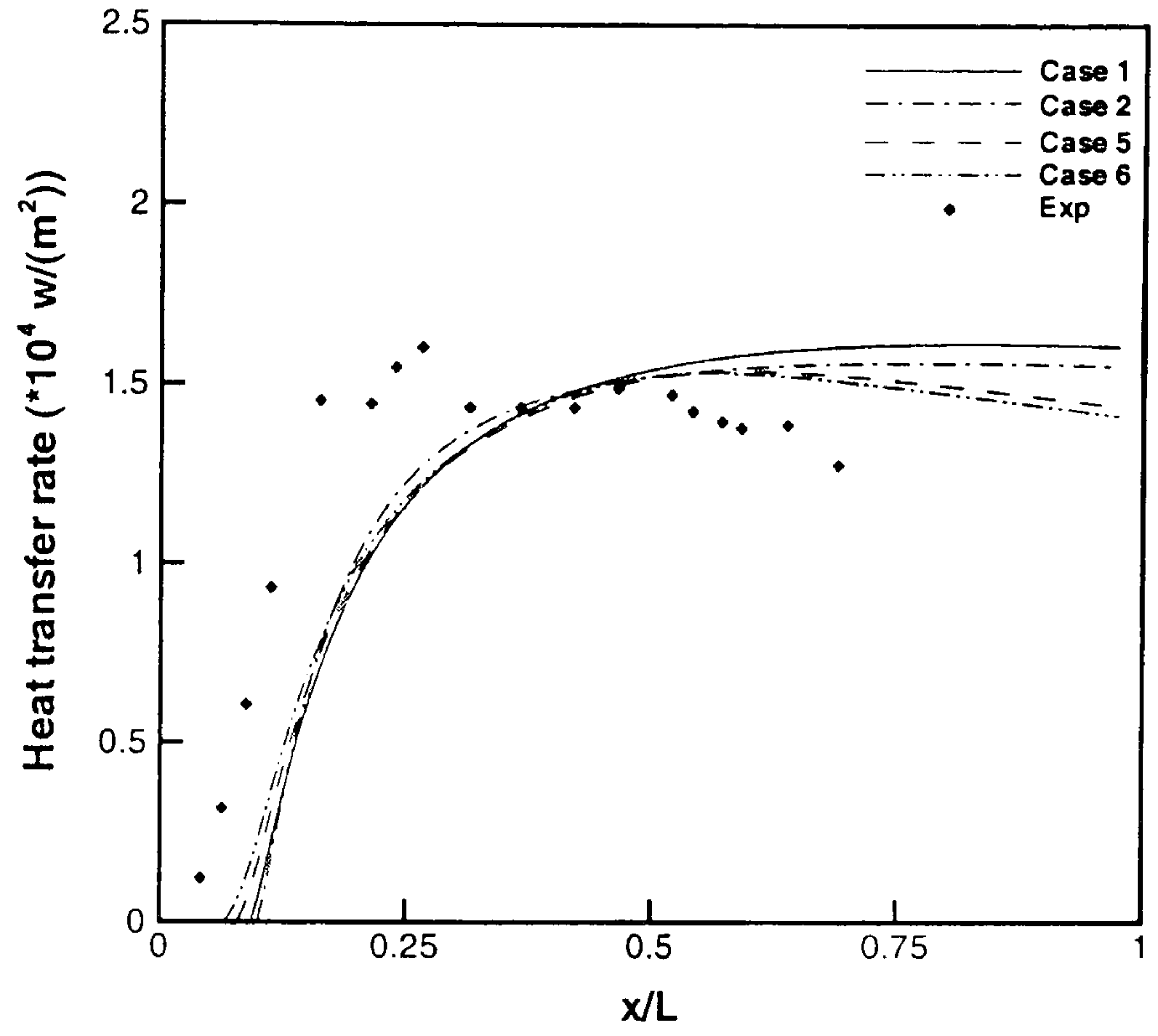

Figure 5.7: *Heat transfer rate comparison of different coolant turbulence levels without coolant inlet extension*

5.3.3 Effect of the coolant injection angle

The coolant injection angle was examined in the laminar film cooling investigation. It is suggested that the coolant flow was injected into the primary flow stream at a certain injection angle, α, even though it was hoped to keep it parallel to the primary flow stream in the experiments. In the laminar film cooling study, the coolant injection angle was observed to be about 10° when the coolant injection rate was set to $5.07 \times 10^{-4}\ kg/s$ with the coolant inlet extension. Two different coolant injection angles, 20° and 45°, were chosen to be tested. The following four cases are considered:

(a) Case 7, $\alpha = 20°$, $\mu_t = 4,000\,\mu_\infty$,

(b) Case 8, $\alpha = 20°$, $\mu_t = 20,000\,\mu_\infty$,

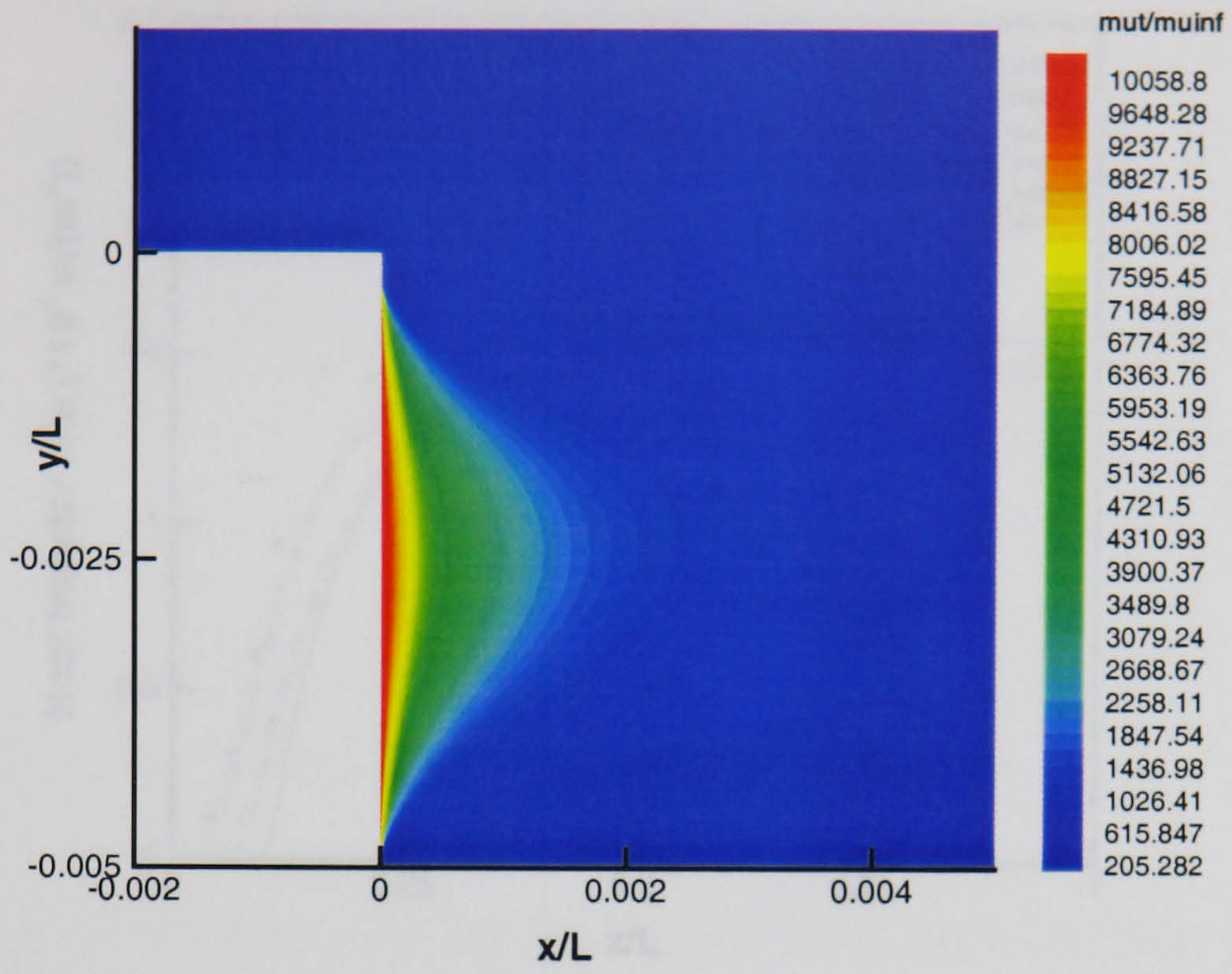

Figure 5.8: *Turbulent eddy viscosity propagation with* $\mu_t = 20,000\,\mu_\infty$ *at the boundary*

(c) Case 9, $\alpha = 45°$, $\mu_t = 4,000\,\mu_\infty$,

(d) Case 10, $\alpha = 45°$, $\mu_t = 20,000\,\mu_\infty$.

In Fig. 5.9, heat transfer rates of the above four cases along with Case 1 ($\alpha = 0°$, $\mu_t = 0.001\,\mu_\infty$ at the slot inlet boundary) and the experimental data are compared. The effect of turbulence level is very small as explained before. The cooling length agrees very well with the experiment when the coolant injection angle is set to 45°. With the coolant injection angle increased, mixing between the coolant and primary flow stream happens earlier. Thus the cooling length is decreased.

Two recirculation bubbles are clearly observed in Fig. 5.10 because of the high injection angle. One bubble locates very close to and upstream of the slot. With high injection angle, the coolant flow acts as an obstruction. The other bubble is situated downstream of the slot which explains the low heat transfer rate in this region.

In summary different parameters include the coolant inlet geometry, the turbulence level of the coolant flow and the coolant injection angle have been studied to investigate their effects on the hypersonic turbulent film cooling problem. In the calculation, due

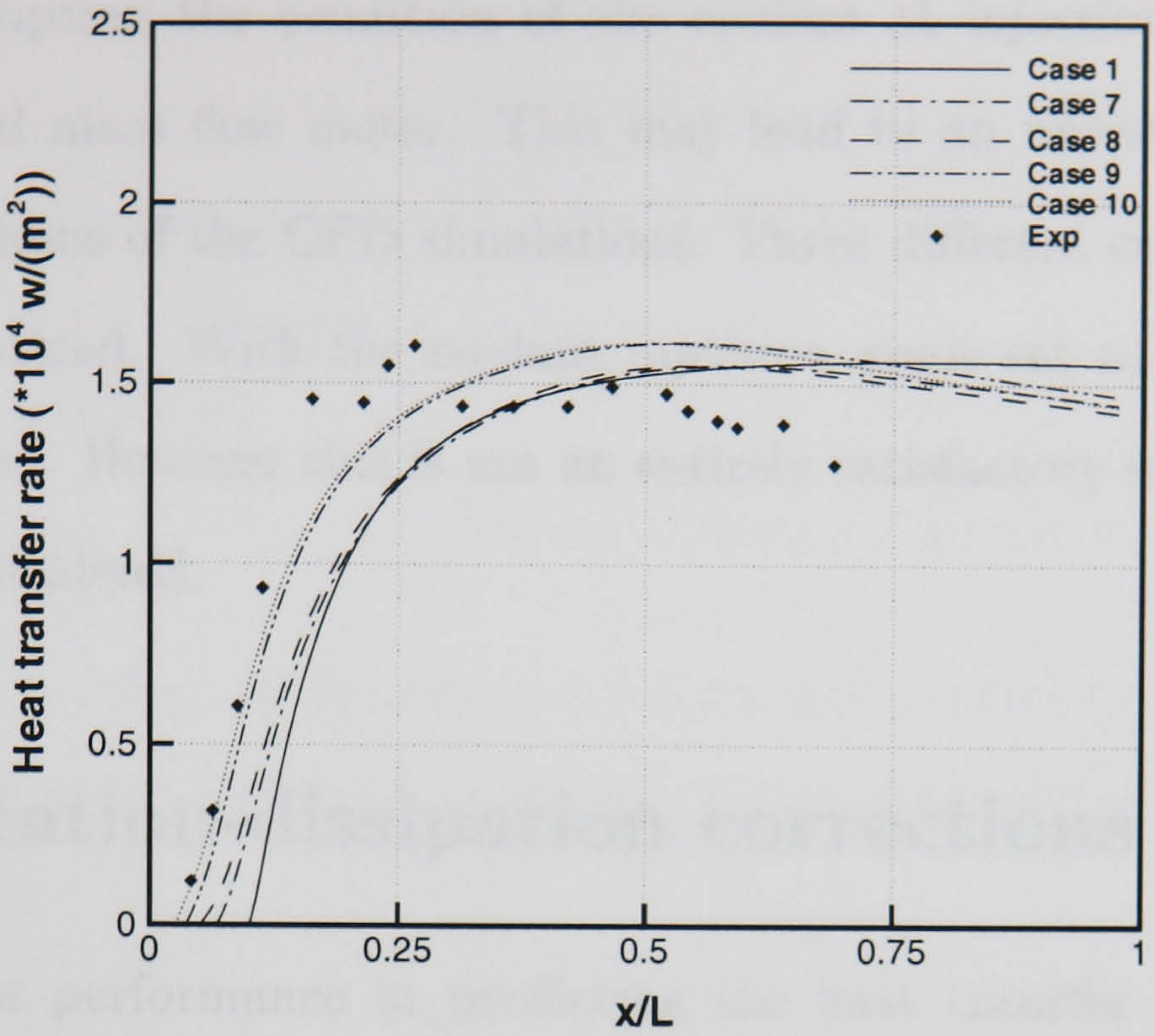

Figure 5.9: *Heat transfer rate comparison of different coolant injection angle without coolant inlet extension*

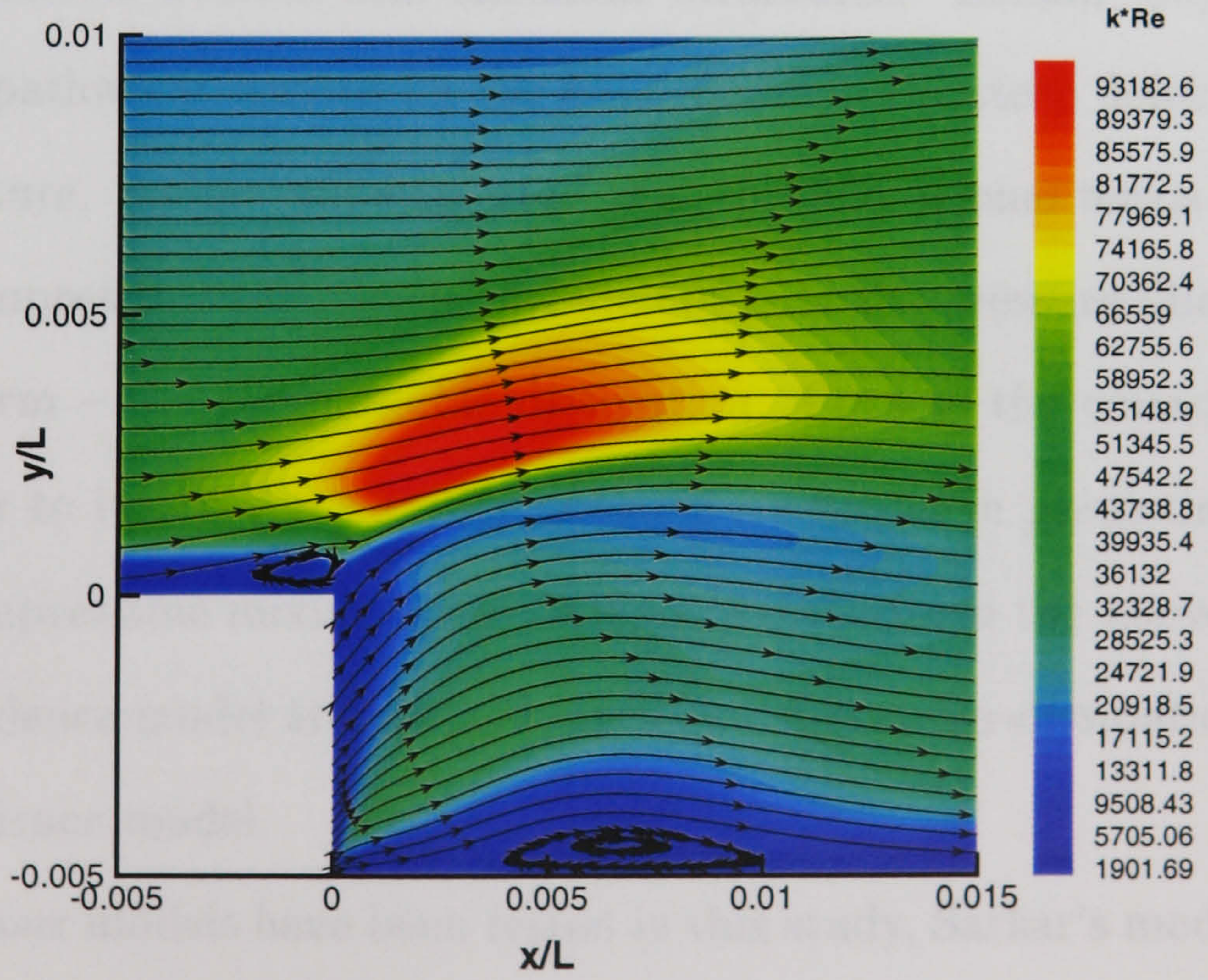

Figure 5.10: *Turbulent kinetic energy contour and streamline distributions (Case 9,* $\alpha = 45^\circ$, $\mu_t = 4,000\,\mu_\infty$*)*

to the small dimension of the slot (1.2192 mm), coolant flow in the coolant inlet was found to remain laminar which makes the cooling length longer than the experimental result. The coolant flow was assumed to be choked at the slot exit in the experiments. From this assumption the condition of the coolant at injection was thus calculated for the measured mass flow meter. This may lead to an uncertainty in defining the boundary conditions of the CFD simulations. Three different coolant injection angles were then considered. With the coolant injection angle set to 45°, good agreement has been achieved. However this is not an entirely satisfactory explanation so another factor is now considered.

5.4 Dilatation-dissipation corrections

Due to the poor performance in predicting the heat transfer rate and the cooling length, dilatation-dissipation corrections are considered for the $k-\omega$ turbulence model. From DNS results, it was found that for a sufficiently large initial density fluctuation level ρ'/ρ, and turbulent Mach number $M_t = q/c > 1$, the computed field of initially solenoidal turbulence evolves into shocklike structures. Zeman [80] introduced the dilatation-dissipation corrections for the $k-\epsilon$ model in the steep density regions of the shocklike structure. Sarkar [49] suggested that the dilatational terms that need to be modelled in compressible turbulence include not only the pressure-dilatation term but also another term – the compressible dissipation. Both of the corrections have been applied in order to improve the ability of the $k-\epsilon$ model in predicting the spreading rate for the compressible mixing layer. Wilcox [81] modified the above corrections for the $k-\omega$ turbulence model and also set up a new dilatation-dissipation correction for the same turbulence model.

Altogether four models have been tested in this study, Sarkar's model, Zeman's free shear flow model (FSF), Zeman's boundary layer model (BL) and Wilcox's model. All the models can be described through modification to β^* and β, as

$$\begin{cases} \beta^* = \beta_0^* \left[1 + \xi^* F(M_t)\right] \\ \beta = \beta_0 - \beta_0^* \xi^* F(M_t), \end{cases} \tag{5.1}$$

Model	Sarkar's	Zeman's FSF	Zeman's BL	Wilcox's
ξ^*	1.0	0.75	0.75	1.5
$F(M_t)$	M_t^2	(a)	(a)	(b)
M_{t0}	-	$0.10[2/(\gamma+1)]^{0.5}$	$0.25[2/(\gamma+1)]^{0.5}$	0.25
Λ	-	0.60	0.66	-

(a) $\left[1 - e^{-0.5(\gamma+1)(M_t - M_{t0})^2/\Lambda^2}\right] H(M_t - M_{t0})$

(b) $[M_t^2 - M_{t0}^2]\,H(M_t - M_{t0})$

Table 5.4: Auxiliary functions of different corrections for the $k - \omega$ turbulence model

where β_0^* and β_0 are the corresponding incompressible values of β^* and β of the $k - \omega$ model by Wilcox [47]. M_t is the turbulent Mach number which can be written in another format as

$$M_t = \sqrt{2k/c^2} \tag{5.2}$$

where k is the turbulent kinetic energy and c is the speed of sound.

Different parameters and auxiliary functions are used in the above four different models. In Table 5.4, $H(x)$ is the Heaviside step function defined in Eqn. (5.3).

$$H(x) = \begin{cases} 0, & x < 0 \\ 1/2, & x = 0 \\ 1, & x > 0 \end{cases} \tag{5.3}$$

The above four models have been implemented into the PMB2D code. The following test cases have been performed based on results of previous tests in hypersonic turbulent film cooling.

5.4.1 Test 1

First, all the four models were tested to check their performance in predicting the heat transfer rate for the film cooling problem. The medium coolant injection rate was selected with the medium slot height. The coolant inlet extension was included in all the test cases here.

Heat transfer rate comparison is shown in Fig. 5.11. Models 0, 1, 2, 3 and 4 are the original Wilcox $k - \omega$ turbulence model, the same model with Sarkar's, Zeman's free shear flow, Zeman's boundary layer and Wilcox's dilatation-dissipation corrections, respectively. It is obvious that the results of all the four corrections are improved compared with the original $k - \omega$ model. Zeman's boundary layer correction (Model 3) does not perform as well as the other three models.

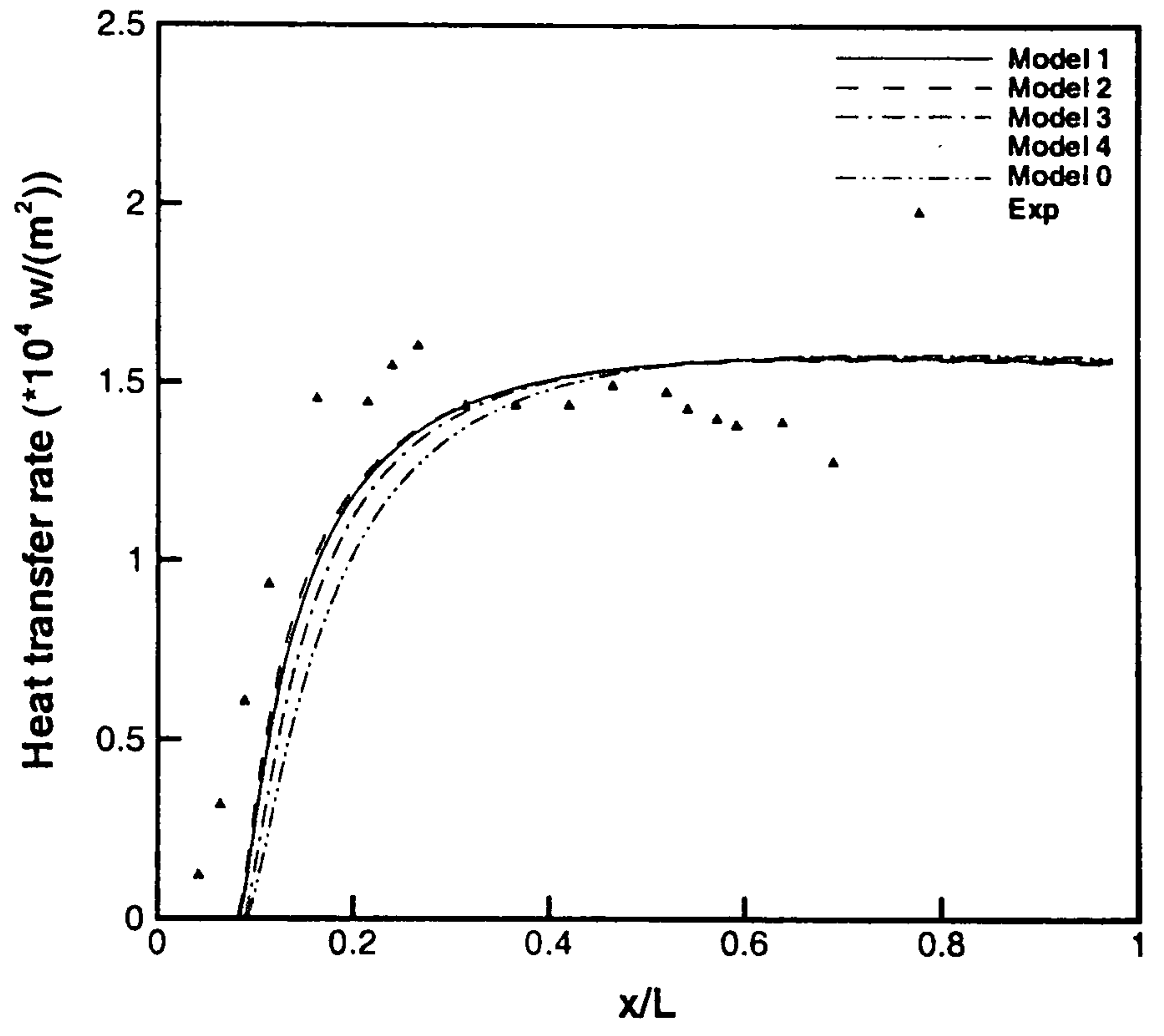

Figure 5.11: *Heat transfer rate comparison: four models*

The convergence history is compared in Fig. 5.12. Except for Wilcox's model, the other three models converge as quickly as the unchanged $k - \omega$ model. Zeman's free shear flow model is selected for further study.

5.4.2 Test 2

Although the improvement of the heat transfer rate is obvious, it is necessary to perform a further test using Zeman's free shear layer model to give more improvement. The parameters in this model were obtained through some trial calculations by Zeman [80] for a mixing layer. It is important to execute some numerical studies here to optimise

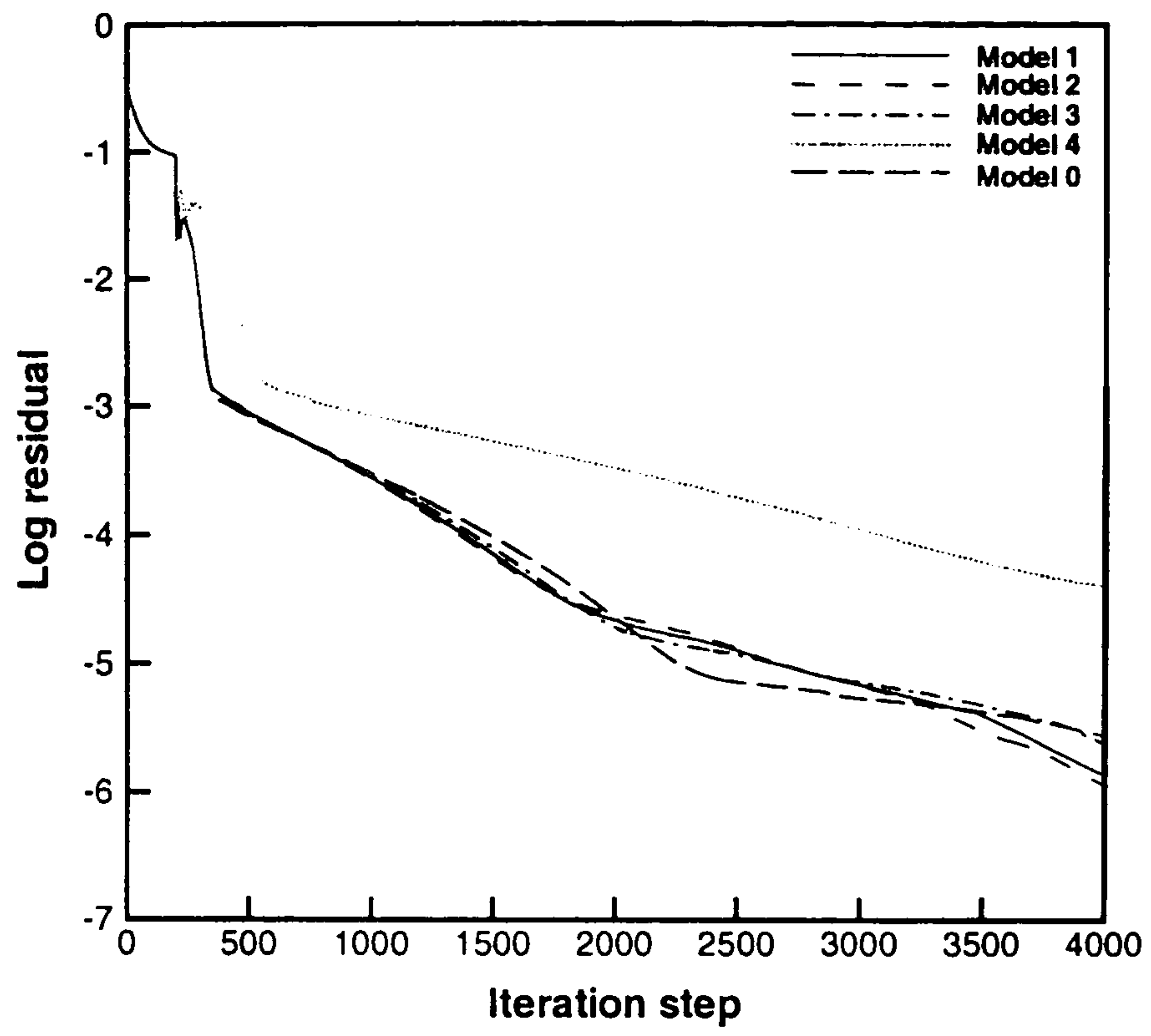

Figure 5.12: *Convergence history comparison: four models*

these parameters for the film cooling problem. Three parameters in the Zeman's free shear flow model, ξ^*, M_{t0}, Λ, plus laminar and turbulent Prandtl number, Pr and Pr_t, together with the coolant flow injection angle have been tested. Each parameter except the coolant injection angle was first chosen to be changed ±10% while other parameters were frozen. The heat transfer rate of all these calculations is compared with the unchanged Zeman's free shear flow model (Model 2), the original Wilcox $k-\omega$ model (Model 0) and the experimental data. Results are shown in Fig. 5.13 to Fig. 5.17.

According to the above results, the following general conclusions are drawn: (1) increasing ξ^* increases the ability of the $k-\omega$ model to predict the heat transfer rate, (2) M_{t0} is not a sensitive parameter, (3) decreasing Λ helps to predict better heat transfer rate both near and far from the slot region, (4) the values of Pr and Pr_t need not be changed according to the above results.

Sommer *et al.* [48] pointed out that the hypothesis of constant turbulent Prandtl number Pr_t is not suitable for compressible flows with highly cooled wall boundary condition under high Mach number. A near-wall variable Pr_t turbulence model has

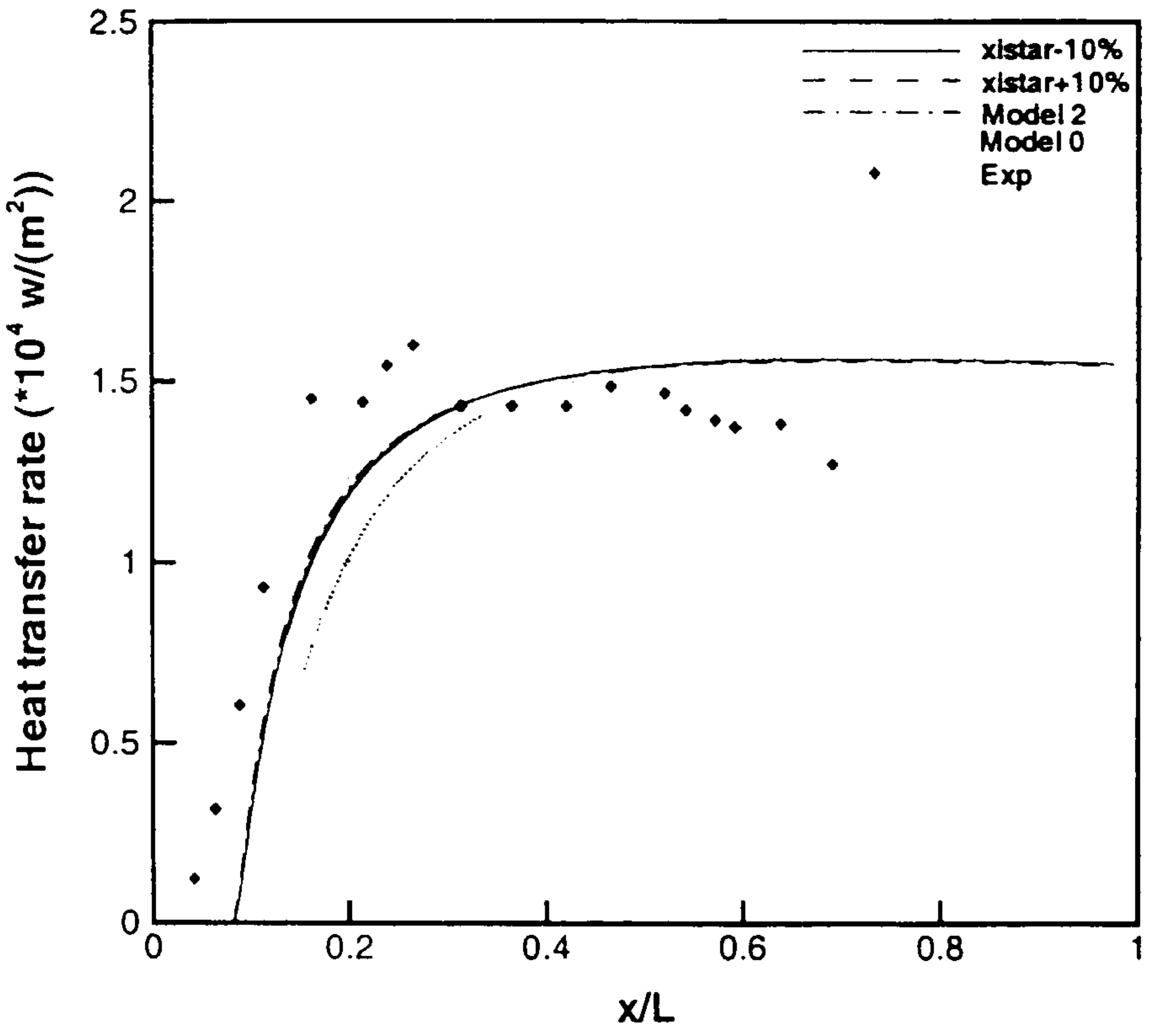

Figure 5.13: *Heat transfer rate comparison: effect of* ξ^*

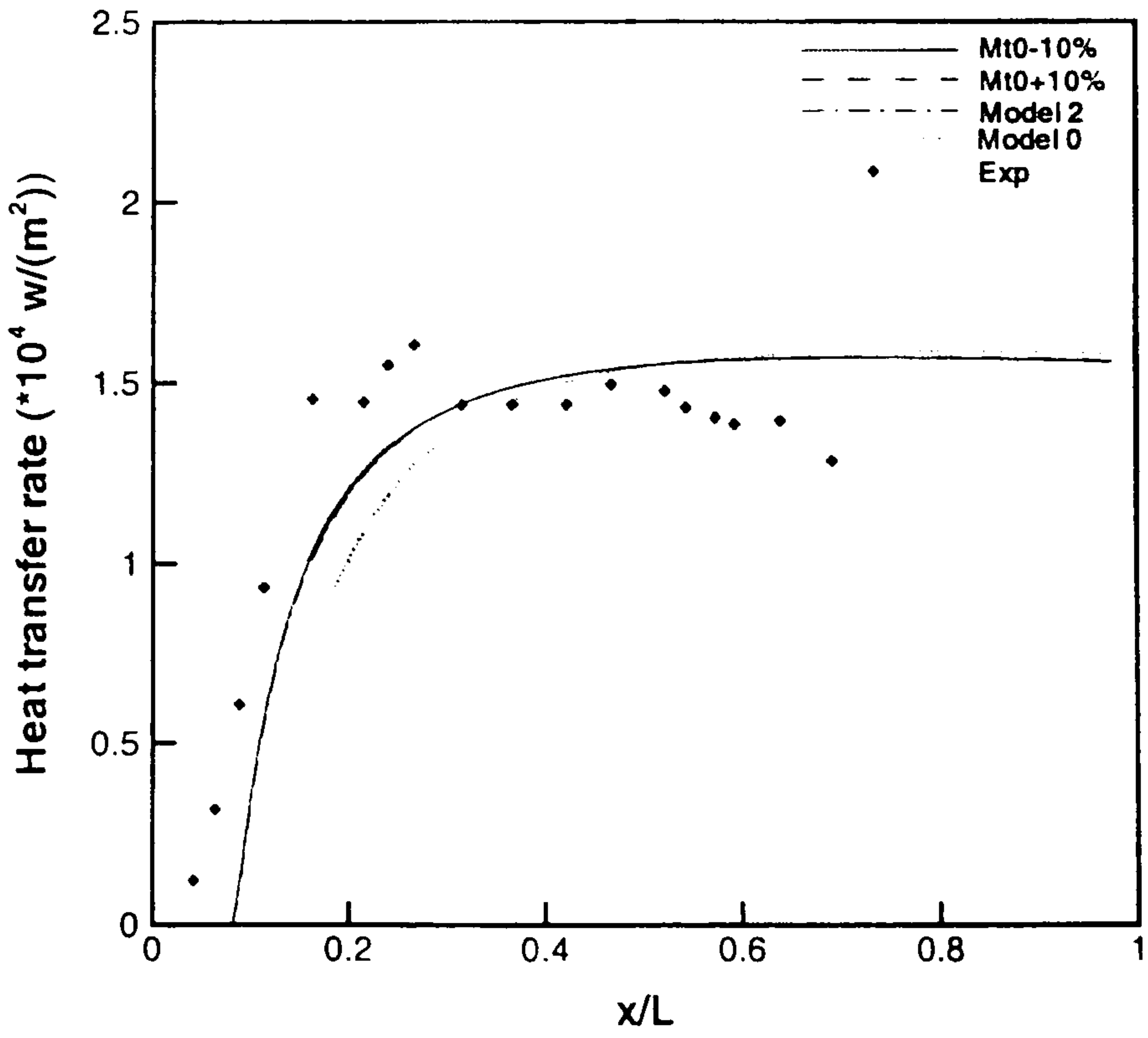

Figure 5.14: *Heat transfer rate comparison: effect of* M_{t0}

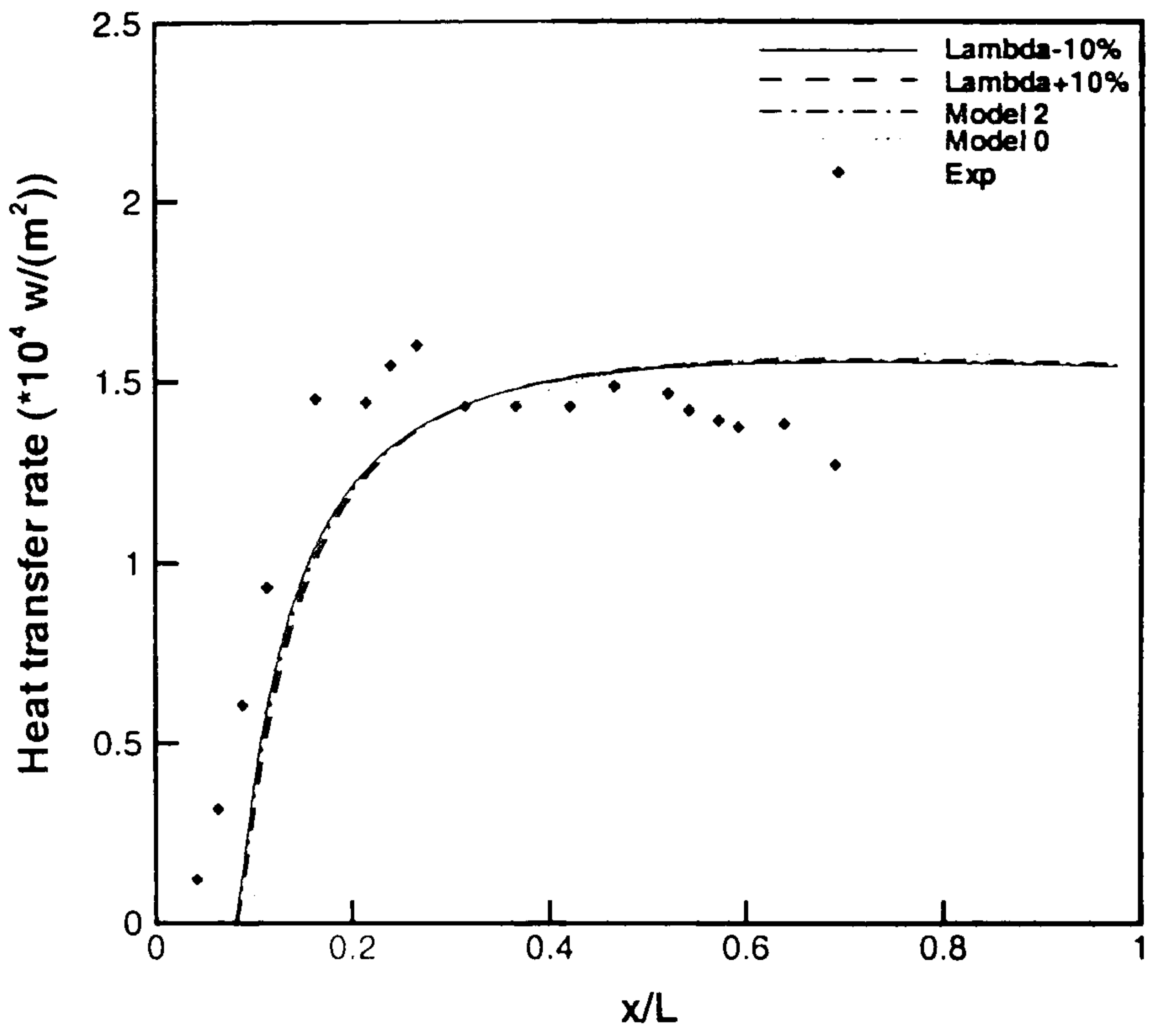

Figure 5.15: *Heat transfer rate comparison: effect of* Λ

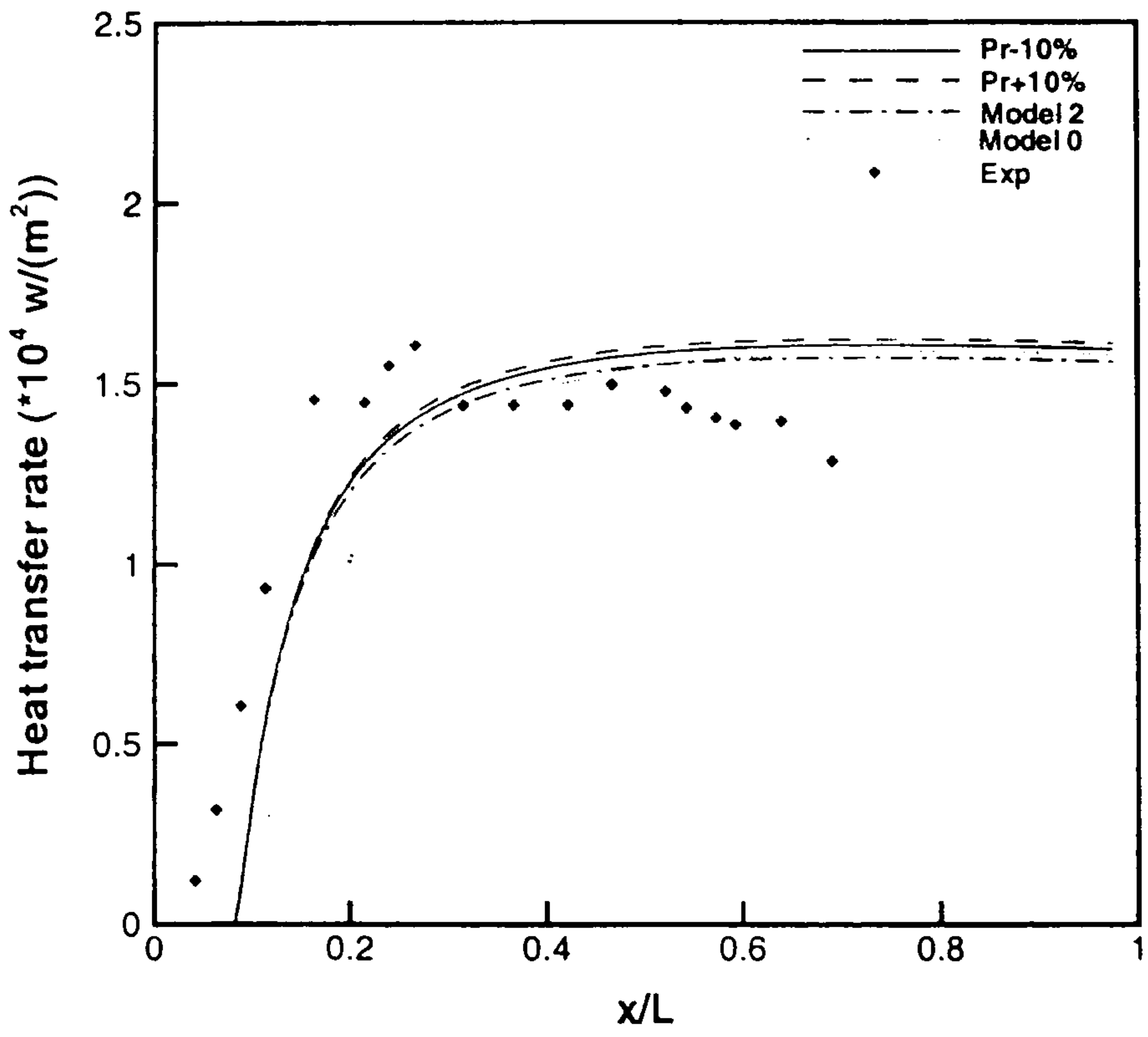

Figure 5.16: *Heat transfer rate comparison: effect of Pr*

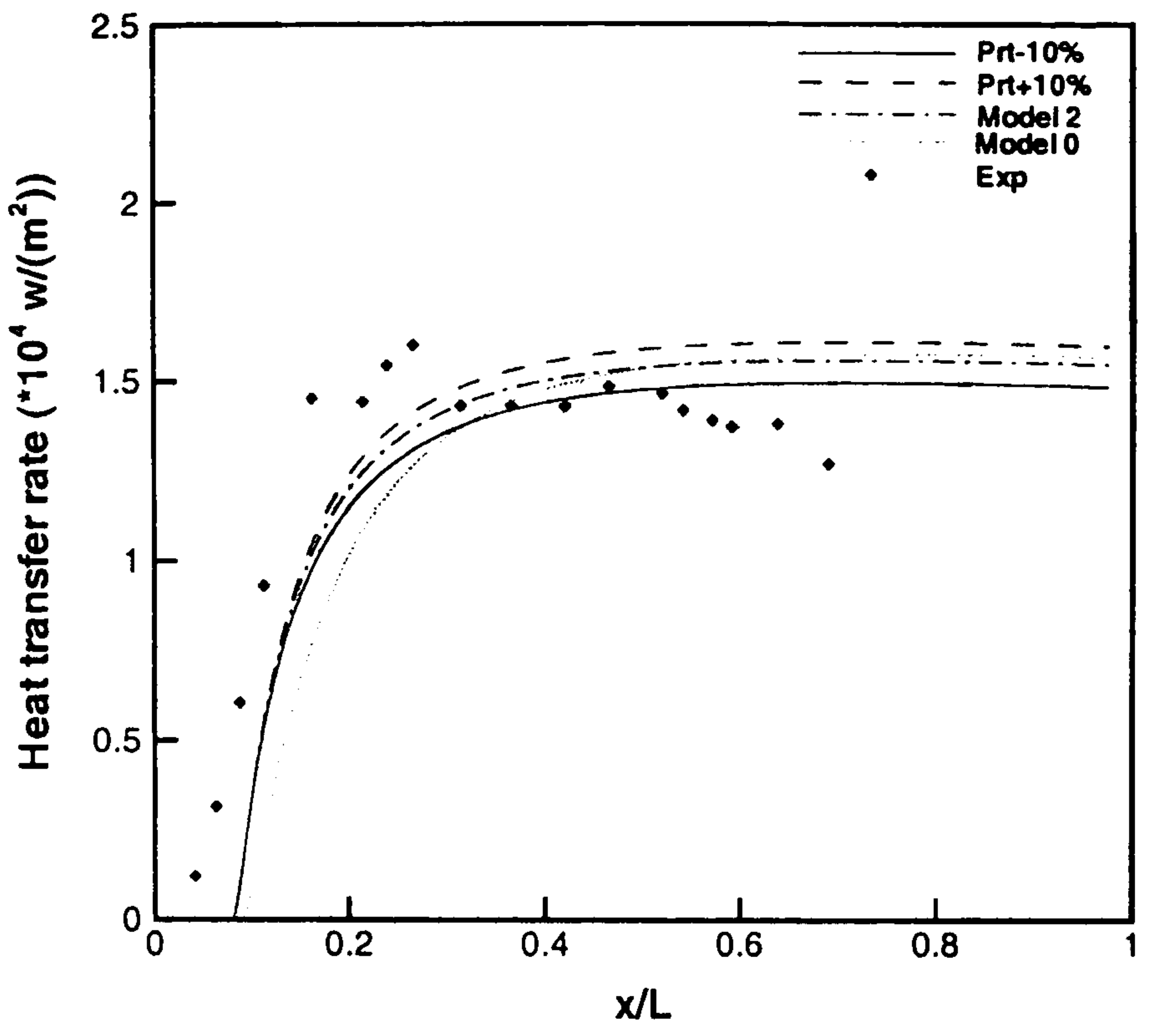

Figure 5.17: *Heat transfer rate comparison: effect of* Pr_t

been developed for compressible flat plate turbulent boundary layers with constant heat flux and constant temperature wall boundary conditions. It was observed that the calculated Pr_t is not a constant but has a wall value of about 0.5 for all test cases considered in [48] (M_∞ = 4.544, 5.29, 8.18 and 10.31), then it increases to about 0.9 at $y_w^+ = 200$. Beyond $y_w^+ = 200$, Pr_t was found to decrease slightly to about 0.8 at the edge of the boundary layer. Consequently, a more complicated model may be introduced in the current study rather than the simple modification of Pr_t.

Besides the computational experiments above, more test cases have been performed: (1) increasing ξ^* up to 50%, (2) decreasing Λ up to 50%, (3) increasing ξ^* by 30% and decreasing Λ by 20%. The last two operations were observed to give better results. The coolant flow injection angle has been tested in the previous study in Section 5.3. Here it is selected to be 20°. It should be mentioned here that when setting up the coolant injection flow angle, the coolant inlet extension is ignored. So in this test a given profile boundary is set up directly at the slot position.

The solid line in Fig. 5.18 indicates the case with ξ^* increased 30% together with

Λ decreased 20% while the dash line indicates the case with ξ^* increased 50%. Both cases were tested with the coolant injection angle 20° and the turbulent eddy viscosity set to $4,000\,\mu_\infty$ at the slot position. According to the favourable results in Fig. 5.18, ξ^* increased by 50% is selected for the following calculations.

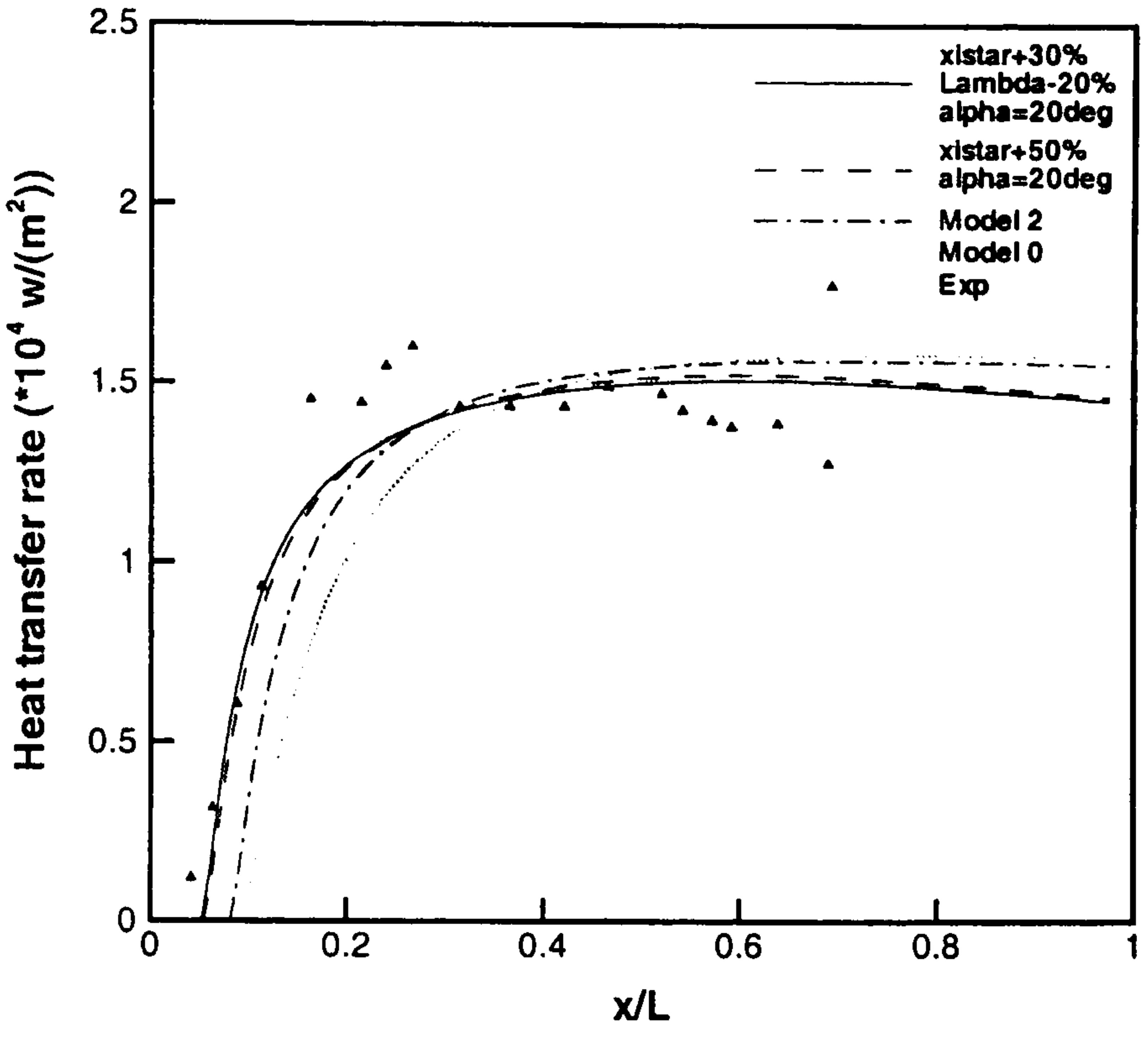

Figure 5.18: *Heat transfer rate comparison:* $\alpha = 20°$

With Zeman's dilatation-dissipation correction applied in the $k - \omega$ turbulence model, heat prediction ability of this model in hypersonic turbulent flow has been improved greatly. Thus it is now possible to study the effect of coolant injection rate and slot height in hypersonic turbulent film cooling. The computational domain used is similar to Case 1, that is, there is no coolant inlet extension. Coolant flow parameters were set up directly at the slot exit as the inlet boundary with $\mu_t = 4,000\,\mu_\infty$, $\alpha = 20°$ applied in all the calculations.

5.5 Different turbulence models

Menter's baseline (BSL) and *SST* turbulence models have also been tested in hypersonic turbulent film cooling. Again TFC Case 3 was chosen to be the test case. The

BSL worked well without the coolant inlet while the *SST* model worked well with the coolant inlet extension. Thus the coolant inlet in Section 5.3.1 was included for the *SST* model. For the BSL model, μ_t was set to $4,000\,\mu_\infty$ at the slot exit with the coolant injection angle $\alpha = 20°$. For the *SST* model, μ_t was also set to $4,000\,\mu_\infty$ at the extended inlet. Heat transfer rate is compared in Fig. 5.19.

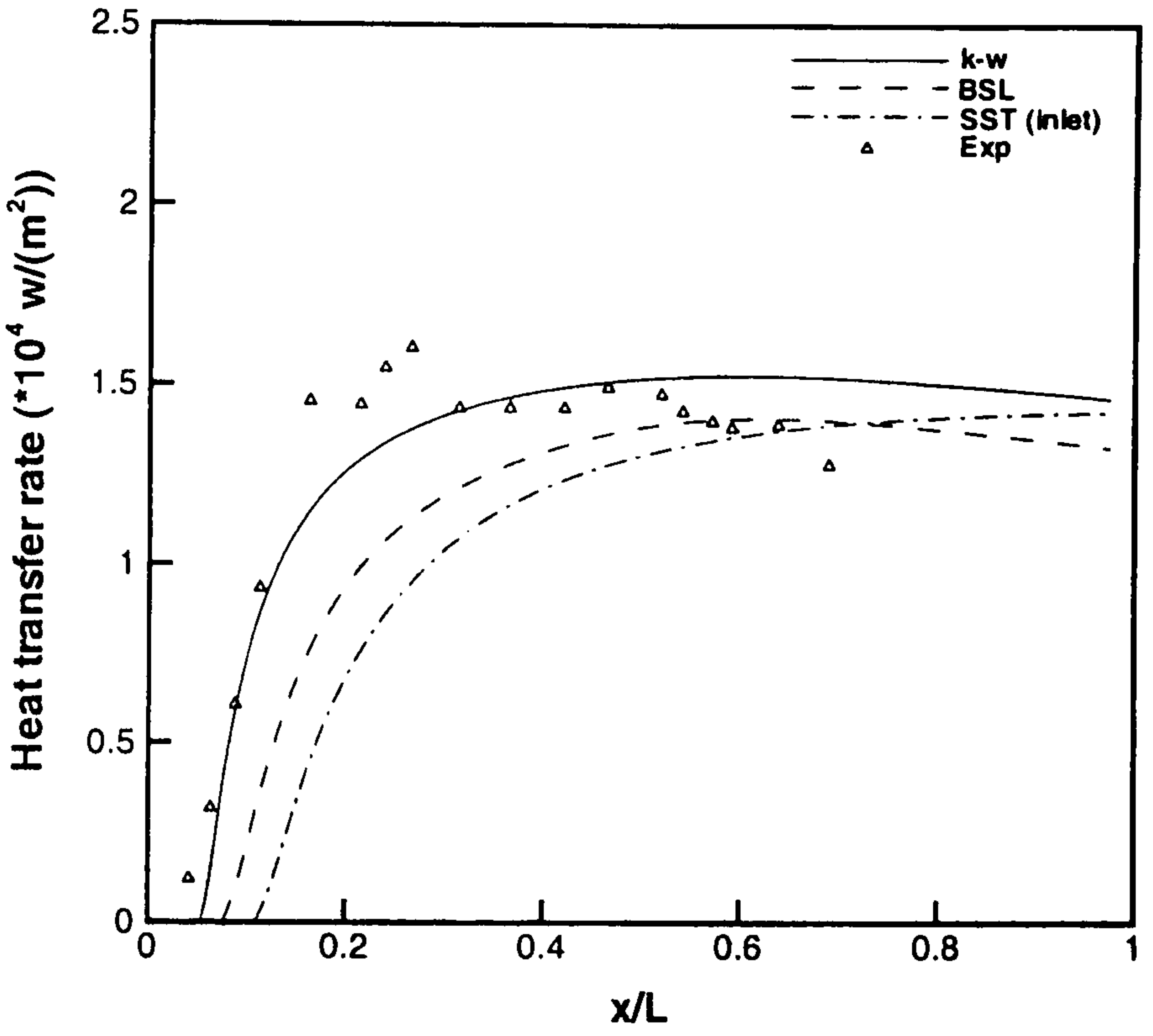

Figure 5.19: *Heat transfer rate comparison of different turbulence models*

From the cooling length in Fig. 5.19, it is clearly seen that Menter's two models delay transition. Because of the limiter used in the *SST* model when calculating the turbulent eddy viscosity, this model delays transition even more than the BSL model. It could be concluded that these two models are not suitable for the film cooling under the flow conditions and geometry configurations in this study without any modifications. Further work is needed in order to apply the Menter's *SST* turbulence model in this film cooling study.

5.6 Effect of coolant injection rate

Detailed coolant flow conditions of the five different coolant injection rates from 5.07×10^{-4} to $30.69 \times 10^{-4}\, kg/s$ called TFC Cases 1 to 5 (Group 1) are listed in Table 5.2. The coolant flow was supposedly injected at a Mach number of 1.0 in these five test cases. It had been observed that under high mass flow rate, Zeman's free shear flow model does not perform as well as under low mass flow rate.

In Fig. 5.20, heat transfer rates of the above five coolant injection rate cases plus the flat plate case are compared with the experimental data. In all the five cases, the experimental cooling length changes only by a small amount. In the computational results, the cooling length has a more definite increase with increase in coolant injection rate because more momentum and energy were injected into the primary flow stream through the given profile applied at the slot position. Although the turbulent eddy viscosity is set to $4,000\, \mu_\infty$, it will peter out so that a laminar region occurs, which will lead to an increase of the cooling length. The coolant flow influences the primary flow even far downstream of the slot in all the cases, but less in the computational study than the experiments.

Increasing the coolant injection rate can be used as an effective method to improve the film cooling effectiveness in hypersonic turbulent flow as shown in Fig. 5.21. For the highest coolant injection rate, TFC Case 5, the effectiveness is about 46% at $50\, s$ downstream of the slot. The effectiveness is only about 14% at the same position in TFC Case 1. The film cooling effectiveness achieves at about 20% at $200\, s$ downstream of the slot in TFC Case 5. A similar result was achieved in the laminar study, but the coolant injection rate here is much higher than in the laminar film cooling and the effect of the increment of the coolant injection rate is not as effective as in the laminar film cooling.

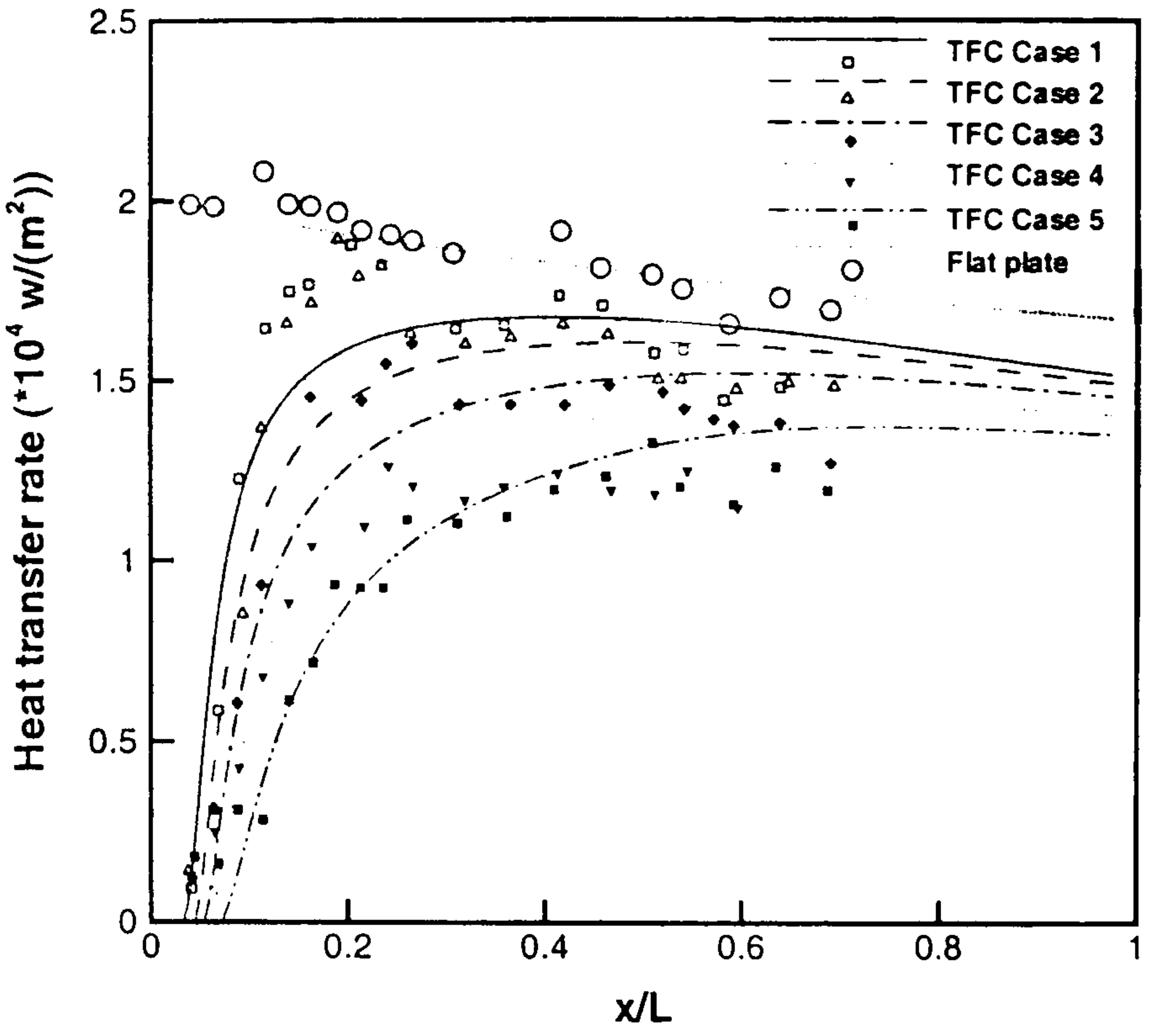

Figure 5.20: *Heat transfer rate comparison: five coolant injection rates*

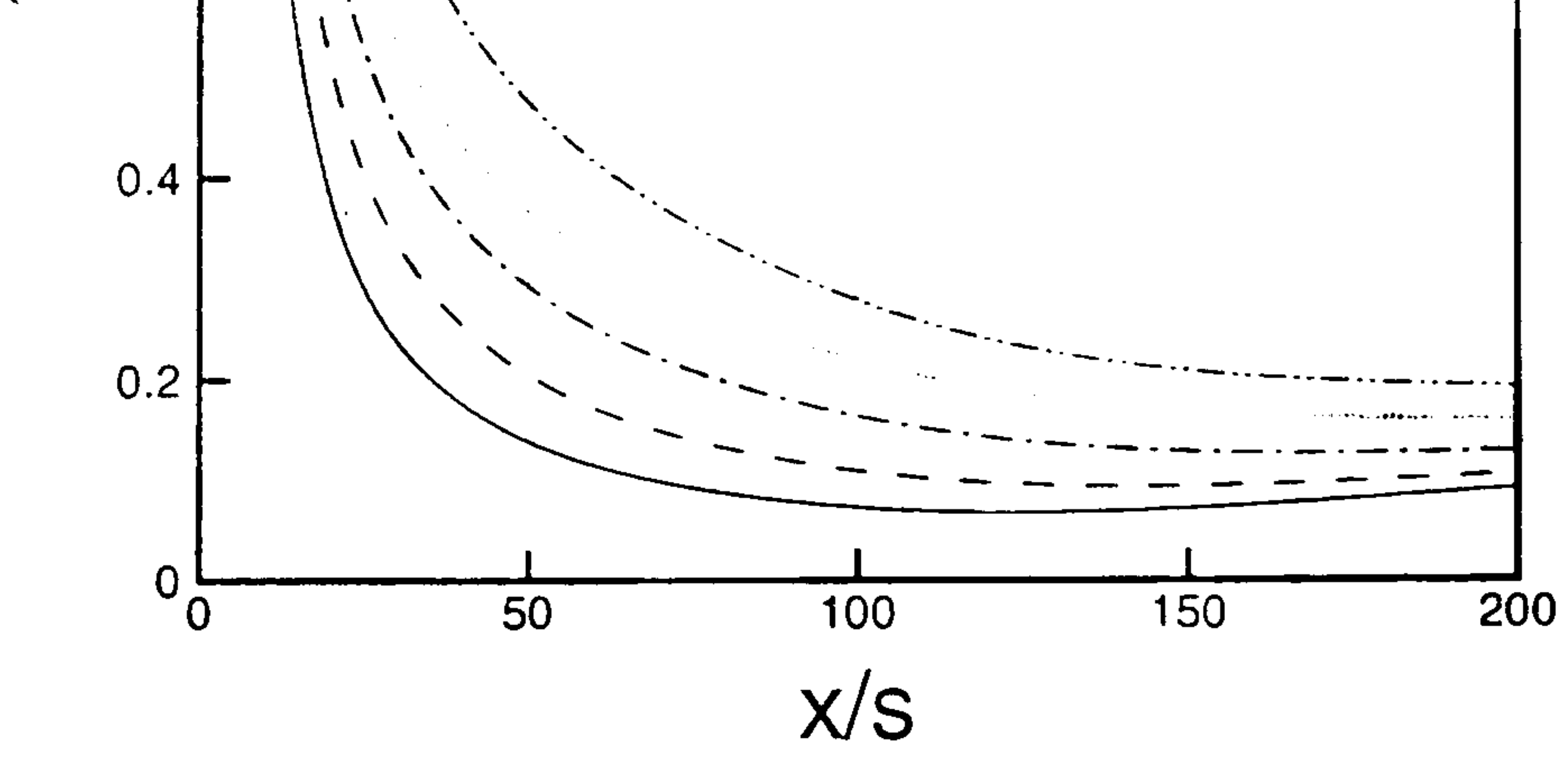

Figure 5.21: *Film cooling effectiveness of different coolant injection rates*

5.7 Effect of slot height

TFC Cases 3, 6 and 7 listed in Table 5.1 were selected to study the effect of slot height in hypersonic turbulent film cooling. Both the primary and the coolant flow conditions were kept the same except that the slot height was different from $0.8382\,mm$ to $1.6002\,mm$. Fig. 5.22 and Fig. 5.23 show the comparison between the computational and experimental results of the heat transfer rate and film cooling effectiveness respectively similar to that obtained in the laminar film cooling study.

For these three different slot heights, the heat transfer rate changes little in the near slot area. But the effect of the slot becomes more obvious far from the slot position in the CFD results.

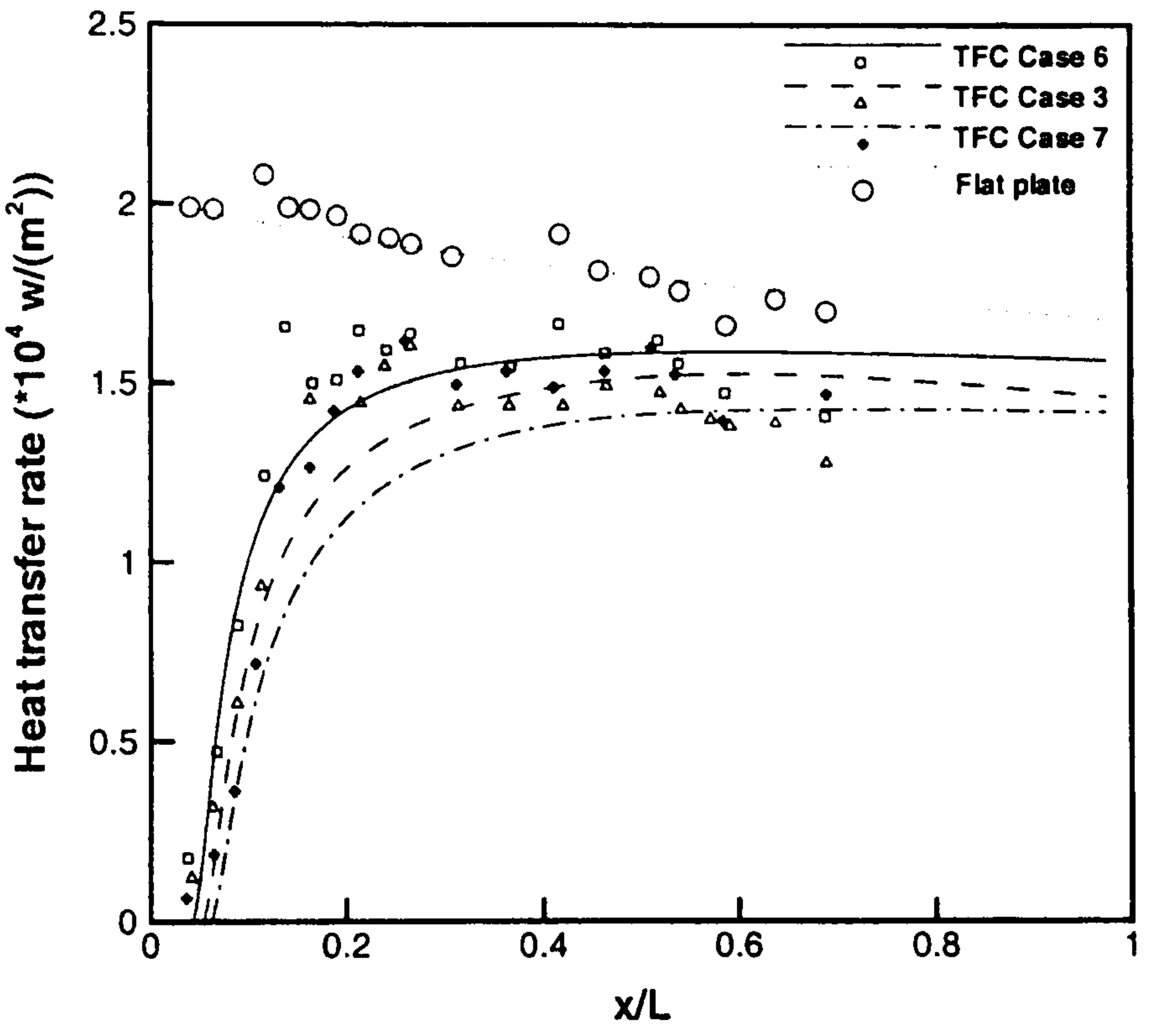

Figure 5.22: *Heat transfer rate comparison: three slot heights*

5.8 Curve fitting – turbulent film cooling

Similar to the laminar calculations in the previous chapter, curve fitting has again been applied to TFC Cases 1 to 5 to estimate the cooling length x_A for hypersonic turbulent film cooling (Eqn. (5.4)). The equation obtained is

$$x_A/h = 24.36\,\dot{m}^{0.44}. \tag{5.4}$$

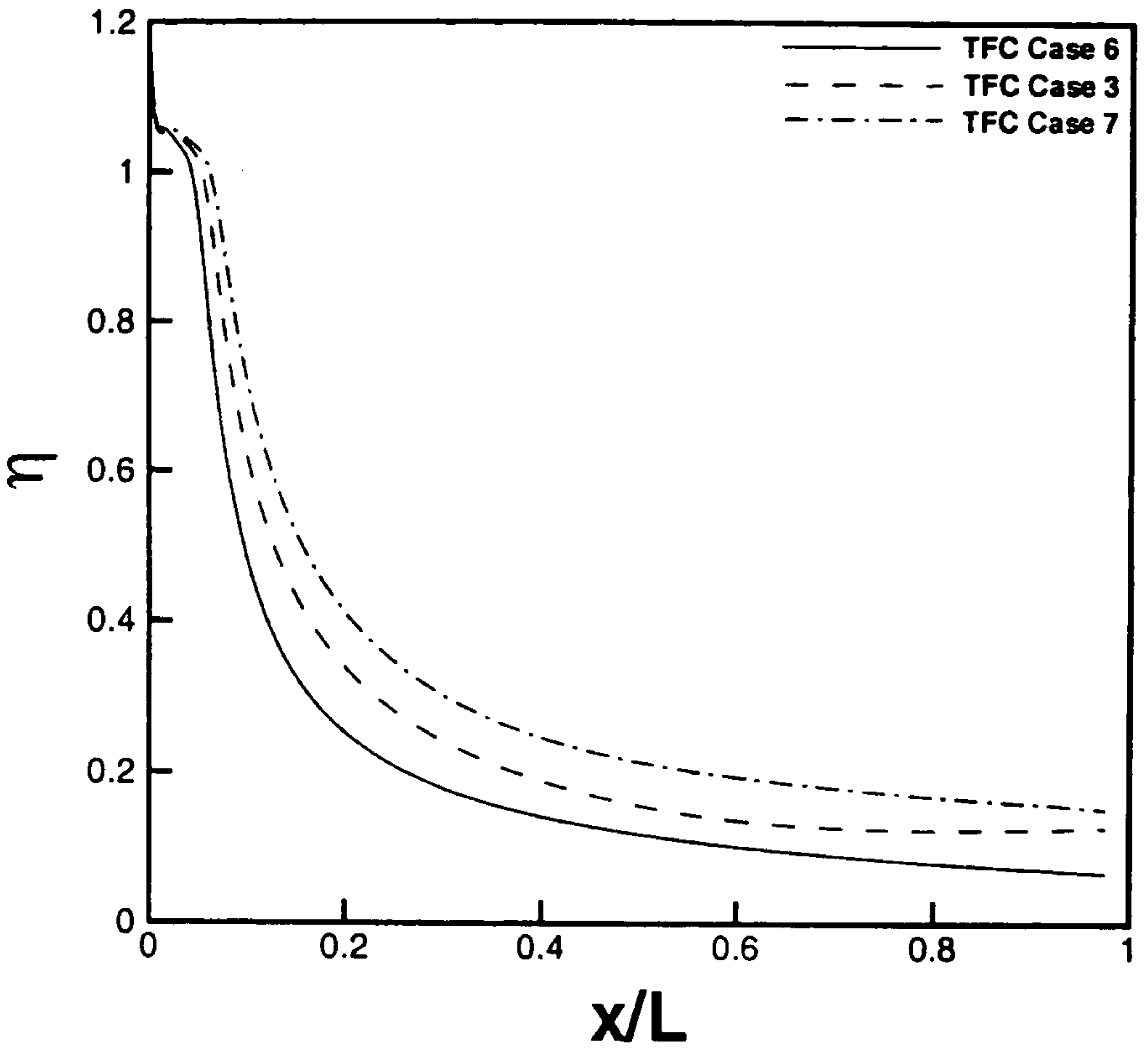

Figure 5.23: *Film cooling effectiveness of different slot heights*

Table 5.5 demonstrates that the equation provides good prediction of the cooling length.

TFC Case	$\dot{m}$	$x_A/h\,(a)$	$x_A/h\,(b)$
1	0.05	6.12	6.44
2	0.08	8.52	8.08
3	0.14	10.60	10.14
4	0.20	11.81	12.05
5	0.29	13.88	14.23

(a) estimated from the numerical result
(b) from Eqn. (5.4)

Table 5.5: Cooling length estimation (turbulent flow)

Film cooling effectiveness is specified in Eqn. (5.5). For this turbulent film cooling study, it was observed that the film cooling effectiveness decreases sharply after the cooling length which could be predicted using a simple relationship. In fact two linear curves in log-log coordinates could be used to describe the film cooling effectiveness as sketched in Fig. 5.24. This agrees well with results presented by other researchers.

The power law in Eqn. (5.5) was found to estimate the efficiency.

$$\eta = \begin{cases} 1 & x \leq x_A \\ 23.92\left(\frac{x}{h\dot{m}}\right)^{-0.74} & x > x_A \end{cases} \tag{5.5}$$

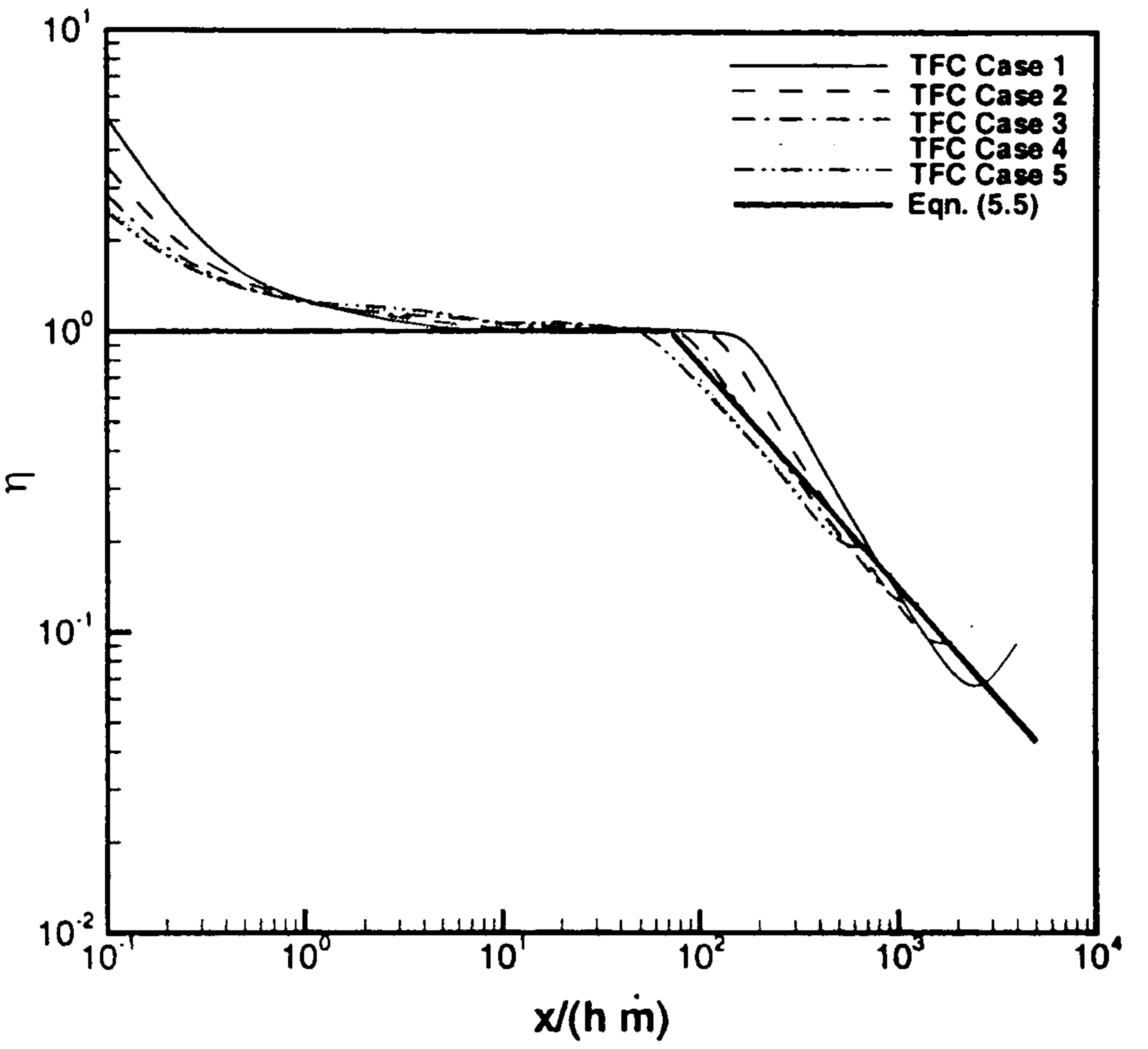

Figure 5.24: *Film cooling effectivenesses of TFC Cases 1 to 5 comparing with curve fitting result*

For both laminar (Chapter 4) and turbulent flows, a two-equation model is found to be suitable for predicting film cooling effectiveness against parameter $x/(h\dot{m})$. The relation could be as simple as linear in turbulent flows while a second-order polynomial curve can be used to fit the laminar film cooling effectiveness in log-log coordinates.

5.9 Summary

After successfully simulating the film cooling problem in hypersonic laminar flows, the same problem has been studied in hypersonic turbulent flows. Different parameters, including the coolant inlet geometry, turbulence level of the coolant flow and the coolant injection angle were first studied to investigate their effects on the hypersonic turbulent film cooling. Due to the small slot (1.2192 mm), coolant flow in the coolant inlet was found to remain laminar in the calculation which makes the cooling length longer than the experimental result. In the experiment, the coolant flow had been arranged to be choked ($M_c = 1.0$) at the slot exit. An assumption based on this may lead to some uncertainties in defining the boundary conditions of the CFD simulations.

It is found necessary to introduce dilatation-dissipation corrections to the $k - \omega$ turbulence model to obtain agreement with measurements. Zeman's free shear flow model was chosen to be tested in this study. For coolant low mass flow rate, a 50% increment of ξ^* can give quite good results compared with the unmodified $k - \omega$ model. But under high mass flow rate, the unchanged Zeman's free shear flow model gave reasonable results. This correction yields improved heat transfer and cooling length prediction.

During the study in which the coolant injection rate and the slot height were varied, coolant flow parameters were set up directly at the slot exit with $\mu_t = 4,000\,\mu_\infty$ and an injection angle at $\alpha = 20°$ applied in all the calculations. It was found that under the same slot height improved film cooling effectiveness can be achieved when the coolant injection rate increased due to more momentum and energy injected into the primary flow stream. Changing slot height again made little difference to film cooling effectiveness.

Besides the Wilcox $k - \omega$ turbulence model, the Menter baseline and SST models were also tested. According to the preliminary results, these two models were found not to be suitable for the hypersonic turbulent film cooling without any modifications.

A two-equation model has been found to describe the relationship between the film cooling effectiveness and the parameter $x/(h\,\dot{m})$. Different from the laminar flow, a straight line is used in the log-log coordinates rather than a second-order polynomial curve for the region after the cooling length.

Chapter 6

Conclusions

6.1 Summary of analysis

The aim of this computational work is to investigate the mechanism and effectiveness of film cooling in hypersonic laminar and turbulent flows. Film cooling is used to provide heat protection for wall surfaces under high thermal load. As a first step, the PMB2D Navier-Stokes solver has been successfully validated in hypersonic laminar and turbulent flows. In Chapter 3, the hypersonic flow over a flat plate without film cooling was studied, this provided a reference datum to check the effectiveness of film cooling. As described in Chapters 4 and 5, the CFD code has been successfully used to simulate the film cooling problem in hypersonic laminar and turbulent flows respectively. According to the computational results, CFD was proven to be a powerful tool able to provide reasonable results for hypersonic cooling flows.

The predictions were sensitive to the way that the appropriate boundary conditions applied for the coolant flow. For laminar film cooling it was necessary to include the development of the flow in the plenum chamber upstream of the slot. For turbulent film cooling under the geometry used in the experiment the injection at an angle of 20° was most appropriate in this numerical study. Different turbulence models including Wilcox's $k-\omega$ model, Menter's baseline and SST model have been tested. It is concluded that the Wilcox's $k-\omega$ turbulence model with dilatation-dissipation correction provides the best heat prediction in this study.

The mechanism of film cooling was well illustrated in the plots of calculated velocity profiles, Mach and temperature contours downstream of the slot exit. The coolant fluid was found to affect the primary boundary layer in two ways:

- initially a separate layer set up by the coolant fluid itself in the near slot area,
- later a mixing layer between the primary and coolant flow streams.

Upstream of the slot it has been observed that there is a band of high temperature air near the wall which provides the positive temperature gradient, hence heating at the wall. The effect of the coolant is to initially remove this temperature gradient. However further downstream there is a mixing of the flows when the initial profile and temperature band is re-established, although more diffused, resulting in an increasing heat transfer rate. Therefore, it can be concluded that film cooling causes the development of the primary boundary layer to be delayed.

A commonly used technique, curve fitting, has been applied in analysing the numerical results. For laminar flow, film cooling effectiveness was observed to obey a second-order curve in the log-log coordinates against $log_{10}\eta = f(log_{10}\frac{x}{h\dot{m}})^2$. For turbulent flow, a linear relation was found suitable to describe the relation between $log_{10}\eta$ and $log_{10}\frac{x}{h\dot{m}}$.

Besides the isothermal wall, an adiabatic wall has also been tested for film cooling in laminar hypersonic flow and was found to give reasonable prediction of the film cooling effectiveness. The application of the adiabatic wall can greatly reduce the computational cost because there is no large temperature gradient between the flow stream and the wall surface. This is an important observation for future 3-D film cooling computational studies.

The following general conclusions about film cooling in hypersonic flows are drawn in this computational study:

- For both laminar and turbulent flows, film cooling is effective but especially in laminar flow. Inside the cooling length downstream of the slot exit, the wall surface is fully protected. For example, the film cooling effectiveness is about 30% for LFC Case 5 (Chapter 4) 200 slot heights downstream of the slot.

- Increasing the coolant injection rate can obviously increase the film cooling effectiveness. Again, this works better in laminar flow than in turbulent flow. The coolant injection rate in turbulent flow should be considered to be high enough to give good heat protection.
- Slot height in both laminar and turbulent flows under the flow conditions in this study was found to be less important, which means other factors can be considered in priority when constructing film cooling systems.
- The primary flow conditions were found to heavily affect the heat transfer rate. Thus when designing film cooling systems, the coolant injection rate should be considered carefully according to the primary flow conditions.
- Under the same flow conditions and step height, the cooling length in both laminar and turbulent flows could be described by a power law of the ratio of coolant mass flux per unit area to primary stream mass flux per unit area $\dot{m}$ and the non-dimensional distance downstream of the slot exit x/h. For film cooling effectiveness in log-log coordinates, a second-order polynomial curve can be used to fit the laminar flows, whilst a straight line is suitable for the turbulent flows.

6.2 Suggestions for future work

The fundamental 2-D film cooling has been successfully studied. The effectiveness of film cooling has been found to be concerned with many parameters, e.g., coolant injection rate, slot/lip height, primary/coolant flow conditions, different coolant gases. Further work about film cooling in hypersonic flows should be executed with some aspects suggested below. All these will go towards actual application of film cooling in engineering.

- Different coolant gases should be studied, especially hydrogen because it is the most commonly used fuel in hypersonic vehicles. It has also been found that its high heat capacity compared to air provides higher film cooling effectiveness.
- A three-dimensional film cooling study should be made with complex structures such as turbine blades. Hole shapes, hole distributions and combination of injection angles are all of interest. An adiabatic wall boundary condition is suggested to be used to study the film cooling effectiveness in 3-D simulations because of its low computational cost.
- More experiments should be performed with careful control of and under a variety of flow conditions to provide a database for CFD validation.
- A more complex study should be made combining film cooling and regenerative cooling.

Appendix A

Implementation and Validation of the S-A Turbulence Model

A.1 Implementation of the S-A turbulence model

A.1.1 S-A turbulence model transport equation

As described in Chapter 2, the S-A turbulence model is a one-equation model developed by Spalart and Allmaras [68, 69]. The transport equation and coefficients of the S-A model were defined using dimensional analysis, Galilean invariance, and selected empirical results. In this model, the Reynolds stresses are given by

$$-\overline{u_i'u_j'} = 2\nu_t S_{ij}, \tag{A.1}$$

where S_{ij} is the mean strain rate tensor. The eddy viscosity ν_t is given by

$$\nu_t = \widetilde{\nu} f_{v1}, \quad f_{v1} = \frac{\chi^3}{\chi^3 + c_{v1}^3}, \quad \chi \equiv \frac{\widetilde{\nu}}{\nu}. \tag{A.2}$$

ν is the molecular viscosity. $\widetilde{\nu}$ is the working variable and obeys the following transport equation

$$\begin{aligned}\frac{D\tilde{\nu}}{Dt} = {} & c_{b1}\left[1-f_{t2}\right]\tilde{\Omega}\tilde{\nu} + \frac{1}{\sigma}\left[\nabla\cdot\left(\left(\nu+\tilde{\nu}\right)\nabla\tilde{\nu}\right) + c_{b2}\left(\nabla\tilde{\nu}\right)^2\right] \\ & - \left[c_{w1}f_w - \frac{c_{b1}}{\kappa^2}f_{t2}\right]\left[\frac{\tilde{\nu}}{d}\right]^2 + f_{t1}\Delta U^2.\end{aligned} \tag{A.3}$$

The left hand side of the equation is the Lagrangian or material derivative of $\tilde{\nu}$: $D\tilde{\nu}/Dt \equiv \partial\tilde{\nu}/\partial t + u_i\partial\tilde{\nu}/\partial x_i$, $\tilde{\Omega}$ is the modified magnitude of the vorticity and d is the distance to the closest wall. Here

$$\tilde{\Omega} \equiv \Omega + \frac{\tilde{\nu}}{\kappa^2 d^2}f_{v2}, \quad f_{v2} = 1 - \frac{\chi}{1+\chi f_{v1}}. \tag{A.4}$$

The other auxiliary functions are defined by

$$\begin{aligned}& f_w = g\left[\frac{1+c_{w3}^6}{g^6+c_{w3}^6}\right]^{1/6}, \quad g = r + c_{w2}\left(r^6 - r\right), \quad r \equiv \frac{\tilde{\nu}}{\tilde{S}\kappa^2 d^2}, \\ & f_{t2} = c_{t3}\,exp\left(-c_{t4}\chi^2\right), \quad f_{t1} = c_{t1}\,g_t\,exp\left(-c_{t2}\frac{\omega_t^2}{\Delta U^2}\left[d^2 + g_t^2 d_t^2\right]\right),\end{aligned} \tag{A.5}$$

f_{t1} is the trip function, d_t is the distance from the field point to the trip, which is on a wall. The parameter ω_t is the wall vorticity at the trip, and ΔU is the difference between the velocity at the field point and the trip. The parameter $g_t \equiv min\left(0.1, \Delta U/\omega_t\Delta x\right)$ where Δx is the grid spacing along the wall at the trip. The constants are

$$\begin{aligned}& \sigma = 2/3, \quad c_{b1} = 0.1355, \quad c_{b2} = 0.622, \quad \kappa = 0.41, \\ & c_{w1} = c_{b1}/\kappa^2 + \left(1+c_{b2}\right)/\sigma, \quad c_{w2} = 0.3, \quad c_{w3} = 2, \quad c_{v1} = 7.1, \\ & c_{t1} = 1.0, \quad c_{t2} = 2.0, \quad c_{t3} = 1.1\,(1.2), \quad c_{t4} = 2.0\,(0.5).\end{aligned} \tag{A.6}$$

where c_{t3} and c_{t4} have two different sets with the values in the brackets considered safer at high Reynolds numbers [69]. The wall boundary condition is $\tilde{\nu} = 0$. In the freestream $\tilde{\nu} \leq 0.1\nu$ is acceptable.

The S-A model includes the treatment of transition, however, in this study only fully turbulent flow is considered. So with all the transition terms ignored, the transport equation of the S-A model Eqn. (A.3) can be written as

$$\frac{D\tilde{\nu}}{Dt} = c_{b1}\tilde{\Omega}\tilde{\nu} + \frac{1}{\sigma}\left[\nabla \cdot \left(\left(\nu + \tilde{\nu}\right)\nabla\tilde{\nu}\right) + c_{b2}\left(\nabla\tilde{\nu}\right)^2\right] - c_{w1}f_w\left[\frac{\tilde{\nu}}{d}\right]^2 . \qquad \text{(A.7)}$$

A.1.2 Non-dimensionalisation

The fully turbulent transport equation of the S-A model Eqn. (A.7) is non-dimensionalised using the freestream flow variables.

$$\begin{array}{lll} x^* = \frac{x}{L} & y^* = \frac{y}{L} & z^* = \frac{z}{L} \\ u^* = \frac{u}{U_\infty} & v^* = \frac{v}{U_\infty} & w^* = \frac{w}{U_\infty} \\ \rho^* = \frac{\rho}{\rho_\infty} & \mu^* = \frac{\mu}{\mu_\infty} & \mu_t^* = \frac{\mu_t}{\mu_\infty} \\ p^* = \frac{p}{\rho_\infty U_\infty^2} & T^* = \frac{T}{T_\infty} & E^* = \frac{E}{\rho_\infty U_\infty^2} \\ t^* = \frac{t}{L/U_\infty} & \tilde{\nu}^* = \frac{\tilde{\nu}}{\nu_\infty} & \end{array} \qquad \text{(A.8)}$$

Variables with superscript notation '*' are local dimensionless flow variables, freestream variables are variables with subscript notation '∞', and L is the reference length. The freestream Reynolds number is defined as

$$Re_\infty = \frac{\rho_\infty U_\infty L}{\mu_\infty}. \qquad \text{(A.9)}$$

Now the non-dimensional transport equation of the S-A model is written as

$$\frac{D\tilde{\nu}^*}{Dt^*} = c_{b1}\tilde{\Omega}^*\tilde{\nu}^* + \frac{1}{\sigma Re_\infty}\left[\nabla \cdot \left(\left(\nu^* + \tilde{\nu}^*\right)\nabla\tilde{\nu}^*\right) + c_{b2}\left(\nabla\tilde{\nu}^*\right)^2\right] - \frac{c_{w1}f_w}{Re_\infty}\left[\frac{\tilde{\nu}^*}{d^*}\right]^2 . \qquad \text{(A.10)}$$

For convenience, the superscript '*' will be dropped so that all the variables are assumed to be non-dimensional values, unless stated otherwise. For the same purpose, the freestream Reynolds number based on the reference length L will be written as Re. Finally the transport equation is written in a similar way as the N-S equations.

$$\frac{\partial W}{\partial t} + \frac{\partial(F^i - F^v)}{\partial x} + \frac{\partial(G^i - G^v)}{\partial y} + \frac{\partial(H^i - H^v)}{\partial z} = S, \qquad \text{(A.11)}$$

where $W = \widetilde{\nu}$, inviscid flux, viscous flux and the source terms are defined as the following

$$\begin{cases} F^i = u\widetilde{\nu} \\ G^i = v\widetilde{\nu} \\ H^i = w\widetilde{\nu} \\ F^v = \frac{\nu+\widetilde{\nu}}{\sigma Re}\frac{\partial\widetilde{\nu}}{\partial x} \\ G^v = \frac{\nu+\widetilde{\nu}}{\sigma Re}\frac{\partial\widetilde{\nu}}{\partial y} \\ H^v = \frac{\nu+\widetilde{\nu}}{\sigma Re}\frac{\partial\widetilde{\nu}}{\partial z} \\ S = S_1 + S_2 + S_3 + S_4. \end{cases} \tag{A.12}$$

The source term is divided into the following four parts

$$\begin{cases} S_1 = c_{b1}\widetilde{\Omega}\widetilde{\nu} \\ S_2 = \frac{c_{b2}}{\sigma Re}\left[\left(\frac{\partial\widetilde{\nu}}{\partial x}\right)^2 + \left(\frac{\partial\widetilde{\nu}}{\partial y}\right)^2 + \left(\frac{\partial\widetilde{\nu}}{\partial z}\right)^2\right] \\ S_3 = -\frac{c_{w1}f_w}{Re}\left[\frac{\widetilde{\nu}}{d}\right]^2 \\ S_4 = \widetilde{\nu}\left(\frac{\partial u}{\partial x} + \frac{\partial v}{\partial y} + \frac{\partial w}{\partial z}\right). \end{cases} \tag{A.13}$$

All the auxiliary functions are redefined in non-dimensional form as

$$\chi \equiv \frac{\widetilde{\nu}}{\nu}, \quad f_{v1} = \frac{\chi^3}{\chi^3 + c_{v1}^3}, \quad f_{v2} = 1 - \frac{\chi}{1 + \chi f_{v1}}$$

$$f_w = g\left[\frac{1 + c_{w3}^6}{g^6 + c_{w3}^6}\right]^{1/6}, \quad g = r + c_{w2}\left(r^6 - r\right), \quad r \equiv \frac{\widetilde{\nu}}{\widetilde{S}\kappa^2 d^2} \cdot \frac{1}{Re}$$

$$\widetilde{\Omega} = \Omega + \frac{\widetilde{\nu}}{\kappa^2 d^2} f_{v2} \cdot \frac{1}{Re}, \quad \Omega \equiv \sqrt{2\Omega_{ij}\Omega_{ij}} \tag{A.14}$$

$$\sigma = 2/3, \quad c_{b1} = 0.1355, \quad c_{b2} = 0.622, \quad \kappa = 0.41$$

$$c_{v1} = 7.1, \quad c_{w1} = c_{b1}/\kappa^2 + (1 + c_{b2})/\sigma, \quad c_{w2} = 0.3, \quad c_{w3} = 2.$$

A.1.3 Curvilinear coordinates

The governing equations are usually transformed from the physical domain (x, y, z, t) to computational domain (ξ, η, ζ, τ) with the grid spacing in the computational space is uniform and of unit length. This produces a computational region that is a cuboid and has a regular uniform mesh (Fig. (A.1)).

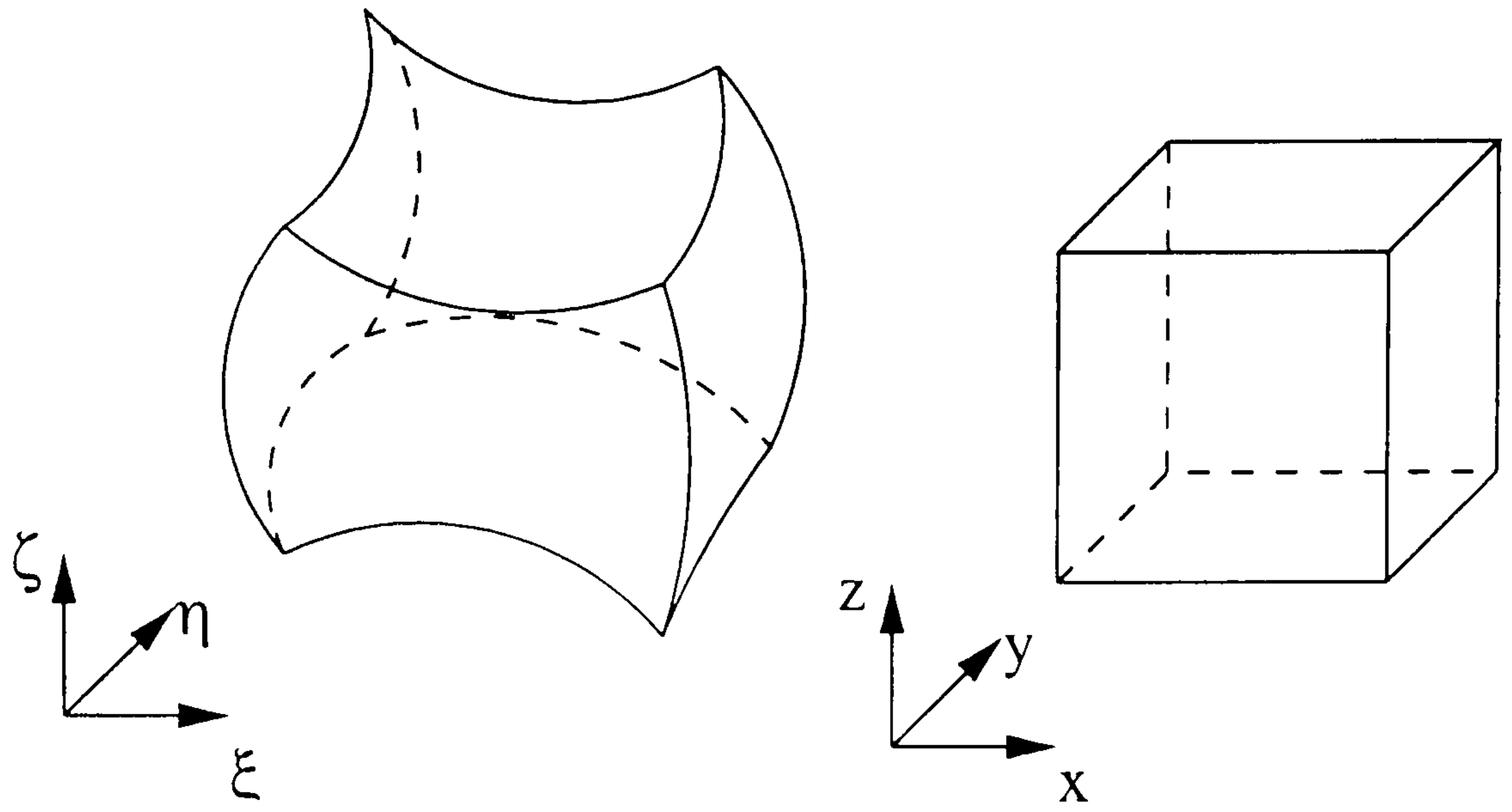

Figure A.1: *Coordinate transformation from physical to computational domain*

The generalised coordinate transformation produces a system of equations that can be applied to any regular and nonsingular geometry or grid system.

$$\begin{cases} \tau = t \\ \xi = \xi(x, y, z, t) \\ \eta = \eta(x, y, z, t) \\ \zeta = \zeta(x, y, z, t) \end{cases} \tag{A.15}$$

The Jacobian matrix is defined as

$$\mathrm{J} = \frac{\partial(\xi, \eta, \zeta, \tau)}{\partial(x, y, z, t)} = \begin{bmatrix} \xi_x & \xi_y & \xi_z & \xi_t \\ \eta_x & \eta_y & \eta_z & \eta_t \\ \zeta_x & \zeta_y & \zeta_z & \zeta_t \\ 0 & 0 & 0 & 1 \end{bmatrix} . \tag{A.16}$$

where

$$\left\{\begin{array}{lll}
\xi_x = J(y_\eta z_\zeta - y_\zeta z_\eta) & \eta_x = J(z_\xi y_\zeta - y_\xi z_\zeta) & \zeta_x = J(y_\xi z_\eta - z_\xi y_\eta) \\
\xi_y = J(z_\eta x_\zeta - x_\eta z_\zeta) & \eta_y = J(x_\xi z_\zeta - x_\zeta z_\xi) & \zeta_y = J(x_\eta z_\xi - x_\xi z_\eta) \\
\xi_z = J(x_\eta y_\zeta - y_\eta x_\zeta) & \eta_z = J(y_\xi x_\zeta - x_\xi y_\zeta) & \zeta_z = J(x_\xi y_\eta - y_\xi x_\eta) \\
\xi_t = -x_\tau \xi_x - y_\tau \xi_y - z_\tau \xi_z & \eta_t = -x_\tau \eta_x - y_\tau \eta_y - z_\tau \eta_z & \zeta_t = -x_\tau \zeta_x - y_\tau \zeta_y - z_\tau \zeta_z
\end{array}\right. \tag{A.17}$$

J is the determinant of the Jacobian matrix and can be calculated by

$$J = (x_\xi y_\eta z_\zeta + x_\zeta y_\xi z_\eta + x_\eta y_\zeta z_\xi - x_\xi y_\zeta z_\eta - x_\eta y_\xi z_\zeta - x_\zeta y_\eta z_\xi)^{-1}. \tag{A.18}$$

All the elements (metrics, e.g., ξ_x, ξ_y, ξ_z) can be obtained from the inverse metrics (e.g., x_ξ, y_ξ, z_ξ). Simple finite difference approximations can be used to calculate these inverse metrics since the grid points are equally spaced in computational space, that is, $\Delta\xi = \Delta\eta = \Delta\zeta = 1$.

The chain rule of partial differentiation is introduced in calculating all the derivatives, for example, the velocity gradient $\frac{\partial u}{\partial x}$ is calculated as

$$\frac{\partial u}{\partial x} = \xi_x \frac{\partial u}{\partial \xi} + \eta_x \frac{\partial u}{\partial \eta} + \zeta_x \frac{\partial u}{\partial \zeta}. \tag{A.19}$$

Now if we apply the generalised transformation to the transport equation of the S-A turbulence model, Eqn. (A.11), the following equation will be achieved

$$\frac{\partial \widehat{W}}{\partial \tau} + \frac{\partial(\widehat{F}^i - \widehat{F}^v)}{\partial \xi} + \frac{\partial(\widehat{G}^i - \widehat{G}^v)}{\partial \eta} + \frac{\partial(\widehat{H}^i - \widehat{H}^v)}{\partial \zeta} = \widehat{S}. \tag{A.20}$$

The variables in the above equation are defined as the following

$$\begin{cases} \widehat{W} = W/J \\ \widehat{F}^i = \xi_t \widehat{W} + (\xi_x F^i + \xi_y G^i + \xi_z H^i)/J \\ \widehat{G}^i = \eta_t \widehat{W} + (\eta_x F^i + \eta_y G^i + \eta_z H^i)/J \\ \widehat{H}^i = \zeta_t \widehat{W} + (\zeta_x F^i + \zeta_y G^i + \zeta_z H^i)/J \\ \widehat{F}^v = (\xi_x F^v + \xi_y G^v + \xi_z H^v)/J \\ \widehat{G}^v = (\eta_x F^v + \eta_y G^v + \eta_z H^v)/J \\ \widehat{H}^v = (\zeta_x F^v + \zeta_y G^v + \zeta_z H^v)/J \\ \widehat{S} = S/J \end{cases} \tag{A.21}$$

Again derivative terms of the velocity and the working viscosity $\widetilde{\nu}$ should be evaluated in computational space (ξ, η, ζ, τ) via the chain rule, as mentioned above.

A.1.4 Finite volume method

The finite volume method uses the integral form of the conservation equation as the starting point

$$\frac{\partial}{\partial t}\int_V \mathbf{W}\, dV + \int_S (\mathrm{M} \cdot \mathrm{n})\, dS = \int_V \mathrm{S}_\phi\, dV, \tag{A.22}$$

$$\mathrm{M} = (F^i - F^v)\mathrm{i} + (G^i - G^v)\mathrm{j} + (H^i - H^v)\mathrm{k}. \tag{A.23}$$

The above integral conservation equation applies to each control volume, as well as to the solution domain as a whole. To obtain an algebraic equation for each control volume, the surface and volume integrals need to be approximated using quadrature formulae.

The usual approach is to define the control volumes by a suitable grid and assign the computational node to the control volume centre. However, it is possible to define the nodal locations first and then construct control volumes around them. Fig. A.2(a) and Fig. A.2(b) illustrate these two different finite volume grids. The former one is

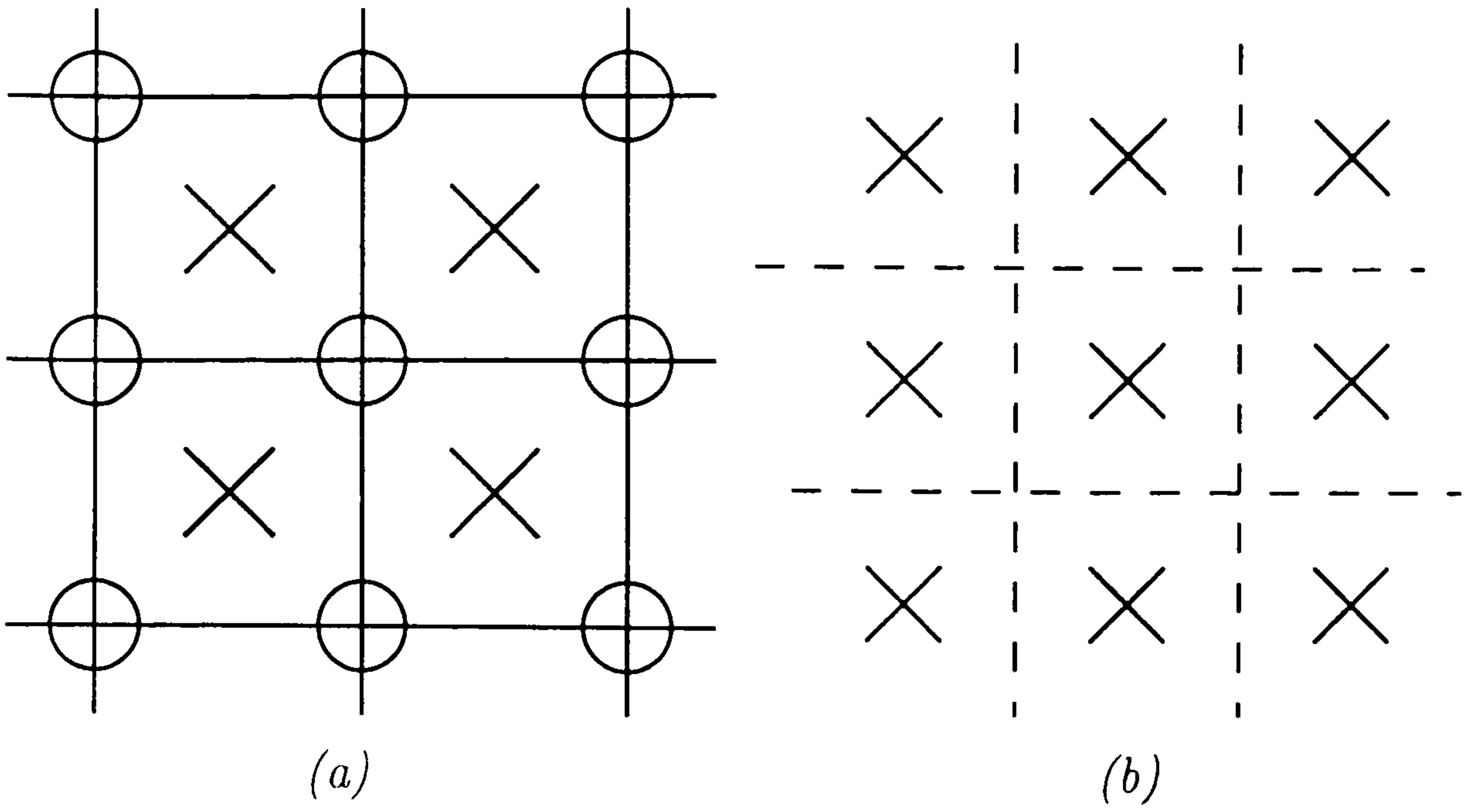

(a) (b)

Figure A.2: *Two types of finite volume grids: (a) nodes centered in CVs (b) CV faces centred between nodes*

used in this study.

A.1.5 Spatial discretisation

The application of the finite volume method leads to the need to calculate the fluxes on the surface of two neighbouring control volumes, e.g., $\widehat{F}^i_{i\pm1/2,j,k}$, $\widehat{F}^v_{i\pm1/2,j,k}$. The inviscid flux terms in this study are discretised by the Engquist-Osher method [82]. The MUSCL interpolation [83] is used to provide the third-order accuracy together with van Albada's limiter [84]. The discretisation of the viscous flux terms is realised by central difference. The source term is evaluated at the cell centre.

Inviscid flux terms

The Engquist-Osher method is used to discretise the inviscid flux terms: $\widehat{F}^i_{i\pm1/2,j,k}$, $\widehat{G}^i_{i,j\pm1/2,k}$ and $\widehat{H}^i_{i,j,k\pm1/2}$. To describe the method, the flux term $\widehat{F}^i_{i+1/2,j,k}$ can be written as

$$\widehat{F}^i_{i+1/2,j,k} = \frac{1}{2}\left(\widehat{F}^i_{i,j,k} + \widehat{F}^i_{i+1,j,k}\right) + \frac{1}{2}\int_{\widehat{W}^-_{i+1/2,j,k}}^{\widehat{W}^+_{i+1/2,j,k}} \left|A(\widehat{W})\right| d\widehat{W}, \qquad (A.24)$$

where $A(\widehat{W})$ is the derivative of $\widehat{F}\left(\widehat{W}\right)$ with respect to $\widehat{W}$. Values for $\widehat{W}^{\pm}_{i+1/2,j,k}$ can be obtained from the MUSCL interpolation with von Albada's limiter in order to improve the accuracy of the results.

$$\left\{\begin{array}{l} \widehat{W}^{-}_{i+1/2,j,k} = \widehat{W}_{i,j,k} + \left[\frac{\left(\Delta_{+}^{2}+\epsilon^{2}\right)\Delta_{-}+\left(\Delta_{-}^{2}+\epsilon^{2}\right)\Delta_{+}}{\Delta_{-}^{2}+\Delta_{+}^{2}+2\epsilon^{2}}\right]_{i,j,k} \\ \widehat{W}^{+}_{i+1/2,j,k} = \widehat{W}_{i+1,j,k} - \left[\frac{\left(\Delta_{+}^{2}+\epsilon^{2}\right)\Delta_{-}+\left(\Delta_{-}^{2}+\epsilon^{2}\right)\Delta_{+}}{\Delta_{-}^{2}+\Delta_{+}^{2}+2\epsilon^{2}}\right]_{i+1,j,k} \end{array}\right. \tag{A.25}$$

where

$$\left\{\begin{array}{l} (\Delta_{-})_{i,j,k} \equiv \widehat{W}_{i,j,k} - \widehat{W}_{i-1,j,k} \\ (\Delta_{+})_{i,j,k} \equiv \widehat{W}_{i+1,j,k} - \widehat{W}_{i,j,k} \end{array}\right. \tag{A.26}$$

and ϵ^2 is a small non-zero constant which can prevent the undesirable clipping of a smooth extremum but otherwise has negligible influence. The value used by van Albada [84] is 0.008. It was found that the results are not very sensitive to the precise value of ϵ^2.

According to Eqn. (A.25), the inviscid flux residual for control volume (i, j, k) is a function of 13 points

$$\begin{aligned} R^{i}_{i,j,k} = \; & R\left(\widehat{W}_{i-2,j,k}, \widehat{W}_{i-1,j,k}, \widehat{W}_{i,j,k}, \widehat{W}_{i+1,j,k}, \widehat{W}_{i+2,j,k}, \widehat{W}_{i,j-2,k},\right. \\ & \left.\widehat{W}_{i,j-1,k}, \widehat{W}_{i,j+1,k}, \widehat{W}_{i,j+2,k}, \widehat{W}_{i,j,k-2}, \widehat{W}_{i,j,k-1}, \widehat{W}_{i,j,k+1}, \widehat{W}_{i,j,k+2}\right). \end{aligned} \tag{A.27}$$

Viscous flux terms

Central differencing is used to discretise the viscous flux terms: $\widehat{F}^{v}_{i\pm1/2,j,k}$, $\widehat{G}^{v}_{i,j\pm1/2,k}$ and $\widehat{H}^{v}_{i,j,k\pm1/2}$. The value of the velocity components and their derivatives, as well as the value and derivative of the working eddy viscosity $\widetilde{\nu}$ are required at the faces of each control volume. Control volume face values are approximated by the average of the two adjacent control volume face values,

$$\widetilde{\nu}_{i+1/2,j,k} = \frac{1}{2}\left(\widetilde{\nu}_{i,j,k} + \widetilde{\nu}_{i+1,j,k}\right). \tag{A.28}$$

Control volume face values of the derivatives are obtained using Green's formula applied to a one-sided auxiliary control volume surrounding the considered face, for example

$$\frac{\partial \widetilde{\nu}}{\partial x} = \frac{1}{V_{aux}} \iint_{S_{aux}} \widetilde{\nu}\, dydz, \tag{A.29}$$

where V_{aux} is the volume of the auxiliary control volume and S_{aux} includes all the six surfaces surrounding the auxiliary control volume. Suppose the centre of the auxiliary control volume is called p, so the following six values are needed

$$\begin{cases} \widetilde{\nu}_b = (\widetilde{\nu}_{i,j,k-1} + \widetilde{\nu}_{i+1,j,k-1} + \widetilde{\nu}_{i+1,j,k} + \widetilde{\nu}_{i,j,k})/4 \\ \widetilde{\nu}_w = \widetilde{\nu}_{i,j,k} \\ \widetilde{\nu}_s = (\widetilde{\nu}_{i,j-1,k} + \widetilde{\nu}_{i+1,j-1,k} + \widetilde{\nu}_{i+1,j,k} + \widetilde{\nu}_{i,j,k})/4 \\ \widetilde{\nu}_n = (\widetilde{\nu}_{i,j,k} + \widetilde{\nu}_{i+1,j,k} + \widetilde{\nu}_{i+1,j+1,k} + \widetilde{\nu}_{i,j+1,k})/4 \\ \widetilde{\nu}_e = \widetilde{\nu}_{i+1,j,k} \\ \widetilde{\nu}_t = (\widetilde{\nu}_{i,j,k} + \widetilde{\nu}_{i+1,j,k} + \widetilde{\nu}_{i+1,j,k+1} + \widetilde{\nu}_{i,j,k+1})/4. \end{cases} \tag{A.30}$$

This means that the viscous flux terms are related to 19 points. For both the inviscid and viscous flux terms, the residual is now a function of 25 different points.

Source term

The source term is evaluated at the control volume centre, using the approach described in Eqn. (A.29).

After the spatial discretisation, the following semi-discrete form of the S-A model is achieved

$$\frac{d\widehat{\mathbf{W}}_{i,j,k}}{d\tau} = -\frac{1}{V_{i,j,k}}\mathbf{R}_{i,j,k} \tag{A.31}$$

where $\mathbf{R}_{i,j,k}$ denotes the discretisation of the spatial and source terms. Considering the whole computational domain, this equation is rewritten in the following form for clarity

$$\frac{d\mathbf{Q}}{dt} = -\frac{1}{V}\mathbf{R}. \tag{A.32}$$

A.1.6 Boundary conditions

The boundary conditions are set by using two rows of halo control volumes. Values are set in the halo according to interior values and boundary values. Once halo values are set then all interior control volumes are treated in an identical fashion. The extrapolations used are shown in Table (A.1). The subscripts 1, 2, b1 and b2 denote values in the interior control volume adjacent to the boundary, the next interior control volume, the first halo control volume and the second halo control volume, respectively.

Boundary type	First halo control volume	Second halo control volume
Solid wall	$\tilde{\nu}_{b1} = -\tilde{\nu}_2$	$\tilde{\nu}_{b2} = -\tilde{\nu}_1$
Far field	$\tilde{\nu}_{b1} = \tilde{\nu}_\infty$	$\tilde{\nu}_{b2} = \tilde{\nu}_\infty$
y-symmetry	$\tilde{\nu}_{b1} = \tilde{\nu}_2$	$\tilde{\nu}_{b2} = \tilde{\nu}_1$
z-symmetry	$\tilde{\nu}_{b1} = \tilde{\nu}_2$	$\tilde{\nu}_{b2} = \tilde{\nu}_1$
Linear extrapolation	$\tilde{\nu}_{b1} = 2\tilde{\nu}_{b2} - \tilde{\nu}_1$	$\tilde{\nu}_{b2} = 2\tilde{\nu}_1 - \tilde{\nu}_2$
Poiseille	$\tilde{\nu}_{b1} = 0$	$\tilde{\nu}_{b2} = 0$
Mirror	$\tilde{\nu}_{b1} = \tilde{\nu}_1$	$\tilde{\nu}_{b2} = \tilde{\nu}_1$
Given profile	$\tilde{\nu}_{b1} = \tilde{\nu}_{pro}$	$\tilde{\nu}_{b2} = \tilde{\nu}_{pro}$
Degenerated x-y	$\tilde{\nu}_{b1} = \tilde{\nu}_2$	$\tilde{\nu}_{b2} = \tilde{\nu}_1$
Degenerated x	$\tilde{\nu}_{b1} = \tilde{\nu}_2$	$\tilde{\nu}_{b2} = \tilde{\nu}_1$
Degenerated interior	$\tilde{\nu}_{b1} = \tilde{\nu}_2$	$\tilde{\nu}_{b2} = \tilde{\nu}_2$

Table A.1: Boundary conditions for the S-A turbulence model

$\tilde{\nu}_\infty$ is freestream value and is set to $0.1\nu_\infty$ by default as suggest by Spalart [68]. This value is also used to initialised the flow field. For a given profile bounday, $\tilde{\nu}_{pro}$ is the value given directly which is set from an input parameter file.

A.1.7 Time discretisation

Steady-state solver

The integration in time of Eqn. (A.32) to a steady-state solution is performed in two phases. First, an explicit scheme is used to smooth out the freestream starting solution.

$$\Delta \mathbf{Q} = -\frac{1}{V}\Delta t\,\mathbf{R}^n, \tag{A.33}$$

where $\Delta \mathbf{Q} = \mathbf{Q}^{n+1} - \mathbf{Q}^n$, n is the current time level, $n+1$ is the new time level.

In order to speed up the calculation, an implicit time-marching scheme is applied

$$\frac{V}{\Delta t}\Delta \mathbf{Q} = -\mathbf{R}^{n+1}. \tag{A.34}$$

This equation represents a system of non-linear algebraic equations. In order to simplify the solution procedure, the flux residual $\mathbf{R}^{n+1}$ is linearised in time as follows

$$\begin{aligned} \mathbf{R}^{n+1} &= \mathbf{R}^n + \tfrac{\partial \mathbf{R}}{\partial t}\Delta t + O(\Delta t^2) \\ &\approx \mathbf{R}^n + \tfrac{\partial \mathbf{R}}{\partial \mathbf{Q}}\tfrac{\partial \mathbf{Q}}{\partial t}\Delta t \\ &\approx \mathbf{R}^n + \tfrac{\partial \mathbf{R}}{\partial \mathbf{Q}}\Delta \mathbf{Q}. \end{aligned} \tag{A.35}$$

Now the following linear system is obtained after applying the above approximation

$$\left(\frac{V}{\Delta t}\mathbf{I} + \frac{\partial \mathbf{R}}{\partial \mathbf{Q}}\right)\Delta \mathbf{Q} = -\mathbf{R}^n. \tag{A.36}$$

As mentioned above, the residual of each control volume is related to 25 points. This leads to a Jacobian matrix $\partial \mathbf{R}/\partial \mathbf{Q}$ which has twenty five non-zero blocks per row. An approximate Jacobian is introduced in order to reduce the memory requirement and CPU time consumption. Only seven non-zero elements are considered so that when calculating the Jacobian the residual is only considered to be a function of these seven points

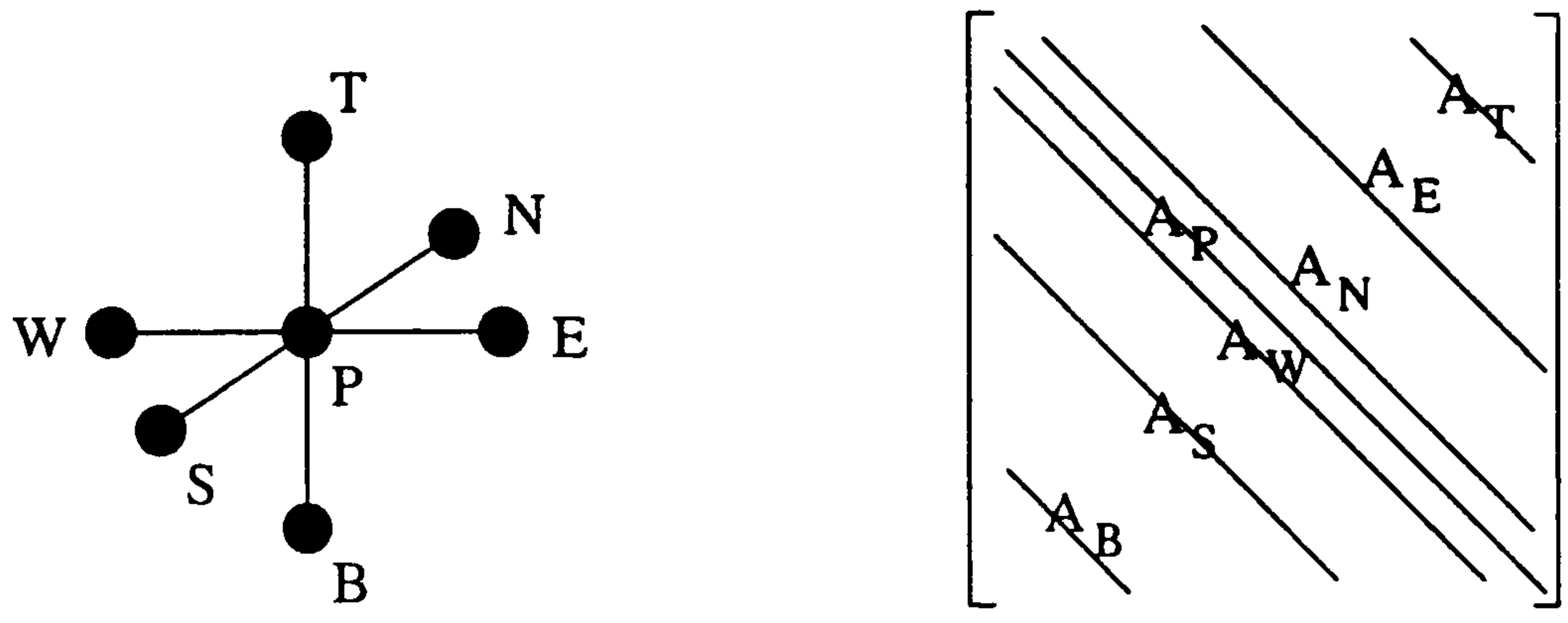

Figure A.3: *Approximate Jacobian matrix*

$$R_{i,j,k} = R\left(Q_{i-1,j,k}, Q_{i,j,k}, Q_{i+1,j,k}, Q_{i,j-1,k}, Q_{i,j+1,k}, Q_{i,j,k-1}, Q_{i,j,k+1}\right). \tag{A.37}$$

This approximation, as shown in Fig. (A.3), which is applied only for the derivation of the Jacobian terms, is also easier for the linear solver because the resulting matrix becomes more diagonally dominant than using the exact Jacobians. As a result, 72% of the memory requirement and matrix-vector multiplication operation are reduced. The method has been successfully applied in the two-dimensional solver PMB2D [61] and the mean flow solver of the PMB3D code.

Unsteady flow solver

The N-S equations and the S-A transport equation for unsteady flow are solved by introducing an iteration through pseudo time τ to the steady state [62], as given by

$$\frac{\mathbf{w}^{n+1,m+1} - \mathbf{w}^{n+1,m}}{\Delta\tau} + \frac{3\mathbf{w}^{k_m} - 4\mathbf{w}^{n} + \mathbf{w}^{n-1}}{2\Delta t} + \mathbf{R}\left(\tilde{\mathbf{w}}^{k_m}, \tilde{\mathbf{q}}^{k_t}\right) = 0 \tag{A.38}$$

$$\frac{\mathbf{q}^{n+1,m+1} - \mathbf{q}^{n+1,m}}{\Delta\tau} + \frac{3\mathbf{q}^{l_t} - 4\mathbf{q}^{n} + \mathbf{q}^{n-1}}{2\Delta t} + \mathbf{S}\left(\tilde{\mathbf{w}}^{l_m}, \tilde{\mathbf{q}}^{l_t}\right) = 0, \tag{A.39}$$

where the *m-th* pseudo time iterate at the $(n+1)th$ real time step are denoted by $\mathbf{w}^{n+1,m}$ and $\mathbf{q}^{n+1,m}$ respectively. Here k_m, k_t, k_m and l_t give the time level of the variables used in the spatial discretisation. The iteration scheme used only effects the efficiency of the method and hence we can sequence the solution in pseudo time without compromising accuracy. For example, using explicit time stepping we can calculate $\mathbf{w}^{n+1,m+1}$ using $k_m = n+1, m$ and $k_t = n+1, m$ and $\mathrm{q}^{n+1,m+1}$ using $l_m = n+1, m+1$ and $l_t = n+1, m$. For implicit time stepping in pseudo time $k_m = l_m = l_t = n+1, m+1$ and $k_t = n+1, m$ can be used. In both of these cases the solution of the equations is decoupled by freezing values but at convergence the real time stepping proceeds with no sequencing error. It is easy to recover a solution which is sequenced in real time from this formulation by setting $k_t = n, m$ throughout the calculation of the pseudo steady state. This facilitates a comparison of the current pseudo time sequencing with the more common real time sequencing.

A.1.8 Linear solver

For the implicit scheme, the result of the discretisation process is a system of algebraic equations, Eqn. (A.36) is written here again.

$$\left(\frac{V}{\Delta t}\mathrm{I} + \frac{\partial \mathrm{R}}{\partial \mathrm{Q}}\right)\Delta \mathrm{Q} = -\mathrm{R}^n. \tag{A.40}$$

For unsteady problems, the equation should be changed because of the additional term in Eqn. (A.39).

The generalised conjugate gradient (GCG) method [85] with the block incomplete LU (BILU) decomposition [86] are chosen to be used to solve this system.

A.2 Validation of the S-A turbulence model

A.2.1 RAE2822 aerofoil Cases 9 and 10

The transonic flow over an aerofoil provides a good test of the turbulence model to predict the boundary layer development along a curved surface. Two cases of RAE2822, Case 9 (no/small separation region) and Case 10 (shock induced separation) with different flow conditions were tested. Flow conditions for these two cases are listed in Table A.2. For both cases, the same C-type grid was generated with 257 points in the streamwise direction, 65 points in the direction normal to the wall and 5 points in the spanwise direction. Since the transitional terms of the S-A turbulence model was ignored in the implementation, flow around this aerofoil was considered fully turbulent.

RAE2822	M_∞	Re	Angle of attack	Transition at x/c
Case 9	0.73	6.5×10^6	2.79°	0.03
Case 10	0.75	6.2×10^6	2.81°	0.03

Table A.2: Flow conditions selected for the RAE2822 Cases 9 and 10

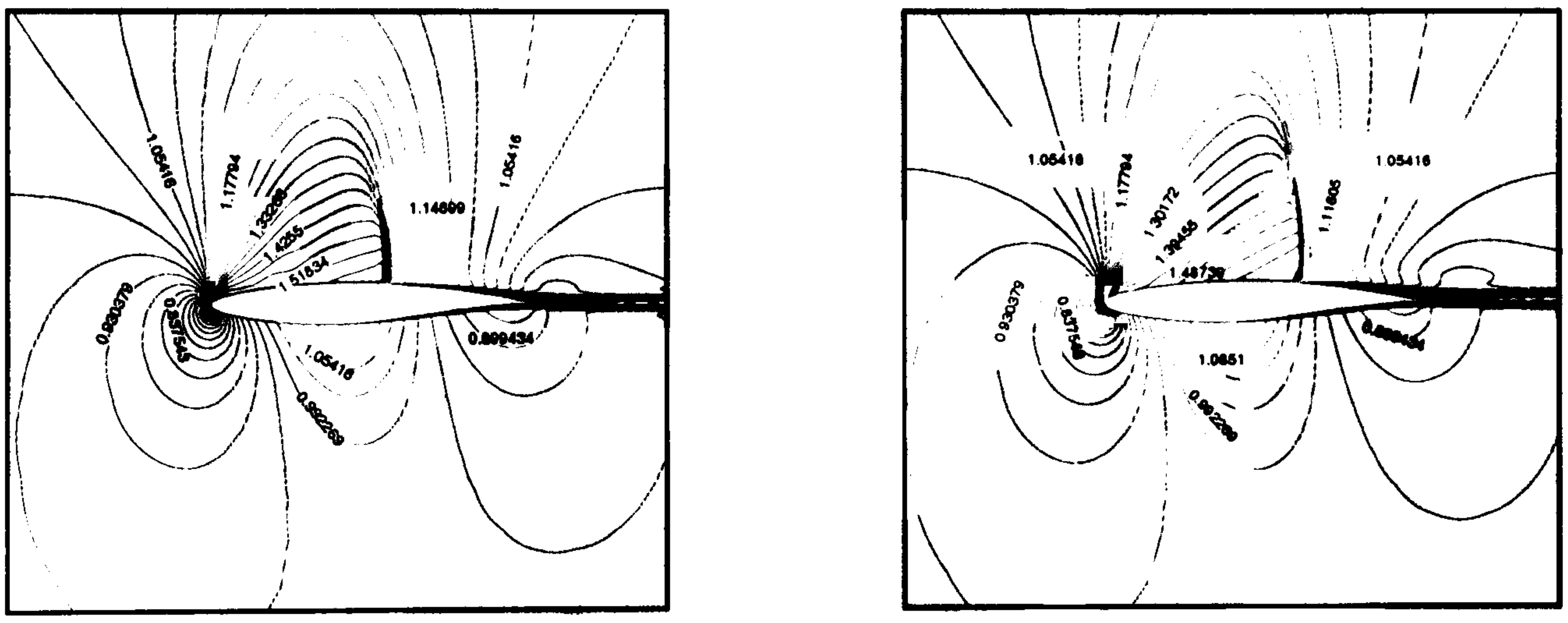

(a) RAE2822 Case 9 *(b) RAE2822 Case 10*

Figure A.4: *Mach number contours around the RAE2822 aerofoil*

Mach contours, pressure and skin friction coefficient distributions for both cases compared with the $k - \omega$ turbulence model and the experimental data are presented in Figs. A.4, A.5 and A.6. Shock was captured in both cases. For Case 9, the location of the shock captured is upstream from the experimental location. For Case 10, the the shock captured is downstream from the experimental data. The $k - \omega$ model gives the shock location downstream of the experimental data in both cases. The angle of attack has a strong influence on the shock location. Since the correct angle of attack is uncertain, the shock location is not a reliable indicator of the turbulence model accuracy in these two cases.

In Fig. A.5, pressure coefficient distributions on lower wall surface are quite good in both cases for both turbulence models. But on the upper wall surface, shock position is not well predicted as mentioned above. Shock induced separation can be observed in Case 10 (Fig. A.6).

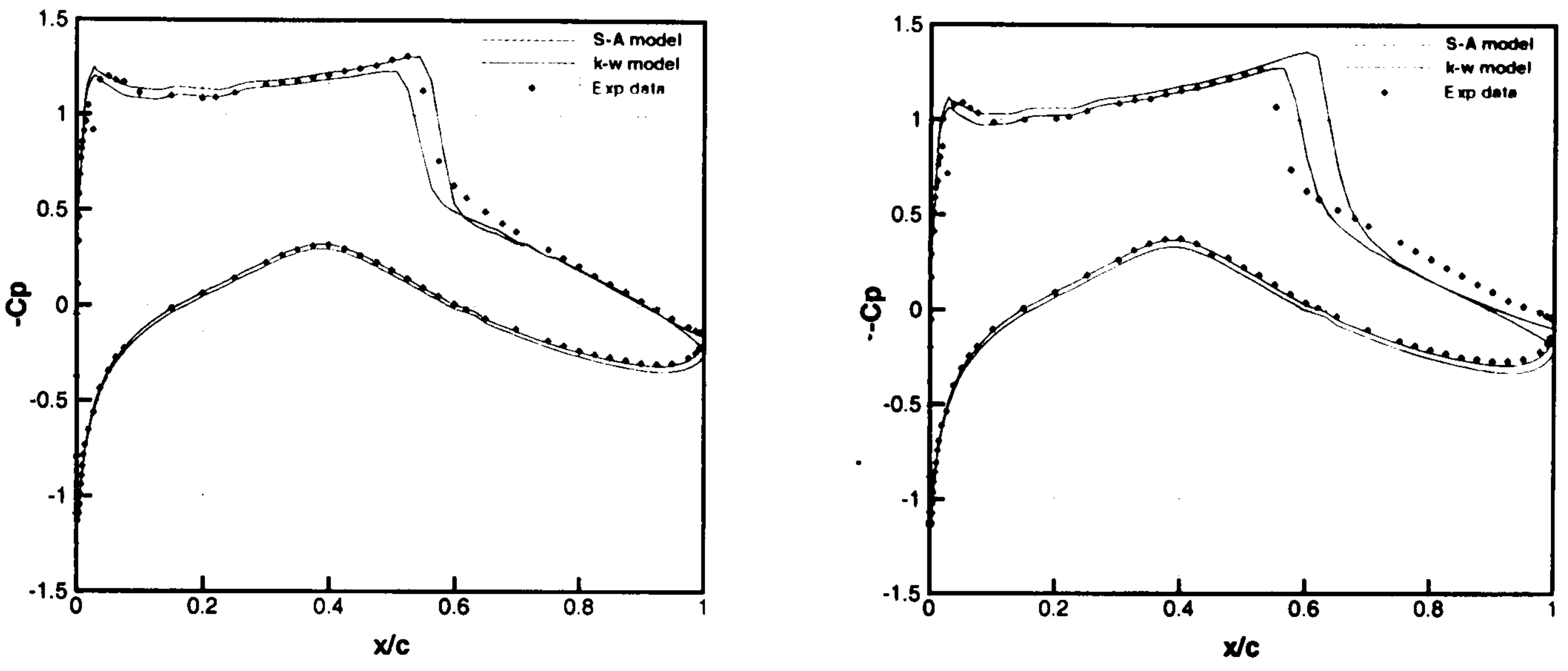

(a) *RAE2822 Case 9* (b) *RAE2822 Case 10*

Figure A.5: *Pressure coefficient distributions for the RAE2822 aerofoil*

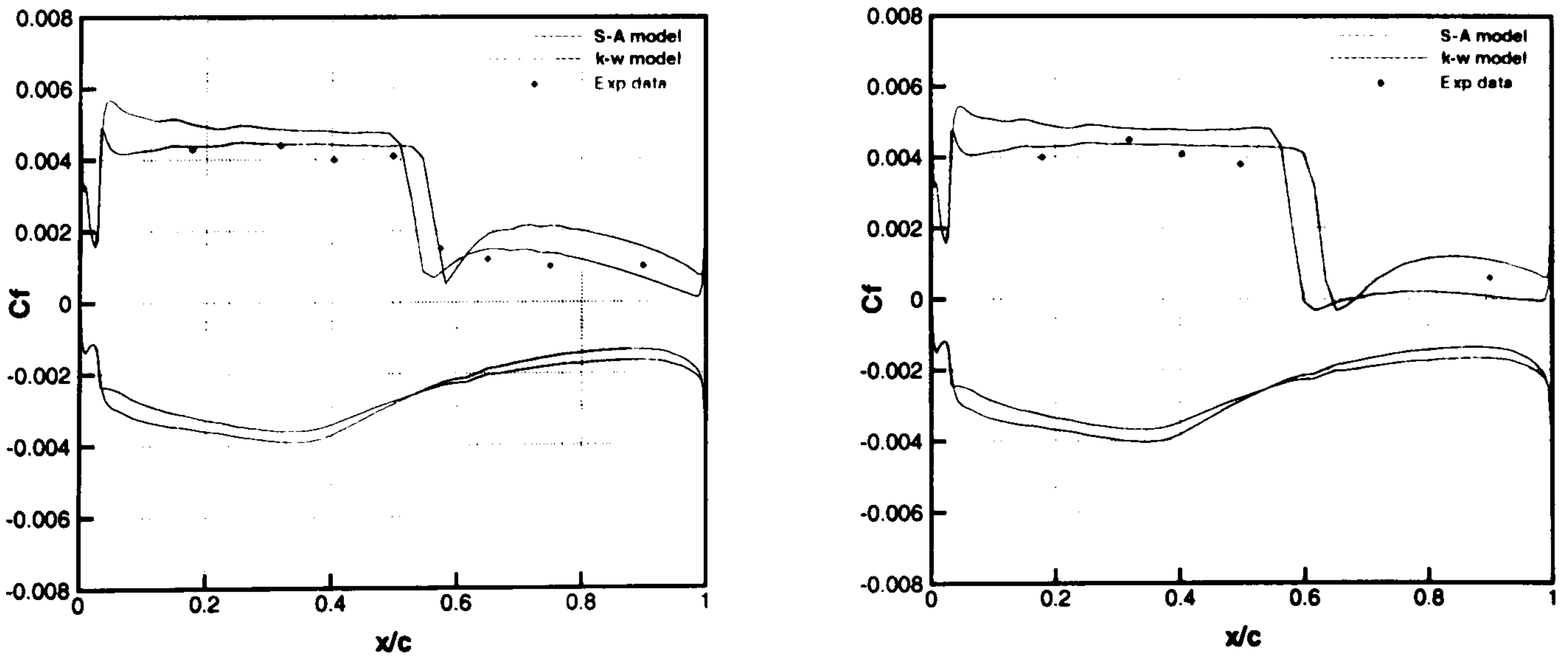

(a) *RAE2822 Case 9* (b) *RAE2822 Case 10*

Figure A.6: *Skin friction coefficient distributions for the RAE2822 aerofoil*

A.2.2 NLR-F5 wing

A second test was made to investigate the flow around a NLR-F5 wing. The flow conditions are as follows: the freestream Mach number is 0.896, the attack angle is 0.497° and the Reynolds number is 5.79×10^6. A C-O type grid which containing $65 \times 33 \times 33$ points was used in this calculation.

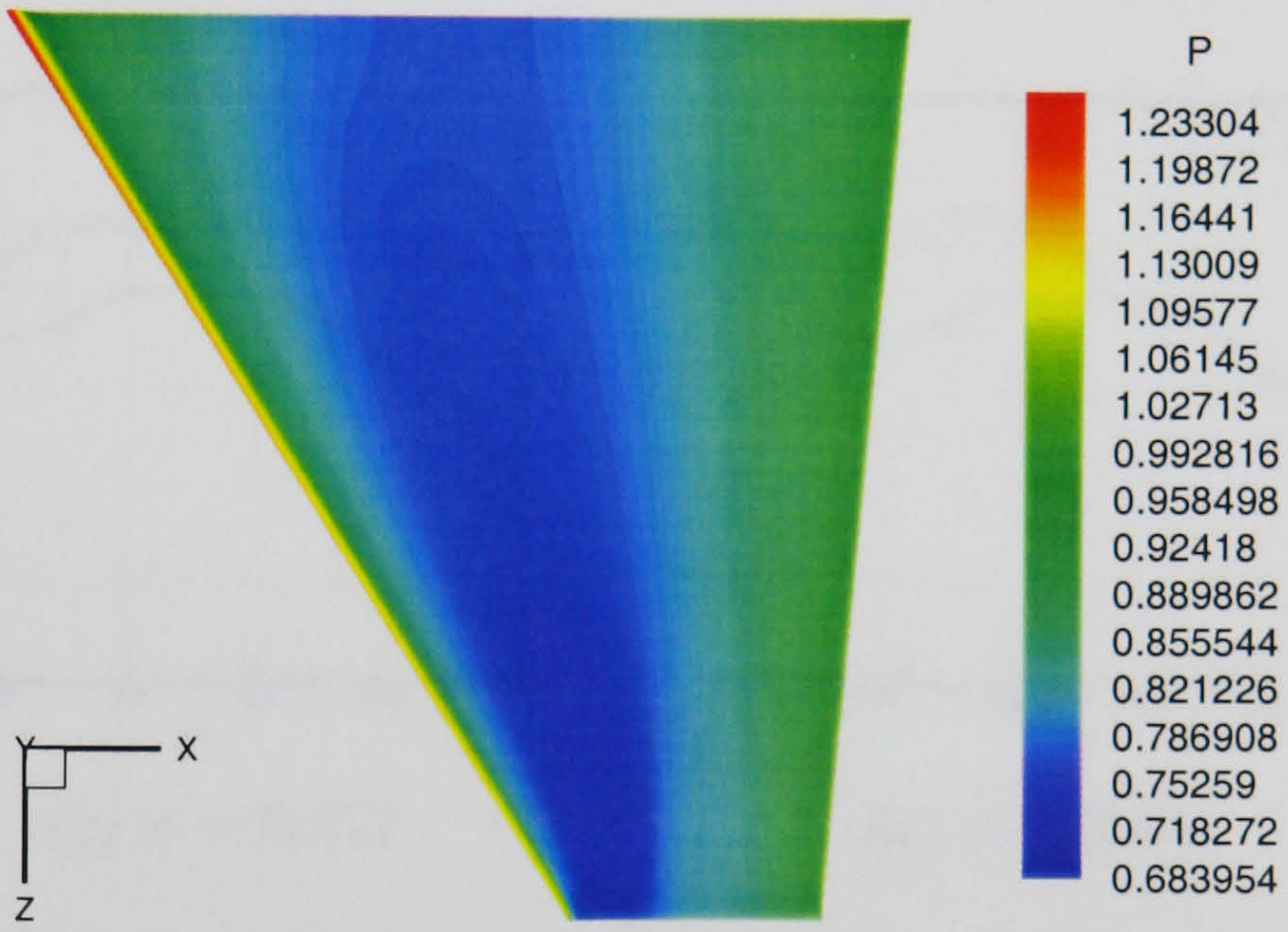

Figure A.7: *Pressure contours for NLR-F5 wing*

Pressure contour is shown in Fig. A.7 with the shock near the leading edge clearly seen. In Fig. A.8, the pressure coefficient distributions are compared with the $k-\omega$ model and the experimental data. η means the position along spanwise direction. In the region near the lower surface leading-edge, the S-A model predicts the suction peak very well. In the area near the tip (Fig. A.8 (g) $\eta = 0.875$ and (h) $\eta = 0.977$) the S-A model does not capture the shock wave on the upper wall surface, while the $k-\omega$ model predicts the shock sharply.

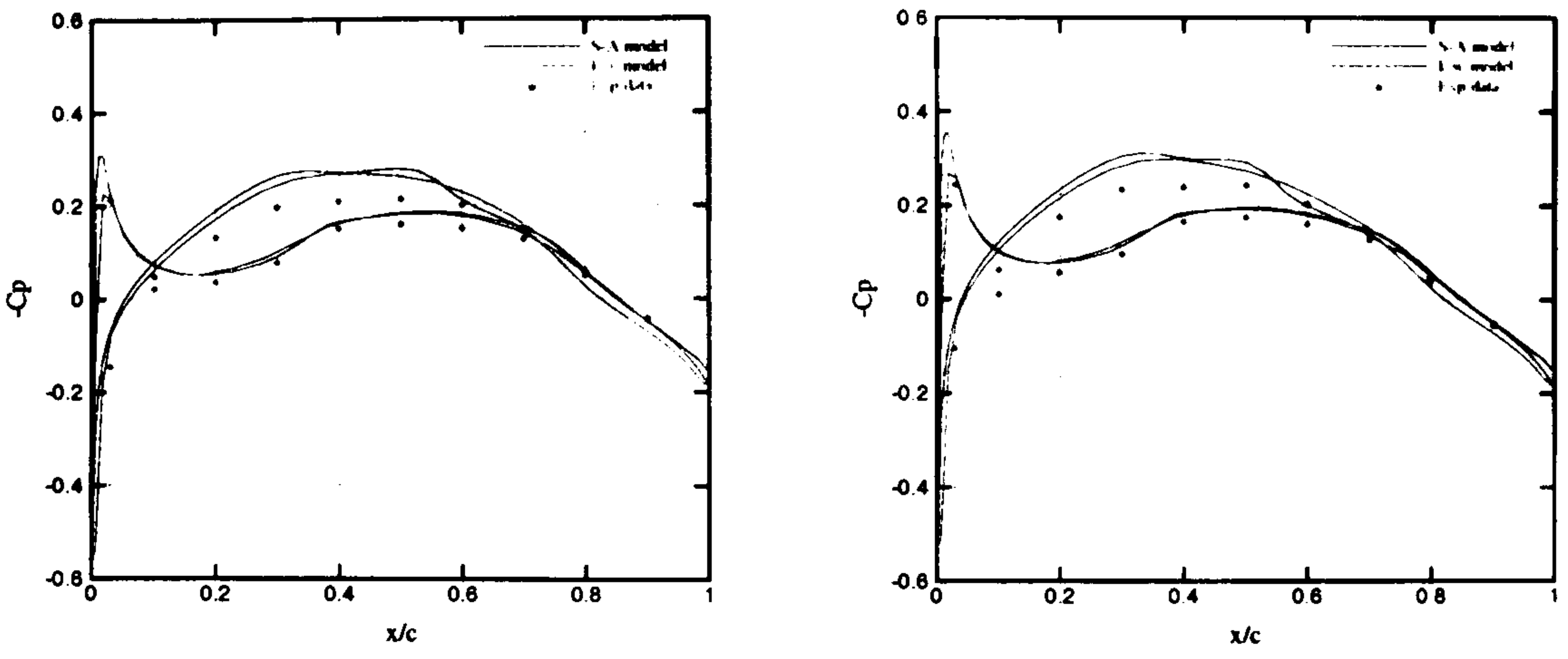

(a) $\eta = 0.181$ (b) $\eta = 0.352$

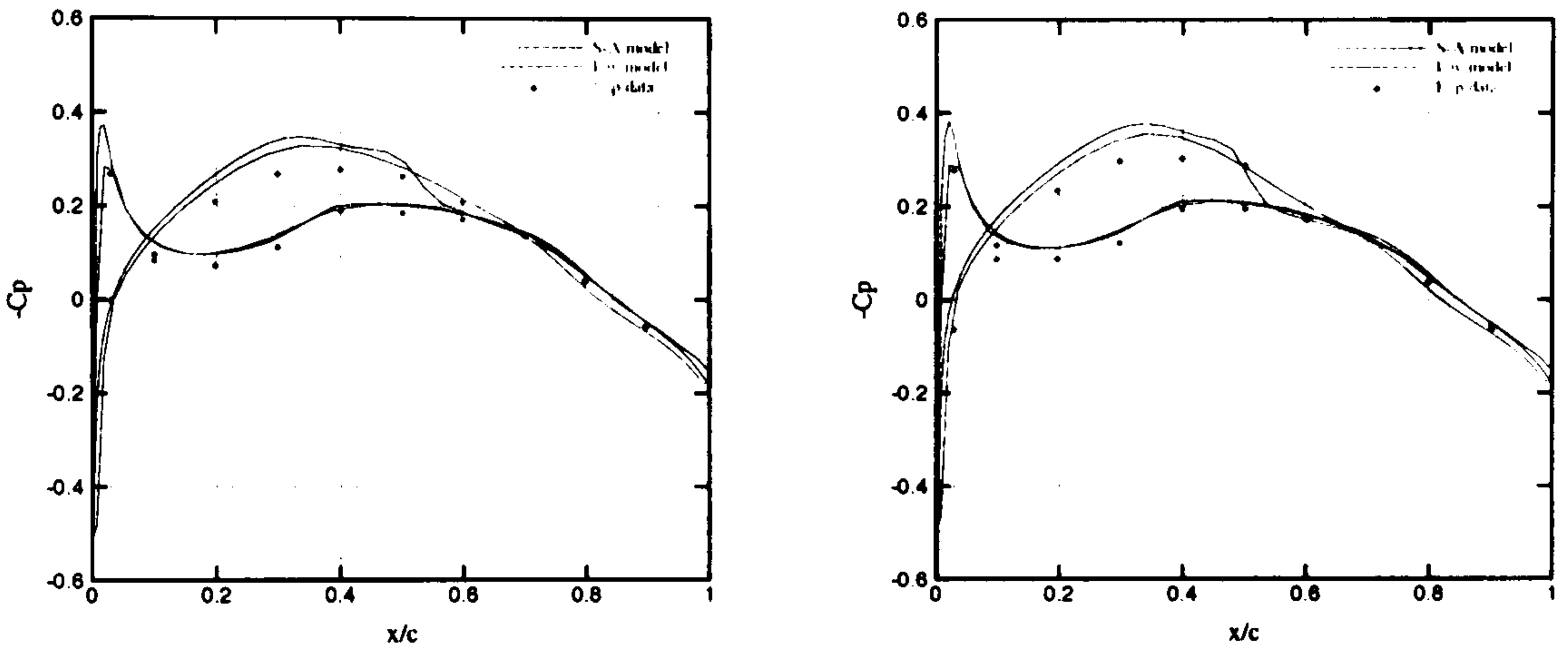

(c) $\eta = 0.512$ (d) $\eta = 0.641$

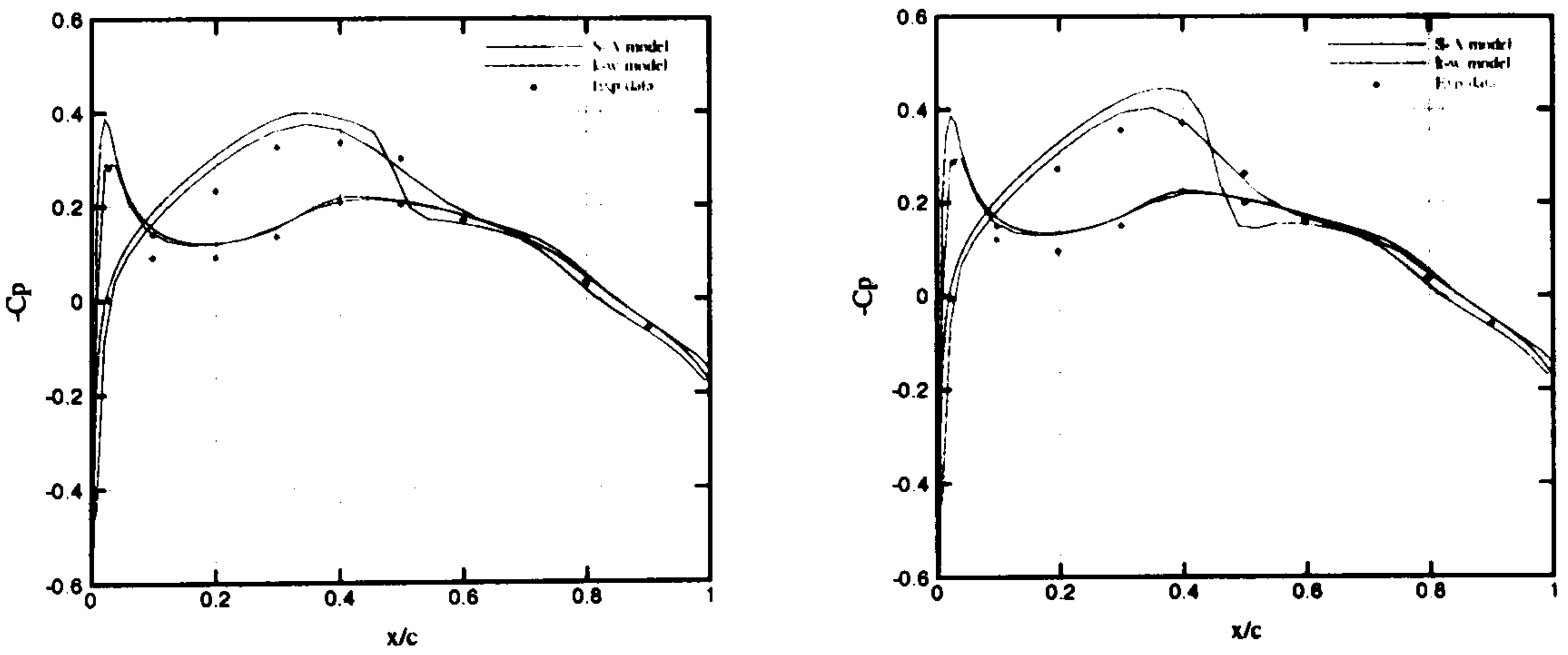

(e) $\eta = 0.721$ (f) $\eta = 0.817$

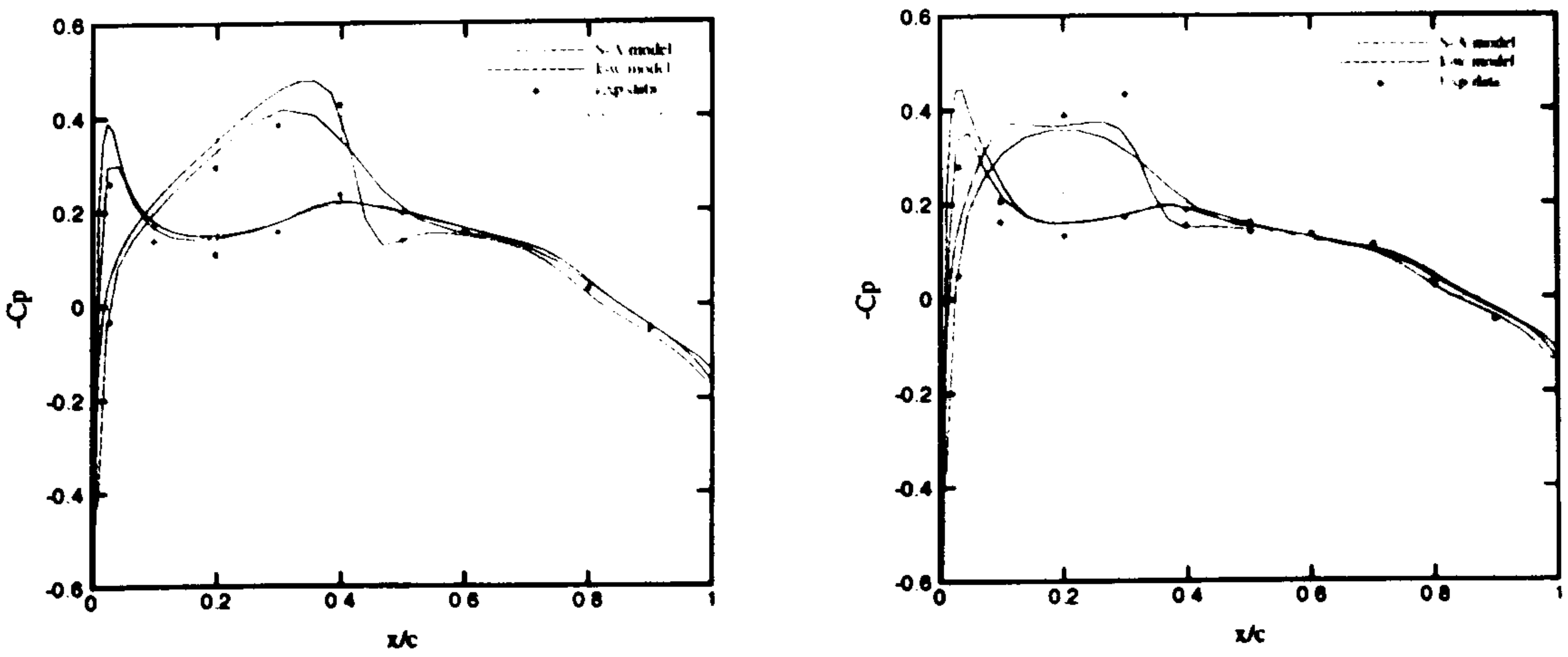

(g) $\eta = 0.875$ (h) $\eta = 0.977$

Figure A.8: *Pressure coefficient distribution for NLR-F5 Wing*

A.3 Conclusions

The implementation of the Spalart-Allmaras turbulence model in the PMB3D code gives some reasonable results in the validation phase. For all the test cases including RAE2822 aerofoil Cases 9 and 10 and NLR-F5 wing, the S-A model captured the main flow phenomena. It seems that this model is promising especially for flows without considerable separation.

References

[1] R.J. Goldstein, E.R.G. Eckert, F.K. Tsou, and A. Haji-Sheikh. Film cooling with air and helium injection through a rearward-facing slot into a supersonic air flow. *AIAA Journal*, 4(6):981–985, 1966.

[2] G.C. Olsen, R.J. Nowak, M.S. Holden, and N.R. Baker. Experimental results for film cooling in 2-d supersonic flow including coolant delivery pressure, geometry, and incident shock effects. *AIAA Paper 90-0605*, 1990.

[3] V.K. Garg. Heat transfer on a film-cooled rotating blade using different turbulence models. *International Journal of Heat and Mass Transfer*, 42:789–802, 1999.

[4] T. Kanda, G. Masuya, F. Ono, and Y. Wakamatsu. Effect of film cooling/regenerative cooling on scramjet engine performances. *Journal of Propulsion and Power*, 10(5):618–624, 1994.

[5] K. Takita. Film cooling effect of hydrogen on cylinder in supersonic airflow. *Journal of Spacecraft and Rockets*, 34(3):285–289, 1997.

[6] I. Gartshore, M. Salcudean, and I. Hassan. Film cooling injection hole geometry: hole shape comparison for compound cooling orientation. *AIAA Journal*, 39(8):1493–1499, 2001.

[7] A.M. Cary Jr. and J.N. Hefner. Film-cooling effectiveness and skin friction in hypersonic turbulent flow. *AIAA Journal*, 10(9):1188–1193, 1972.

[8] J.L. Stollery and A.A.M. El-Ehwany. A note on the use of a boundary-layer model for correlating film-cooling data. *International Journal of Heat and Mass Transfer*, 8:55–65, 1965.

[9] K. Parthasarathy and V. Zakkay. An experimental investigation of turbulent slot injection at Mach 6. *AIAA Journal*, 8(7):1302–1307, 1970.

[10] D.B. Spalding. Heat and mass transfer in boundary layers, part 2. film cooling. Technical report, Northern Research and Engineering Corp., Report No. 1058-2, Sep. 1962.

[11] J.P. O'Connor and A. Haji-Sheikh. Numerical study of film cooling in supersonic flow. *AIAA Journal*, 30(10):2426–2433, 1992.

[12] R.A. Seban. Heat transfer and effectiveness for a turbulent boundary layer with tangential fluid injection. *ASME Journal of Heat Transfer, Series C*, 82:303–312, 1960.

[13] R.A. Seban and L.H. Back. Velocity and temperature profiles in turbulent boundary layers with tangential injection. *ASME Journal of Heat Transfer, Series C*, 84:45–54, 1962.

[14] J.H. Chin, S.C. Skirvin, L.E. Hayes, and F. Burggraf. Film cooling with multiple slots and louvers. *ASME Journal of Heat Transfer, Series C*, 83:281–292, 1961.

[15] J.P. Hartnett, R.C. Birkebak, and E.R.G. Eckert. Velocity distributions, temperature distributions, effectiveness and heat transfer for air injected through a tangential slot into a turbulent boundary layer. *ASME Journal of Heat Transfer, Series C*, 83:293–306, 1961.

[16] W.K. Burns and J.L. Stollery. The influence of foreign gas injection and slot geometry on film cooling effectiveness. *International Journal of Heat and Mass Transfer*, 12:935–951, 1969.

[17] V.P. Lebedev, V.V. Lemanov, S.YA. Misyura, and V.I. Terekhov. Effects of flow turbulence on film cooling efficiency. *International Journal of Heat and Mass Transfer*, 38(11):2117–2125, 1995.

[18] J.S. Lee and I.S. Jung. Effects of bulk flow pulsations on film cooling with compound angle holes. *International Journal of Heat and Mass Transfer*, 45:113–123, 2002.

[19] H.W. Lee, J.J. Park, and J.S. Lee. Flow visualization and film cooling effectiveness measurements around shaped holes with compound angle orientations. *International Journal of Heat and Mass Transfer*, 45:145–156, 2002.

[20] R.L. Clark Jr., W.F. Ng, D.A. Walker, and J.A. Schetz. Large-scale structure in a supersonic slot-injected flowfield. *AIAA Journal*, 28(6):1045–1051, 1990.

[21] C.R. Hyde, B.R. Smith, J.A. Schetz, and D.A. Walker. Turbulence measurement for heated gas slot injection in supersonic flow. *AIAA Journal*, 28(9):1605–1614, 1990.

[22] F.T. Kwok, P.L. Andrew, W.F. Ng, and J.A. Schetz. Experimental investigation of a supersonic shear layer with slot injection of helium. *AIAA Journal*, 29(9):1426–1435, 1991.

[23] R. Bass, L. Hardin. R. Rodgers. and R. Ernst. Supersonic film cooling. *AIAA Paper 90-5239*, 1990.

[24] M.A. Stafford and R.J. Hartfield, Jr. Experimental investigation of slot injection into supersonic flow with and adverse pressure gradient. *AIAA Paper 93-2442*, 1993.

[25] T. Hansmann, H. Wilhelmi, and D. Bohn. An experimental investigation of the film-cooling process at high temperatures and velocities. *AIAA Paper 93-5062*, 1993.

[26] K.A. Juhany, M.L. Hunt, and J.M. Sivo. Influence of injectant Mach number and temperature on supersonic film cooling. *Journal of Thermophysics and Heat Transfer*, 8(1):59–67, 1994.

[27] K.A. Juhany and M.L. Hunt. Flowfield measurements in supersonic film cooling including the effect of shock-wave interaction. *AIAA Journal*, 32(3):578–585, 1994.

[28] T. Kanda, F. Ono, M. Takahashi, T. Saito, and Y. Wakamatsu. Experimental studies of supersonic film cooling with shock wave interaction. *AIAA Journal*, 34(2):265–271, 1996.

[29] T. Kanda and F. Ono. Experimental studies of supersonic film cooling with shock wave interaction (ii). *Journal of Thermophysics and Heat Transfer*, 11(4):590–593, 1997.

[30] B.E. Richards. Film cooling in hypersonic flow. PhD thesis, University of London, January 1967.

[31] B.E. Richards and J.L. Stollery. Turbulent gaseous film cooling in hypersonic flow. In *The Euromech 21 meeting on Transitional and Turbulent Boundary Layers, Toulouse*, 7th-11th Sep., 1970.

[32] B.E. Richards and J.L. Stollery. Laminar film cooling experiments in hypersonic flow. *Journal of Aircraft*, 16(3):177–180, 1979.

[33] V. Zakkay, C.R. Wang, and M. Miyazawa. Effect of adverse pressure gradient on film cooling effectiveness. *AIAA Journal*, 12(5):708–709, 1974.

[34] J.A. Majeski and R.H. Weatherford. Development of an empirical correlation for film-cooling effectiveness. *AIAA Paper 88-2624*, 1988.

[35] I.E. Beckwith and D.M. Bushnell. Calculation by a finite-difference method of supersonic turbulent boundary layers with tangential slot injection. Technical report, NASA TN D-6221, 1971.

[36] J. Wang. Prediction of turbulent mixing and film-cooling effectiveness for hypersonic flows. *AIAA Paper 89-1867*, 1989.

[37] W.P. Jones and B.E. Launder. The prediction of laminarization with a two-equation model of turbulence. *International Journal of Heat and Mass Transfer*, 15:301–314, 1972.

[38] R.J. Goldstein, E.R.G. Eckert, F.K. Tsou, and A. Haji-Sheikh. Film-cooling with air and helium injection through a rearward-facing slot into a supersonic air flow. Technical report, University of Minnesota, Heat Transfer Lab., TR60, Minneapolis, MN, Feb. 1965.

[39] B.R. Smith. The $k - kl$ turbulence and wall layer model for compressible flows. *AIAA Paper 90-1483*, 1990.

[40] B. Aupoix, A. Mignosi, S. Viala, F. Bouvier, and R. Gaillard. Experimental and numerical study of supersonic film cooling. *AIAA Journal*, 36(6):915–923, 1998.

[41] T. Cebeci. Calculation of compressible turbulent boundary layers with heat and mass transfer. *AIAA Journal*, 9(6):1091–1097, 1971.

[42] B.S. Baldwin and H. Lomax. Thin layer approximation and algebraic model for separated turbulent flows. *AIAA Paper 78-257*, 1978.

[43] B.E. Launder and B.I. Sharma. Application of the energy dissipation model of turbulence to the calculation of flows near a spinning disk. *Letters in Heat and Mass Transfer*, 1:131–138, 1974.

[44] K.Y. Chien. Predictions of channel and bounday-layer flows with a low-Reynolds-number turbulence model. *AIAA Journal*, 20(1):33–38, 1982.

[45] Y. Nagano and M. Tagawa. An improved $k - \epsilon$ model for boundary layer flows. *Journal of Fluids Engineering*, 112:33–39, 1990.

[46] R.M.C. So, H.S. Zhang, and C.G. Speziale. Near-wall modelling of the dissipation-rate equation. *AIAA Paper 92-0441*, 1992.

[47] D.C. Wilcox. Reassessment of the scale-determining equation for advanced turbulence models. *AIAA Journal*, 26(11):1299–1310, 1988.

[48] T.P. Sommer, R.M.C. So, and H.S. Zhang. Near-wall variable-Prandtl-number turbulence model for compressible flows. *AIAA Journal*, 31(1):27–35, 1993.

[49] S. Sarkar, G. Erlebacher, M.Y. Hussaini, and H.O. Kreiss. The analysis and modelling of dilatational terms in compressible turbulence. *Journal of Fluid Mechanics*, 227:473–493, 1991.

[50] D.C. Wilcox. Simulation of transition with a two-equation turbulence model. *AIAA Journal*, 32(2):247–255, 1994.

[51] T.J. Coakley. Turbulence modelling methods for the compressible Navier-Stokes equations. *AIAA Paper 83-1693*, 1983.

[52] P.G. Kassimatis, G.C. Bergeles, T.V. Jones, and J.W. Chew. Numerical investigation of the aerodynamics of the near-slot film cooling. *International Journal for Numerical Methods in fluids*, 32:97–117, 2000.

[53] K. Takita and G. Masuya. Effects of combustion and shock impingement on supersonic film cooling by hydrogen. *AIAA Journal*, 38(10):1899–1906, 2000.

[54] C.K.G. Lam and K. Bremhorst. A modified form of the $k - \epsilon$ model for predicting wall turbulence. *Transactions of the ASME, Journal of Fluids Engineering*, 103:456–460, 1981.

[55] Y.L. Lin and T.I.P. Shih. Film cooling of a cylindrical leading edge with injection through rows of compound-angle holes. *ASME Journal of Heat Transfer*, 123:645–654, 2001.

[56] F.R. Menter. Two-equation eddy-viscosity turbulence models for engineering applications. *AIAA Journal*, 32(8):1598–1605, 1994.

[57] D. Feszty, K.J. Badcock, and B.E. Richards. Numerical simulation of steady supersonic and hypersonic flows over simple bodies of revolution. Aero report 9902, University of Glasgow, March 3, 1999.

[58] P.L. Roe. Approximate Riemann solvers, parameter vectors, and difference schemes. *Journal of Computational Physics*, 135:250–258, 1997.

[59] D. Feszty. Numerical simulation and analysis of high-speed unsteady spiked body flows. PhD thesis, University of Glasgow, May 2001.

[60] P.A. Gnoffo. Point-implicit relaxation strategies for viscous, hypersonic flows. In *Computational Methods in Hypersonic Aerodynamics, edited by T.K.S. Murthy, Kluwer Academic Publishers*, pages 115–151, 1993.

[61] F. Cantariti, L. Dubuc, B. Gribben, M. Woodgate, K. J. Badcock, and B. E. Richards. Approximate Jacobians for the solution of the Euler and Navier-Stokes equations. Technical report, 5, University of Glasgow, UK, 1997.

[62] K. Badcock, F. Cantariti, and B. Gribben. Theory guide to PMB2D version 3.0. Technical report, University of Glasgow, UK, July 1998.

[63] K.J. Badcock, B.E. Richards, and M.A. Woodgate. Elements of computational fluid dynamics on block structured grids using implicit solvers. *Progress in Aerospace Sciences*, 36(5-6):351–392, 2000.

[64] D.C. Wilcox. *Turbulence modeling for CFD*. DCW Industries. Inc., 5354 Palm Drive, La Cañada, Calif., 1993.

[65] D.A. Johnson and L.S. King. A mathematically simple turbulence closure model for attached and separated turbulent boundary layers. *AIAA Journal*, 23(11):1684–1692, 1985.

[66] J.E. Bardina, P.G. Huang, and T.J. Coakley. Turbulence modeling validation, testing and development. NASA TM-110446, National Aeronautics and Space Administration, April 1997.

[67] L.D. Kral. Recent experience with different turbulence models applied to the calculation of flow over aircraft components. *Progress in Aerospace Sciences*, 34(7-8):481–541, 1998.

[68] P.R. Spalart and S.R. Allmaras. A one-equation turbulence model for aerodynamic flows. *AIAA Paper 92-0439*, 1992.

[69] P.R. Spalart and S.R. Allmaras. A one-equation turbulence model for aerodynamic flows. *La Recherche Aérospatiale*, 1:5–21, 1994.

[70] B.S. Baldwin and T.J. Barth. A one-equation turbulence transport model for high Reynolds number wall-bounded flows. *AIAA Paper 91-0610*, 1991.

[71] C.L. Rumsey and V.N. Vatsa. A comparison of the predictive capabilities of several turbulence models using upwind and central-difference computer codes. *AIAA Paper 93-0192*, 1993.

[72] M. Mani, P. Willhite, and J. Ladd. Performance of one-equation turbulence models in cfd applications. *AIAA Paper 95-2221*, 1995.

[73] G.R. Srinivasan, J.A. Ekaterinaris, and W.J. McCroskey. Evaluation of turbulence models for unsteady flows of an oscillating airfoil. *Computers & Fluids*, 24(7):833–861, 1995.

[74] V.A. Sai and F.M. Lutfy. Analysis of the Baldwin-Barth and Spalart-Allmaras one-equation turbulence models. *AIAA Journal*, 33(10):1971–1974, 1995.

[75] J.R. Edwards and S. Chandra. Comparison of eddy viscosity-transport turbulence models for three-dimensional, shock-separated flowfields. *AIAA Journal*, 34(4):756–763, 1996.

[76] R. Paciorri, W. Dieudonné, G. Degrez, J.M. Charbonnier, and H. Deconinck. Exploring the validity of the Spalart-Allmaras turbulence model for hypersonic flows. *AIAA Journal*, 35(2):121–126, 1998.

[77] A. Hellsten. Implementation of a one-equation turbulence model into the FINFLO flow solver. Report No B-49, Series B, Laboratory of Aerodynamics, Helsinki University of Technology, September 1996.

[78] U. Goldberg. Hypersonic flow heat transfer prediction using single equation turbulence models. *Journal of Heat Transfer*, 123:65–69, 2001.

[79] ICEM CFD Engineering Meshing Tutorial Manual Version 4.1. Tutorial manual, ICEM CFD Engineering, September 2000.

[80] O. Zeman. Dilatation dissipation: the concept and application in modelling compressible mixing layers. *Physics of Fluids A*, 2(2):178–188, 1990.

[81] D.C. Wilcox. Dilatation-dissipation corrections for advanced turbulence models. *AIAA Journal*, 30(11):2639–2646, 1992.

[82] B. Enquist and S. Osher. One-sided difference approximations for nonlinear conservation laws. *Mathematics of Computation*, 36(154):321–351, 1981.

[83] B. van Leer. Towards the ultimate conservative difference scheme. V. A second-order sequel to Godunov's method. *Journal of Computational Physics*, 32:101–136, 1979.

[84] G.D. van Albada, B. van Leer, and Jr. W.W. Roberts. A comparative study of computational methods in cosmic gas dynamics. *Astronomy and Astrophysics*, 108:76–84, 1982.

[85] O. Axelsson. *Iterative Solution Methods*. Cambridge University Press, 1994.

[86] J.H. Ferziger and M. Perić. *Computational Methods for Fluid Dynamics*. Springer, 1997.